UNIVERSITY OF OKLAHOMA

GRADUATE COLLEGE

IMITATING NATURE: THE EFFECTS OF ASYMMETRY AND STRAIN ON COPPER AND IRON COMPLEXES WITH SCHIFF BASE LIGANDS

A DISSERTATION

SUBMITTED TO THE GRADUATE FACULTY

in partial fulfillment of the requirements for the

Degree of

DOCTOR OF PHILOSOPHY

By

ANNA MARIA JOZWIUK
Norman, Oklahoma
2013

IMITATING NATURE: THE EFFECTS OF ASYMMETRY AND STRAIN ON COPPER AND IRON COMPLEXES WITH SCHIFF BASE LIGANDS

A DISSERTATION APPROVED FOR THE
DEPARTMENT OF CHEMISTRY AND BIOCHEMISTRY

BY

_____
Dr. Daniel T. Glatzhofer, Chair

_____
Dr. Robert P. Houser

_____
Dr. Robert K. Thomson

_____
Dr. Kenneth M. Nicholas

_____
Dr. Ronald L. Halterman

_____
Dr. Lee R. Krumholz

For my grandparents María and Jerzy

Acknowledgements

First and foremost I want to thank my main advisor, Dr. Robert Houser, for the great freedom in my projects and your faith in my independent work. At the same time you gave enough guidance and suggestions to accomplish the research projects. You managed to always make time for my cultural misunderstandings and any research related difficulties no matter how busy you were. Secondly, but certainly not less, I am thanking my current advisor, Dr. Daniel Glatzhofer, for adopting me into your group after Dr. Houser's departure and allowing me to complete my dissertation with a reasonably sized and fitting project. You showed me how to look at problems from the organic perspective.

Thanks to my committee members Dr. Nicholas, Dr. Thomson, Dr. Halterman and Dr. Krumholz, and also to the ones previously served on my committee, Dr. Cichewicz and Dr. Nanny. I would like to acknowledge the Richter-Addo and the Nicholas group for letting me use some of their instrumentation. I value the work of Dr. Powell, who did all the crystallography presented in this dissertation and Dr. Foster who performed the mass spectrometry measurements. Very much appreciated are GC-MS measurements conducted by Dr. Smith for Chapter 4. Dr. Warhausen's help with the spectro-electro chemical measurements is also greatly appreciated.

Thanks to my former group members Zhaodong, Audrey, especially Mike and Adam for your great friendship and support in the group. Sachin, thank you for allowing me to have a smooth start in the new group and for an encouraging atmosphere in the final steps of our dissertations! I also want to thank my current group members for accepting me into the group and for a warm transition.

Further I want to thank the staff at the Chemistry Department, in particular our glass blower Jim and Chad & Carl from the electronic shop. Without their support, part of my projects could not have been realized.

I am thankful for my roommates, Mike and Whitney, for giving me a second home and being my family in the US.

I am extremely grateful for the dedication and support from my parents, without whom it would have not been possible to accomplish this goal of graduating with a Ph. D. I also want to thank my grandparents who always believed in me. Thanks to my brother, Peter, for his spiritual support during my entire chemistry career.

Last but not least, thanks to the department of aviation for allowing me to enroll in flight classes and providing some respite from chemistry, especially during difficult times and transition to the new group. Chip, you were a great flight instructor and I am very thankful for your hard work with me and faith to accomplish my goal to earn my license.

Table of Contents

List of Tables

List of Figures

List of Schemes

Abbreviations

ADP	Adenosine diphosphate
Asp	Aspartate
ATP	Adenosine triphosphate
BC	Blue copper
CT	Charge transfer
CV	Cyclic voltammetry
Cys	Cysteine
deg	Degrees
DMF	Dimethylformamide
DMSO	Dimethyl sulfoxide
DNA	Deoxyribonucleic acid
EPR	Electron paramagnetic resonance
ESI	Electrospray ionization
Et_3N	Triethylamine
Fc	Ferrocene
GC-MS	Gas chromatography mass spectrometry
Glu	Glutamate
H_2L	2,2'-(2-Methyl-2-(pyridin-2-yl)propane-1,3-diyl)bis(azanediyl)-bis(methylene)diphenol
H_2L^1	2,2’-(2-Methyl-2-(pyridin-2-yl)propane-1,3-diyl)bis(azan-1-yl-1-ylidene)- bis(methan-1-yl-1-ylidene)diphenol

$H_2L^{5\text{-gem}}$	Pseudo-gem-N,N'-bissalicylidene-4,15-diamino[2.2]paracyclophane
$H_2L^{5\text{-ortho}}$	Pseudo-ortho-N,N'-bissalicylidene-4,16-diamino[2.2]paracyclophane
H_2L^{NO2}	2,2'-(2-Methyl-2-(pyridin-2-yl)propane-1,3-diyl bis(azanediyl)-bis(methylene)bis(4-nitrophenol)
$H_2L^{t\text{-Bu}}$	6,6'-(2-Methyl-2-(pyridin-2-yl)propane-1,3-diyl)bis(azanediyl)-bis(methylene)bis(2,4-di-tert-butylphenol)
$HBpz_3$	Hydrotripyrazol
His	Histidine
HL^2	2-((2-Methyl-2-(pyridin-2-yl)-3-(pyridin-2-ylmethyleneamino)propylimino)- methyl)phenol
HOMO	Highest occupied molecular orbital
Hr	Hemerythin
IR	Infrared
L^3	2-Methyl-2-(pyridin-2-yl)-$\boldsymbol{N}^1$,$\boldsymbol{N}^3$-bis(pyridin-2-ylmethylene)propane-1,3-diamine
L^4	5-Methyl-2,5-di(pyridin-2-yl)hexahydropyrimidine
LMCT	Ligand to metal charge transfer
MeCN	Acetonitrile
MeOH	Methanol
Me_2Fc	1,1'-Dimethylferrocene
Me_3TACN	1,4,7-Trimethyl-triazacyclononane

Met	Methionine
MLCT	Metal to ligand charge transfer
MMO	Methane monooxygenase
Mp	Melting point
MS	Mass spectrometry
m/z	Mass to charge ratio
NHE	Normal hydrogen electrode
NMR	Nuclear magnetic resonance
PAP	Purple acid phosphatase
PC	Plastocyanin
pMMO	Particulate methane monooxygenase
ppda	2-Methyl-2-pyridin-2-yl-propane-1,3-diamine
Rbr	Rubrerythrin
RNR	Ribonucleotide reductase
Salen	N,N'-Bis(salicylidene)ethylenediamine
SCE	Standard calomel electrode
sMMO	Soluble methane monooxygenase
SOMO	Singly occupied molecular orbital
TACN	1,4,7-Triazacylononane
TBAH	Tetrabutylammonium hexafluorophosphate
T_d	Tetrahedral
TMC	N-tetramethylcyclam
TPA	Tris(pyridyl)amine

μB	Effective magnetic moment
UV-Vis	Ultraviolet-visible
VSEPR	Valence shell electron pair repulsion

Abstract

Metalloenzymes are incredibly complex “machines” which catalyze reactions essential for life. Metal ions are found in more than half of all known proteins; particularly, copper and iron are abundant in active sites performing complex reactions. The coordination environment around the metal center itself drives the metal ion to undergo biospecific, highly optimized, and selective reactions, such as the oxidation of methane to methanol, splitting of water, or generation of ammonia. Most of the active sites are asymmetric and some metal ions are forced into strained geometries. These factors facilitate catalysis and electronic tuning. Against this background, aspects of strain and asymmetry were probed in model complexes with iron and copper ions. Utilizing Schiff base ligands as molecules that can be easily manipulated in steric and electronic properties *via* building block assembly, iron and copper complexes were synthesized.

The ferric diiron complexes $[(FeL)_2(\mu\text{-}OH)]^+$, $[(FeL^{NO2})_2(\mu\text{-}OH)]^+$ and $[(FeL)_2(\mu\text{-}O)]$ (L = 2,2'-(2-Methyl-2-(pyridin-2-yl)propane-1,3-diyl)bis(azanediyl)-bis(methylene)- diphenolate and L^{NO2} = 2,2'-(2-Methyl-2-(pyridin-2-yl)propane-1,3-diyl bis(azanediyl)- bis(methylene)bis(4-nitrophenolate)) show structural and spectroscopic similarities to bridged hydr(oxo)diiron containing active sites of metalloproteins. Unique properties of the ligand create asymmetry of the diiron unit as well as bent Fe–O–Fe structures. The stability of the bio-relevant mixed-valence state was investigated by electrochemical means, as well as by chemical reduction. Unfortunately, the Fe(II)/Fe(III) state is not accessible in the complex presented here. However, a mechanistic pathway of decomposition is suggested and an interesting feature of the

ligand used in this study may allow for stabilization and characterization of the mixed-valence state, and even further, it may reveal the role of a unique amino acid residue interaction with the diiron site in rubrerythrin.

Two copper(II) complexes (dimeric $[Cu(HL^2)]_2(ClO_4)_4$ and monomeric $[Cu(L^3)](ClO_4)_2$) with novel, related Schiff base ligands (HL^2 = 2-((2-Methyl-2-(pyridin-2-yl)-3-(pyridin-2-ylmethyleneamino)propylimino)- methyl)phenol and L^3 = 2-Methyl-2-(pyridin-2-yl)-$\boldsymbol{N}^1$,$\boldsymbol{N}^3$-bis(pyridin-2-ylmethylene)propane-1,3-diamine) were synthesized and characterized. One series of studies revealed a synthesis plan for asymmetric Schiff base complexes through unique properties of the ligand. It was shown that intermediate electronic tuning of the copper(II) complex is possible in the asymmetric complex compared to the fully symmetric analogues.

In another study, the aspect of geometrical strain was investigated. The distorted copper(II) complexes $[CuL^{5\text{-gem}}]$ and $[CuL^{5\text{-ortho}}]$ ($L^{5\text{-gem}}$ = Pseudo-gem-N,N'-bissalicylidene-4,15-diamino[2.2]paracyclophane and $L^{5\text{-ortho}}$ = Pseudo-ortho-N,N'-bissalicylidene-4,16-diamino[2.2]paracyclophane) which were obtained in this study are reminiscent of blue copper protein centers which allow for fast electron transfer by having geometries between tetrahedral and square planar. Structural and spectroscopic studies show that strain is present in both the solid and solution state. The distortion causes a shift in redox potential of about half a volt compared to square planar analogues. Initial studies revealed that strained complexes with other divalent metal ions are possible to form (e.g. $[CoL^{5\text{-gem}}]$ was isolated and characterized). Strained complexes are interesting for catalysis as geometrical strain may enhance reactivity.

CHAPTER 1

Introduction

1.1 Bioinorganic Chemistry

Life as we know it would not be possible without metal ions; about half of all the proteins contain metals [1]. Particularly, transition metals play a big role in metabolic processes, which are essential for life [2-4]. Compared to other metals found in metalloproteins like Mn, Mo, Ni, Co and Zn, Fe and Cu are by far the most common metal ions found in proteins. This is not surprising because iron and copper are particularly abundant in nature and this probably led to evolution of natural systems with these two metals. Iron is by far the most abundant transition metal *in vivo* averaging 60 mg/kg of body weight (about 75% of the iron is bound in hemoglobin) [5]. Copper on the other hand is considered a trace element, and about 150 mg are found in an adult human body [5].

In the first part of this chapter the reader will be given a broad overview of the role of metals in biological systems and the great diversity of different functions *in vivo*. Then the idea behind mimicking bioinorganic systems will be explained. Some examples of the state-of-the-art model chemistry will be shown. Finally, the background for the three projects of this dissertation will be introduced, which will lead into the individual project goals.

Bioinorganic chemistry is the science of metal species in biology. In this dissertation, the focus lies on metalloproteins and metalloenzymes. Metalloproteins are proteins which contain a metal center but do not catalyze a chemical reaction; examples are dioxygen carrying proteins [6] (e.g. hemerythrin, hemoglobin and hemocyanin), electron transfer proteins [7] (e.g. rubredoxin, plastocyanin) or metal ion storage/transfer proteins [8] (e.g. siderophores, ferritin). Metalloenzymes on the other

hand are biological units which perform catalytic reactions at a metal site. Some important catalytic reactions are given below, and different metal sites, with one example for each of several transition metal ions, are chosen to emphasize the diversity of biological systems. Molybdenum is found in nitrogenases, which are capable of nitrogen fixation [9], manganese is involved in the splitting of water (oxygen evolving complex in photosystem II) [10], iron plays a role in the oxidation of methane to methanol in soluble methane monooxygenase [11], cobalt is found in the active site of cobalamin and is involved in the metabolism of every cell [12], copper occupies the active site in nitrous oxide reductase and catalyzes the conversion of N_2O to molecular nitrogen as the last step in denitrification [13], zinc is found in superoxide dismutase, an enzyme which catalyzes the disproportionation of superoxide to hydrogen peroxide and dioxygen [14], nickel is part of the active site in hydrogenase, which catalyzes the reversible oxidation of dihydrogen [15].

When looking at a given metal ion, once placed into the proper (evolved) coordination environment in organisms, the metal ion will have a highly specialized function, acting as a specific bio-catalyst. Distinct environments and/or geometries and the oxidation state of the metal ion result in a different function of the active site. For example when looking at copper, this metal ion acts as an electron relay shuttling between Cu(II) and Cu(I) in electron transfer proteins such as blue copper proteins [16]. In different sites, it binds O_2 reversibly (e.g. in hemocyanin [6]), or activates dioxygen [17-19]. A subsequent reaction of the oxygen (oxidase, mono- and dioxygenase-like activity) can be observed. In oxidases the O-atom is not actually transferred onto a substrate but rather acts as an oxidizing agent (electron acceptor). O_2 is then converted

to either hydrogen peroxide ($2e^-$ redox process) or water ($4e^-$ redox process). An example for an oxidase is laccase, which is found in higher plants and fungi; it is involved in cell wall formation [20]. If the active site has mono- or dioxygenase activity, one or both O-atoms, respectively are added onto a substrate. Tyrosinase, a monooxygenase, catalyzes the hydroxylation of monophenols to *o*-diphenols, and therefore is involved in the initial step of L-DOPA biosynthesis [21]. Flavonol 2,4-dioxygenase, a dioxygenase, is an enzyme which catalyzes oxidative C–C bond cleavage [22].

On the other hand, it is also possible that different metal ions fulfill the same function and selected examples will be discussed below. The iron or copper metal center can function as an electron relay and therefore act as a redox mediator. Proper coordination environment will influence the redox potential of the metal ion [23]. In photosynthesis, ferredoxin, an iron-sulfur cluster [24], as well as blue copper proteins [25], play an important role as electron mediators for fast electron transfer processes.

The *in vivo* transport of dioxygen, for most organisms, requires the interaction of copper or iron with O_2. In vertebrates, hemoglobin, a heme-based iron complex, is responsible for reversibly binding dioxygen, while organisms like marine invertebrates use hemerythrin and mollusks use hemocyanin, a non-heme diiron and a dicopper site, respectively [26].

Methanotrophic bacteria, which are capable of oxidizing methane to methanol, show two active enzymes, particulate and soluble methane monooxygenase (pMMO and sMMO). Under normal conditions, pMMO is expressed [27], which is believed to be copper based. However, in the event of copper deficit, iron can be used and the well-

characterized iron based enzyme, sMMO, is expressed which catalyzes the same reaction. Active sites of a variety of copper and iron proteins will be discussed in more detail in Chapters 2-4.

Thus far, active sites containing different metals have been described. However, the complexity of biological systems deserves mentioning as well. First, the advantage of a protein environment around the active site will be explained, followed by an example of more complex protein-protein interactions. A cartoon is shown in Figure 1.1 and should simplify the complexity of proteins. In blue is shown a metalloenzyme with its active metal site imbedded (red). Several channels are depicted, a green channel for substrate intake and a blue one for product transport. Most proteins also have some kind of chain mechanism for electron transfer, commonly found are iron sulfur clusters which act as electron mediators (purple). The yellow structure symbolizes a regulatory protein which can close a different substrate channel (depicted in black) upon association with the main protein.

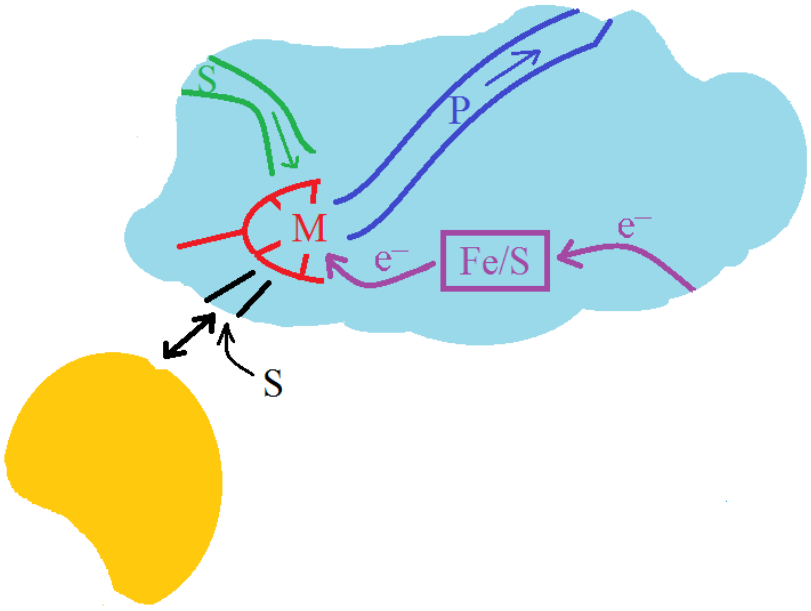

Figure 1.1. Cartoon which simplifies the complexity of a protein. Light blue: metalloenzyme; red: active site (containing a metal center = M) which is embedded in the protein; green: substrate channel (S = substrate); dark blue: product channel (P = product); purple: electron transfer chain (Fe/S = iron-sulfur cluster, e^- = electrons); yellow: regulatory protein which can cut off a channel entrance for a substrate (black).

The protein environment protects the active site and at the same time allows for selective substrate delivery and transport of the products away from the catalytic center. Some enzymatic sites cycle through high valent metal-oxo intermediates [28, 29], which are very reactive. In order to keep unwanted substrates away from getting oxidized, including the protein itself, and also to not quench the active species prematurely, it has to be "shielded" and only specific channels and their polarities allow for selected substrate diffusion and proton or electron transfer to the active site [30-32]. Proton shuttling and e-transfer within the protein have been studied recently in hydrogenase [33].

The enzyme sMMO, which is particularly interesting for scientists as it catalyzes remarkably the oxidation of methane, is chosen as an example for the importance of

protein-protein interactions. sMMO, which is a multicomponent monooxygenase, contains a regulatory protein (MMOB), the hydroxylase component, which hosts the active diiron core (MMOH), and a reductase (MMOR), which provides the source of electrons. Recently the Lippard group has investigated the interaction of MMOB with MMOH [34]. They report that binding of MMOB to MMOH closes pores which regulate the transport of dioxygen, methane, as well as protons, to the active site. This is an excellent example of the communication between two subunits, which allows for controlled oxidation and the addition of exact equivalents of electrons, protons and substrates to efficiently oxidize methane.

Bioinorganic chemistry is an interdisciplinary field for biochemists, coordination chemists and spectroscopists. Scientists either study the properties of metal containing natural systems or they mimic the structure or function of it. The goal of this research is to understand how natural systems work by studying the isolated natural system or by artificial mimicry to understand structure-function relationships. Since it is generally impractical to isolate enzymes and use them to perform reactions on a large scale, the ultimate goal is to construct rather simple artificial systems that perform catalysis reactions on industrial scale, comparable to metalloenzymes. Particularly important is C–H activation catalysis and harvesting of visible light for energy generation. Rather than trying to mimic entire complex natural systems, it is important to first understand smaller concepts, such as: Why do metal ion complexes have specific coordination geometries? How does the type of donor (e.g. N vs. O atom) influence the properties of the metal ion? Why do dimetallic centers have particular bridging units

(e.g. O vs. OH, carboxylate)? The next section will explore the idea behind bioinorganic mimicry and the difficulties associated with it.

1.2 Bioinorganic Modeling

Metal centers in biology are ligated by amino acid residues which hold the metal ion in distinct positions. The kind and number of ligands create a specific coordination geometry and give the metal center unique properties. Some of the important "bio-ligands" (including their donor functional group) are tyrosine (phenolate), histidine (imidazole), aspartate/glutamate (both carboxylate), cysteine (thiolate) and methionine (thioether), where typically the O, N, or S are donor atoms, which coordinate to the metal ion. Bioinorganic chemists try to isolate enzymes and structurally and spectroscopically characterize the active site in order to understand reactivity. Unfortunately, enzymes are difficult to purify while leaving their active sites intact, and even if successfully purified, the amounts of isolated enzymes are extremely small. The other problem in purification is the contamination of the active site by use of buffers where the native active structures can lose the original metal ion and bind different metal ions which were used during purification steps. Therefore, bioinorganic mimicry of active sites represents a major, important research field where active sites are synthetically generated. The active site is structurally mimicked and tested for reactivity to gain an understanding of structure-to-function relationships. If a model complex shows similar spectroscopic properties to an enzyme, it is very likely that both have similar structural features. Synthetic models are typically generated with the use of ligands, which are small organic molecules that have multiple donor atoms and mimic

distinct coordination geometries around the metal ion. By using model complexes and varying their substructures, one can sometimes understand why certain structural motifs in the natural active sites are important [3]. Despite the complexity of the protein environment, nature's active sites themselves are commonly asymmetric and great activity in the metal ion is achieved through strain, which causes pre-organization towards the transition state. The aspects of strain and asymmetry are discussed in later chapters.

In the following, an overview of popular ligands used in model chemistry will be given. The following figure shows tri- (first row), tetra- (second row) and pentadentate (third row) ligands. Probably most widely used are the ligands Me_3TACN, TPA, TMC and various porphyrin derivatives. Some references, where these ligands were used to answer bioinorganic chemistry related questions are given in the figure caption of Figure 1.2.

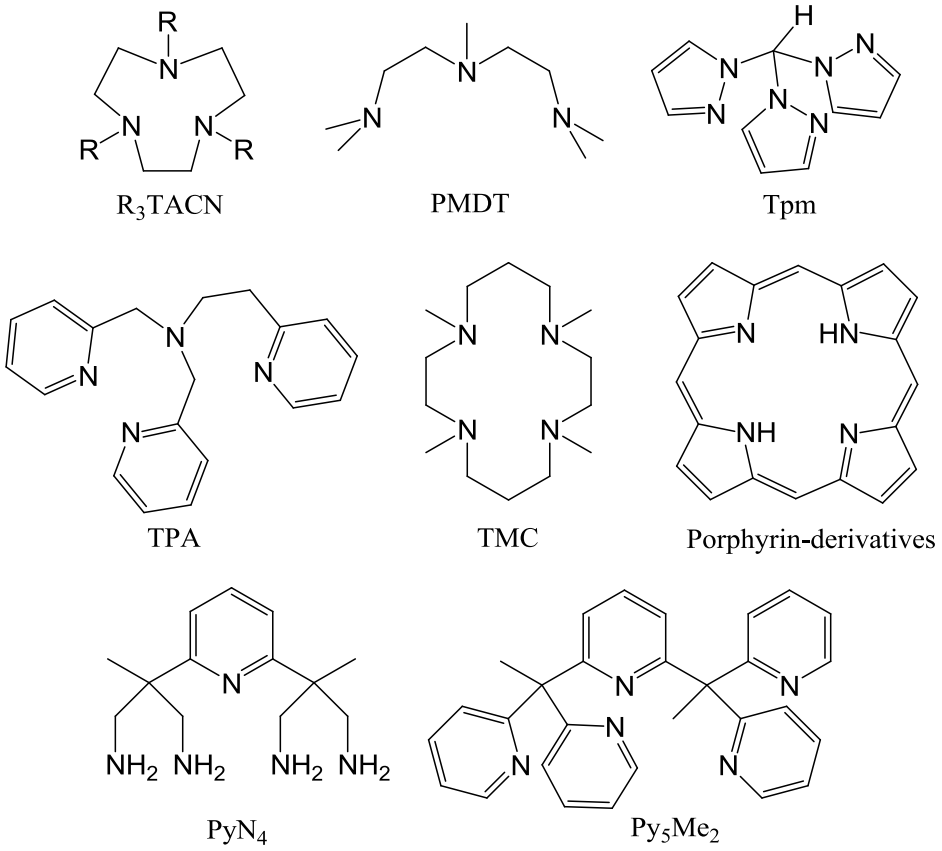

Figure 1.2. Examples of ligands used in bioinorganic model chemistry. TACN = triazacylononane [35]; PMDT = pentamethyldiethylenetriamine [36]; Tpm = tris(pyrazolyl)methane [37]; TPA = tris(2-pyridylmethyl)amine [38]; TMC = N-tetramethylcyclam [39]; Porphyrin-derivatives = porphyrins are usually substituted [40]; PyN_4 = and derivatives [41, 42]; Py_5Me_2 = 2,6-bis(1,1-bis(2-pyridyl)ethyl)pyridine [43].

There are several types of modeling; broken up into structural, functional and spectroscopical modeling. In structural modeling, scientists try to exactly remodel the active site with respect to coordination geometry and similarity in donors. An impressive example is given by the group of Agapie. They were able to build a structural model for the oxygen evolving complex, a manganese cluster, and with that gain further insight into the structure-function relationship of the active site.

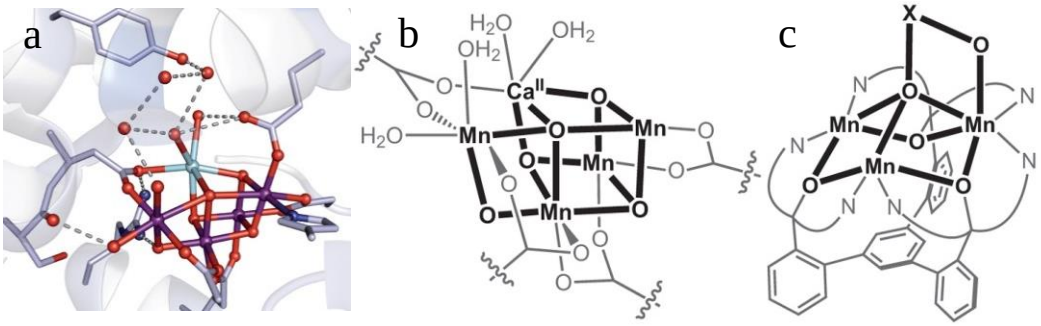

Figure 1. 3. a) Molecular structure of the oxygen evolving complex (O shown in red, Mn shown in purple and Ca shown in teal. b) Schematic depiction of the Mn_4O_5Ca cluster. c) Schematic depiction of the model complex by Agapie. Figure is adapted from reference [44].

The manganese cluster is the active site in photosystem II and catalyzes the splitting of water into dioxygen with release of four equivalents of protons and electrons (see Figure 1.3 a and b). The model complex (Figure 1.3 c) allowed for variation of the non-manganese ion within the cluster. Their studies revealed the role of calcium, which is crucial for the native enzyme in order to function properly, in the model complex. When calcium is replaced by other metal ions, such as sodium, strontium, zinc or yttrium, the redox properties of the cluster change [45].

An example for functional modeling is the work done by Meyer and coworkers [46]. They synthesized a diiron complex (see Figure 1.4 (right)), which mimics certain properties of Rieske proteins. Rieske centers contain a [2Fe-2S] cluster, which is involved in electron transfer reactions. Even though the model complex does not mimic the structure of the natural site it behaves very similarly. Figure 1.4 shows a schematic depiction of the Rieske center and the structure of the model compound for comparison. Meyer's group revealed that the model complex shows a shift in redox potential upon protonation and undergoes proton-coupled electron transfer, just like the natural site.

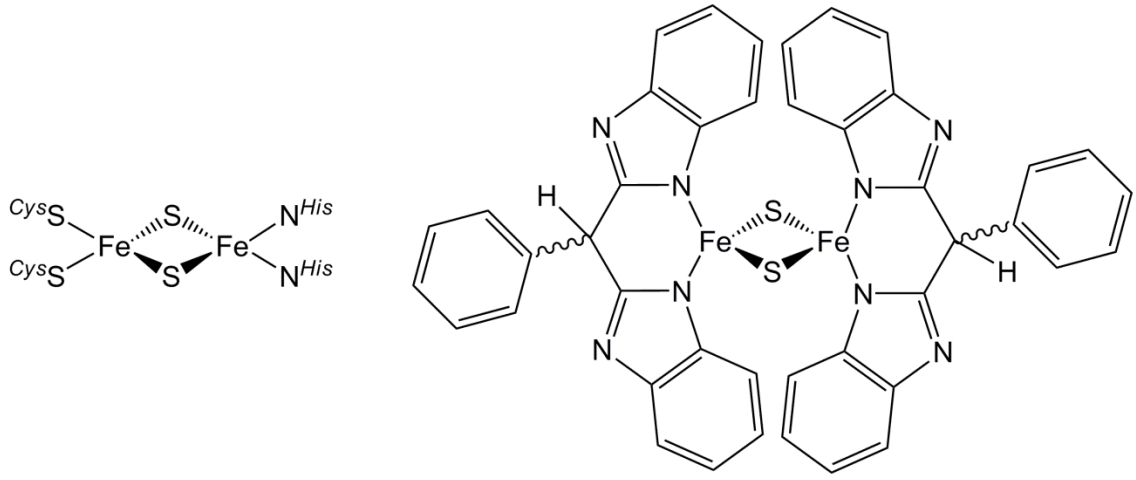

Figure 1.4. Schematic structure of the active site in Rieske proteins (left) and the model complex by Meyer (right).

Finally, an example of spectroscopical modeling will be given. Houser et al. [47] have modeled Cu_A, a copper site which is responsible for transfering electrons during turnover of nitrous oxide reductase and cytochrome c oxidase. Figure 1.5 shows the structures of the natural site of Cu_A and the model complex for comparison. Again, the structures are comparable, but the donor atoms are different. As evidenced by EPR spectroscopy, it was possible to mimic the mixed-valence ($Cu^{1.5}Cu^{1.5}$) state of the resting-state of Cu_A. Both cores give a seven-line hyperfine coupling pattern which is indicative of a delocalized unpaired electron shared between the two copper ions.

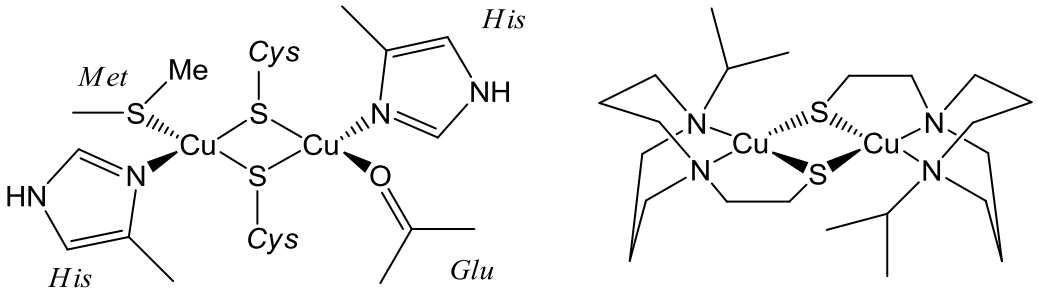

Figure 1.5. Structure of the active site in Cu_A (left) and model complex synthesized by Houser et al. (right).

A few examples of active site mimicry were given and structural, functional as well as spectroscopic modeling was explained. While all these studies are important to gain further understanding of the active site in metalloproteins, progress is under way to take model chemistry to the next level of complexity. One excellent example of a highly engineered model complex is presented by the group of Chan [48]. A functional inorganic complex with a "protective capsule" similar to the protective environment in proteins, has been synthesized. The complex is able to oxidize methane to methanol. It has been speculated that pMMO may contain a tricopper cluster in the active site. With that inspiration the authors have made the tricopper complex shown in Figure 1.6. The active species is believed to be a [Cu(II)Cu(II)(μ-$O)_2$Cu(III)] cluster, created upon reaction of [Cu(I)Cu(I)Cu(I)] with molecular oxygen.

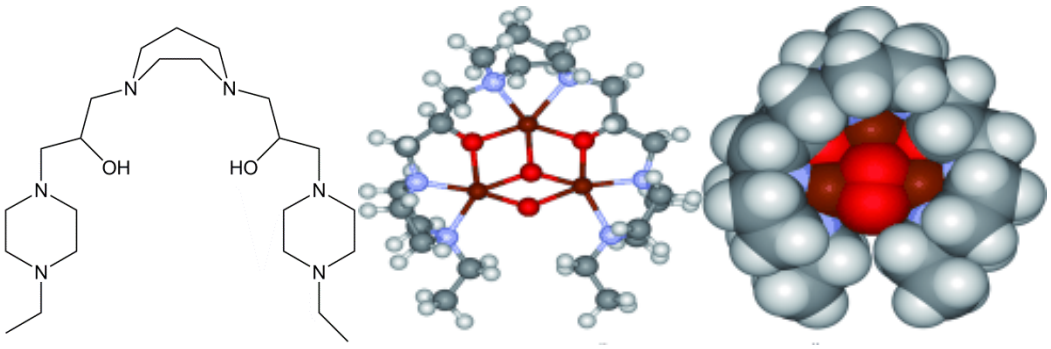

Figure 1.6. Ligand used in the model study by Chang (left) and computed structure of the tricopper cluster [Cu(II)Cu(II)(μ-$O)_2$Cu(III)] (nitrogen in blue; copper in dark red; oxygen in light red) with space filling model (right). Right side of figure is adapted from reference [48].

1.3 Previous Studies

The ligands shown in Figure 1.2 as well as those used in the model examples are rather complicated to synthesize and variations of them (meaning sterically or electronically changed) are not easily obtained. Keeping synthetic ligands simple allows for efficient synthesis with only a few steps. Schiff base ligands are fairly easily obtained upon condensation of an amine with an aldehyde. Both the amino unit and the aldehyde can be varied and allow for building block variations, which results in diverse variation of the final ligand (see Chapter 3 for an expanded discussion of Schiff base ligands). The synthesis of asymmetric ligands is definitely more complicated, but there are some procedures that can be applied (see Chapter 3). Ligands can also be varied by addition of steric groups to protect certain sites around the metal ion. Strain can be generated by the use of double bonds or incorporation of strain-inducing linkers. Electronic changes can also be made by substitution of non-coordinating residues. In this thesis the induction of strain and asymmetry, electronic tuning and some concepts of asymmetric synthesis are applied to Schiff base derivatives and discussed below.

Schiff bases contain a $R^1R^2C=NR^3$ functional group (imine) and are condensation products of the reaction of primary amines with aldehydes. Here, either 2-methyl-2-pyridine-2-ylpropane-1,3-diamine (ppda) (in Chapters 2 and 3) or diamino[2.2]paracyclophane (in Chapter 4) is used as the amine unit (see Figure 1.7), and either salicylic aldehyde or 2-pyridinecarboxaldehyde is used as the aldehyde for the Schiff base condensation reaction. While salicylic aldehyde is a standard aldehyde used in Schiff base chemistry, derivatives of 2-pyridinecarboxaldehyde are also explored. The latter is much more electron deficient and will allow for electronic tuning.

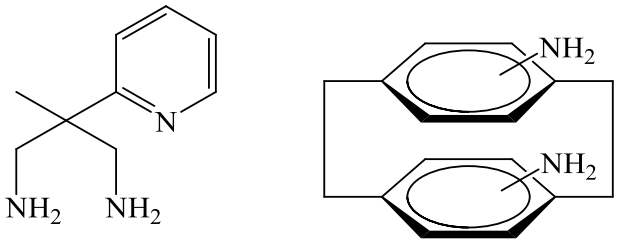

Figure 1.7. Structure of ppda and diamino[2.2]paracyclophane, respectively.

Ppda was introduced for the first time by L. Gade in 1997 [49]. The research group of Dr. Houser has used this pyridyldiamine as a common backbone to derive imine, amine and amide ligands (see Figure 1.8) and initial complexation studies with iron and copper revealed interesting results [50, 51].

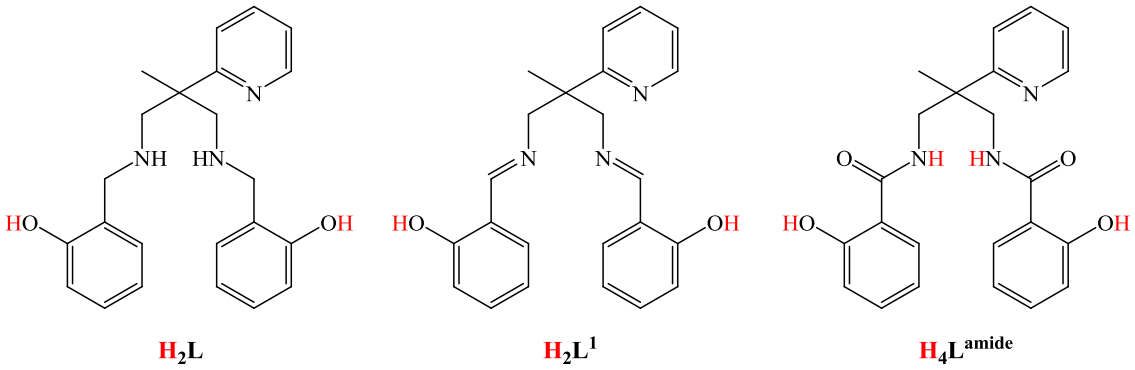

Figure 1.8. Amine, imine and amide ligands derived from ppda. Highlighted in red are hydrogen atoms which can be readily removed using weak bases.

The ligand H_2L (see Figure 1.8) has reduced strain due to the single C–N bonds but having a secondary amine present, the N–H group is available for H-bonding interactions. Hydrogen bonding between N–H and the phenolate O-atom causes asymmetry and strain in binuclear iron complexes, previously shown by R. Shakya et al. [50]. A simplified representation of the coordination mode of that diiron complex is depicted in Figure 1.9. The OH-bridged diiron complex (OH originated from water) is structurally supported by intramolecular hydrogen bonding. This results in an off-linear bridging mode of the Fe–O–Fe unit and also causes a distinct, asymmetric coordination around each iron center. It was shown that introduction of *t*Bu-groups into the phenol units changed the electronic effects of the diiron complex and the bulkiness of the *t*Bu-substituent caused the formation of an almost linear oxo-bridged complex without any inter-ligand hydrogen bonding.

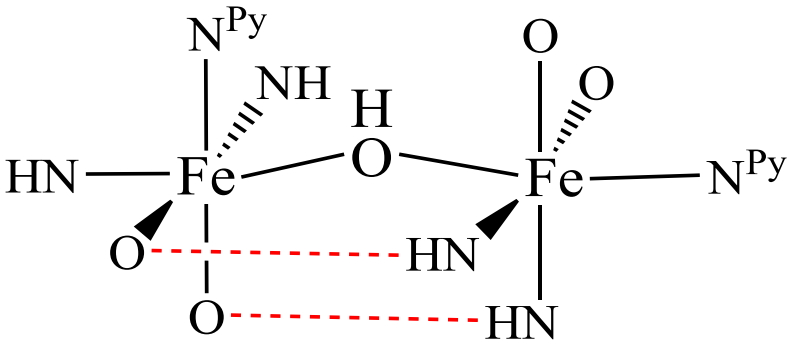

Figure 1.9. Asymmetric coordination around the iron centers caused by NH–O hydrogen bonding. Each iron center is coordinated through L (N_3O_2 donor) in a pentadentate fashion, where N^{py} represents the pyridyl-nitrogen atom, NH is the amine and O is from phenolate (note: the bridging OH ligand originates from water).

In a different study, using the three ligands depicted in Figure 1.8, we showed that nuclearity of copper complexes changes depending on the use of the amine, imine or amide functional group [51]. We obtained mono-, tri- and hexanuclear complexes. The pyridyl nitrogen atom does not coordinate in complexes with H_2L and H_2L^1 (see representation of the copper(II) ion coordination environment in Figure 1.10) while when using H_4L^{amide} pyridine does act as a donor (see Figure 1.11). The electrochemical behavior of the three complexes was studied and only the mononuclear complex [CuL] showed electrochemical reversibility.

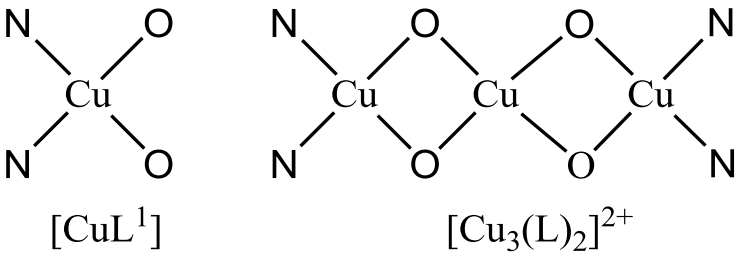

Figure 1.10. Represenation of the coordination environment around the copper ions for complexes using H_2L and H_2L^1.

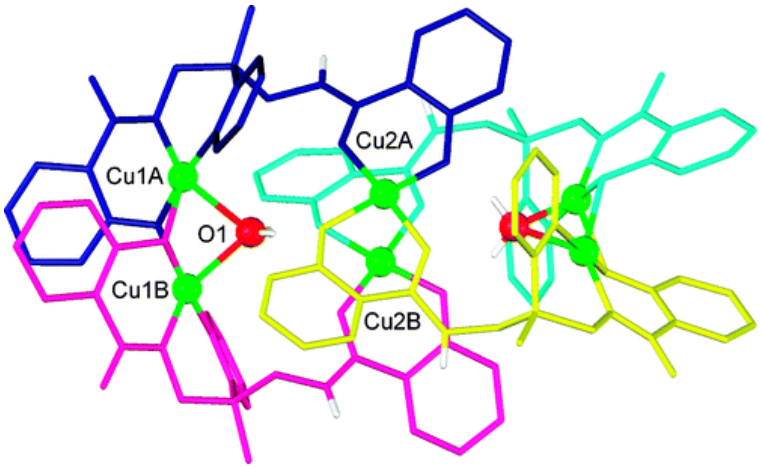

Figure 1.11. Representation of the X-ray crystal structure of $[Cu_6(HL^{amide})_4(H_2O)_2]$. Each ligand is illustrated in a different color for clarity (green: copper, red: oxygen). Figure is adapted from reference [51].

Figure 1.12 illustrates the ligands pseudo-ortho-N,N'-bissalicylidene-4,12-diamino[2.2]paracyclophane ($H_2L^{5\text{-ortho}}$) and pseudo-gem-N,N'-bissalicylidene-4,13-diamino[2.2]paracyclophane ($H_2L^{5\text{-gem}}$) which are used in this work. The Schiff base formed from pseudo-ortho-4,12-diamino[2.2]paracyclophane produces a chiral complex when coordinated to the metal ion. Previously, Morvant has shown that $H_2L^{5\text{-ortho}}$, in the presence of copper, catalyzes cyclopropanation of alkenes [52]. However, the copper(II) complex was not characterized in the solid state and was only superficially characterized spectroscopically.

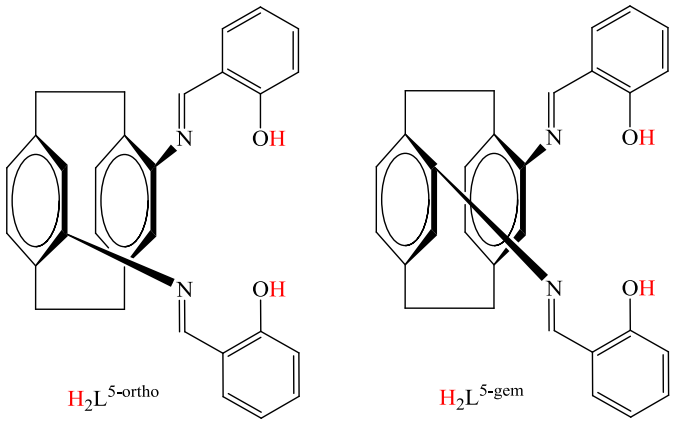

Figure 1.12. Structures of the ligands $H_2L^{5\text{-ortho}}$ and $H_2L^{5\text{-gem}}$. Highlighted in red are hydrogen atoms which can be readily removed using weak bases.

1.4 Project Goals

One of the project goals was to continue work on asymmetric diferric complexes using the reduced Schiff base H_2L and explore whether the asymmetry caused by hydrogen bonding of the ligand would allow for stabilization of a mixed-valence diiron(II/III) complex, commonly found as an intermediate in catalytic cycles of asymmetric diiron enzymes. Thus far, one symmetric model complex has been made. However, it was shown to be very unstable. Additionally, it should be investigated if an electron withdrawing substituent (like NO_2) on the ligand would significantly lower the reduction potential of the diferric complex, and if it would allow for the isolation of a more stable mixed-valence complex. Progress on the diiron chemistry is summarized in Chapter 2.

Different copper complexes with ligands depicted in Figure 1.8 were formed to probe the electronic nature of the Cu(I)/Cu(II) redox couple. The use of the Schiff base H_2L^1 resulted in reversible electrochemical behavior. Following up on the electronic studies, it should be explored how much the redox potential of the copper ion could be

tuned by using different aldehydes. 2-Pyridinecarboxaldehyde seemed an appropriate candidate due to its electron poor nature and, hypothetically, it should allow for easier reduction of the complex. Using ppda as the amine and two equivalents of 2-pyridinecarboxaldehyde yielded the symmetric ligand without any complications. One of the research goals was to synthesize the asymmetric ligand using one equivalent of each carbonyl with ppda to allow for accessibility of an intermediate redox potential. In order to obtain the pure asymmetric ligand, the ring structured hexahydropyrimidine intermediate was discovered to be important in aiding the synthesis of the asymmetric ligand. This chemistry is discussed in Chapter 3. Substantial parts of this chapter have been published in a journal article: Jozwiuk, A; Wang, Z.; Powell, D. R; Houser, R. P., *Copper(II) complexes of symmetric and asymmetric bis(imine) ligands: Tuning the Cu(I)/Cu(II) redox couple.* Inorganica Chimica Acta **2013,** *394,* 415-422.

We know that the pyridyl group of H_2L^1 is non-coordinating and complexes that are formed with copper(II) ions are square planar. Instead of using ppda, diamino[2.2]paracyclophane would allow for significant addition of strain and force the metal center into a tense coordination environment. The question arose of how that would affect the geometry and electronic properties of the copper complex. The goal was to structurally and electrochemically characterize the pseudo-ortho and pseudo-gem Schiff base derivatives and compare and contrast those. Initial studies where $H_2L^{5\text{-ortho}}$ and $H_2L^{5\text{-gem}}$ could be used as a catalyst in allylic oxidation reactions were performed and the question answered how the two conformers differ in reactivity. Attempts were also made on the synthesis of other metal complexes with the two ligands. The results are presented in Chapter 4.

1.4 References

1. Thomson, A. J.; Gray, H. B., *Bio-inorganic chemistry*. Current Opinion in Chemical Biology **1998,** *2*, 155-158.

2. Frausto da Silva, J. J. R.; Williams, R. J. P., *The biological chemistry of the elements. The inorganic chemistry of life*. 2001, New York, USA: Oxford University Press.

3. Lippard, S. J.; Berg, J. M., *Principles of Bioinorganic Chemistry*. 1994, USA: University Science Books.

4. Kaim, W.; Schwederski, B., *Bioinorganic Chemistry; Inorganic Elements in the Chemistry of Life*. 1994: Wiley.

5. Alsfasser, R.; Janiak, C.; Klapötke, T.; Meyer, H.-J., *Moderne Anorganische Chemie*, ed. E. Riedel. 2008, Berlin: Walter de Gruyter GmbH & Co. KG.

6. Kurtz Jr., D. M., *Oxygen-carrying proteins: three solutions to a common problem.* Essays in Biochemistry **1999,** *34*, 85-100.

7. Gray, H. B.; Ellis Jr., W. R., *Electron Transfer*. Bioinorganic Chemistry. 1194, Mill Valley, CA: University Science Books.

8. Theil, E. C.; Raymond, K. N., *Transition-Metal Storage, Transport, and Biomineralization*. Bioinorganic Chemistry. 1994, Mill Valley, CA: University Science Books.

9. Seefeldt, L. C.; Hoffman, B. M.; Dean, D. R., *Mechanism of Mo-Dependent Nitrogenase.* Annual Review of Biochemistry **2009,** *78*, 701-722.

10. Cady, C. W.; Crabtree, R. H.; Brudvig, G. W., *Functional models for the oxygen-evolving complex of photosystem II.* Coordination Chemistry Reviews **2008,** *252*, 444-455.

11. Merkx, M.; Kopp, D. A.; Sazinsky, M. H.; Blazyk, J. L.; Müller, J.; Lippard, S. J., *Dioxygen Activation and Methane Hydroxylation by Soluble Methane Monooxygenase: A Tale of Two Irons and Three Proteins.* Angewandte Chemie International Edition **2001,** *40*, 2782-2807.

12. Roth, J.; Lawrence, J.; Bobik, T., *COBALAMIN (COENZYME B12): Synthesis and Biological Significance.* Annual Review of Microbiology **1996,** *50*, 137-181.

13. Pauleta, S. R.; Dell'Acqua, S.; Moura, I., *Nitrous oxide reductase.* Coordination Chemistry Reviews **2013,** *257*, 332-349.

14. Fridovich, I., *Superoxide Dismutases.* Annual Review of Biochemistry **1975,** *44*, 147-159.

15. Ogata, H.; Lubitz, W.; Higuchi, Y., *[NiFe] hydrogenases: structural and spectroscopic studies of the reaction mechanism.* Dalton Transactions **2009,** *0*, 7577-7587.

16. Bertini, G.; Stiefel, V., *Biological Inorganic Chemistry Structure & Reactivity*, ed. J. Stiefel. 2007, USA: University Science Books.

17. Mirica, L. M.; Ottenwaelder, X.; Stack, T. D. P., *Structure and Spectroscopy of Copper−Dioxygen Complexes.* Chemical Reviews **2004,** *104*, 1013-1046.

18. Bento, I.; Carrondo, M. A.; Lindley, P. F., *Reduction of dioxygen by enzymes containing copper.* J Biol Inorg Chem **2006,** *11*, 539-547.

19. Solomon, E. I.; Sundaram, U. M.; Machonkin, T. E., *Multicopper Oxidases and Oxygenases.* Chemical Reviews **1996,** *96*, 2563-2606.

20. Riva, S., *Laccases: blue enzymes for green chemistry.* Trends in biotechnology **2006,** *24*, 219-226.

21. Sánchez-Ferrer, Á.; Neptuno Rodríguez-López, J.; García-Cánovas, F.; García-Carmona, F., *Tyrosinase: a comprehensive review of its mechanism.* Biochimica et Biophysica Acta (BBA) - Protein Structure and Molecular Enzymology **1995,** *1247*, 1-11.

22. Kaizer, J.; Pap, J. S.; Speier, G., *Copper Dioxygenases*, in *Copper-Oxygen Chemistry*. 2011, John Wiley & Sons, Inc. p. 23-52.

23. Moore, G. R.; Pettigrew, G. W.; Rogers, N. K., *Factors influencing redox potentials of electron transfer proteins.* Proceedings of the National Academy of Sciences **1986,** *83*, 4998-4999.

24. Johnson, D. C.; Dean, D. R.; Smith, A. D.; Johnson, M. K., *STRUCTURE, FUNCTION, AND FORMATION OF BIOLOGICAL IRON-SULFUR CLUSTERS.* Annual Review of Biochemistry **2005,** *74*, 247-281.

25. Bendall, D., *Protein Electron Transfer*. 1996, UK: BIOS Scientific Publishers Ltd.

26. Bertini, I.; Gray, H. B.; Stiefel, E. I.; Valentine; Selverstone, J., *Biological Inorganic Chemistry - Structure & Reactivity*. 2007, USA: University Science Books.

27. Balasubramanian, R.; Smith, S. M.; Rawat, S.; Yatsunyk, L. A.; Stemmler, T. L.; Rosenzweig, A. C., *Oxidation of methane by a biological dicopper centre.* Nature **2010,** *465*, 115-119.

28. Shaik, S.; Hirao, H.; Kumar, D., *Reactivity of High-Valent Iron–Oxo Species in Enzymes and Synthetic Reagents: A Tale of Many States.* Accounts of Chemical Research **2007,** *40*, 532-542.

29. Lee, J. Y.; Lee, Y.-M.; Kotani, H.; Nam, W.; Fukuzumi, S., *High-valent manganese(v)-oxo porphyrin complexes in hydride transfer reactions.* Chemical Communications **2009,** *0*, 704-706.

30. Exner, T.; Keil, M.; Moeckel, G.; Brickmann, J., *Identifification of Substrate Channels and Protein Cavities.* J Mol Model **1998,** *4*, 340-343.

31. Barney, B. M.; Yurth, M. G.; Dos Santos, P. C.; Dean, D. R.; Seefeldt, L. C., *A substrate channel in the nitrogenase MoFe protein.* J Biol Inorg Chem **2009,** *14*, 1015-1022.

32. Huang, X.; Holden, H. M.; Raushel, F. M., *CHANNELING OF SUBSTRATES AND INTERMEDIATES IN ENZYME-CATALYZED REACTIONS.* Annual Review of Biochemistry **2001,** *70*, 149-180.

33. McCullagh, M.; Voth, G. A., *Unraveling the Role of the Protein Environment for [FeFe]-Hydrogenase: A New Application of Coarse-Graining.* The Journal of Physical Chemistry B **2013,** *117*, 4062-4071.

34. Lee, S. J.; McCormick, M. S.; Lippard, S. J.; Cho, U.-S., *Control of substrate access to the active site in methane monooxygenase.* Nature **2013,** *494*, 380-384.

35. Fry, F. H.; Fischmann, A. J.; Belousoff, M. J.; Spiccia, L.; Brügger, J., *Kinetics and Mechanism of Hydrolysis of a Model Phosphate Diester by [Cu(Me3tacn)(OH2)2]2+ (Me3tacn = 1,4,7-Trimethyl-1,4,7-triazacyclononane).* Inorganic Chemistry **2005,** *44*, 941-950.

36. Patel, R. N.; Kumar, S.; Pandeya, K. B., *E.s.r., visible and SOD studies of imidazolate bridged Cu2II,II, CuIIZnII and CuIINiII complexes with pentamethyldiethylenetriamine as capping ligand: a plausible model for superoxide dismutase.* Journal of Inorganic Biochemistry **2002,** *89*, 61-68.

37. Bigmore, H. R.; Lawrence, S. C.; Mountford, P.; Tredget, C. S., *Coordination, organometallic and related chemistry of tris(pyrazolyl)methane ligands.* Dalton Transactions **2005,** *0*, 635-651.

38. Lim, M. H.; Rohde, J.-U.; Stubna, A.; Bukowski, M. R.; Costas, M.; Ho, R. Y. N.; Münck, E.; Nam, W.; Que, L., *An FeIVO complex of a tetradentate tripodal nonheme ligand.* Proceedings of the National Academy of Sciences **2003,** *100*, 3665-3670.

39. Fukuzumi, S.; Morimoto, Y.; Kotani, H.; Naumov, P.; Lee, Y.-M.; Nam, W., *Crystal structure of a metal ion-bound oxoiron(IV) complex and implications for biological electron transfer.* Nat Chem **2010,** *2*, 756-759.

40. Goodrich, L. E.; Roy, S.; Alp, E. E.; Zhao, J.; Hu, M. Y.; Lehnert, N., *Electronic Structure and Biologically Relevant Reactivity of Low-Spin {FeNO}8 Porphyrin Model Complexes: New Insight from a Bis-Picket Fence Porphyrin.* Inorganic Chemistry **2013**.

41. Grohmann, A., *Tetrapodal pentadentate ligands: Single site reactivity and bond activation in iron(II) complexes.* Dalton Transactions **2010,** *39*, 1432-1440.

42. Jozwiuk, A.; Ünal, E. A.; Leopold, S.; Boyd, J. P.; Haryono, M.; Kurowski, N.; Escobar, F. V.; Hildebrandt, P.; Lach, J.; Heinemann, F. W.; Wiedemann, D.; Irran, E.; Grohmann, A., *Copper Complexes of "Superpodal" Amine Ligands and Reactivity Studies towards Dioxygen.* European Journal of Inorganic Chemistry **2012,** *2012*, 3000-3013.

43. Karunadasa, H. I.; Montalvo, E.; Sun, Y.; Majda, M.; Long, J. R.; Chang, C. J., *A Molecular MoS2 Edge Site Mimic for Catalytic Hydrogen Generation.* Science **2012,** *335*, 698-702.

44. Cook, S. A.; Borovik, A. S., *Inorganic chemistry: Deconstructing water oxidation.* Nat Chem **2013,** *5*, 259-260.

45. Tsui, E. Y.; Tran, R.; Yano, J.; Agapie, T., *Redox-inactive metals modulate the reduction potential in heterometallic manganese–oxido clusters.* Nat Chem **2013,** *5*, 293-299.

46. Albers, A.; Bayer, T.; Demeshko, S.; Dechert, S.; Meyer, F., *A Functional Model for the Rieske Center: Full Characterization of a Biomimetic N-Ligated [2Fe-2S] Cluster in Different Protonation States.* Chemistry – A European Journal **2013**, DOI: 10.1002/chem.201301760.

47. Houser, R. P.; Young, V. G.; Tolman, W. B., *A Thiolate-Bridged, Fully Delocalized Mixed-Valence Dicopper(I,II) Complex That Models the CuA Biological Electron-Transfer Site.* Journal of the American Chemical Society **1996,** *118*, 2101-2102.

48. Chan, S. I.; Lu, Y.-J.; Nagababu, P.; Maji, S.; Hung, M.-C.; Lee, M. M.; Hsu, I. J.; Minh, P. D.; Lai, J. C. H.; Ng, K. Y.; Ramalingam, S.; Yu, S. S. F.; Chan, M. K., *Efficient Oxidation of Methane to Methanol by Dioxygen Mediated by Tricopper Clusters.* Angewandte Chemie International Edition **2013,** *52*, 3731-3735.

49. Friedrich, S.; Schubart, M.; Gade, L. H.; Scowen, I. J.; Edwards, A. J.; McPartlin, M., *Titanium and Zirconium Complexes Containing a Novel Dianionic Trifunctional Amido Ligand.* Chemische Berichte **1997,** *130*, 1751-1759.

50. Shakya, R.; Powell, D. R.; Houser, R. P., *Unsupported μ-Oxo- and μ-Hydroxo-Iron(III) Dimers and Mononuclear Iron(III) Complexes with Pyridylbis(aminophenol) Ligands.* European Journal of Inorganic Chemistry **2009,** *2009*, 5319-5327.

51. Shakya, R.; Jozwiuk, A.; Powell, D. R.; Houser, R. P., *Synthesis and Characterization of Polynuclear Copper(II) Complexes with Pyridylbis(phenol) Ligands.* Inorganic Chemistry **2009,** *48*, 4083-4088.

52. Morvant, M. C., *Synthesis, properties, and applications of polynitro- and polyamino[2.2]paracyclophanes.* Dissertation **1996,** Norman, Oklahoma.

CHAPTER 2

Unsupported, Asymmetric (Hydr)oxo-bridged Diiron Complexes

2.1 Background

2.1.1 Proteins with Diiron Cores

The (hydr)oxo bridged diiron unit (see Figure 2.1) is commonly found in active sites of proteins [1-3]. This is not surprising due to the high stability and readily formation of this sub-structure in solution. The synthetic "spontaneous self-assembly" of a (μ-oxo)bis(carboxylato)diiron(III) core with different capping ligands L and carboxylates indicates a high thermodynamic stability of the diiron unit [1]. Typically, an iron(III) salt can be combined with NaO_2CR and a ligand L in solution to yield $[Fe_2O(CO_2R)_2L]$ [4, 5].

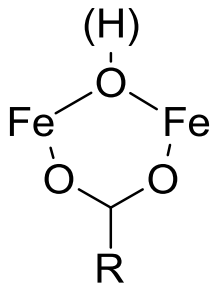

Figure 2.1. Schematic depiction of the μ-((hydr)oxo)diiron unit commonly found in diiron centers of proteins; some structures show one or two further supporting carboxylates (RCO_2^-).

In (hydr)oxo-bridged diiron enzymatic active sites, carboxylate groups from the amino acids aspartate and glutamate are found to further support the core. Diiron proteins are nicely summarized in a review by Lippard [3] and some proteins will be discussed in the following to give the reader a broad introduction to the structural variety and the function of the individual sites.

Hemerythrin (Hr), a protein found in marine invertebrates, is capable of reversibly binding dioxygen [6]. The active site contains a diiron unit that is hydroxo-bridged and asymmetric. One iron ion is sixfold coordinated while the other iron has

five ligands. Two bridging acetate groups from aspartate and glutamate support the diiron unit by bridging the two iron centers (see Figure 2.2). The remaining ligands are five imidazoles from histidine residues. In the fully reduced state (deoxyHr) the diiron unit is hydroxo bridged and one iron site has only five donors, leaving one open coordination spot, where O_2 can bind. After redox interaction with the metal centers, dioxygen is reduced to the hydroperoxo ion, the iron centers are oxidized to the diferric state and an oxo bridge remains (oxyHr). The hydroperoxo species is stabilized *via* hydrogen bonding to the bridging oxygen [7-9].

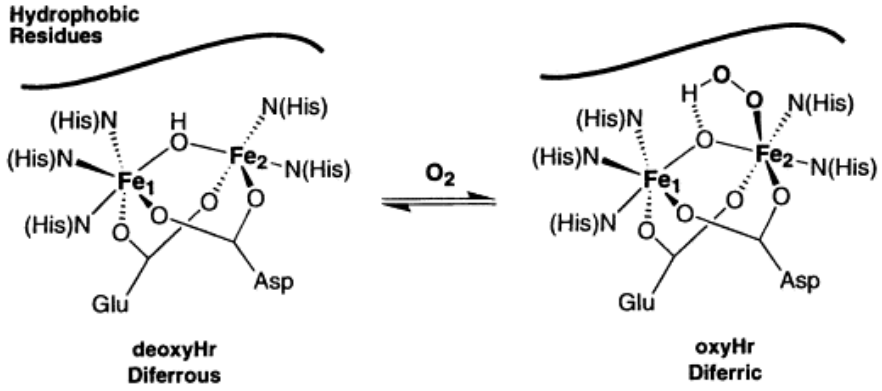

Figure 2.2. Reversible O_2 binding at the diiron site of hemerythrin. Figure is adapted from reference [7].

Another class of enzymes, namely soluble methane monooxygenase (sMMO), activates molecular oxygen and is capable of transferring one of the oxygen atoms onto a substrate (monooxygenase activity). This enzyme is found in methanotrophic bacteria (see Figure 2.3 for an illustration of the active site) and catalyzes the oxidation of methane to methanol [7]. This reaction is particularly of interest because the enzyme is capable of activating the C–H bond without over oxidation, a task difficult to mimic in synthetic chemistry. Currently the synthesis of methanol on industrial scale is performed via high pressure and high temperature syngas synthesis indirectly from

methane. First methane is converted with water to generate syngas (H_2 and CO) which is then further reacted to give methanol in another step [10].

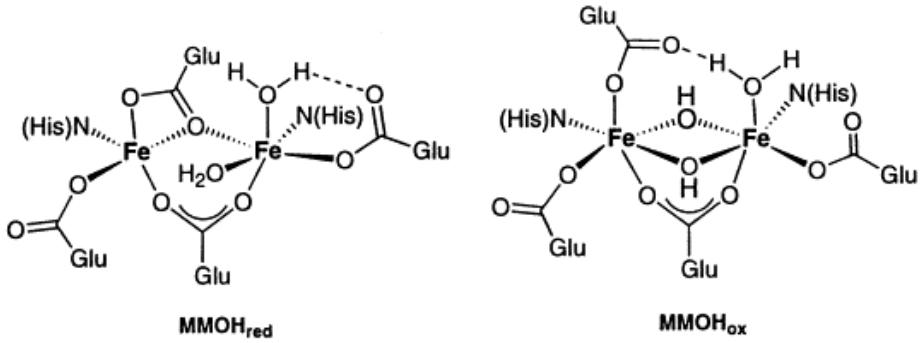

Figure 2.3. Active site (hydroxylase component) of sMMO in its reduced and oxidized (resting, MMOH) state, respectively. Figure is adapted from reference [7].

In the resting state of the active site ($MMOH_{ox}$) two iron(III) ions are bridged through two hydroxo ligands and one glutamate [11]. $MMOH_{ox}$ can be reduced to create the diferrous intermediate $MMOH_{red}$, which is capable of activating dioxygen. The reduced form shows one five- and one six-coordinated iron center. One glutamate is bridging in 1,3-fashion while the other glutamate shows a 1,1-fashion and is chelating one iron site. Upon O–O bond scission, eventually a high-valent diiron(IV) diamond core, $Fe_2(\mu\text{-}O)_2$ (intermediate Q), forms [12]. The latter is capable of breaking the alkane C–H bond of substrates and a proposed mechanistic pathway can be found elsewhere [13]. It is of great interest to understand the enzymatic reaction process of this enzyme to build simpler, synthetic, models that could act as a catalyst under ambient conditions.

Class I ribonucleotide reductase (RNR) represents a class of proteins where the diiron unit (found in the R2 domain of the protein) is interacting with dioxygen but the iron centers themselves are not involved in catalysis. Instead, a tyrosine residue, which

is in close proximity to the metal site, is transformed into a radical by the diiron center [7, 14]. The radical itself is then involved in the conversion of ribonucleotides to deoxyribonucleotides. This enzyme is found in a variety of species, from *E. coli* to humans. Since it is important for DNA biosynthesis, further studies on RNR could reveal important new attacking points for novel anticancer treatments/drugs.

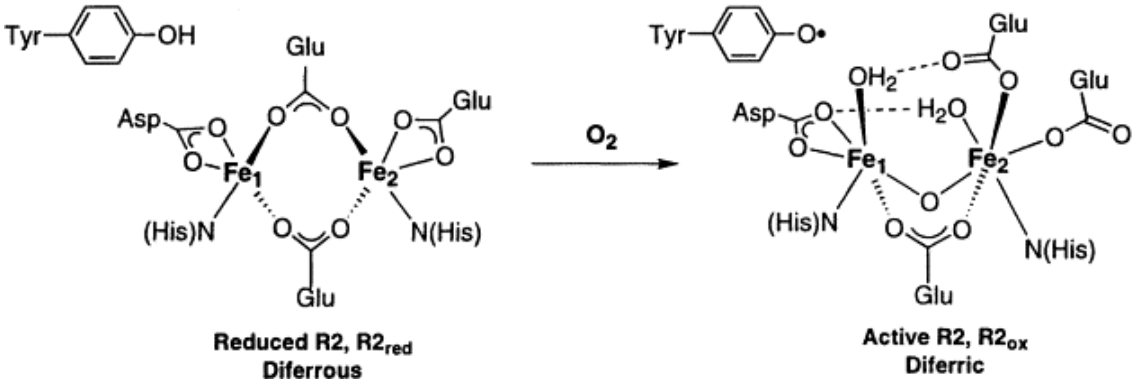

Figure 2.4. Representation of the active site in ribonucleotide reductase. Figure is adapted from reference [7].

The above depicted (Figure 2.4) active site R2 in RNR is shuttling in oxidation states between the diferric and diferrous form. In the reduced form, the iron centers are bridged via two glutamates and overall five-coordinated. The diferric site shows an oxo-bridge between the iron ions and the metals are only bridged through one glutamate [14]. The second glutamate has shifted and only coordinates to one iron center in a terminal mode. Additionally, one water molecule is found at each iron site resulting in overall sixfold coordination. Exposure to O_2 causes the transformation from the reduced to the oxidized species and the formation of the tyrosine radical. Proposed mechanisms for this transformation can be found in the literature [15].

The active sites of Hr, MMOH and R2 in RNR have a diiron core in common, in which both iron centers are redox-active. In addition, the iron ions are held in position

by glutamate, histidine and aspartate (no aspartate in MMOH). In their reduced states all have at least one iron center which is ligated by only five donors. This allows for interaction with dioxygen through the open coordination spot and all diiron centers, in fact, are sensitive to O_2. R2 and MMOH are structurally similar in the sense that one μ-1,3-glutamate remains coordinated to both iron centers during catalytic turnover. The other glutamate, even though coordinating in 1,1-fashion in $MMOH_{red}$ and 1,3-fashion in $R2_{red}$, similarly shifts to one iron center upon oxidation which results in terminal coordination. On the other hand, the discussed diiron centers are different because of unique coordination environments and differences in bridging modes and the kind of ligands used for bridging. Hr is structurally very different from MMOH and R2. This probably explains the difference in interaction with molecular oxygen; allowing Hr to reversibly bind O_2.

While mixed-valence states of the diiron sites in hemerythrin [16], ribonucleotide reductase [17] and methane monooxygenase [18] have been artificially induced and subsequently characterized, there is no evidence for the presence of a naturally occurring mixed-valence state in these proteins. However, there are other diiron sites, found in proteins, which transition through the mixed-valence states in the catalytic cycle of reactions. Here, two proteins, namely rubrerythrin and purple acid phosphatase, will be introduced with the focus on their mixed-valence intermediate.

Rubrerythrin (Rbr) is found in thermophilic bacteria and plays a role as an oxidative stress inhibitor as it catalyzes the reduction of hydrogen peroxide to two equivalents of water [19]. It was found that Rbr, in stark contrast to the previously discussed diiron sites, only reacts slowly with dioxygen, implying it has no O_2

activation function [20]. The active site in Rbr has the most “plastic” iron centers, meaning the most change in movement of one of the iron centers during the catalytic cycle is observed compared to other diiron containing enzymes, and a schematic description of the iron movement upon change in valence is shown in Figure 2.5 [19]. This figure also represents the coordination environment around the iron centers. X-ray crystallographic data has only been obtained for the all-ferric and all-ferrous state of the enzyme [21]. Both oxidation states have in common that two glutamate residues are bridging the iron centers. Additionally, the fully oxidized site has an oxo-bridge which connects the two iron centers. While there is not much of a structural change in the iron center depicted on the right site, the iron shown on the left site undergoes glutamate to histidine ligation switch upon reduction. In the ferric state E97 functions as a terminal donor and H56 does not interact with the iron ion. After reduction to iron(II) the metal center moves almost 2Å towards the histidine allowing coordination to H56, and E97 dissociates. Redox change of this iron center also causes movement of glutamate E20.

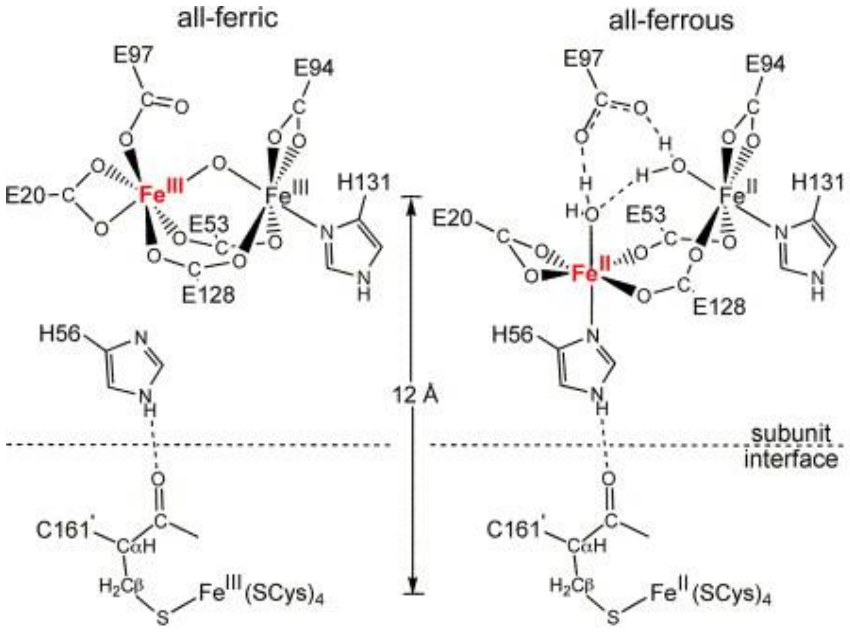

Figure 2.5. Schematic representation of the movement of the iron ion in rubrerythrin upon change in oxidation state. Figure is adapted from reference [22].

A proposed catalytic cycle for the reduction of hydrogen peroxide is shown below in Figure 2.6. The all-ferrous site is sixfold-coordinated. However, there is one labile water ligand at each iron center. Upon coordination of H_2O_2, these two water ligands are displaced. A redox reaction occurs and the active site is oxidized to an oxo-bridged species. One of the dihydroperoxo oxygen atoms was incorporated into the bridge while the other one is lost as a water molecule. The diiron unit is then reduced and protonated yielding in a mixed-valence hydroxo-bridged species. The addition of another proton and electron finally results in the regeneration of the initial diferrous state. The bridging O(H) is eventually lost as another molecule of water during turnover. It should be highlighted that a glutamate residue (E97), which sits right above the diiron center, is interacting with the diiron unit by allowing hydrogen bond formation with certain intermediates (see Figure 2.6). This interaction of a carboxylate

residue is exceptional for diiron active sites. Studies on mutants, which lack E97, revealed that a mixed-valence state of the enzyme cannot be observed as an intermediate, implying that E97 has an important function in the catalytic cycle und the formation of the mixed-valence state [23].

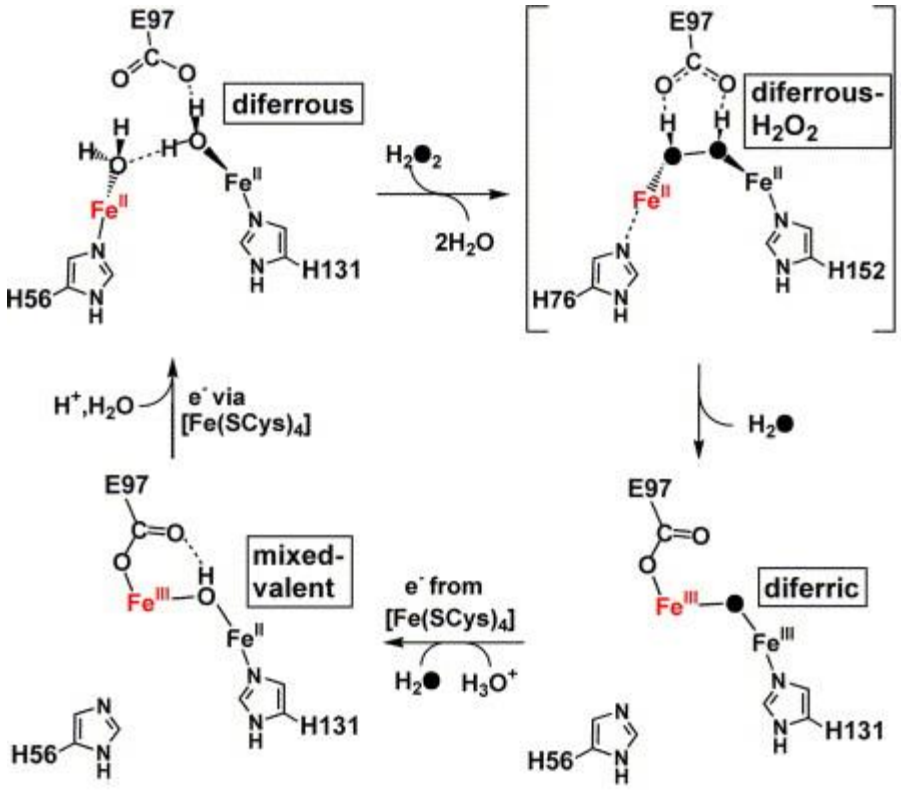

Figure 2.6. Proposed catalytic cycle of hydrogen peroxide reduction at the diiron site in rubrerythrin. (Two iron bridging glutamates have been removed for clarity). Figure is adapted from reference [19].

Purple acid phosphatase (PAP) is a diiron containing enzyme, which catalyzes the hydrolysis of phosphoric acid monoesters and anhydrides, such as ADP and ATP [24]. Mechanistic pathways of this hydrolysis are proposed [25, 26]; it appears that the metal ions of the active site act as Lewis acids, being coordinated by a phosphoester to facilitate a nucleophilic attack by hydroxide onto the phosphorus atom. This protein was isolated mostly in spleens, bones and lungs of humans, and high levels of PAP have

been associated with some diseases like hairy cell leukemia [27] and AIDS [28]. While the active form of PAP in mammals is in the mixed-valence diiron state (Fe(III)/Fe(II)), plants exhibit a Fe(III)/Zn(II) active site (see Figure 2.7) [24]. The mammalian protein is not active in the diferric sate and it has been speculated that the oxidation/reduction allows for *in vivo* regulation to turn the activity off/on, respectively [29]. In the following we will focus on the diiron containing active site of mammals. One hydroxo ligand, as well as one oxygen atom from a carboxylate group (aspartate), is bridging the two iron centers. This active site is particularly interesting because of the great asymmetry in coordination around each iron site (see Figure 2.7). The "chromophoric" site (left in Figure 2.7) causes the purple color of the enzyme due to a charge transfer transition from tyrosinate to iron(III). The absorption is located at around 550 nm with an extinction coefficient of 3000 M^{-1} cm^{-1}. The Solomon group has nicely described the nature of the phenolate to iron bonding [30].

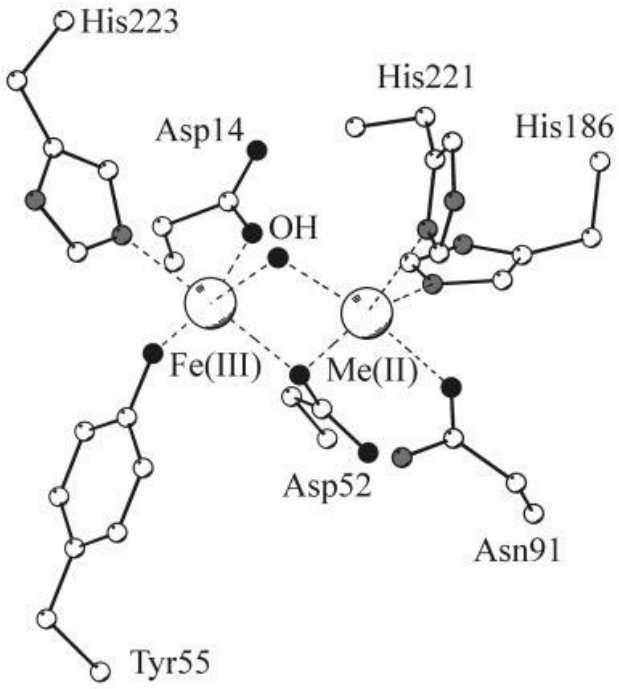

Figure 2.7. Active site of purple acid phosphatase with Me(II) = Fe(II) or Zn(II) in mammals or plants, respectively. Figure is adapted from reference [24].

The other metal site (right in Figure 2.7) is referred to as the "redox active site". This term appears a bit misleading as the ferric state inactivates the function. It is suspected, that PAP plays several other roles *in vivo*, such as the transport of iron [31], bone resorption [32] and immune response [33]. It is also believed that the enzyme catalyzes reactions via Fenton-like chemistry [34-36].

Rbr and PAP are both non O_2-activating enzymes and have in common that a mixed-valence species is involved in catalysis. While in PAP, the Fe(II)/Fe(III) state is essential to start a turnover, in Rbr the mixed-valence state is part of the turnover cycle. The main difference between the two enzymes is that the metal centers in PAP act most likely as Lewis acids in the case of phosphoester hydrolysis. There is only some evidence that the iron centers could undergo Fenton-like chemistry in which case the iron centers act as redox-active sites. In Rbr the iron ions undergo redox changes from

the all-ferric to the all-ferrous state and a mixed-valence state is detected during the catalytic cycle.

In summary, there are a variety of diiron active sites known thus far. It was shown that even though all proteins have a diiron unit with similar bridging ligands ((hydr)oxo and carboxylate residues) in common, each protein has a different function in biology. Model compounds, which mimic these active sites in proteins have been introduced to the literature during the last couple of decades and in the following section an overview of these synthetic complexes with a focus on mixed-valence diiron model complexes will be given.

2.1.2 Model Complexes for Diiron Sites

A good number of unsupported, only O-bridged diiron complexes have been synthesized in mostly the ferric state [1]. Unsupported OH-bridged complexes on the other hand, are very rare. Particularly for the Fe(II)/Fe(II) state there is only one example, which was reported by Grohmann et al. The diferrous complex was synthesized with a pentadentate pyridyl-tetra(amine) ligand and the structure of the complex is shown in Figure 2.8 [37]. Mixed-valence forms of mono-bridged (oxo or hydroxo bridged) diiron complexes have not been isolated thus far. Unsupported, singly O(H)-bridged complexes do not seem to be very relevant for diiron active site structural model studies because of the difference in the bridging angle. In proteins the structures are bent (between around 120° to 130°) due to additional bridging carboxylates and there is only a small change in bending when the bridge is de/protonated [2].

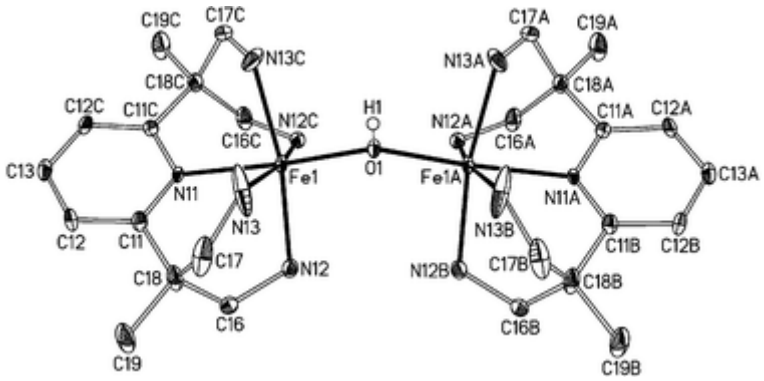

Figure 2.8. Crystal structure of the only OH-bridged, unsupported, diferrous complex. Figure is adapted from reference [37].

(μ-Oxo)bis(μ-carboxylato)diiron(III) complexes are structurally the closest model compounds for diiron enzyme active sites. They assemble when tridentate N-donor ligands are dissolved in the presence of iron salts and carboxylates. The tridentate ligands hydrotripyrazol ($HBpz_3$), tris(pyridyl)amine (TPA) or 1,4,7-trimethyl-triazacyclononane (Me_3TACN) have been used widely and the ligand structures are shown in Figure 2.9 [2].

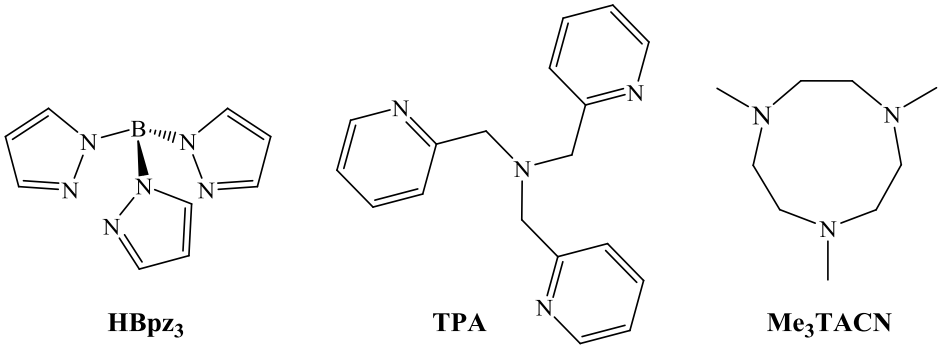

Figure 2.9. Structures of $HBpz_3$, TPA and Me_3TACN.

Common for all tri-bridged diiron structures is symmetry within the complex which gives the molecule two equivalent iron sites. Figure 2.11 a) and b) shows crystal structures with the (μ-oxo)bis(μ-carboxylato)diiron(III) core which are representative

for this class of structural mimics [4, 5, 38-40]. While the iron–ligand bonds found in these synthetic complexes match well with the ones found in differic enzymes, the Fe···Fe distances are shorter and the Fe–O–Fe angles are significantly smaller. Some of these complexes have been partially characterized in their mixed-valence form, which will be discussed at the end of the background section.

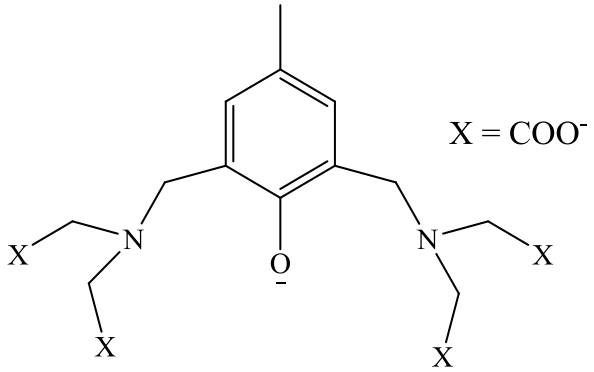

Figure 2.10. Structure of 5-Me-HXTA.

Another class of model complexes has been studied where phenolate or other alkoxo-groups are bridging. A structure of a representative complex of this class, $(Me_4N)[Fe_2(5\text{-Me-HXTA}(OAc)_2]$, using the 5-Me-HXTA ligand (see Figure 2.10) is shown in Figure 2.11 d) [41]. Structurally these complexes are unrelated to natural diiron sites but they can be isolated in their mixed-valence states and appear stable [42-45]. In the solid state, the valences are localized giving distinct differences in iron–ligand bond lengths but in solution they behave like class II mixed-valence compounds [46].

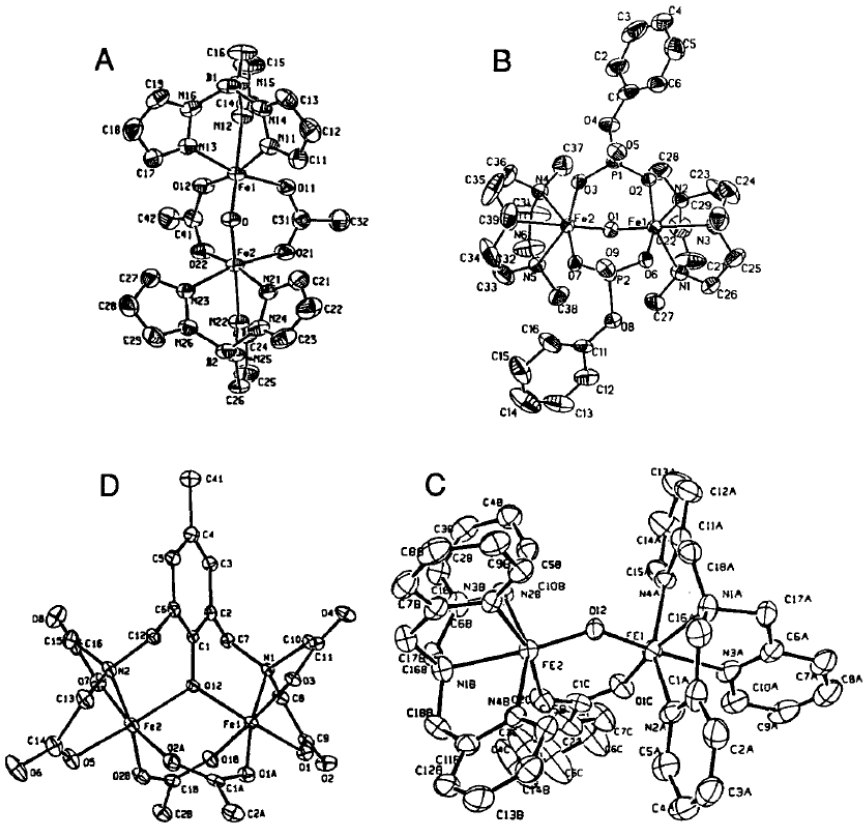

Figure 2.11. Crystal structures of selected diiron-containing enzyme model complexes. (a) $[Fe_2O(OAc)_2(HBpz_3)_2]$, (b) $[Fe_2O(O_2P(OPh))_2(Me_3TACN)_2]$, (c) $[Fe_2O(OBz)(TPA)_2](ClO_4)_3$, (d) $(Me_4N)[Fe_2(5\text{-Me-HXTA}(OAc)_2]$. Figure is adapted from reference [2].

An unexpected complex was derived with the use of TPA as a ligand. Figure 2.11 c) shows the structure of $[Fe_2O(OBz)(TPA)_2](ClO_4)_3$. This is the only example of a ligand coordinating each iron site in different fashion. It results in asymmetric bond lengths on either iron site. The authors speculated that unfavorable H–H interactions would arise in the symmetric version of the complex [47], [48].

Before the mixed-valence model complexes will be discussed, the reader should gain more understanding in the classification of mixed-valence compounds. Therefore, the next section will focus on examples for the different kinds of mixed-valence classifications according to Robin and Day.

Prussian blue [49-51], not only the first synthetic coordination compound, was probably also the first mixed-valence compound and up to now many more have been synthesized, with the use of different metal ions [52-54]. Not all mixed-valence complexes are alike. Today's most valid classification of mixed-valence complexes is based on the work of Robin and Day [55], who categorized mixed-valence complexes based on the strength and symmetry of the ligand fields about each metal center. The classes I-III are used to describe the mixed-valence situation.

Complexes within the class I exhibit different symmetry and ligand field strength at each metal center. The interaction between the two metal centers due to the different environment or great distance to each other results in properties which are typical for isolated metal centers. For example, a complex where M(III) is in the low spin configuration and M(II) is high spin. Therefore, spectra of theses complexes appear as a sum of the fully oxidized and fully reduced complex. Those complexes appear mostly colorless, do not show coupling between the metal ions and are insulators.

In contrast, if the M(II) and M(III) ions are in equal environments, the complex falls into class III and the electrons are considered delocalized. Both metals couple strongly and the material shows conductivity. Overall, properties of these complexes are completely different from the isolated fully oxidized/reduced species. The coupling depends strongly on the distance of the metal ions to each other. The shorter the inter-metal distance, the stronger the coupling.

The class II represents complexes where the two coordination sites are distinguishable but delocalization of electrons occurs. A typical example for a mixed-valence class II complex is a compound which has the reduced and oxidized ion in

octahedral sites but exhibits different metal-ligand bond distances. It is common that bridged metal complexes fall into the class II.

Class II complexes feature absorptions in the visible region from 14000–27000 cm^{-1} (~714–370 nm) which are not present in spectra of the fully oxidized or reduced species. The transition (intervalence electron transfer) is assigned to M(II) + M(III) to M(III) + M(II). There is magnetic coupling between the two metal centers which can be detected via magnetic susceptibility measurements. Overall complexes within this class show low conductivity.

Two synthetic O(H)-bridged diiron complexes have been isolated thus far which fall into class II. Both of them have symmetric sites and are described below.

The OH-bridged mixed-valence complex synthesized by Wieghardt and coworkers [56] is the only example for a synthetic ferrous/ferric hydroxo bridged complex. $[LFe^{III}(\mu\text{-}OH)(\mu\text{-}piv)_2Fe^{II}L](ClO_4)_2$, a blue-violet complex (with L = Me_3TACN), can be isolated in crystalline form at low temperature, whereas in solution, even if kept free of dioxygen, this complex readily decomposes. The crystal structure of the mixed-valence complex is depicted in Figure 2.12.

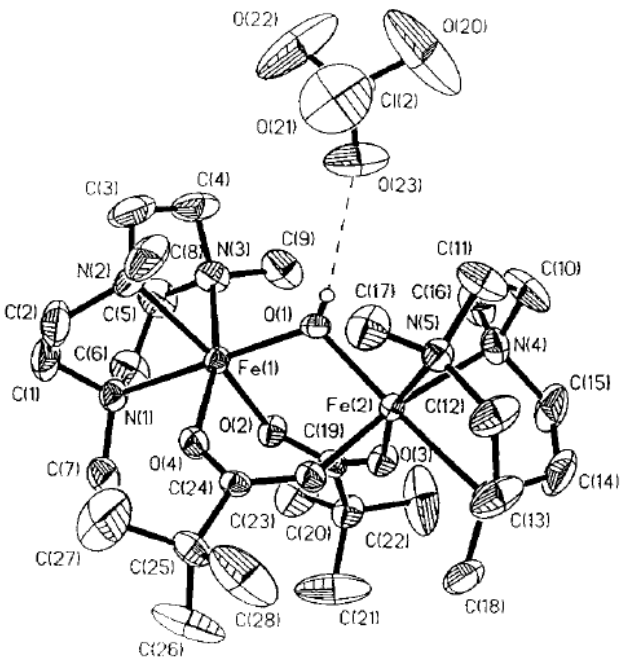

Figure 2.12. Structure of $[LFe^{III}(\mu\text{-}OH)(\mu\text{-}piv)_2Fe^{II}L](ClO_4)_2$. Figure is adapted from reference [56].

$[LFe^{III}(\mu\text{-}OH)(\mu\text{-}piv)_2Fe^{II}L](ClO_4)_2$ exhibits an Fe···Fe distance of 3.400(3) Å and a bond angle of 118.1(2)° for the Fe–O–Fe bridge. Interestingly the Fe–O distances are not equal (Fe(1)–O(1) = 2.005(5) Å whereas Fe(2)–O(1) = 1.961(5) Å). This difference in bond length is interpreted as a localized, class II, mixed-valence complex according to Robin and Day. Therefore, Fe(2) can be formally assigned to the Fe(III) oxidation state and Fe(1) to the Fe(II) oxidation state. The magnetic coupling accounts for $J = -12.9$ cm^{-1} with a ground state of S = ½. EPR spectra taken at 10 K confirm the S = ½ ground state. According to Mössbauer spectroscopy the valence of this complex appears to be localized with both iron ions being in the high spin state.

When the mixed-valence complex is dissolved in aceto- or butyronitrile at room temperature it decomposes within half an hour, which is indicated by a color change to orange. The product is identified to be the oxo-bridged diferric analogue $[LFe^{III}(\mu\text{-}O)(\mu\text{-}$

piv)$_2$Fe^{III}L]$^+$ but quantitative analyses revealed that only half of the mixed-valence species was converted to the differic complex. It is assumed that the other half reacted to [LFe^{II}(μ-OH)(μ-piv)$_2$Fe^{II}L] because the intensity of the band representing [LFe^{III}(μ-O)(μ-piv)$_2$Fe^{III}L]$^+$ doubles upon exposure to air. Wieghardt et al. propose a mechanism for the disproportionation of [LFe^{III}(μ-OH)(μ-piv)$_2$Fe^{II}L]$^{2+}$ which is depicted in Scheme 2.1.

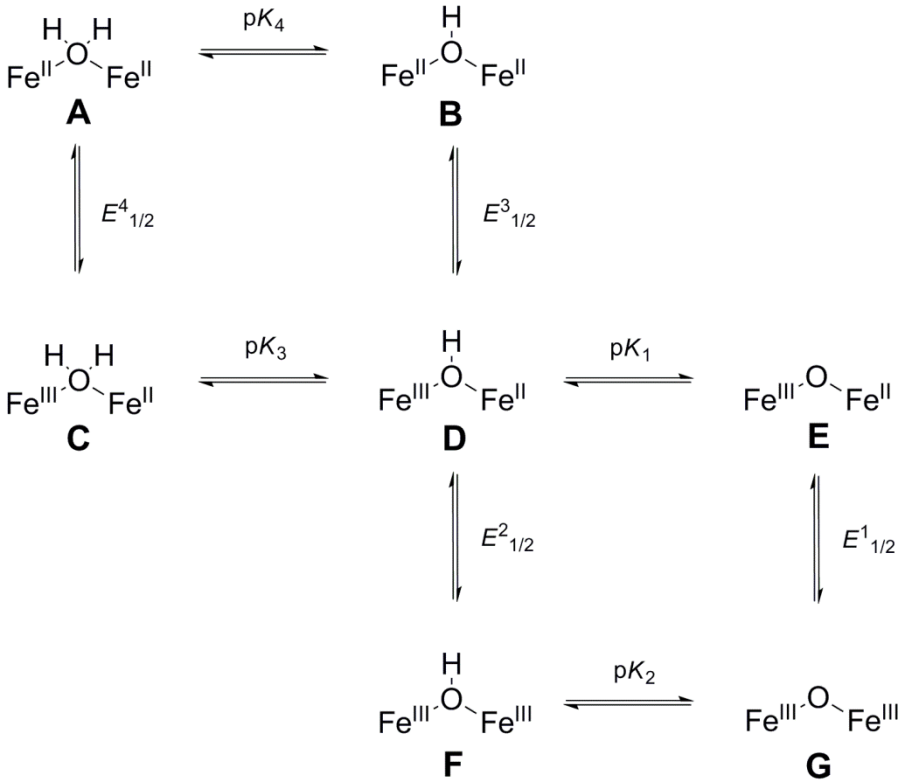

Scheme 2.1. Possible protonated and redox species of the diiron centers. Scheme is redrawn from reference [56].

The starting mixed-valence complex **D**, as shown in Scheme 2.1, is in equilibrium with its de/protonated forms **E** and **C**. The more protonated species is a stronger oxidizer (e. g. **C** is a stronger oxidizer than **D**) and will cause intermolecular electron transfer from **D** to **C** when both species are present. This results in the

formation of **A** and **F**, respectively. By analogy, **D** and **E** will result in the formation of **B** and **G**. Since **F** is a fairly strong acid, **G** is readily formed and autocatalysis is enhanced through protonation of **D**.

Using the same ligand (Me_3TACN), a mixed-valence diiron oxo-bridged complex was formed *in situ* upon controlled-potential coulometry of $[Fe_2O(OAc)_2(Me_3TACN)_2](PF_6)_2$ [5]. Instead of pivalic acid, two acetate molecules act as bridging ligands. The mixed-valence species is described as a green complex, and initial EPR and Mössbauer data were collected. The mixed-valence complex exhibits a high spin iron(II) and a high spin iron (III) ion with a ground state of S = ½.

About 10 years later, the group of Sanders-Loehr [57] successfully isolated the first oxo-bridged trapped-valence $Fe^{II}Fe^{III}$ complex, $[Fe_2O(O_2\text{-}CCPh_3)_2L_2]^+$ (L = Me_3TACN), and determined its crystal structure. Bulkier triphenylacetates have been used in their study to support the diiron unit. Scheme 2.2 summarizes the different synthetic routes that have been tried in order to obtain the green mixed-valence complex from the fully reduced $[Fe_2OH(O_2\text{-}CCPh_3)_2L_2](BPh_4)$. Starting from the hydroxo-bridged diferrous complex, the mixed-valence state can be formed upon reaction with molecular dioxygen, hydrogen peroxide or 4-methylmorpholine *N*-oxide. EPR and magnetic data of the mixed-valence species indicate a spin state of S = ½, which is consistent with the mixed-valence assignment to the complex. Resonance Raman studies provide insight into the symmetry of the Fe–O stretch and revealed that the isolated complex in fact shows trapped-valence character. The crystal structure of $[Fe_2O(O_2\text{-}CCPh_3)_2L_2]BPh_4$ reveals an iron···iron distance for the mixed-valence state to be 3.155(1) Å and a bond angle of Fe–O–Fe = 123.4(2)°. The similar length of 1.818(4)

Å and 1.844 (4) Å for the Fe–oxo bond does not allow for distinction between a delocalized or trapped-valence classification. Further analysis of this complex is provided in a different publication by Payne et al. [58]. They isolated the same mixed-valence complex with a different counter ion, $[Fe_2O(O_2\text{-}CCPh_3)_2L_2]OTf$. The difference between the Fe–O bonds is more significant with 1.800(4) and 1.847(4) Å indicating class II character with distinguishable iron ions.

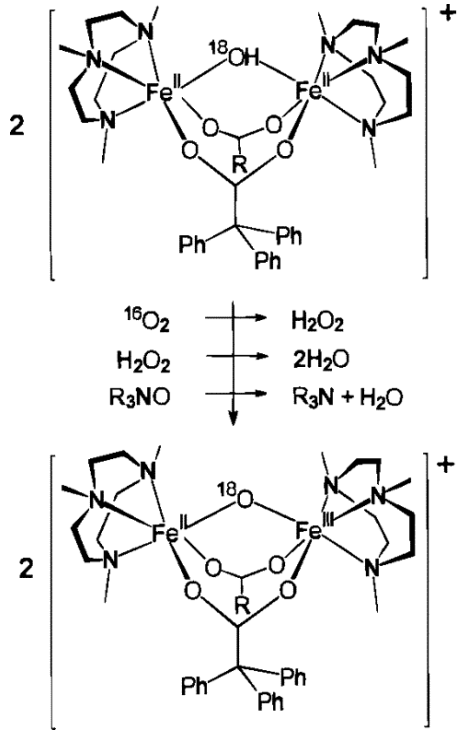

Scheme 2.2. Conversion of the OH-bridged differic complex to the mixed-valence oxo-bridged species. (R = CPh_3, R_3NO = 4-methylmorpholine *N*-oxide). A second equivalent of each oxidant converts the mixed-valence species to the oxo-bridged diferric complex. Scheme is adapted from reference [57].

Given the fact that there are only few mixed-valence intermediates for μ-(hydr)oxodiiron complexes, it is obvious that they are difficult to access and study. All mixed-valence complexes characterized thus far utilize Me_3TACN as a capping ligand

and two supporting RCO_2^- bridges. It seems that oxo-bridged mixed-valence complexes are more stable than OH-bridged complexes.

2.2 Introduction

The group of Dr. Houser synthesized the first O(H) bridged, unsupported (singly bridged) but asymmetric diiron complexes [59]. Scheme 2.3, below, summarizes the syntheses of the iron complexes previously studied.

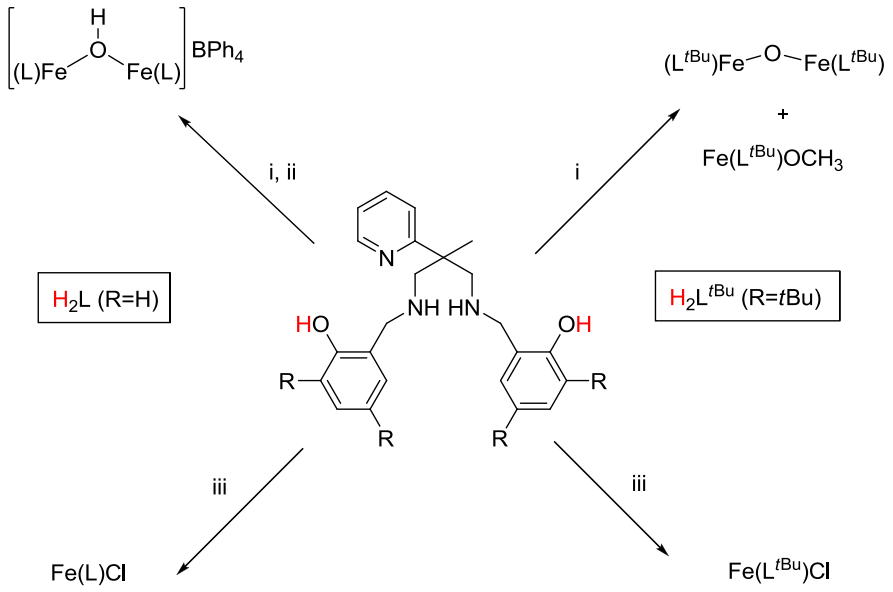

Scheme 2.3. Representation of the synthesis of complexes done by R. Shakya. (i) $Fe(ClO_4)_3 \cdot 6H_2O$, Et_3N, CH_3OH. (ii) $NaBPh_4$, CH_3OH. (iii) $FeCl_3$, Et_3N, CH_2Cl_2. Protons highlighted in red represent readily deprotonable hydrogens. Scheme is redrawn from reference [59], small changes were made to the labeling.

The reduced Schiff bases, H_2L and H_2L^{tBu}, are generated from condensation of ppda with salicylic aldehyde or 3,5-Di-tertbutyl-2-hydroxybenzaldehyde, respectively and subsequent reduction. Monomeric or dimeric iron complexes are obtained depending on the nature of the anionic counter ion. While the use of chloride facilitates

the formation of the pentadentate monomeric complexes with a coordinating chloride in the sixth position, the use of non-coordinating ions like perchlorate allows the formation of dimers. The focus will be on the dimeric complexes which are structurally related to the diiron containing enzymatic active sites. The crystal structure of $[(FeL)_2(\mu\text{-}OH)]BPh_4$, shown below in Figure 2.13, reveals the asymmetric nature of the complex.

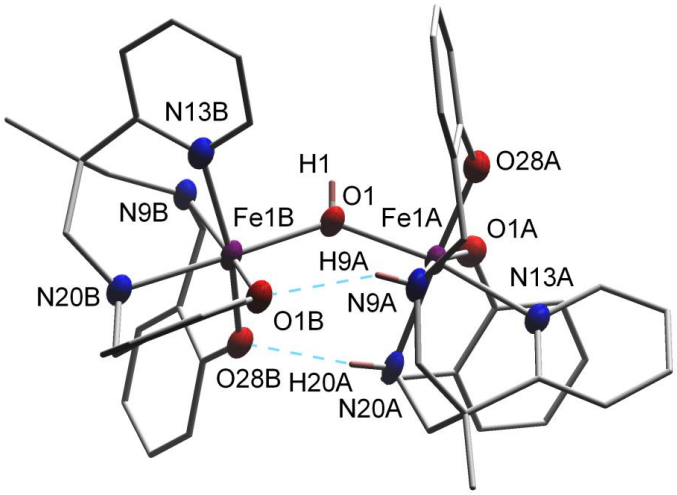

Figure 2.13. Crystal structure of $[(FeL)_2(\mu\text{-}OH)]BPh_4$. The counter ion and trapped solvent molecules are omitted for clarity. Figure is adapted from reference [59].

The internal hydrogen bonding, which is caused by our unique ligand manifold, results in a bent structure and a distinct coordination environment around each iron center. On the other hand, when the ligand was substituted with *t*Bu-groups, an oxo-bridged dimer without internal hydrogen bonding was obtained. The crystal structure is shown in Figure 2.14.

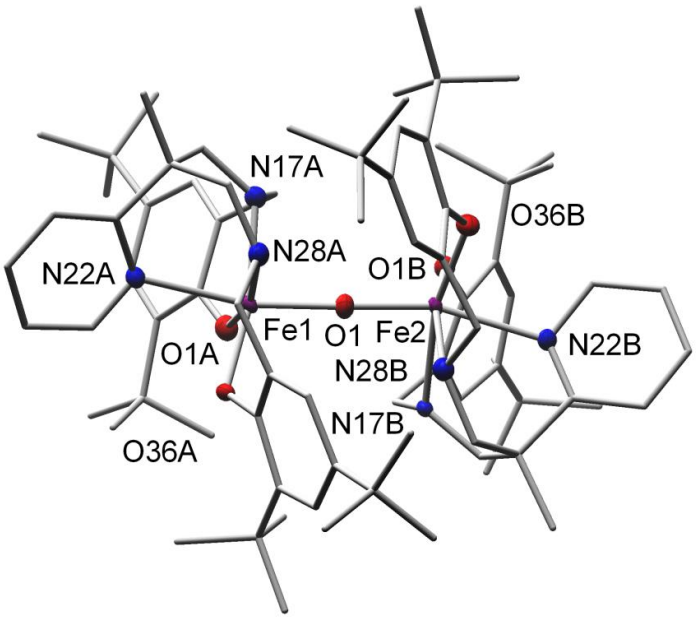

Figure 2.14. Crystal structure of $[(FeL^{tBu})_2(\mu\text{-}O)]$. Figure is adapted from reference [59].

The electrochemical behavior of the two dimers was studied through cyclic voltammetry, and both voltammograms are overlayed in Figure 2.15. $[(FeL)_2(\mu\text{-}OH)]BPh_4$ shows metal centered redox couples at –630 mV (ΔE = 120 mV) and –1190 mV (ΔE = 165 mV) and one irreversible ligand oxidation at around + 830 mV vs. Ag/AgCl. $[(FeL^{tBu})_2(\mu\text{-}O)]$ does not show any metal-centered redox features within the solvent window. This means that metal-based redox reactions are not accessible for this complex under the conditions picked. Instead two quasi-reversible and one irreversible ligand based oxidations are observed at 550 mV (ΔE = 130), 825 mV (ΔE = 156) and 1086 mV (ΔE = 270) vs. Ag/AgCl, respectively.

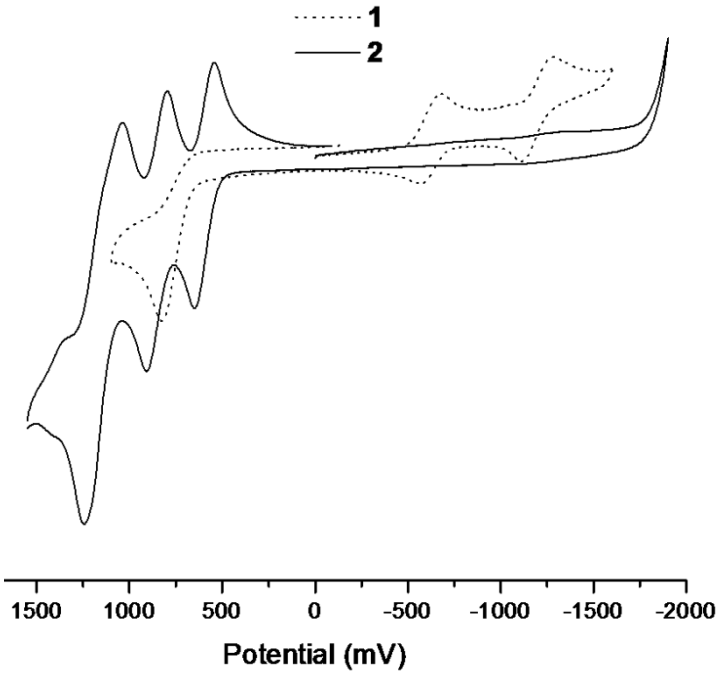

Figure 2.15. Cyclic voltammogram of $[(FeL)_2(\mu\text{-}OH)]BPh_4$ (1) and $[(FeL^{tBu})_2(\mu\text{-}O)]$ (2) vs. Ag/AgCl, sample concentrations about 1.0 mM in CH_2Cl_2, scan rates 150 mV/s, 0.1 M TBAH supporting electrolyte. Figure is adapted from reference [59].

The work by R. Shakya left several questions open to be answered. According to the CV of $[(FeL)_2(\mu\text{-}OH)]BPh_4$ the comproportionation constant can be calculated and with that the stability of the mixed-valence complex estimated.

$$K_c = 10^{\Delta E/59\,mV} = \frac{[M^{(n-1)}]^2}{[M][M^{(n-2)}]} \qquad \text{Eq. 2.1}$$

$$M + M^{(n-2)} \rightleftharpoons^{K_c} 2\,M^{(n-1)} \qquad \text{Eq. 2.2}$$

In equation 2.1 K_c represents the comproportionation constant (higher values indicate a more stable mixed-valence complex) and ΔE represents the difference between two redox couples (here diferric/mixed-valence and mixed-valence/diferrous) [60], [61]. Equation 2.2 represents the comproportionation equilibrium reaction. With a K_c of $\approx 10^{11}$ for $[(FeL)_2(\mu\text{-}OH)]BPh_4$, a reasonably stable mixed-valence complex is expected, and the crystal structure of $[(FeL)_2(\mu\text{-}OH)]BPh_4$ suggests the formation of a localized mixed-valence complex upon reduction due to the different coordination environment around each iron center. In this chapter, the stability of the mixed-valence form is studied. Does asymmetry in our complex result in stabilization of the mixed-valence intermediate? The synthesis and characterization of a nitro-substituted ligand should answer the question of whether the electronic changes in the ligand would allow for easier reduction and maybe better stabilization of a potential mixed-valence complex.

Further, it was speculated whether the deprotonated complex $[(FeL)_2(\mu\text{-}O)]BPh_4$ would show a bent structure like $[(FeL)_2(\mu\text{-}OH)]BPh_4$ or rather be linear like $[(FeL^{tBu})_2(\mu\text{-}O)]$.

2.3 Syntheses

Scheme 2.4 summarizes the syntheses and reaction pathways of $[(FeL)_2(\mu\text{-}O)]$, $[FeL(MeOH)]$, $[(FeL)_2]$, $[(FeL^{NO2})_2(\mu\text{-}OH)]ClO_4$, and their relationship to $[(FeL)_2(\mu\text{-}OH)]BPh_4$.

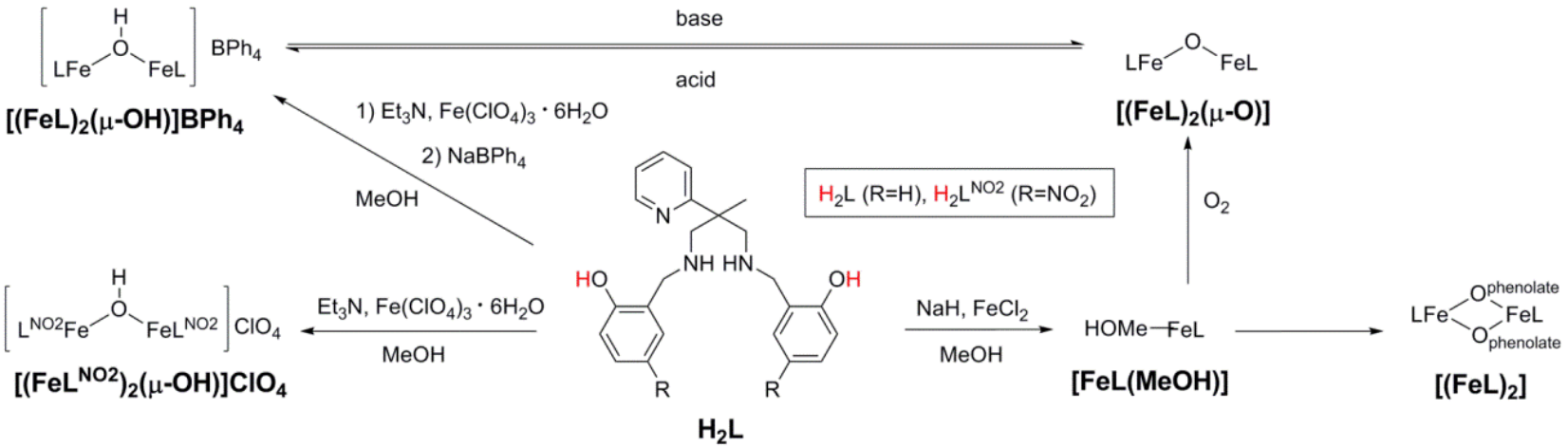

Scheme 2.4. Syntheses and interconversions of iron complexes used in this chapter. Protons highlighted in red represent readily deprotonable hydrogens.

The ligand H_2L is prepared by Schiff base condensation of ppda with two equivalents of salicylic aldehyde in methanol followed by reduction with sodium borohydride. For this work, the preparation of $[(FeL)_2(\mu\text{-}OH)]BPh_4$ differed slightly from what was previously published [59]. Upon deprotonation of H_2L in MeOH, a solution of ferric perchlorate was added. After counterion metathesis with $NaBPh_4$, the complex precipitated out of solution. It was then dried, redissolved in dichloromethane, and recrystallized by vapor diffusion with pentane to obtain $[(FeL)_2(\mu\text{-}OH)]BPh_4 \cdot CH_2Cl_2$, in contrast to the previous study where it was crystallized from methanol and $[(FeL)_2(\mu\text{-}OH)]BPh_4 \cdot MeOH$ was isolated. Conversion between $[(FeL)_2(\mu\text{-}OH)]BPh_4$ and $[(FeL)_2(\mu\text{-}O)]$ was achieved via (de)protonation, and $[(FeL)_2(\mu\text{-}O)]$ can also be obtained by reducing $[(FeL)_2(\mu\text{-}OH)]BPh_4$ with cobaltocene in dichloromethane solution, followed by spontaneous disproportionation, deprotonation, and subsequent oxidation under atmospheric conditions, which will be discussed later. $[(FeL)_2(\mu\text{-}O)]$ is also generated through oxidation of the ferrous complex [FeL(MeOH)], which was synthesized by treatment of H_2L with NaH to deprotonate the phenol group, then reaction with ferrous chloride in methanol. When [FeL(MeOH)] is recrystallized from MeCN, the dimeric complex $[(FeL)_2] \cdot (MeOH)_2$ was obtained. $[(FeL^{NO2})_2(\mu\text{-}OH)]ClO_4$ was produced upon reaction of H_2L^{NO2} with ferric perchlorate in the presence of Et_3N in methanol.

2.4 Solid State Structures

2.4.1 X-ray Crystal Structures

Similar to the previously published complex $[(FeL)_2(\mu\text{-}OH)]BPh_4 \cdot MeOH$, structures of $[(FeL)_2(\mu\text{-}O)]$ and $[(FeL^{NO2})_2(\mu\text{-}OH)]ClO_4$ show coordination to the ferric ion through all donor atoms of the pentadentate ligands $(L)^{2-}$ and $(L^{NO2})^{2-}$, respectively, and exhibit the same kind of intramolecular hydrogen bonding between the two subunits. A (hydr)oxo ligand acts as the sixth donor and bridges two ferric ions. On the other hand, the diferrous complex $[(FeL)_2]$ is doubly bridged through one of the phenolate donors of each ligand, resulting in sixfold coordination of the metal center with absence of additional donors. All of our μ-OH complexes are able to hydrogen bond to a solvent molecule via one of the amine N–H's and the bridging OH. In $[(FeL)_2(\mu\text{-}OH)]BPh_4$ methanol is trapped, while in $[(FeL^{NO2})_2(\mu\text{-}OH)]ClO_4$ water is present. Similarly, the N–H of $[(FeL)_2(\mu\text{-}O)]$ hydrogen bonds to acetone. This phenomenon is discussed in detail later.

The neutral complex $[(FeL)_2(\mu\text{-}O)]$ (see Figure 2.16) shows distorted octahedral coordination around the Fe(III) centers, utilizing the N_3O_2 donors from $(L)^{2-}$ and the O from an oxo ligand. The latter connects two iron centers via μ-fashioned coordination (Figure 2.16). Again, as in $[(FeL)_2(\mu\text{-}OH)]BPh_4$, the coordination environment of each iron site differs. While Fe1 has the oxo bridge O1 and the pyridine nitrogen N18A trans to each other, Fe2 shows the oxo bridge O1 and the amine nitrogen N20B coordinating opposite to another.

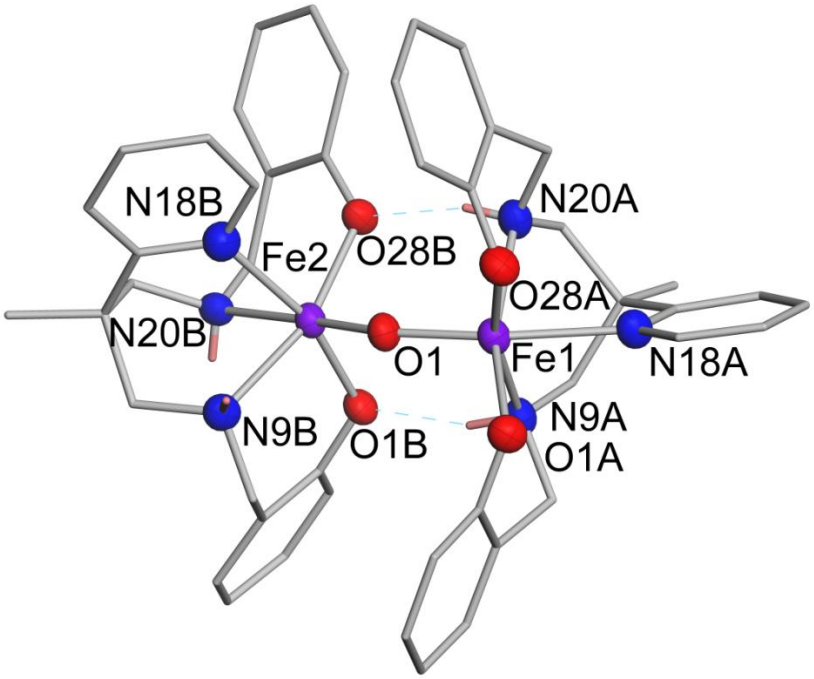

Figure 2.16. Representation of the X-ray structure of $[(FeL)_2(\mu\text{-}O)]$ with H-atoms removed for clarity (except H-atoms which are involved in intramolecular hydrogen bonding).

The different coordination environments around each iron center results in slightly different Fe–donor bond lengths on the two different sites, as can be seen in Table 2.1 In order to distinguish the two iron sites, the terms $^{trans\text{-}Py}$Fe–O and $^{cis\text{-}Py}$Fe–O are used; $^{trans\text{-}Py}$Fe–O refers to the iron ion having the pyridine-N atom *trans* to the μ-O(H) and $^{cis\text{-}Py}$Fe–O refers to the iron ion having the pyridine-N atom *cis* to the μ-O(H).

Table 2.1. Comparison of Fe–O–Fe core unit parameters. Parameters for $[(FeL)_2(\mu\text{-}OH)]BPh_4 \cdot MeOH$ and $[(FeL^{tBu})_2(\mu\text{-}O)]$ are taken from reference [59].

Complex	Fe–O–Fe (deg)	$^{trans\text{-}Py}$Fe–O (Å)	$^{cis\text{-}Py}$Fe–O (Å)	Fe···Fe (Å)
$[(FeL)_2(\mu\text{-}OH)]BPh_4 \cdot MeOH$	138.64(9)	2.0174(16)	2.0033(17)	3.7616(7)
$[(FeL)_2(\mu\text{-}OH)]BPh_4 \cdot CH_2Cl_2$	138.96(6)	2.0292(11)	1.9901(11)	3.7643(4)
$[(FeL^{NO2})_2(\mu\text{-}OH)]ClO_4$	140.05(9)	2.0028(16)	1.9689(16)	3.733(5)
$[(FeL)_2(\mu\text{-}O)]$	143.70(10)	1.8192(17)	1.8160(17)	3.454(7)
$[(FeL^{tBu})_2(\mu\text{-}O)]^a$	169.4(6)	1.844(10)	1.793(10)	3.621(4)
$[(FeL)_2]$	N/A	N/A	N/A	3.354(9)

[a] In complex $[(FeL^{tBu})_2(\mu\text{-}O)]$ both pyridine ligands are *trans* to the oxo-bridge.

In stark contrast to $[(FeL)_2(\mu\text{-}OH)]BPh_4$, the Fe–O1 bond lengths for each subunit are very similar with 1.8192(17) Å for Fe1–O1 and 1.8160(17) Å for Fe2–O1 (see Table 2.2 for selected bond lengths and angles). It is likely that the stronger antiferromagnetic coupling through an oxo vs. a hydroxo bridge [62] compensates for the asymmetric charge distribution of the individual units. Overall, the Fe–O1 bonds in $[(FeL)_2(\mu\text{-}O)]$ are shorter than in $[(FeL)_2(\mu\text{-}OH)]BPh_4$, which can be explained with the higher electrostatic interaction between iron(III) and an oxo donor compared to iron(III) and hydroxo. The hydrogen bonding between the amine NH group from N9A/N20A and phenolate O O1B/O28B most likely causes the bent structure with an Fe1–O1–Fe2 bond angle of 143.70(10)°. Due to this unique intramolecular hydrogen bonding, the

bridging angle in $[(FeL)_2(\mu\text{-}O)]$ is only 5° more obtuse than in our OH-bridged complex $[(FeL)_2(\mu\text{-}OH)]BPh_4$. Most unsupported oxo-bridged diferric complexes have Fe-O-Fe angles of 160° to 180° [1] with a few exceptions, showing bridging angles of 140° [63] and 143° [64]. Our previously synthesized O-bridged complex with the same ligand backbone (but *t*Bu-substituted) does not show hydrogen bonding between the two subunits and the bridging angle is almost linear with 169.4(6)° [59]. Only the heme-like unsupported structure (μ-oxo)bis(tetraphenylporphyrinato)iron(III), which is sterically hindered, is another example where the bridging angle does not change significantly compared to its hydroxo-bridged analogue (differences of 3° and 7°, depending on the counter-anion of the complex) [65]. While unsupported oxo-bridged diferric complexes are rather linear, it is common for complexes with additional carboxylato bridges to range in Fe–O–Fe angles from 118°-138°, depending on the kind and number of bridging ligands [1].

The X-ray structure of $[(FeL^{NO2})_2(\mu\text{-}OH)]ClO_4$ also reveals a dimeric structure with two distinct coordination environments around each iron center, which is caused by a different orientation of the ligands due to hydrogen bonding interactions between the two subunits mentioned earlier. The structure of $[(FeL^{NO2})_2(\mu\text{-}OH)]ClO_4$ (see Figure 2.17) is very similar to $[(FeL)_2(\mu\text{-}OH)]BPh_4$ but the counter ion in $[(FeL^{NO2})_2(\mu\text{-}OH)]ClO_4$ is perchlorate.

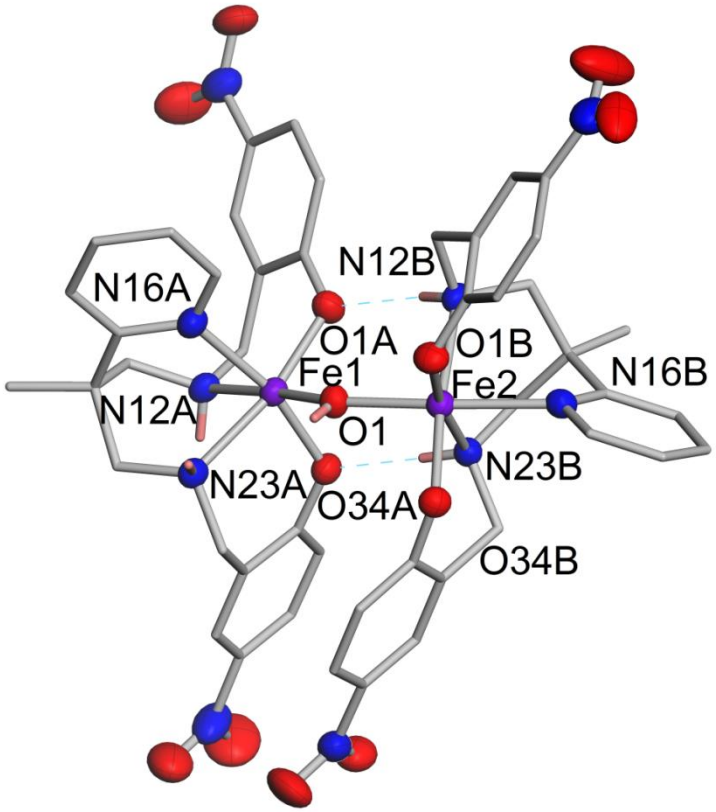

Figure 2.17. Representation of the X-ray structure of the cationic portion of $[(FeL^{NO2})_2(\mu\text{-}OH)]ClO_4$ with H-atoms removed for clarity (except H-atoms which are involved in intramolecular hydrogen bonding and bridging OH).

As in $[(FeL)_2(\mu\text{-}OH)]BPh_4$, the bond lengths of the hydroxo O-atom to Fe(III) are different for each site with Fe1–O1 being 1.9689(16) Å and Fe2–O1 being 2.0028(16) Å (see Table 2.3 for selected bond lengths and angles). Both bonds are significantly shorter than in $[(FeL)_2(\mu\text{-}OH)]BPh_4$. This is probably due to the electron withdrawing properties of the nitro-substituted ligand, which cause a slightly higher positive charge on the iron(III) ion and therefore stronger interactions with the bridging hydoxo ligand. Similar to $[(FeL)_2(\mu\text{-}OH)]BPh_4$, the different coordination environment around each iron center in $[(FeL^{NO2})_2(\mu\text{-}OH)]ClO_4$ show different bond lengths for the Fe–donor bonds as can be seen in Table 2. $[(FeL^{NO2})_2(\mu\text{-}OH)]ClO_4$ has a Fe–O–Fe bond

angle of 140.05(9)° which is similar to the one in $[(FeL)_2(\mu\text{-}OH)]BPh_4$ (138.64(9)°).

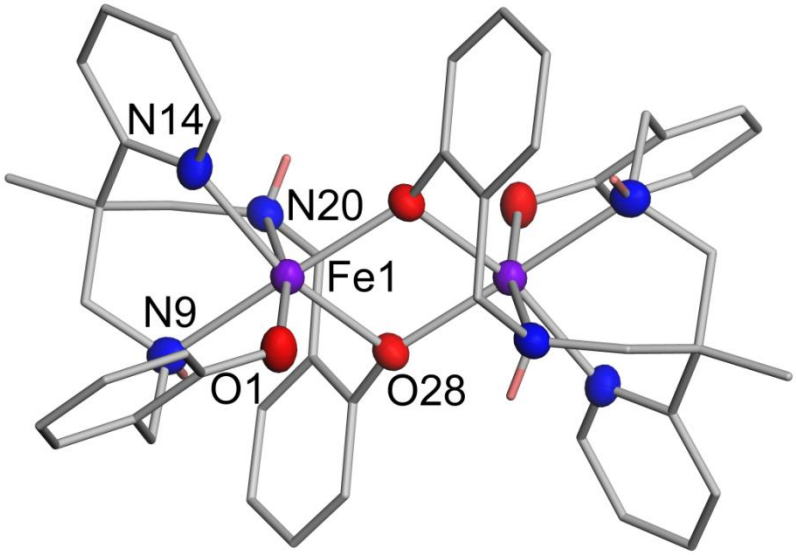

Figure 2.18. Representation of the X-ray structure of $[(FeL)_2]$ with H-atoms removed for clarity (except NH-atoms from the amines).

The complexes $[(FeL)_2(\mu\text{-}OH)]BPh_4$, $[(FeL)_2(\mu\text{-}O)]$ and $[(FeL^{NO2})_2(\mu\text{-}OH)]ClO_4$ are very similar with respect to asymmetric coordination fashion. The bridging angle ranges from 139 to 144° and there is only a small difference between the oxo and hydroxo bridged complex with L as the ligand which is most likely due to the fact that the diiron unit is held together in a bent fashion by two hydrogen bonds. The $^{trans\text{-}Py}$Fe–O bond is longer than the $^{cis\text{-}Py}$Fe–O bond in all complexes. The hydroxo-bridged complexes have longer Fe···Fe distances (around 3.7 Å) and longer Fe–O bonds than the oxo-bridged complex $[(FeL)_2(\mu\text{-}O)]$ (Fe···Fe = 3.5 Å). All Fe–O–Fe core parameters are listed in Table 2.1 for comparison. $[(FeL^{tBu})_2(\mu\text{-}O)]$ has a different structure than the complexes mentioned before. It features symmetric coordination with both pyridine groups being *trans* to the bridging oxo-group. Also, there are no hydrogen bonds between the two subunits and the bridging angle is much higher (169°). The *t*Bu

substituent most likely causes too much steric hindrance and therefore does not allow for similar alignment of the ligands as seen in the other complexes.

The crystal structure of $[(FeL)_2]$ will be discussed separately as it is a diferrous complex and shows a significantly different coordination mode. In $[(FeL)_2]$, $(L)^{2-}$ is the only donor and allows for distorted octahedral coordination via the μ-bridging abilities of the ligand (see Figure 2.18). The N_3O_2 donor set accounts for pentadentate coordination and one phenolate O-atom of each ligand bridges to the adjacent iron ion resulting in overall six-coordinate iron centers (see Table 2.4 for selected bond lengths and angles). This kind of metal bridging ability of the phenolate ligand is very common [66-70]. $[(FeL)_2]$ is a neutral complex and contains an inversion center which allows to transform equivalent atoms via -x+1, -y+1, -z+1. Although it is common for phenolate to act as a bridging moiety between two metal centers, to the best of my knowledge, diferrous bis(μ-phenoxy) complexes with an additional N3 donor around each iron center have not been reported thus far. Yet, N_2O_2 reduced Schiff base iron(II) complexes have been synthesized where two phenolate anions act as a bridge between the two units, resulting in overall pentadentate coordination around the metal center [71].

Table 2.2. Selected bond lengths (Å) and angles (deg) for $[(FeL)_2(\mu\text{-}O)]$.

Fe1-O1	1.8192(17)	Fe2-O1	1.8160(17)
Fe1-O1A	1.9673(17)	Fe2-O28B	1.9785(18)
Fe1-O28A	2.0003(17)	Fe2-O1B	1.9967(17)
Fe1-N9A	2.227(2)	Fe2-N9B	2.186(2)
Fe1-N20A	2.254(2)	Fe2-N18B	2.231(2)
Fe1-N18A	2.273(2)	Fe2-N20B	2.238(2)
Fe1⋯Fe2	3.454(7)	Fe2-O1-Fe1	143.70(10)
O1-Fe1-O1A	105.55(8)	O1-Fe2-O28B	95.40(7)
O1-Fe1-O28A	101.83(7)	O1-Fe2-O1B	96.19(7)
O1A-Fe1-O28A	87.49(7)	O28B-Fe2-O1B	102.23(7)
O1-Fe1-N9A	92.05(8)	O1-Fe2-N9B	95.65(8)
O1A-Fe1-N9A	89.36(7)	O28B-Fe2-N9B	162.77(7)
O28A-Fe1-N9A	166.11(8)	O1B-Fe2-N9B	89.67(8)
O1-Fe1-N20A	89.91(8)	O1-Fe2-N18B	95.23(7)
O1A-Fe1-N20A	164.41(8)	O28B-Fe2-N18B	88.03(8)
O28A-Fe1-N20A	87.36(7)	O1B-Fe2-N18B	163.83(8)
N9A-Fe1-N20A	92.13(8)	N9B-Fe2-N18B	77.83(8)
O1-Fe1-N18A	162.02(7)	O1-Fe2-N20B	177.79(8)
O1A-Fe1-N18A	88.81(7)	O28B-Fe2-N20B	86.68(7)
O28A-Fe1-N18A	89.34(7)	O1B-Fe2-N20B	84.08(7)
N9A-Fe1-N18A	77.06(8)	N9B-Fe2-N20B	82.15(8)
N20A-Fe1-N18A	76.43(8)	N18B-Fe2-N20B	84.08(8)

Table 2.3. Selected bond lengths (Å) and angles (deg) for $[(FeL^{NO2})_2(\mu\text{-}OH)]ClO_4$.

Fe1-O1A	1.9315(17)	Fe2-O1B	1.9134(16)
Fe1-O34A	1.9554(16)	Fe2-O34B	1.9308(16)
Fe1-O1	1.9689(16)	Fe2-O1	2.0028(16)
Fe1-N16A	2.171(2)	Fe2-N12B	2.1681(19)
Fe1-N23A	2.1716(19)	Fe2-N23B	2.1756(19)
Fe1-N12A	2.1716(19)	Fe2-N16B	2.1987(19)
Fe1⋯Fe2	3.733(5)	Fe1-O1-Fe2	140.05(9)
O1A-Fe1-O34A	98.87(7)	O1B-Fe2-O34B	92.56(7)
O1A-Fe1-O1	92.91(7)	O1B-Fe2-O1	98.98(7)
O34A-Fe1-O1	94.58(7)	O34B-Fe2-O1	94.81(7)
O1A-Fe1-N16A	92.14(7)	O1B-Fe2-N12B	91.08(7)
O34A-Fe1-N16A	166.24(7)	O34B-Fe2-N12B	173.91(7)
O1-Fe1-N16A	93.05(7)	O1-Fe2-N12B	89.44(7)
O1A-Fe1-N23A	168.67(7)	O1B-Fe2-N23B	171.41(7)
O34A-Fe1-N23A	89.71(7)	O34B-Fe2-N23B	89.74(7)
O1-Fe1-N23A	93.76(7)	O1-Fe2-N23B	89.06(7)
N16A-Fe1-N23A	78.37(7)	N12B-Fe2-N23B	85.96(7)
O1A-Fe1-N12A	90.49(7)	O1B-Fe2-N16B	90.87(7)
O34A-Fe1-N12A	84.18(7)	O34B-Fe2-N16B	91.40(7)
O1-Fe1-N12A	176.52(7)	O1-Fe2-N16B	168.09(7)
N16A-Fe1-N12A	87.53(7)	N12B-Fe2-N16B	83.66(7)
N23A-Fe1-N12A	83.00(7)	N23B-Fe2-N16B	80.80(7)

Table 2.4. Selected bond lengths (Å) and angles (deg) for $[(FeL)_2]$.

Fe1-O1	2.0159(17)	Fe1-N14	2.194(2)
Fe1-O28	2.1307(17)	Fe1-N9	2.248(2)
Fe1-O28#1	2.1329(17)	Fe1-N20	2.288(2)
Fe1⋯Fe1#1	3.354(9)		
O1-Fe1-O28	98.48(7)	O28-Fe1-N9	99.39(7)
O1-Fe1-O28#1	99.14(7)	O28#1-Fe1-N9	173.84(7)
O28-Fe1-O28#1	76.23(7)	N14-Fe1-N9	87.77(8)
O1-Fe1-N14	97.86(7)	O1-Fe1-N20	165.65(8)
O28-Fe1-N14	162.60(7)	O28-Fe1-N20	84.98(7)
O28#1-Fe1-N14	95.28(7)	O28#1-Fe1-N20	95.22(7)
O1-Fe1-N9	85.71(7)	N14-Fe1-N20	80.65(7)
N9-Fe1-N20	79.98(8)	Fe1-O28-Fe1#1	103.77(7)

Symmetry transformations used to generate equivalent atoms: for $[(FeL)_2]$
#1 –x+1, –y+1, –z+1

2.4.2 Hydrogen Bonding Pocket

Complexes $[(FeL)_2(\mu\text{-}OH)]BPh_4$, $[(FeL)_2(\mu\text{-}O)]$, and $[(FeL^{NO2})_2(\mu\text{-}OH)]ClO_4$ have the capability of H-bond formation to H-bond acceptor molecules (see Figure 2.19 for illustration).

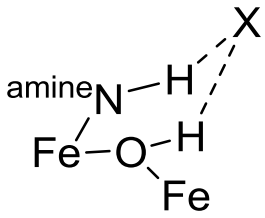

Figure 2.19. Schematic depiction of the hydrogen bonding pocket ($^{amine}N$ bonded to the H-atom represents the amine from the ligand; X represents a solvent donor atom capable of H-bonding; H atom attached to the oxo-bridge is either part of the hydroxo-bridge or H atom from the solvent donor atom X in the case of $[(FeL)_2(\mu\text{-}O)]$).

$[(FeL)_2(\mu\text{-}OH)]BPh_4$ was previously synthesized from methanol [59] and shows hydrogen bonding to methanol via the ligand N–H and the bridging O–H hydrogen bond donors (see Figure 2.20, top). The H-acceptor atom from the solvent molecule forms a six-membered ring with the complex unit. However, when $[(FeL)_2(\mu\text{-}OH)]BPh_4$ is recrystallized from CH_2Cl_2/pentane, the pocket is open (see Figure 2.20, bottom) and no guest molecule is observed in the solid state; CH_2Cl_2 occupies other lattice space within the crystal.

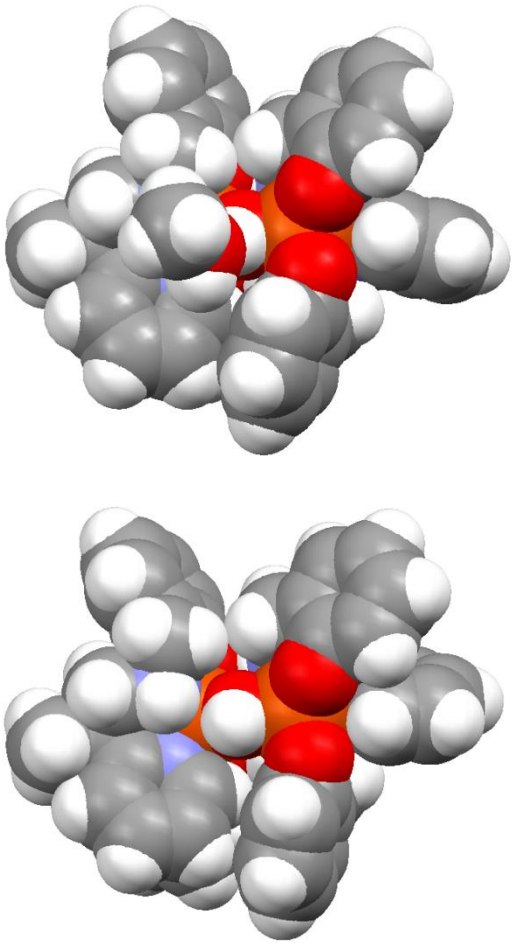

Figure 2.20. Space filling model of $[(FeL)_2(\mu\text{-}OH)]^+$. Top: from R. Shakya: crystallized from methanol; bottom: my work: crystallized from CH_2Cl_2.

Similar to $[(FeL)_2(\mu\text{-}OH)]BPh_4$, $[(FeL^{NO2})_2(\mu\text{-}OH)]ClO_4$ shows one molecule of water in the pocket (see Figure 2.21).

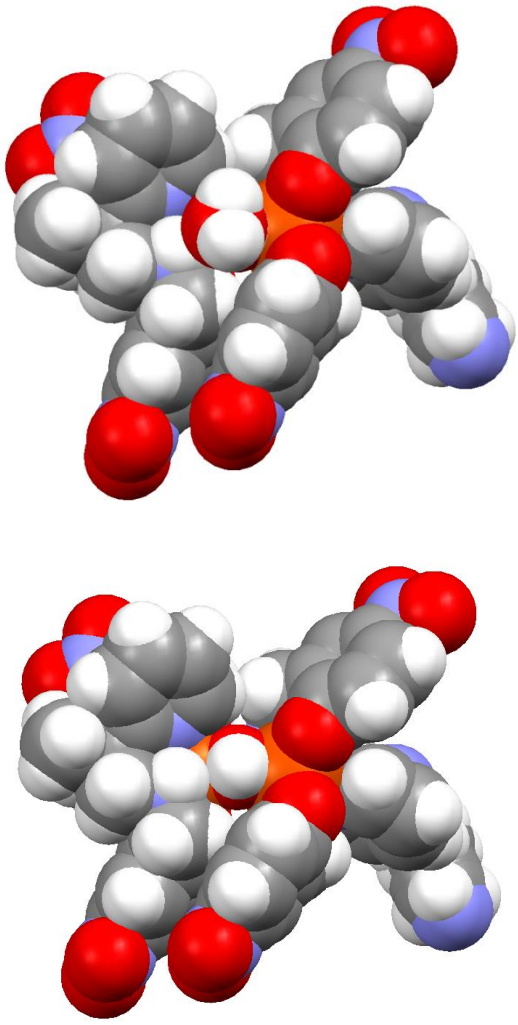

Figure 2.21. Space filling model of $[(FeL^{NO2})_2(\mu\text{-}OH)]^+$. Top: with water; bottom: water removed to show pocket.

In contrast to $[(FeL)_2(\mu\text{-}OH)]BPh_4$ and $[(FeL^{NO2})_2(\mu\text{-}OH)]ClO_4$, $[(FeL)_2(\mu\text{-}O)]$ only exhibits one H-bond donor which is the ligand N–H, and when $[(FeL)_2(\mu\text{-}O)]$ is recrystallized from wet acetone/pentane, one molecule of acetone interacts with the described hydrogen bond (see Figure 2.22), and a molecule of water and a second acetone are present elsewhere in the lattice.

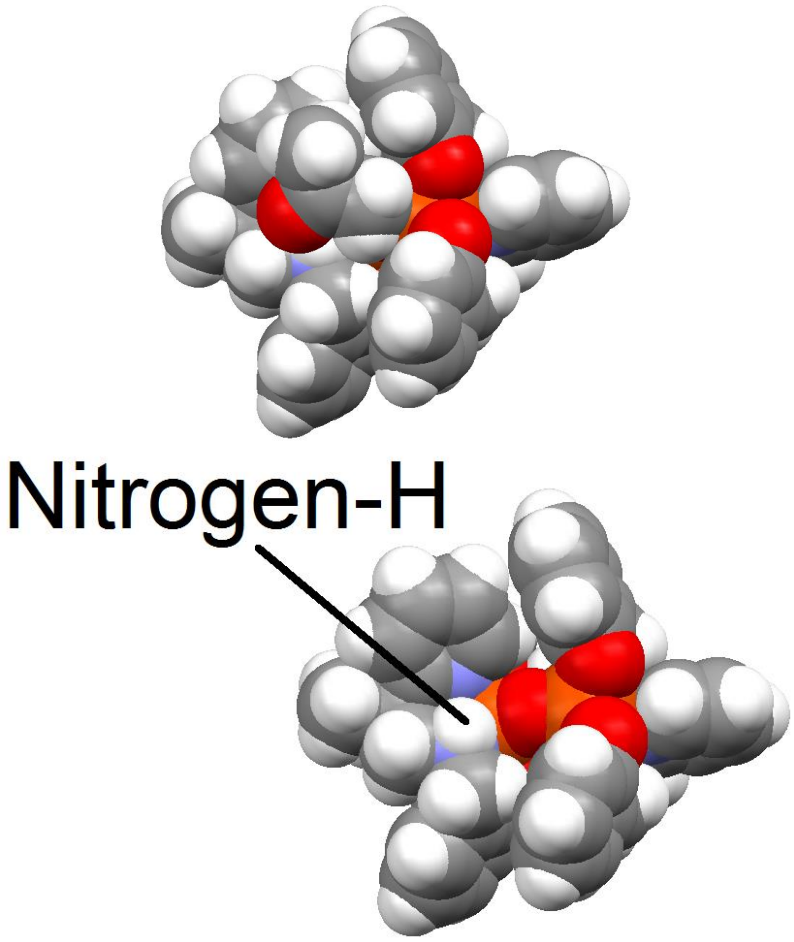

Figure 2.22. Space filling model of [$(FeL)_2(\mu\text{-}O)$]. Top: with acetone; bottom: acetone removed to show pocket.

If one considers the space filling model (see Figure 2.22), clearly the O-bridge seems sterically inaccessible and this is probably the reason why the highly basic O-bridge does not get protonated by the water present in solution. On the other hand, when crystals are crushed up and dried under high vacuum, elemental analysis matches best with a formula of [$(FeL)_2(\mu\text{-}O)$]·H_2O.

The H-bonding pocket, when occupied by an H-bond acceptor, X, can be compared to the H-bonding configuration in the mixed-valence state of the active site of rubrerythrin (see Figure 2.23) [19, 72].

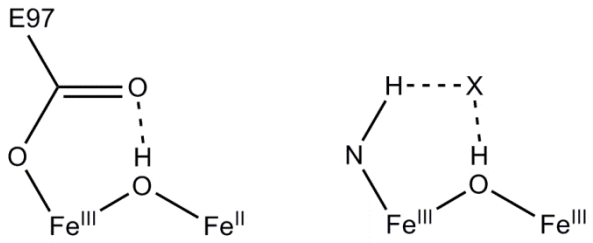

Figure 2.23. Hydrogen bonding in the mixed-valence state of rubrerythrin (left) and in the diferric model complexes presented in this work (right).

It seems likely that this H-bonding with glutamate (E97) stabilizes the mixed-valence state in the enzyme by preventing proton transfer. Studies of Rbr mutants revealed that E97, which seems to be unique to this enzyme, is essential for the formation of a mixed-valent intermediate [23]. Model studies conducted by Wieghardt and colleagues [56] show that proton transfer from the bridging (hydr)oxo ligand is a key step in disproportionation. This suggests that an appropriate H-bond acceptor, X, might be able to trap the bridging proton in our complexes, thereby preventing proton exchange and ultimately stabilizing a mixed-valence state. A series of studies needs to be conducted to find a suitable X; if X is too basic, it will simply deprotonate the hydroxo bridge, but if it is too acidic, it may introduce free protons into the system.

2.5 Chemical Reduction of $[(FeL)_2(\mu\text{-}OH)]BPh_4$

In a previous publication the synthesis and characterization of $[(FeL)_2(\mu\text{-}OH)]BPh_4$ were presented [59]. From the CV of $[(FeL)_2(\mu\text{-}OH)]BPh_4$ (see Figure 2.15) it is possible to estimate the stability of a potential mixed-valence complex (FeII, FeIII) using equation 1. With a K_c of $\approx 10^{11}$ for $[(FeL)_2(\mu\text{-}OH)]BPh_4$, a reasonably stable mixed-valence complex is expected, and the crystal structure of $[(FeL)_2(\mu\text{-}OH)]BPh_4$

suggests the formation of a localized mixed-valence complex upon reduction due to the different coordination environment around each iron center. Cobaltocene ($CoCp_2$) is an appropriate reductant according to its high reduction potential of –1.33V vs. Fc (in CH_2Cl_2) [73], and the fact that its potential lies in between the two redox couples.

The reaction of the purple complex $[(FeL)_2(\mu\text{-}OH)]BPh_4$ with $CoCp_2$ in CH_2Cl_2 resulted in a color change to yellow-orange and the formation of a yellow precipitate which was filtered off and identified as $[CoCp_2]BPh_4$. After removal of the solvent, a crude orange precipitate was isolated and $[(FeL)_2(\mu\text{-}O)]$ was obtained after recrystallization in the presence of air.

To further investigate the formation of $[(FeL)_2(\mu\text{-}O)]$ upon reduction of $[(FeL)_2(\mu\text{-}OH)]BPh_4$, a titration study was conducted in MeCN. After addition of $CoCp_2$ solution to $[(FeL)_2(\mu\text{-}OH)]BPh_4$, the band at 496 nm in the UV-Vis spectrum disappears while a new band grows in at 412 nm. Three isosbestic points can be detected at about 313, 358 and 434 nm. The absorption at 412 nm has about half of the intensity as the band at 496 nm after the addition of one equivalent of reductant (Figure 2.24). The side product $[CoCp_2]BPh_4$ only adds slightly to the band at 412nm. (see Figure 2.25, absorption spectrum of $[CoCp_2]BPh_4$). After exposure to O_2 the new band increases in intensity by about twofold without a significant shift in λ_{max}.

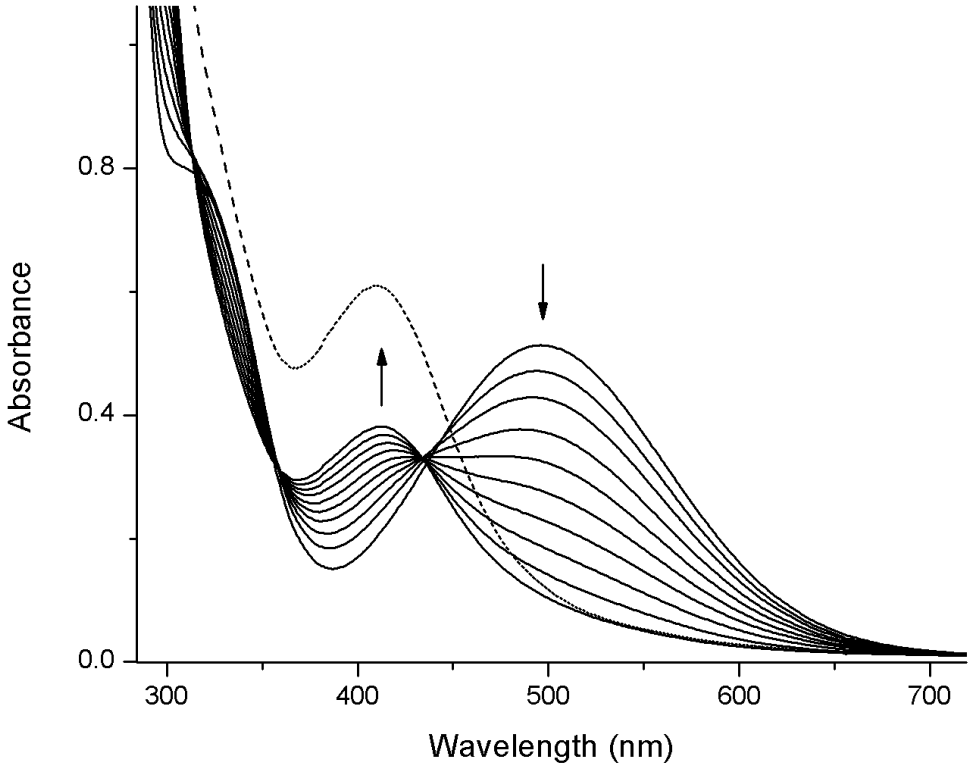

Figure 2.24. Titration of $[(FeL)_2(\mu\text{-}OH)]BPh_4$ (7.3×10^{-5} M) with up to 1eq. $CoCp_2$ in MeCN monitored by UV-Vis spectroscopy (solid lines) and subsequent addition of O_2 (dashed line).

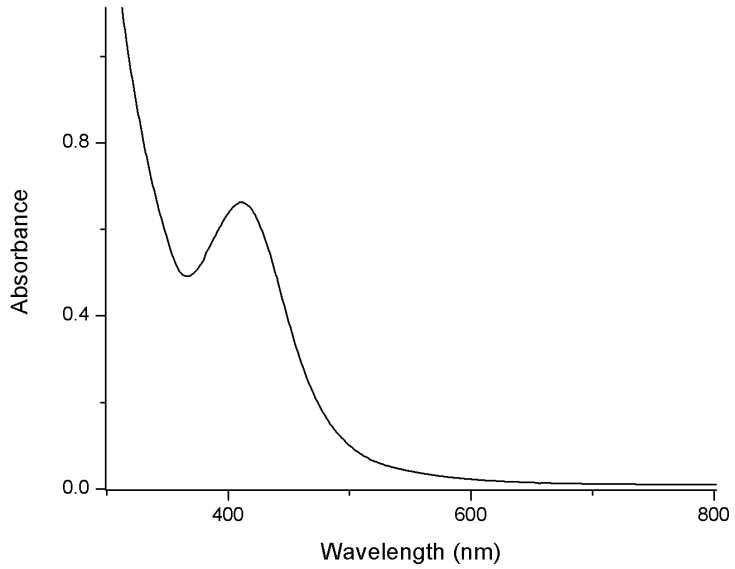

Figure 2.25. UV-Vis of $[CoCp_2]BPh_4$ (0.9×10^{-3} M) in MeCN. Molar absorptivity at 412 nm = 262 $M^{-1}cm^{-1}$.

It is likely that half an equivalent of $[(FeL)_2(\mu\text{-}O)]$ is formed from one equivalent of $[(FeL)_2(\mu\text{-}OH)]BPh_4$ after reduction, and after subsequent exposure to O_2 all material is converted to $[(FeL)_2(\mu\text{-}O)]$. A mechanism is proposed, which is depicted in Scheme 2.5 and two paths for decomposition upon reduction are likely, both yielding $[(FeL)_2(\mu\text{-}O)]$ and $[(FeL)_2(\mu\text{-}OH_2)]$ (see blue box in Scheme 2.5). The typically pale diferrous species barely contributes to the UV-Vis absorption [56].

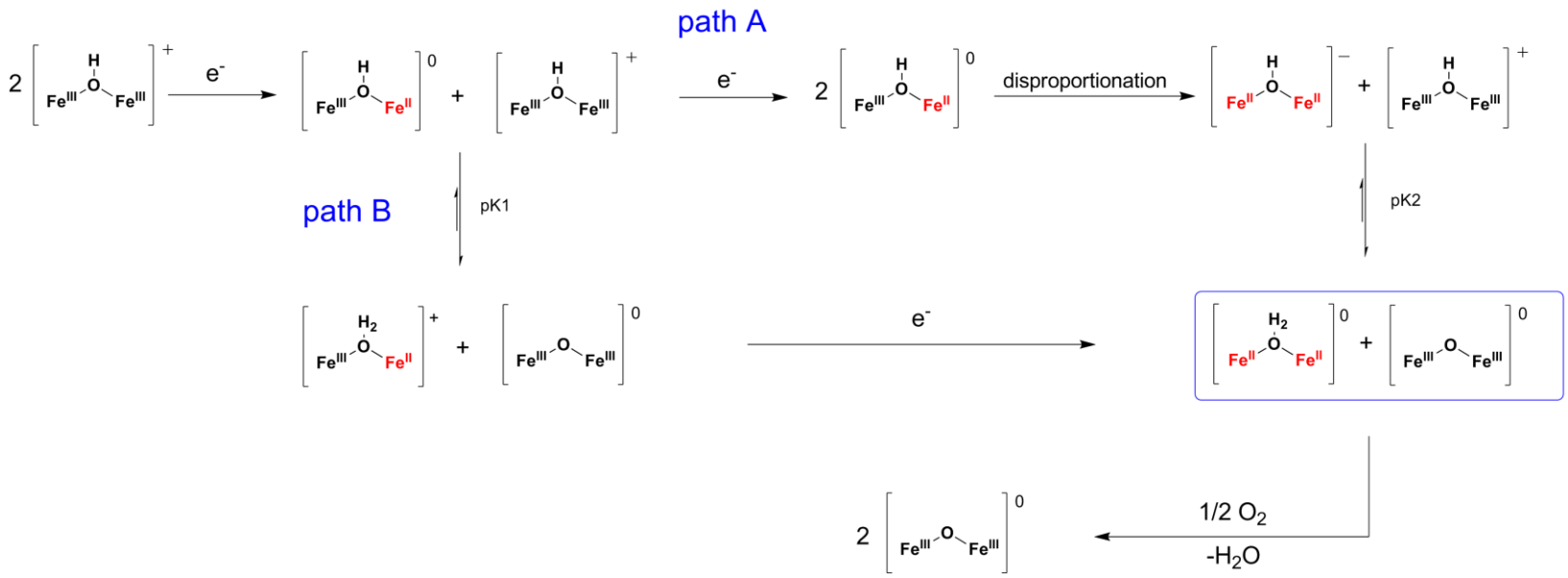

Scheme 2.5. Reaction of $[(FeL)_2(\mu\text{-}OH)]BPh_4$ upon reduction and subsequent exposure to O_2.

The question which arises is how the products in the blue box are generated or what the mechanistic pathway could be like. Two paths are suggested (see path A and B in the scheme, Fe(II) ions are shown in red). In path A, two equivalents of $[(FeL)_2(\mu\text{-}OH)]^+$ are reduced, which results in the formation of two equivalents of mixed-valence $[(FeL)_2(\mu\text{-}OH)]$. If two of these species are in close proximity, disproportionation may occur, yielding diferric $[(FeL)_2(\mu\text{-}OH)]^+$ and diferrous $[(FeL)_2(\mu\text{-}OH)]^-$. The pK_a of the differic complex should be lower (its bridging-oxygen atom is less basic because more electron density is shared with the iron(III) centers) than that of the diferrous complex, which causes formation of $[(FeL)_2(\mu\text{-}O)]$ and $([(FeL)_2(\mu\text{-}OH_2)]$ (see blue box). The alternate path for decomposition is also shown (path B). It is possible that upon addition of substoichiometric amounts of reductant, some of the mixed-valence complex $[(FeL)_2(\mu\text{-}OH)]$ is formed. When mixed-valence $[(FeL)_2(\mu\text{-}OH)]$ and unreacted $[(FeL)_2(\mu\text{-}OH)]^+$ are in close proximity, proton transfer should occur from the ferric to the mixed-valence complex due to a difference in pK_a, resulting in products $[(FeL)_2(\mu\text{-}OH_2)]^+$ and $[(FeL)_2(\mu\text{-}O)]$. With the addition of another electron, it is probably more likely to reduce the cationic species. This results, again, in formation of the same products shown in the blue box.

The difference between the two paths is that path A follows a disproportionation reaction, while in path B, two separate reductions occur. Both paths may yield in the same products. Moreover it could be that both paths occur simultaneously and even more equilibria between different species are transpiring. If path B is very fast, and path A may not be thermodynamically as favorable, it could be possible to trap the mixed-valence complex by fixation of the bridging OH proton. The proper hydrogen bonded

host molecule, X, may hold the proton in position. This could allow for isolation and characterization of the mixed-valence complex.

The oxo-bridged dimer has about a 1.2-fold higher absorption than the hydroxo-bridged complex; this explains the difference in intensities in the final spectrum after oxygenation. Even under argon at –78°C, no other intermediates were captured when $[(FeL)_2(\mu\text{-}OH)]BPh_4$ was treated with cobaltocene. Further studies, which are discussed in the electrochemistry section below, support the described decomposition of $[(FeL)_2(\mu\text{-}OH)]BPh_4$ upon electrochemical reduction.

The reaction pathway upon reduction of $[(FeL)_2(\mu\text{-}OH)]BPh_4$ stays in good agreement with the work done by Wieghardt and coworkers, who trapped an OH-bridged mixed-valence species and followed its decomposition to the oxo-bridged complex after time [56]. Yet, it is surprising that the mixed-valence species of $[(FeL)_2(\mu\text{-}OH)]BPh_4$ is so unstable compared to Wieghardt's complex which is stable for about half an hour at room temperature. It is possible that the difference in pK_a from our complex compared to Wieghardt's complex causes faster proton exchange, which drives the decomposition faster than for his complex.

2.6 Electrochemistry

The redox behavior of $[(FeL)_2(\mu\text{-}OH)]BPh_4$ was previously described in methylene chloride [59]. In the work presented in this dissertation, all complexes are explored through cyclic voltammetry in acetonitrile solutions and the CV of $[(FeL)_2(\mu\text{-}OH)]BPh_4$ was repeated in acetonitrile in order to allow for reasonable comparison. Similar to what was seen in methylene chloride, complex $[(FeL)_2(\mu\text{-}OH)]BPh_4$ exhibits

two quasi-reversible metal centered reductions at $E_{½}$ = –1052 mV (ΔE = 131 mV) and $E_{½}$ = –1724 mV (ΔE = 192 mV) versus ferrocene which were initially assigned to the Fe(III)Fe(III) /Fe(II)Fe(III) and Fe(II)Fe(III) /Fe(II)Fe(II) couples, respectively. At positive potentials an irreversible ligand centered oxidation is found at +356 mV (Figure 2.26).

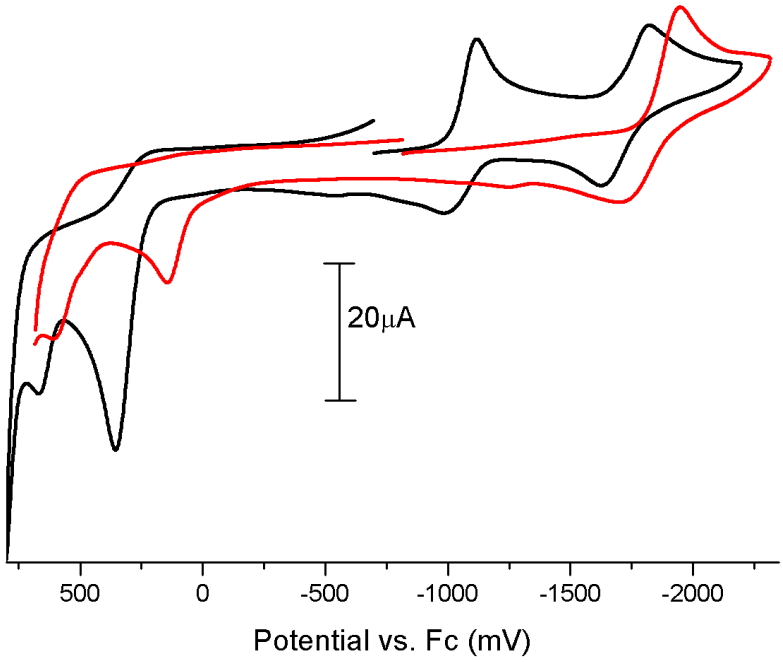

Figure 2.26. Cyclic voltammograms (scan rate = 100 mV s^{-1}; 0.1 M $TBAPF_6$ supporting electrolyte) of 1.0 mM solutions of $[(FeL)_2(\mu\text{-}OH)]BPh_4$ (black line) and $[(FeL)_2(\mu\text{-}O)]$ (red line) in MeCN.

In contrast, $[(FeL)_2(\mu\text{-}O)]$ shows only one quasi-reversible reduction feature at $E_{½}$= –1824 (ΔE = 246 mV) assigned to the Fe(III)Fe(III)/Fe(II)Fe(III) redox couple. The second reduction feature is not accessible due to the limitations of the solvent window. There is also one irreversible feature at +145 mV which corresponds to ligand oxidation (Figure 2.26). The potential shift of the differic to ferrous/ferric couple, compared to that of $[(FeL)_2(\mu\text{-}OH)]BPh_4$, seems reasonable because the oxo ligand in

$[(FeL)_2(\mu\text{-}O)]$ causes higher electron density at the metal centers and therefore inertia towards reduction.

Initial CV studies on powdered material having sufficient purity (according to elemental analysis) of $[(FeL^{NO2})_2(\mu\text{-}OH)]ClO_4$ show similar redox features to $[(FeL)_2\mu\text{-}OH]BPh_4$. The metal featured redox couples are shifted 475 mV more positive (see Figure 2.27). This shift is reasonable due to the electron-withdrawing nature of the nitro-substituted ligand, resulting in more positive iron centers and thus more favorable reduction. No oxidative processes were observed within the solvent window of MeCN. In order to explore the nature of the metal centered redox features in more depth, more crystalline material of the complex has to be obtained. This is problematic because the crystallization is low yielding and takes several months.

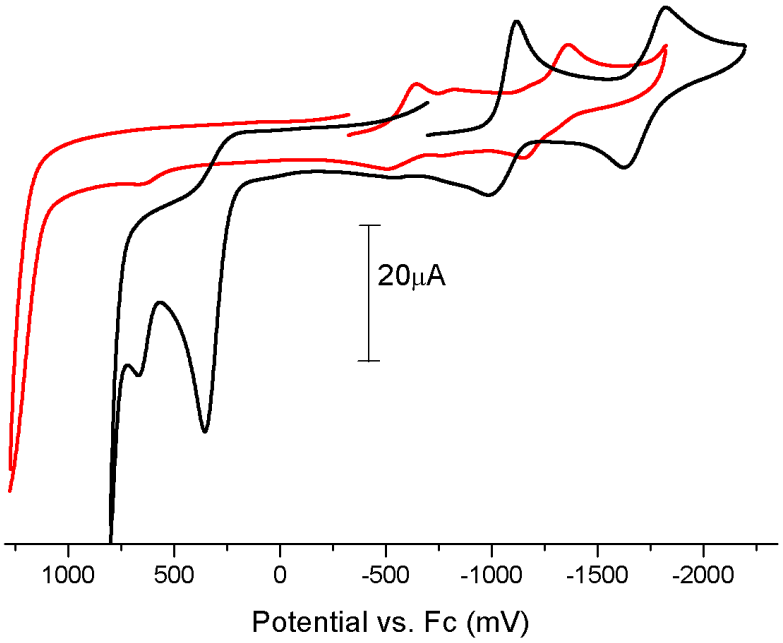

Figure 2.27. Cyclic voltammograms (scan rate = 100 mV s^{-1}; 0.1 M $TBAPF_6$ supporting electrolyte) of 1.0 mM solutions of $[(FeL)_2\mu\text{-}OH]BPh_4$ (black line) and $[(FeL^{NO2})_2(\mu\text{-}OH)]ClO_4$ (red line) in MeCN.

Further studies on the electrochemistry of $[(FeL)_2\mu\text{-}OH]BPh_4$ using different scan rates revealed more complex behavior. The first redox couple, assigned to Fe(II)/Fe(III), is chemically irreversible and electrochemically quasi-reversible. The quasi reversible behavior is valid because of the following criteria [74]: (1) $E_{½}$ does not change significantly with scan rates; (2) $\Delta E_p > 60$ mV and increases with the scan rate; (3) $I_{pa}/I_{pc} < 1$ (here $I_{pa}/I_{pc} \sim 0.5$). At faster scan rates the back oxidation seems more reversible (see Figure 2.28) suggesting a follow-up reaction upon reduction of $[(FeL)_2\mu\text{-}OH]^+$.

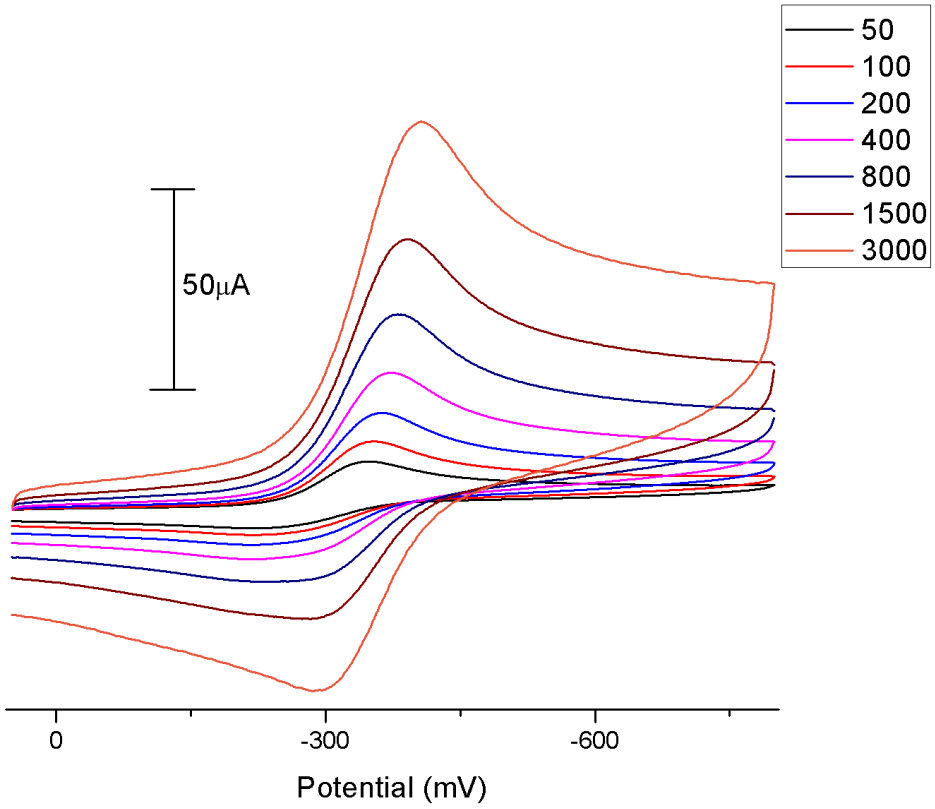

Figure 2.28. CV of the first reduction peak of $[(FeL)_2\mu\text{-}OH]BPh_4$ at different scan rates.

Scanning to more negative potentials indicates that the second redox feature cannot be assigned to the mixed-valence to Fe(II)/Fe(II) couple. When the scan rate is

increased additional peaks show up in the CV (see Figure 2.29). It can be suggested that the incoming reduction peak at –1100 mV is actually related to the Fe(III)/Fe(II) to Fe(II)/Fe(II) couple. At low scan rates this peak is not observed because of the quick disproportionation of the mixed-valence complex. The peak centered at –1200 mV is more likely to be the Fe(III)/Fe(III) to Fe(III)/Fe(II) couple of $[(FeL)_2\mu\text{-}O]$, which is one of the direct products of disproportionation described here. The incoming oxidative peak at –400 mV could be assigned to an oxidation of the diferrous complex. It would be difficult to calculate a new comproportionation constant K_c, without knowing, which peaks exactly corresponds to the Fe(III)/Fe(II) to Fe(II)/Fe(II) couple. However, since the incoming peaks at faster scan rates lie at more positive potentials, one can say that the separation of the two metal centered redox couples is smaller than estimated before and hence K_c will be smaller. This would be in agreement with the high instability of the mixed-valence species.

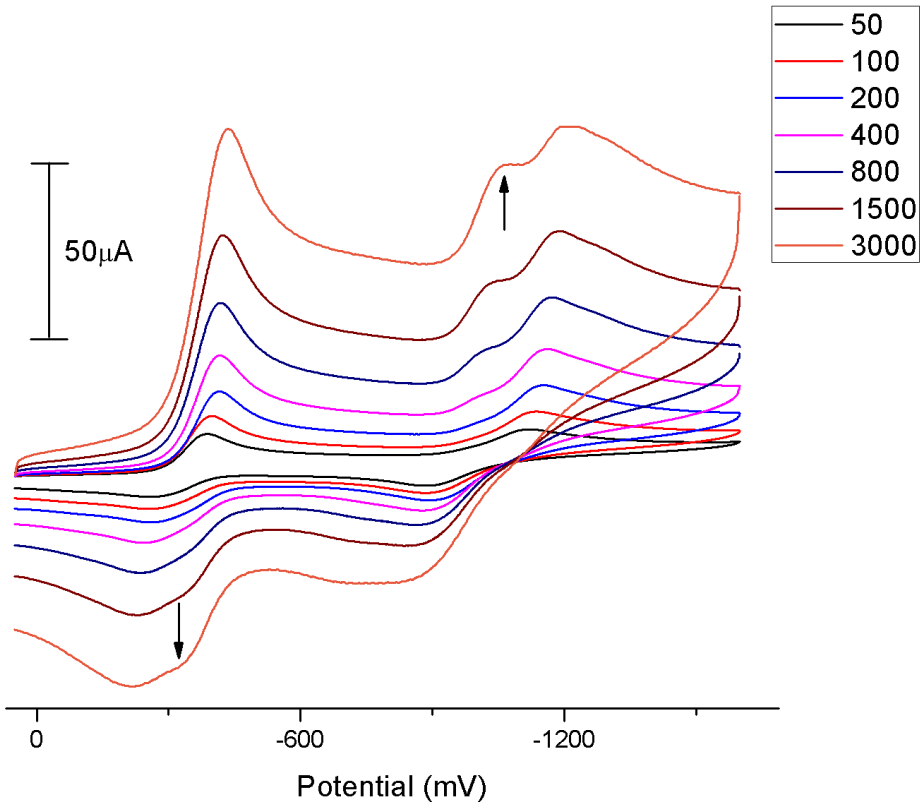

Figure 2.29. CV of the reduction peaks of $[(FeL)_2\mu\text{-}OH]BPh_4$ at different scan rates.

2.7 Spectroscopic Properties of Complexes

The spectroscopic features of $[(FeL)_2(\mu\text{-}OH)]BPh_4$ and $[(FeL)_2(\mu\text{-}O)]$ are described in the following section. The main difference between the two complexes is the dramatic color change from dark purple for the hydroxo-bridged complex to an orange-yellow for the oxo-bridged complex (see photo of both powders in a vial in Figure 2.30).

Figure 2.30. Powdered complex of $[(FeL)_2(\mu\text{-}O)]$ (left vial) and $[(FeL)_2(\mu\text{-}OH)]BPh_4$ (right vial).

The UV-Visible spectra of $[(FeL)_2(\mu\text{-}OH)]BPh_4$ and $[(FeL)_2(\mu\text{-}O)]$ exhibit three distinct bands in the range of 200 to 1000 nm. The near-UV features (less than 300 nm) are assigned as π–π^* transitions of the phenolate groups [75]. The high energy transition (335-430 nm) is assigned to the CT from the out of plane $p\pi$ orbital (HOMO) of the phenolate oxygen to the d-orbital of the iron center. The low energy band (475-550 nm) arises from the in-plane $p\pi$ orbital (POMO) of the phenolate to the d π^* orbital of the iron(III) ion [76]. The position and intensity of the LMCT band is sensitive towards the coordination environment of the iron center [30]. In $[(FeL)_2(\mu\text{-}OH)]BPh_4$, the purple color, and therefore the band at around 500 nm brings to mind the CT band of purple acid phosphatase's active site which is located at 510-560 nm (see introduction of Chapter 2) [25]. This is not surprising due to similarities in ligands that cause the CT band (phenolate here vs. tyrosinate in PAP).

In $[(FeL)_2(\mu\text{-}O)]$ the two high energy bands are similar to $[(FeL)_2(\mu\text{-}OH)]BPh_4$. The iron ion in $[(FeL)_2(\mu\text{-}O)]$ is a weaker Lewis acid than in $[(FeL)_2(\mu\text{-}OH)]BPh_4$ because of the stronger electron donation from the oxo ligand versus the hydroxo

ligand, respectively. Thus the d-orbitals in $[(FeL)_2(\mu\text{-}O)]$ are higher in energy and create a greater energy gap for the LMCT (phenolate to iron) resulting in a blue shift [77]. There is only a slight increase in absorption for $[(FeL)_2(\mu\text{-}O)]$ compared to $[(FeL)_2(\mu\text{-}OH)]BPh_4$ which is reasonable considering that the overall coordination is similar. The decrease of the O–Fe bond length in $[(FeL)_2(\mu\text{-}O)]$ compared to $[(FeL)_2(\mu\text{-}OH)]BPh_4$ most likely causes the higher probability for the LMCT due to greater overlap of the orbitals. The significant difference in the absorption maximum of the POMO band in $[(FeL)_2(\mu\text{-}OH)]BPh_4$ compared to $[(FeL)_2(\mu\text{-}O)]$ makes it convenient to monitor the interconversion of the two complexes by UV-Vis spectroscopy.

The absorption spectrum of $[(FeL^{NO2})_2(\mu\text{-}OH)]ClO_4$ is dominated by a broad band at 380 nm with significantly higher molar absorptivity than seen in $[(FeL)_2(\mu\text{-}OH)]BPh_4$. This band is mainly assigned to π–π^* transition within the nitrophenolate unit [78]. Most likely this band covers the higher energy LMCT. The lower energy LMCT is shifted to higher energy and also falls into the broad high absorbing feature [79]. The fact that the band at 380 nm masks the absorption features which reflect the nature of the coordination environment around the metal center, does not allow for pK_a determination via UV-Vis titrations.

2.8 Characterization of $[(FeL)_2]$ and Its Lability Towards Dioxygen

The reaction of H_2L with the ferrous salts $FeCl_2$ or $Fe(OTf)_2$ in the presence of base in methanol yields the complex [FeL(MeOH)] according to elemental analysis. The crude powder is either a monomer with MeOH in the sixth coordination position or a dimer with two molecules of methanol hydrogen bonded to the complex (even after

drying under high vacuum and heat the solvent molecule could not be removed). Upon recrystallization the neutral dimer [$(FeL)_2$] is formed which still shows hydrogen bonding to one molecule of methanol for each dimer (solvent is omitted in the crystal structure depiction, Figure 2.18, for clarity).

A solution of complex [FeL(MeOH)] in DCM rapidly reacts with O_2 to give [$(FeL)_2(\mu$-O)]. This reaction was monitored via UV-Vis spectroscopy where a change in absorption from 471 nm to 420 nm with a strong increase in absorptivity occurs (see Figure 2.31). Similar reactions have been observed in the past and a mechanistic pathway is proposed (see Scheme 2.6) [3].

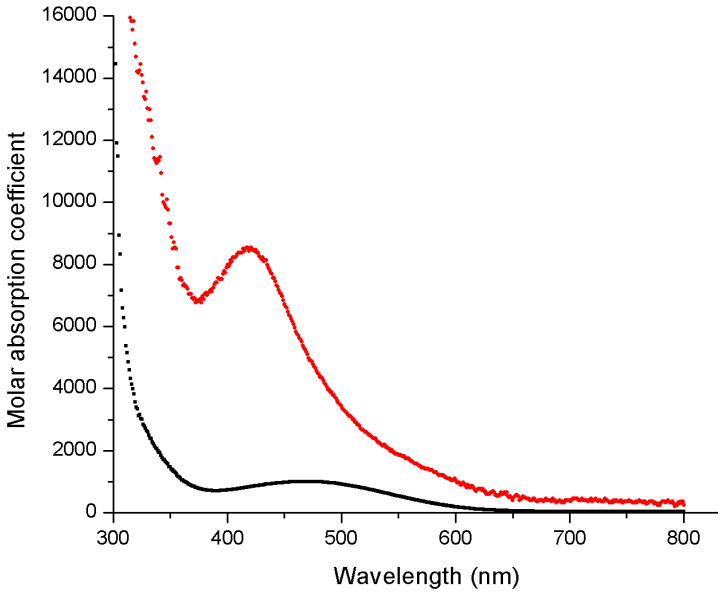

Figure 2.31. UV-Vis spectrum of [$(FeL)_2$] in MeCN (λ_{max} at 471 nm, ε = 1000) (black) and after exposure to air (λ_{max} at 420 nm, ε = 8500), (red).

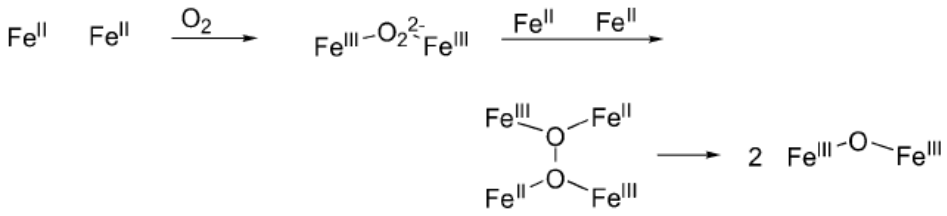

Scheme 2.6. Mechanistic oxidation of Fe(II) by O_2. Scheme is adapted from reference [3].

In a different experiment, complex [FeL(MeOH)] was prepared in methanol and immediately exposed to air. Diethyl ether diffusion under atmospheric conditions gave crystals of $[(FeL)_2(\mu\text{-}OH)]^+$ (OTf^- was the counter ion). The formation of the hydroxo-bridged complex over the oxo-bridged is not surprising due to the high basicity of $[(FeL)_2(\mu\text{-}O)]$. Mass spectra of [FeL(MeOH)] only show m/z = 879.2606, which corresponds to the protonated oxygenated product, $[(FeL)_2(\mu\text{-}OH)]^+$. The coordination of tetradentate salan ligands to the Fe(II)-ion and the ability of the phenolate-O to act as a bridging unit has been studied recently and similar O_2 reactivity was shown [71].

2.9 Conclusion

In summary, the synthesis and characterization of new model complexes for active sites of asymmetric (hydr)oxo bridged diiron containing enzymes are presented. The complexes show unique intermolecular hydrogen bonding, which supports the bridging (hydr)oxo group and holds the iron units together in a bent configuration. De/protonation does not affect the bridging angle significantly. Further, a hydrogen bonding pocket was discovered at the differic center which should cause high pKa values of the oxo-bridge. This pocket also mimics the configuration in the mixed-valence state of rubrerythrin's active site. Further studies, with the use of different H-

bond acceptors, X, will reveal if the proton from the hydroxo-bridge, once held in position, will allow for stabilization of the mixed-valence state. These studies will help to reveal the role of H-bonding between Glu97 and the diiron core in rubrerythrin. Further, it was shown that $[(FeL)_2(\mu\text{-}OH)]BPh_4$ decomposes upon one electron reduction and subsequent proton exchange produces $[(FeL)_2(\mu\text{-}O)]$. This behavior is consistent for both chemical and electrochemical reduction. A reasonable mechanism for the decomposition is presented. Preliminary studies of $[(FeL^{NO2})_2(\mu\text{-}OH)]ClO_4$ suggest that it is easier to reduce, and ongoing experiments will explore its potential to form a mixed-valence complex. It was also shown that $[(FeL)_2(\mu\text{-}O)]$ can be made via the ferrous precursor [FeL(MeOH)] upon exposure to air.

2.10 Experimental

2.10.1 General

Unless otherwise stated, all reagents were used as received from commercial sources. 2-methyl-2-(pyridine-2-yl)propane-1,3-diamine (ppda) was synthesized according to the published procedure [80]. H_2L^H and H_2L^{NO2} were synthesized according to the published procedures [70], [81]. Solvents used were doubly purified using alumina columns in a MBraun solvent purification system (MB-SPS). Infrared spectra were measured from 4000 to 400 cm^{-1} as KBr pellets, suspensions in Nujol or solutions on a Bio-Rad FTS155 FTIR spectrometer. ^{1}H NMR spectra were measured using a Varian 300 MHz instrument using solvent as an internal standard. Mass spectra were measured on a Q-TOF quadrupole time-of-flight mass spectrometer (Micromass, Manchester, U.K.) equipped with a Z-spray electrospray ionization (ESI) source.

Elemental analyses were performed by Atlantic Microlab, Norcross, GA. Cyclic voltammetry experiments were performed using a BAS 50W potentiometer and a standard three-electrode cell with a glassy-carbon working electrode, a Pt-wire auxiliary electrode, and an Ag pseudo reference electrode under an inert atmosphere at room temperature.

Caution! *Perchlorate salts of metal complexes with organic ligands are potentially explosive. Although no difficulty was encountered during the syntheses described herein, complexes should be prepared in small amounts and handled with caution.*

2.10.2 Synthesis of $[(FeL)_2(\mu\text{-}OH)]BPh_4$ via alternate route

The synthesis of $[(FeL)_2(\mu\text{-}OH)]BPh_4$ was varied slightly to the previously published [59]. $Fe(ClO_4)_3 \cdot 6H_2O$ (0.143 g, 0.310 mmol) in methanol (1 mL) was added to a methanolic solution (10 mL) of ligand (0.117 g, 0.310 mmol) and NEt_3 (0.075 g, 0.691 mmol) and the solution subsequently turned dark wine-red. After stirring for one hour at room temperature, solid $NaBPh_4$ (0.160 g, 0.468 mmol) was added and a purple precipitate formed immediately. The slurry was refluxed overnight and the purple precipitate collected by filtration. The crude powder of $[(FeL)_2(\mu\text{-}OH)]BPh_4$ was obtained (180 mg, 94%) after washing with methanol and diethyl ether and drying. $[(FeL)_2(\mu\text{-}OH)]BPh_4 \cdot 2H_2O$: $C_{70}H_{75}BFe_2N_6O_7$ (1234.88): calcd. C 68.08, H 6.12, N 6.81; found C 68.17, H 5.91, N 6.47. The crude powder was dissolved in CH_2Cl_2 and a small amount of insoluble residue removed by filtration through celite. After pentane diffusion into the dichloromethane filtrate, a microcrystalline dark purple solid, $[(FeL)_2(\mu\text{-}OH)]BPh_4 \cdot CH_2Cl_2$, was obtained which was collected and dried. This

material was suitable for X-ray diffraction. Crystalline $[(FeL)_2(\mu\text{-}OH)]BPh_4 \cdot CH_2Cl_2$: $C_{71}H_{73}BCl_2Fe_2N_6O_5$ (1283.78): calcd. C, 66.43; H, 5.73; N, 6.55; found C, 66.81; H, 5.74; N, 6.54. UV/Vis (MeCN): λ_{max} (ε, $M^{-1}cm^{-1}$) = 496 (7,000) nm.

2.10.3 Titration of $[(FeL)_2(\mu\text{-}OH)]BPh_4$ with Cobaltocene

Air-free titrations of $[(FeL)_2(\mu\text{-}OH)]BPh_4$ with $CoCp_2$ were monitored by UV-Vis spectroscopy in MeCN. Solutions of $[(FeL)_2(\mu\text{-}OH)]BPh_4$ (7.3×10^{-5} M, 3.25 mL) in a gas tight cuvette capped with a septum and $CoCp_2$ (2.5×10^{-3} M, 100 μL) in an airtight gas syringe were prepared in a dry box under nitrogen. The $CoCp_2$ solution was added in aliquots of 11 μL to the solution of $[(FeL)_2(\mu\text{-}OH)]BPh_4$ and a UV-Vis spectrum was collected after each addition. A total of one equivalent reducing agent was added to the diiron solution. Subsequently 0.5 mL of oxygen was added to the reacted solution and a final spectrum collected (see Figure 2.24).

2.10.4 Synthesis of $[(FeL)_2(\mu\text{-}O)]$: Reaction of $[(FeL)_2(\mu\text{-}OH)]BPh_4$ with Cobaltocene

$[(FeL)_2(\mu\text{-}OH)]BPh_4 \cdot 2H_2O$ (149.5 mg, 0.121 mmol) was dissolved in CH_2Cl_2 (14 mL), and to this stirring solution $CoCp_2$ (23.6 mg, 0.125 mmol) in DCM (1 mL) was added. The color changed immediately from dark purple to orange with formation of some yellow precipitate. The solution was stirred for 15 more minutes and diethylether (30 mL) was added to complete the precipitation. The reaction was worked up under air. The yellow ppt (58 mg, 0.114 mmol, 94%) was isolated after filtration and identified by NMR as well as X-ray diffraction as $CoCp_2BPh_4$. ^{1}H NMR (300 MHz, d–acetone, 293K) δ 5.88 (s, 10H, Cp^-), 6.78 (t, 4H, p-BPh_4), 6.93 (t, 8H, BPh_4), 7.34 (m,

8H, BPh_4). In a different experiment single crystals of $CoCp_2BPh_4$ were obtained from a dilute reaction solution.

The filtrate was concentrated in high vacuo and crude powder of $[(FeL)_2(\mu\text{-}O)]$ was obtained (110 mg, 0.120 mmol, 99%). $[(FeL)_2(\mu\text{-}O)]\cdot 2H_2O$: $C_{46}H_{54}Fe_2N_6O_7$ (914.65): calcd. C 60.40, H 5.95, N 9.19; found: C 60.50, H 6.22, N 8.74. Single crystals (41%) suitable for X-ray diffraction were obtained after vapor diffusion of pentane into acetone solution of crude $[(FeL)_2(\mu\text{-}O)]$. $[(FeL)_2(\mu\text{-}O)]\cdot H_2O$: $C_{46}H_{52}Fe_2N_6O_6$ (896.63): calcd. C 61.62, H 5.85, N 9.37; found: C 61.63, H 6.08, N 9.20. UV/Vis (CH_2Cl_2): λ_{max} (ε, $M^{-1}cm^{-1}$) = 235 (35,100), 270 (28,000), 420 (7,900) nm; (MeCN) = 412 (8,400) nm. FTIR (CH_2Cl_2): $\tilde{\nu}$ = 3686, 3605, 3277, 3048, 2913, 2860, 1714, 1593, 1566, 1481, 1454, 1359, 1292, 874, 596 cm^{-1}; (Nujol): 3250, 3111, 3057, 2958, 2922, 2851, 1714, 1638, 1593, 1566, 1481, 1454, 1359, 1287, 1225, 1072, 1013, 879, 757 cm^{-1}. ESI-MS (CH_2Cl_2): *m/z* = 431.1301 $[FeL]^+$, 879.2593 $[(FeL)_2(\mu\text{-}OH)]^+$.

2.10.5 Synthesis of [(FeL)$_2$]

NaH (18 mg, 0.750 mmol) in methanol (0.5 mL) was added dropwise to a solution of H_2L (140 mg, 0.371 mmol) in methanol (4 mL), and stirred for a few minutes. $FeCl_2$ (47 mg, 0.371 mmol) in MeOH (0.5 mL) was added dropwise to the ligand solution and the color of the solution turned orange-red with some precipitate. The solution was immediately filtered through glass wool followed by continued stirring of the filtrate. Formation of more precipitate started after 30 min., but the solution was allowed to stir overnight to complete precipitation. The precipitate was

collected through filtration, washed with methanol and diethyl ether and dried. A pink powder was obtained (110 mg, 0.237 mmol) in 64 % yield. Elemental analysis suggests that the crude material is LFe with MeOH as a coordinating solvent (methanol did not leave after drying under high vacuum). $C_{24}H_{29}FeN_3O_3$ (463.35): calcd. C 62.21, H 6.31, N 9.07; found: C 62.65, H 6.32, N 9.18. UV/Vis (CH_2Cl_2): λ_{max} (ε, $M^{-1}cm^{-1}$) = 471 (1,000) nm. FTIR (KBr): $\tilde{\nu}$ = 3278, 3253, 2857, 1593, 1476, 1450, 1279, 1108, 1032, 872, 755 cm^{-1}. ESI-MS (CH_2Cl_2): *m*/*z* = 431.1291 $[FeL]^+$, 879.2496 $[(FeL)_2(\mu\text{-}OH)]^+$. Recrystallization of the crude powder was obtained through slow evaporation of a MeCN solution to yield $[(FeL)_2]$.

2.10.6 Reactivity of the Diferrous Complex

A solution of $[(FeL)_2]$ in dichloromethane, when exposed to air shifts in UV-vis absorption from λ_{max} = 471 nm to 420 nm , which corresponds to $[(FeL)_2(\mu\text{-}O)]$. In a different experiment, complex [FeL(MeOH)] was created in a methanolic solution *in situ* upon addition of $Fe(OTf)_2$ to a solution of deprotonated ligand (as described in Synthesis of $[(FeL)_2]$) and immediately exposed to air. When trying to crystallize the reaction product through diethyl ether diffusion, the solution was kept under atmospheric conditions and crystals of $[(FeL)_2(\mu\text{-}OH)]OTf$ were obtained.

2.10.7 $[(FeL^{NO2})_2(\mu\text{-}OH)]ClO_4$

H_2L^{NO2} (0.060 g, 0.128 mmol) was dissolved in a mixture of methanol and dichloromethane (3:1 mL) and deprotonated with NEt_3 (0.030 g, 0.295 mmol). $Fe(ClO_4)_3 \cdot 6H_2O$ (0.060 g, 0.130 mmol) in methanol (1 mL) was added to the ligand

solution and the solution subsequently turned orange with immediate formation of dark brown-orange precipitate. After stirring overnight at room temperature the solid was collected by filtration and washed with methanol and diethylether. Crude powder of $[(FeL^{NO2})_2(\mu\text{-}OH)]ClO_4$ was obtained (27 mg, 36% yield). $[(FeL^{NO2})_2(\mu\text{-}OH)]ClO_4 \cdot 2H_2O$: $C_{46}H_{51}ClFe_2N_{10}O_{19}$ (1195.10): calcd. C 46.23, H, 4.30, N 11.72; found C 46.53, H 4.09, N 11.67. UV/Vis (MeCN): λ_{max} (ε, $M^{-1}cm^{-1}$) = 380 (54,860) nm. FTIR (KBr): $\tilde{\nu}$ = 2371, 2345, 1599, 1479, 1436, 1333, 1290, 1119, 1093, 926, 836, 784, 759, 669 cm^{-1}. ESI-MS (MeCN): *m*/*z* = 521.0993 $[FeL^{NO2}]^+$, 1059.2016 $[(FeL^{NO2})_2(\mu\text{-}OH)]^+$. Crystalline material of $[(FeL^{NO2})_2(\mu\text{-}OH)]ClO_4$ was obtained upon diffusion of CH_2Cl_2 into a solution of crude material in MeCN.

2.10.8 X-ray Crystal Structure Determination

X-ray quality crystals of $[(FeL)_2(\mu\text{-}OH)]BPh_4 \cdot CH_2Cl_2$ were obtained by diffusion of pentane into a methylene chloride solution of $[(FeL)_2(\mu\text{-}OH)]BPh_4$. Single crystals of $[(FeL)_2(\mu\text{-}O)]$ were obtained by slow evaporation of pentane into an acetone solution of $[(FeL)_2(\mu\text{-}O)]$. Single crystals of $[(FeL)_2]$ were obtained by slow evaporation of an acetonitrile solution of $[(FeL)_2]$. Single crystals of $[(FeL^{NO2})_2(\mu\text{-}OH)]ClO_4$ were obtained by slow evaporation of methylene chloride into a solution of $[(FeL^{NO2})_2(\mu\text{-}OH)]ClO_4$ in acetonitrile. Intensity data for all the compounds were collected using a diffractometer with a Bruker APEX ccd area detector [82, 83] and graphite-monochromated Mo-*K*α radiation (λ = 0.71073 Å). The samples were cooled to 100(2) K. Cell parameters were determined from a non-linear least-squares fit of the data. The data were corrected for absorption by the semi-empirical method [84]. The structure

was solved by direct methods and refined by full-matrix least-squares methods on F^2 [85, 86]. Hydrogen atom positions of hydrogen atoms bonded to carbon atoms were initially determined by geometry and were refined by a riding model. Hydrogen atoms bonded to nitrogen or oxygen atoms were located on a difference map, and their positions were refined independently. Non-hydrogen atoms were refined with anisotropic displacement parameters. Hydrogen atom displacement parameters were set to 1.2 (1.5 for methyl) times the displacement parameters of the bonded atoms. Crystal data for $[(FeL)_2(\mu\text{-}O)]\cdot(C_3H_6O)_2\cdot(H_2O)$, $[(FeL^{NO2})_2(\mu\text{-}OH)]ClO_4\cdot(H_2O)\cdot(C_2H_3N)\cdot(CH_2Cl_2)$ and $[(FeL)_2]\cdot(CH_4O)_2$ are summarized in Table 2.5. Selected bond lengths and angles for $[(FeL)_2(\mu\text{-}O)]$, $[(FeL^{NO2})_2(\mu\text{-}OH)]ClO_4$ and $[(FeL)_2]$ are summarized in Table 2.2, 2.3 and 2.4, respectively.

Table 2.5. Crystallographic data for $[(FeL)_2(\mu\text{-}O)]\cdot 2C_3H_6O\cdot H_2O$, $[(FeL)_2]\cdot 2(CH_4O)$ and $[(FeL^{NO2})_2(\mu\text{-}OH)]ClO_4\cdot H_2O\cdot C_2H_3N\cdot CH_2Cl_2$.

	$[(FeL)_2(\mu\text{-}O)]\cdot 2C_3H_6O\cdot H_2O$	$[(FeL)_2]\cdot 2(CH_4O)$	$[(FeL^{NO2})_2(\mu\text{-}OH)]ClO_4\cdot H_2O\cdot C_2H_3N\cdot CH_2Cl_2$
formula	$C_{52}H_{64}Fe_2N_6O_8$	$C_{48}H_{58}Fe_2N_6O_6$	$C_{49}H_{54}Cl_3Fe_2N_{11}O_{18}$
fw	1012.79	926.70	1303.08
Crystal system	triclinic	monoclinic	monoclinic
Space group	$P\bar{1}$	$P2_1/n$	$P2_1/n$
a (Å)	11.074(2)	12.8640(18)	11.9637(6)
b (Å)	12.872(2)	13.4112(19)	20.2286(11)
c (Å)	17.425(3)	13.0923(19)	22.2512(12)
α (deg)	84.588(4)	90	90
β (deg)	86.831(4)	103.606(3)	95.204(2)
γ (deg)	83.527(5)	90	90
V (Å^3)	2454.5(7)	2195.3(5)	5362.8(5)
Z	2	2	4
ρ_{calcd} (mg/m^3)	1.370	1.402	1.614
μ (mm^{-1})	0.652	0.718	0.777
θ (deg)	1.18 to 28.32	2.00 to 28.41	1.84 to 28.34
$R1$,[a] $wR2$[b] [$I>2\sigma(I)$]	0.0502, 0.1231	0.0504, 0.1104	0.0493, 0.1212
GOF on F^2	1.017	1.006	1.004

(a) $R1 = \Sigma||F_{obs}| - |F_{cacl}|| / \Sigma|F_{obs}|$. (b) $wR2 = \{\Sigma[w(F_{obs}^2 - F_{calc}^2)^2] / \Sigma[w(F_{obs}^2)^2]\}^{½}$.

2.11 References

1. Kurtz, D. M., *Oxo- and hydroxo-bridged diiron complexes: a chemical perspective on a biological unit.* Chemical Reviews **1990,** *90*, 585-606.

2. Que, L.; True, A. E., *Dinuclear Iron- and Manganese-Oxo Sites in Biology*, in *Progress in Inorganic Chemistry*. 2007, John Wiley & Sons, Inc. p. 97-200.

3. Tshuva, E. Y.; Lippard, S. J., *Synthetic Models for Non-Heme Carboxylate-Bridged Diiron Metalloproteins: Strategies and Tactics.* Chemical Reviews **2004,** *104*, 987-1012.

4. Armstrong, W. H.; Lippard, S. J., *(.mu.-Oxo)bis(.mu.-acetato)bis(tri-1-pyrazolylborato)diiron(III), [(HBpz3)FeO(CH3CO2)2Fe(HBpz3)]: model for the binuclear iron center of hemerythrin.* Journal of the American Chemical Society **1983,** *105*, 4837-4838.

5. Hartman, J. A. R.; Rardin, R. L.; Chaudhuri, P.; Pohl, K.; Wieghardt, K.; Nuber, B.; Weiss, J.; Papaefthymiou, G. C.; Frankel, R. B.; Lippard, S. J., *Synthesis and characterization of (.mu.-hydroxo)bis(.mu.-acetato)diiron(II) and (.mu.-oxo)bis(.mu.-acetato)diiron(III) 1,4,7-trimethyl-1,4,7-triazacyclononane complexes as models for binuclear iron centers in biology; properties of the mixed valence diiron(II,III) species.* Journal of the American Chemical Society **1987,** *109*, 7387-7396.

6. Kurtz Jr, D. M., *8.10 - Dioxygen-binding Proteins*, in *Comprehensive Coordination Chemistry II*, J.A.M. Editors-in-Chief: and T.J. Meyer, Editors. 2003, Pergamon: Oxford. p. 229-260.

7. Du Bois, J.; Mizoguchi, T. J.; Lippard, S. J., *Understanding the dioxygen reaction chemistry of diiron proteins through synthetic modeling studies.* Coordination Chemistry Reviews **2000,** *200–202*, 443-485.

8. Stenkamp, R. E.; Sieker, L. C.; Jensen, L. H.; McCallum, J. D.; Sanders-Loehr, J., *Active site structures of deoxyhemerythrin and oxyhemerythrin.* Proceedings of the National Academy of Sciences **1985,** *82*, 713-716.

9. Holmes, M. A.; Le Trong, I.; Turley, S.; Sieker, L. C.; Stenkamp, R. E., *Structures of deoxy and oxy hemerythrin at 2.0 Å resolution.* Journal of Molecular Biology **1991,** *218*, 583-593.

10. LeBlanc, J. R.; Schneider III, R. V.; Strait, R. B., *Methanol Production And Use*, ed. H.H.K. Wu-Hsum Cheng. 1994, USA: Marcel Dekker, Inc.

11. Elango, N. A.; Radhakrishnan, R.; Froland, W. A.; Wallar, B. J.; Earhart, C. A.; Lipscomb, J. D.; Ohlendorf, D. H., *Crystal structure of the hydroxylase component of methane monooxygenase from Methylosinus trichosporium OB3b.* Protein Science **1997,** *6*, 556-568.

12. Shu, L.; Nesheim, J. C.; Kauffmann, K.; Münck, E.; Lipscomb, J. D.; Que, L., *An Fe2IVO2 Diamond Core Structure for the Key Intermediate Q of Methane Monooxygenase.* Science **1997,** *275*, 515-518.

13. Jin, Y.; Lipscomb, J. D., *Probing the Mechanism of C−H Activation: Oxidation of Methylcubane by Soluble Methane Monooxygenase from Methylosinus trichosporium OB3b†.* Biochemistry **1999,** *38*, 6178-6186.

14. Eriksson, M.; Jordan, A.; Eklund, H., *Structure of Salmonella typhimurium nrdF Ribonucleotide Reductase in Its Oxidized and Reduced Forms†,‡.* Biochemistry **1998,** *37*, 13359-13369.

15. Saleh, L.; Bollinger, J. M., *Cation Mediation of Radical Transfer between Trp48 and Tyr356 during O2 Activation by Protein R2 of Escherichia coli Ribonucleotide Reductase: Relevance to R1−R2 Radical Transfer in Nucleotide Reduction?†.* Biochemistry **2006,** *45*, 8823-8830.

16. Babcock, L. M.; Bradic, Z.; Harrington, P. C.; Wilkins, R. G.; Yoneda, G. S., *Preparation, disproportionation, and reactions of two semi-met forms of hemerythrin.* Journal of the American Chemical Society **1980,** *102*, 2849-2850.

17. Atta, M.; Andersson, K. K.; Ingemarson, R.; Thelander, L.; Graeslund, A., *EPR Studies of Mixed-Valent [FeIIFeIII] Clusters formed in the R2 Subunit of Ribonucleotide Reductase from Mouse or Herpes Simplex Virus: Mild Chemical Reduction of the Diferric Centers.* Journal of the American Chemical Society **1994,** *116*, 6429-6430.

18. Fox, B. G.; Surerus, K. K.; Münck, E.; Lipscomb, J. D., *Evidence for a mu-oxo-bridged binuclear iron cluster in the hydroxylase component of methane monooxygenase. Mössbauer and EPR studies.* Journal of Biological Chemistry **1988,** *263*, 10553-6.

19. Kurtz Jr, D. M., *Avoiding high-valent iron intermediates: Superoxide reductase and rubrerythrin.* Journal of Inorganic Biochemistry **2006,** *100*, 679-693.

20. Coulter, E. D.; Shenvi, N. V.; Kurtz Jr, D. M., *NADH Peroxidase Activity of Rubrerythrin.* Biochemical and Biophysical Research Communications **1999,** *255*, 317-323.

21. Jin, S.; Kurtz, D. M.; Liu, Z.-J.; Rose, J.; Wang, B.-C., *X-ray Crystal Structures of Reduced Rubrerythrin and Its Azide Adduct: A Structure-Based Mechanism for a Non-Heme Diiron Peroxidase.* Journal of the American Chemical Society **2002,** *124*, 9845-9855.

22. Crichton, R. R.; Declercq, J.-P., *X-ray structures of ferritins and related proteins.* Biochimica et Biophysica Acta (BBA) - General Subjects **2010,** *1800*, 706-718.

23. Coulter, E. D.; Shenvi, N. V.; Beharry, Z. M.; Smith, J. J.; Prickril, B. C.; Kurtz Jr, D. M., *Rubrerythrin-catalyzed substrate oxidation by dioxygen and hydrogen peroxide.* Inorganica Chimica Acta **2000,** *297*, 231-241.

24. Vogel, A.; Spener, F.; Krebs, B., *Purple Acid Phosphatase*, in *Encyclopedia of Inorganic and Bioinorganic Chemistry*. 2011, John Wiley & Sons, Ltd.

25. Schenk, G.; Mitić, N.; Hanson, G. R.; Comba, P., *Purple acid phosphatase: A journey into the function and mechanism of a colorful enzyme.* Coordination Chemistry Reviews **2013,** *257*, 473-482.

26. Comba, P.; Gahan, L. R.; Mereacre, V.; Hanson, G. R.; Powell, A. K.; Schenk, G.; Zajaczkowski-Fischer, M., *Spectroscopic Characterization of the Active FeIIIFeIII and FeIIIFeII Forms of a Purple Acid Phosphatase Model System.* Inorganic Chemistry **2012,** *51*, 12195-12209.

27. Yam, L. T.; Li, C. Y.; Lam, K. W., *Tartrate-resistant acid phosphatase isoenzyme in the reticulum cells of leukemic reticuloendotheliosis.* The New England Journal of Medicine **1971,** *284*, 357-360.

28. Schindelmeiser, J.; Gullotta, F.; Münsterman, D., *Purple Acid Phosphatase of Human Brain Macrophages in AIDS Encephalopathy.* Pathology - Research and Practice **1989,** *185*, 184-186.

29. Bernhardt, P. V.; Schenk, G.; Wilson, G. J., *Direct Electrochemistry of Porcine Purple Acid Phosphatase (Uteroferrin)†.* Biochemistry **2004,** *43*, 10387-10392.

30. Davis, M. I.; Orville, A. M.; Neese, F.; Zaleski, J. M.; Lipscomb, J. D.; Solomon, E. I., *Spectroscopic and Electronic Structure Studies of Protocatechuate 3,4-Dioxygenase: Nature of Tyrosinate−Fe(III) Bonds and Their Contribution to Reactivity.* Journal of the American Chemical Society **2002,** *124*, 602-614.

31. Roberts, R. M.; Bazer, F. W., *Uteroferrin: A protein in search of a function.* BioEssays **1984,** *1*, 8-11.

32. Hayman, A. R.; Jones, S. J.; Boyde, A.; Foster, D.; Colledge, W. H.; Carlton, M. B.; Evans, M. J.; Cox, T. M., *Mice lacking tartrate-resistant acid phosphatase (Acp 5) have disrupted endochondral ossification and mild osteopetrosis.* Development **1996,** *122*, 3151-3162.

33. Schindelmeiser, J.; Münstermann, D.; Witzel, H., *Histochemical investigations on the localization of the purple acid phosphatase in the bovine spleen.* Histochemistry **1987,** *87*, 13-19.

34. Fenton, H. J. H., *LXXIII.-Oxidation of tartaric acid in presence of iron.* Journal of the Chemical Society, Transactions **1894,** *65*, 899-910.

35. Brillas, E.; Sirés, I.; Oturan, M. A., *Electro-Fenton Process and Related Electrochemical Technologies Based on Fenton's Reaction Chemistry.* Chemical Reviews **2009,** *109*, 6570-6631.

36. Sibille, J. C.; Doi, K.; Aisen, P., *Hydroxyl radical formation and iron-binding proteins. Stimulation by the purple acid phosphatases.* Journal of Biological Chemistry **1987,** *262*, 59-62.

37. Lopez, J. P.; Kampf, H.; Grunert, M.; Gutlich, P.; Heinemann, F. W.; Prakash, R.; Grohmann, A., *A non-heme dinuclear iron(ii) complex containing a single, unsupported hydroxo bridge.* Chemical Communications **2006,** *0*, 1718-1720.

38. Armstrong, W. H.; Spool, A.; Papaefthymiou, G. C.; Frankel, R. B.; Lippard, S. J., *Assembly and characterization of an accurate model for the diiron center in hemerythrin.* Journal of the American Chemical Society **1984,** *106*, 3653-3667.

39. Armstrong, W. H.; Lippard, S. J., *Reversible protonation of the oxo bridge in a hemerythrin model compound. Synthesis, structure, and properties of (.mu.-hydroxo)bis(.mu.-acetato)bis[hydrotris(1-pyrazolyl)borato]diiron(III) [(HB(pz)3)Fe(OH)(O2CCH3)2Fe(HB(pz)3)2]+*. Journal of the American Chemical Society **1984,** *106*, 4632-4633.

40. Wieghardt, K.; Pohl, K.; Gebert, W., *[{(C6H15N3)Fe}2(μ-O)(μ-CH3CO2)2]2+ a Dinuclear Iron, (III)Complex with a Metazidohemerythrin-Type Structure.* Angewandte Chemie International Edition in English **1983,** *22*, 727-727.

41. Murch, B. P.; Boyle, P. D.; Que, L., *Structures of binuclear and tetranuclear iron(III) complexes as models for ferritin core formation.* Journal of the American Chemical Society **1985,** *107*, 6728-6729.

42. Borovik, A. S.; Papaefthymiou, V.; Taylor, L. F.; Anderson, O. P.; Que, L., *Models for iron-oxo proteins. Structures and properties of FeIIFeIII, ZnIIFeIII, and FeIIGaIII complexes with (.mu.-phenoxo)bis(.mu.-carboxylato)dimetal cores.* Journal of the American Chemical Society **1989,** *111*, 6183-6195.

43. Schepers, K.; Bremer, B.; Krebs, B.; Henkel, G.; Althaus, E.; Mosel, B.; Müller-Warmuth, W., *ZnIIFeIII and FeIIFeIII Complexes Containing a Novel (μ-Phenoxo)bis(μ-diphenylphosphato)-dimetal(II,III) Core as Model Complexes for Active Sites of Purple Phosphatases.* Angewandte Chemie International Edition in English **1990,** *29*, 531-533.

44. Mashuta, M. S.; Webb, R. J.; McCusker, J. K.; Schmitt, E. A.; Oberhausen, K. J.; Richardson, J. F.; Buchanan, R. M.; Hendrickson, D. N., *Electron transfer in iron(II)iron(III) model complexes of iron-oxo proteins.* Journal of the American Chemical Society **1992,** *114*, 3815-3827.

45. Bernard, E.; Moneta, W.; Laugier, J.; Chardon-Noblat, S.; Deronzier, A.; Tuchagues, J.-P.; Latour, J.-M., *A Mixed-Valent, Unsymmetrical FeIIFeIII Complex with a Terminal Phenolato Ligand as a Model for the Active Site of Purple Acid Phosphatases.* Angewandte Chemie International Edition in English **1994,** *33*, 887-889.

46. Borovik, A. S.; Murch, B. P.; Que, L.; Papaefthymiou, V.; Munck, E., *Models for iron-oxo proteins: a mixed valence iron(II)-iron(III) complex.* Journal of the American Chemical Society **1987,** *109,* 7190-7191.

47. Yan, S.; Cox, D. D.; Pearce, L. L.; Juarez-Garcia, C.; Que, L.; Zhang, J. H.; O'Connor, C. J., *A (.mu.-oxo)(.mu.-carboxylato)diiron(III) complex with distinct iron sites.* Inorganic Chemistry **1989,** *28,* 2507-2509.

48. Norman, R. E.; Yan, S.; Que, L.; Backes, G.; Ling, J.; Sanders-Loehr, J.; Zhang, J. H.; O'Connor, C. J., *(.mu.-Oxo)(.mu.-carboxylato)diiron(III) complexes with distinct iron sites. Consequences of the inequivalence and its relevance to dinuclear iron-oxo proteins.* Journal of the American Chemical Society **1990,** *112,* 1554-1562.

49. *Proceedings of the Chemical Society. March 1959.* Proceedings of the Chemical Society **1959,** *0,* 73-108.

50. Hofmann, K. A.; Resenscheck, F., *Ueber die blauen Eisencyanverbindungen und die Ursache ihrer Farbe.* Justus Liebigs Annalen der Chemie **1905,** *342,* 364-374.

51. Buser, H. J.; Schwarzenbach, D.; Petter, W.; Ludi, A., *The crystal structure of Prussian Blue: Fe4[Fe(CN)6]3.xH2O.* Inorganic Chemistry **1977,** *16,* 2704-2710.

52. Creutz, C.; Taube, H., *Direct approach to measuring the Franck-Condon barrier to electron transfer between metal ions.* Journal of the American Chemical Society **1969,** *91,* 3988-3989.

53. Demadis, K. D.; Hartshorn, C. M.; Meyer, T. J., *The Localized-to-Delocalized Transition in Mixed-Valence Chemistry.* Chemical Reviews **2001,** *101,* 2655-2686.

54. Beley, M.; Collin, J. P.; Louis, R.; Metz, B.; Sauvage, J. P., *3,3',5,5'-Tetrapyridylbiphenyl, a bis-cyclometalating bridging ligand with a high coupling ability in ruthenium(III), ruthenium(II) mixed valence systems.* Journal of the American Chemical Society **1991,** *113,* 8521-8522.

55. Robin, M. B.; Day, P., *Mixed Valence Chemistry-A Survey and Classification*, in *Advances in Inorganic Chemistry and Radiochemistry*, H.J. Emeléus and A.G. Sharpe, Editors. 1968, Academic Press. p. 247-422.

56. Bossek, U.; Hummel, H.; Weyhermüller, T.; Bili, E.; Wieghardt, K., *The First μ(OH)-Bridged Model Complex for the Mixed-Valent FeIIFeIII Form of Hemerythrin.* Angewandte Chemie International Edition in English **1996,** *34*, 2642-2645.

57. Cohen, J. D.; Payne, S.; Hagen, K. S.; Sanders-Loehr, J., *Raman Evidence for a Trapped-Valence FeII−O−FeIII Complex Formed from an Outer-Sphere Reaction of Diiron(II) with Dioxygen.* Journal of the American Chemical Society **1997,** *119*, 2960-2961.

58. Payne, S. C.; Hagen, K. S., *Steric Control of Reactivity of Non-Heme μ-Hydroxo Diiron(II) Complexes with Oxygen: Isolation of a Strongly Coupled μ-Oxo Fe(II)Fe(III) Dimer.* Journal of the American Chemical Society **2000,** *122*, 6399-6410.

59. Shakya, R.; Powell, D. R.; Houser, R. P., *Unsupported μ-Oxo- and μ-Hydroxo-Iron(III) Dimers and Mononuclear Iron(III) Complexes with Pyridylbis(aminophenol) Ligands.* European Journal of Inorganic Chemistry **2009,** *2009*, 5319-5327.

60. Kaim, W.; Klein, A.; Glöckle, M., *Exploration of Mixed-Valence Chemistry: Inventing New Analogues of the Creutz-Taube Ion.* Accounts of Chemical Research **2000,** *33*, 755-763.

61. Glöckle, M.; Kaim, W.; Klein, A.; Roduner, E.; Hübner, G.; Zalis, S.; van Slageren, J.; Renz, F.; Gütlich, P., *The Stable Diiron(2.5) Complex Ion [(NC)5Fe(μ-tz)Fe(CN)5]5-, tz = 1,2,4,5-Tetrazine, and Its Neighboring Oxidation States.* Inorganic Chemistry **2001,** *40*, 2256-2262.

62. Rodriguez, J. H.; McCusker, J. K., *Density functional theory of spin-coupled models for diiron-oxo proteins: Effects of oxo and hydroxo bridging on geometry, electronic structure, and magnetism.* The Journal of Chemical Physics **2002,** *116*, 6253-6270.

63. Davies, J. E.; Gatehouse, B. M., *The crystal and molecular structure of unsolvated [mu]-oxo-bis[N,N'-ethylenebis(salicylaldiminato)iron(III)]*. Acta Crystallographica Section B **1973,** *29*, 1934-1942.

64. Weiss, M. C.; Goedken, V. L., *Synthesis and crystal and molecular structure of the oxo-bridged, iron(III) macrocyclic dimer [Fe(C22H22N4)]2O.CH3CN: .mu.-oxo-bis[7,16-dihydro-6,8,16,17-tetramethyldibenzo[b,i][1,4,8,11]tetraazacyclotetradecinato]iron(III)-acetonitrile.* Inorganic Chemistry **1979,** *18*, 819-826.

65. Evans, D. R.; Mathur, R. S.; Heerwegh, K.; Reed, C. A.; Xie, Z., *Protonierung einer linearen, Oxo-verbrückten Dieisen-Einheit ohne Rehybridisierung des verbrückenden Sauerstoffatoms: Struktur des (μ-Hydroxy)bis(tetraphenyl-porphyrinato)eisen(III)-Kations.* Angewandte Chemie **1997,** *109*, 1394-1396.

66. Grünwald, K. R.; Volpe, M.; Mösch-Zanetti, N. C., *Phenolate-bridged zinc(II) complexes relevant to biological phosphoester cleavage.* Journal of Coordination Chemistry **2012,** *65*, 2008-2020.

67. Yahsi, Y.; Kara, H., *Synthesis, structural analysis and magnetic properties of two novel doubly oxygen bridged binuclear manganese(III) and copper(II) complexes with ONO tridentate ligands.* Inorganica Chimica Acta **2013,** *397*, 110-116.

68. Das, L. K.; Biswas, A.; Frontera, A.; Ghosh, A., *Polymorphism in hetero-metallic tri-nuclear CuII2CdII complexes of salicylaldimine ligand: Structural analysis and theoretical study.* Polyhedron **2013,** *52*, 1416-1424.

69. Novotný, M.; Padělková, Z.; Holeček, J.; Růžička, A., *O,N-Chelated germanium, tin and lead compounds containing 2-[N,N-(dimethylamino)methyl]phenolate as ligand.* Journal of Organometallic Chemistry **2013,** *733*, 71-78.

70. Shakya, R.; Jozwiuk, A.; Powell, D. R.; Houser, R. P., *Synthesis and Characterization of Polynuclear Copper(II) Complexes with Pyridylbis(phenol) Ligands.* Inorganic Chemistry **2009,** *48*, 4083-4088.

71. Whiteoak, C. J.; Torres Martin de Rosales, R.; White, A. J. P.; Britovsek, G. J. P., *Iron(II) Complexes with Tetradentate Bis(aminophenolate) Ligands: Synthesis and Characterization, Solution Behavior, and Reactivity with O2.* Inorganic Chemistry **2010,** *49*, 11106-11117.

72. Iyer, R.; Silaghi-Dumitrescu, R.; Kurtz, D., Jr.; Lanzilotta, W., *High-resolution crystal structures of Desulfovibrio vulgaris (Hildenborough) nigerythrin: facile, redox-dependent iron movement, domain interface variability, and peroxidase activity in the rubrerythrins.* J Biol Inorg Chem **2005,** *10*, 407-416.

73. Connelly, N. G.; Geiger, W. E., *Chemical Redox Agents for Organometallic Chemistry.* Chemical Reviews **1996,** *96*, 877-910.

74. Neves, A.; Rossi, L. M.; Vencato, I.; Haase, W.; Werner, R., *A new bis([small mu]-alkoxo) diiron(III) complex and its implications regarding the number of Fe(III)-phenolate bonds and the redox potential in uteroferrin.* Journal of the Chemical Society, Dalton Transactions **2000,** *0*, 707-712.

75. Hasan, K.; Fowler, C.; Kwong, P.; Crane, A. K.; Collins, J. L.; Kozak, C. M., *Synthesis and structure of iron(iii) diamine-bis(phenolate) complexes.* Dalton Transactions **2008,** *0*, 2991-2998.

76. Palaniandavar, M.; Velusamy, M.; Mayilmurugan, R., *Iron(III) complexes of certain tetradentate phenolate ligands as functional models for catechol dioxygenases.* Journal of Chemical Sciences **2006,** *118*, 601-610.

77. Ramesh, K.; Mukherjee, R., *Trends in the spectral and redox potential data of mononuclear iron(III)(S=) phenolate complexes.* Journal of the Chemical Society, Dalton Transactions **1992,** *0*, 83-89.

78. Merkel, M.; Müller, F. K.; Krebs, B., *Novel iron(III) complexes with phenolate containing tripodal tetradentate ligands as model systems for catechol 1,2-dioxygenases.* Inorganica Chimica Acta **2002,** *337*, 308-316.

79. Mayilmurugan, R.; Sankaralingam, M.; Suresh, E.; Palaniandavar, M., *Novel square pyramidal iron(iii) complexes of linear tetradentate bis(phenolate) ligands as structural and reactive models for intradiol-cleaving 3,4-PCD enzymes: Quinone formation vs. intradiol cleavage.* Dalton Transactions **2010,** *39*, 9611-9625.

80. Friedrich, S.; Schubart, M.; Gade, L. H.; Scowen, I. J.; Edwards, A. J.; McPartlin, M., *Titanium and Zirconium Complexes Containing a Novel Dianionic Trifunctional Amido Ligand.* Chemische Berichte **1997,** *130*, 1751-1759.

81. Shakya, R.; Wang, Z.; Powell, D. R.; Houser, R. P., *Tetradentate vs Pentadentate Coordination in Copper(II) Complexes of Pyridylbis(aminophenol) Ligands Depends on Nucleophilicity of Phenol Donors.* Inorganic Chemistry **2011,** *50*, 11581-11591.

82. *SMART, Software Reference Manual*. 1998, Madison, WI, USA: Bruker AXS.

83. *SAINT, Software Reference Manual*. 1998, Madison, WI, USA: Bruker AXS.

84. Sheldrick, G. M., *SADABS, Program for empirical absorption correction of area detector data*, 2002: University of Göttingen, Germany.

85. Sheldrick, G. M., *SHELXTL Version 6.10 Reference Manual*. 2000, Madison, WI, USA: Bruker AXS.

86. *International Tables for Crystallography*. Vol. C. 1995, Boston: Kluwer.

CHAPTER 3

Copper(II) Complexes of Symmetric and Asymmetric Bis(imine) Ligands: Tuning the Cu(I)/Cu(II) Redox Couple

3.1 Background

Copper is one of the most abundant redox active metals and plays an important role in many biological processes [1], which were introduced in chapter 1. Herein the focus will be on electronic tuning of the copper ion. While copper(II) ions prefer a square planar geometry, copper(I) complexes are usually found in tetrahedral coordination environments. This trend is explained fairly easily when the degeneracy of the 3d-orbitals in different geometrical fields and crystal field stabilization energies are considered (see Figure 3.1). In the configuration of d^9 (Cu(II)), the more favorable geometry is square planar. The crystal field stabilization energy for square planar geometry is lower (–1.21 Δ_o) versus –0.4 Δ_t (or for comparison = –0.18 Δ_o) for tetrahedral geometry, therefore being more stable. (Relative energy values of the 3d-orbitals in crystal fields of different symmetry are taken from reference [2] and [3] for T_d and square planar, respectively; Δ_t and Δ_o can be interconverted *via* the relationship $\Delta_t = 4/9\ \Delta_o$ [2].)

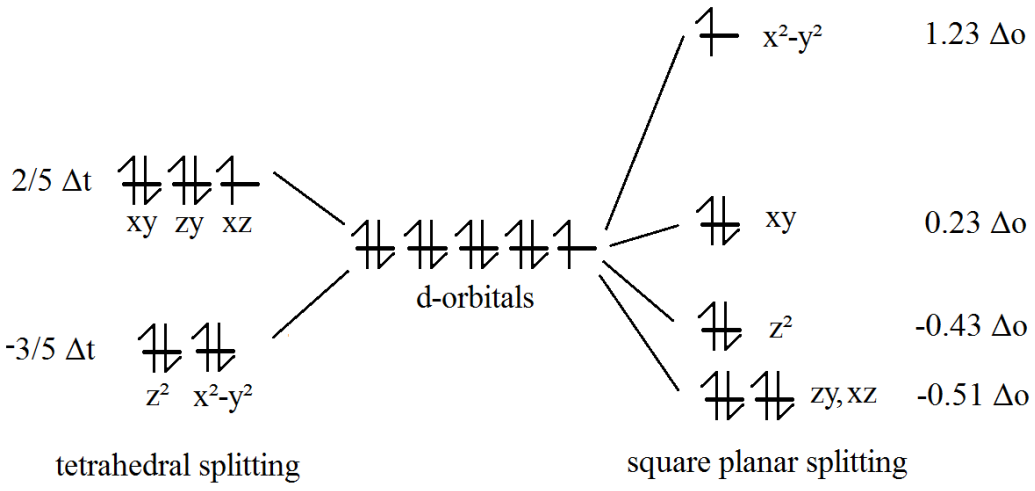

Figure 3.1. Schematic representation of the crystal field splitting for tetrahedral and square planar geometry.

The copper(I) ion has a d^{10} configuration and does not result in energy gain upon distortion of the geometry. The most favorable geometry for a metal ion with four ligands is tetrahedral, only considering ligand-ligand interactions to produce a complex where all donors are farthest apart. This is consistent with the VSEPR model for a central atom with four substituents.

In nature, blue copper electron transfer proteins use copper as a one electron relay to shuttle between the cupric (Cu(II)) and cuprous (Cu(I)) oxidation states [4]. The coordination geometry in some of these proteins is strained between square planar and tetrahedral which lowers the redox barrier because the reorganization energy (geometrical change and change in bond lengths) upon reduction/oxidation is lowered [5]. A crystal structure of the active site of plastocyanin, a blue copper protein, is shown below in Figure 3.2. A more detailed background on blue copper proteins is given in chapter 4.

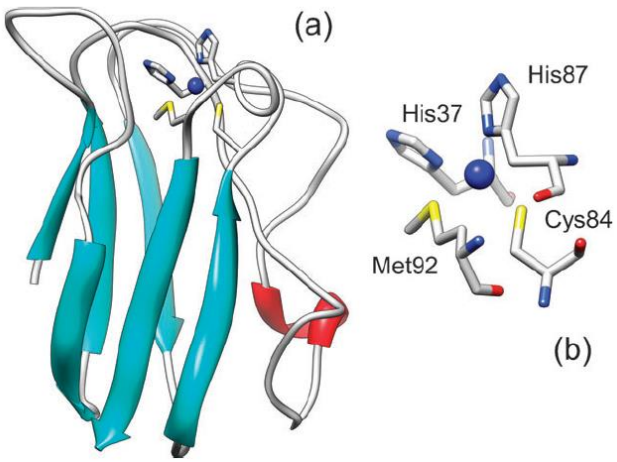

Figure 3.2. a) Protein structure of plastocyanin and b) the amino acid residues surrounding the copper ion. Figure is adapted from reference [6].

While most blue copper proteins are very similar in structure and geometry [5], metal center redox potential fine tuning can still be achieved. It was shown that in azurin (a blue copper protein) secondary interactions can influence the redox potential of the Cu(II)/Cu(I) couple. Hydrogen bonding and hydrophobicity can cause a change in potential up to 700 mV without perturbation of the metal binding site [7]. The tuning of the Cu(II)/Cu(I) redox couple is a critical component of electron transfer in blue copper proteins, and is also important in synthetic complexes where copper plays a role as the redox center in catalysis. The relationship between redox potential and structure has therefore received considerable attention for many years [8-12]. The effect of tuning the redox potential in catalysis to influence reactivity and selectivity was shown by Jacobsen [13]. Das *et al.* have reported the change in reactivity of a copper complex towards aerobic oxidation of alcohols by electronic tuning [14].

In the following sections it will be discussed how synthetic metal complexes can be electronically tuned. While geometric constraints, e.g. tetrahedral versus square planar, already discussed above, are of great importance, ligand donor atoms are also a key factor in redox potential control. Sigma- and pi-donor ligands push more electron density on the metal ion, moving the Cu(II)/Cu(I) redox potential to lower (more negative) potentials [15-17]. Sigma-donors stabilize the higher oxidation state of the metal ion by donation of electron density while pi-acceptors stabilize the metal ion in its lower oxidation state by pulling electron density off the metal ion.

This chapter will be focused on copper complexes with chelating Schiff base ligands. Schiff bases are important ligands because of their synthetic simplicity and the diversity of possible ligands owing to the mix-and-match ability of the condensation of

various amines with different aldehydes. In particular, tetradentate Schiff base ligands, including salen and its derivatives, have been used for a wide variety of coordination chemistry with copper and other transition metals [18-25]. Salen ligands are derived from ethylenediamine, and typically salen corresponds to the condensation product of ethylenediamine and two equivalents of 2-hydroxybenzaldehyde. On the other hand, salen-type ligands can have any amine linker R^1 but still show the [O,N,N,O]-donor manifold and thus form tetradentate bis-Schiff bases [26], [27] (see Figure 3.3).

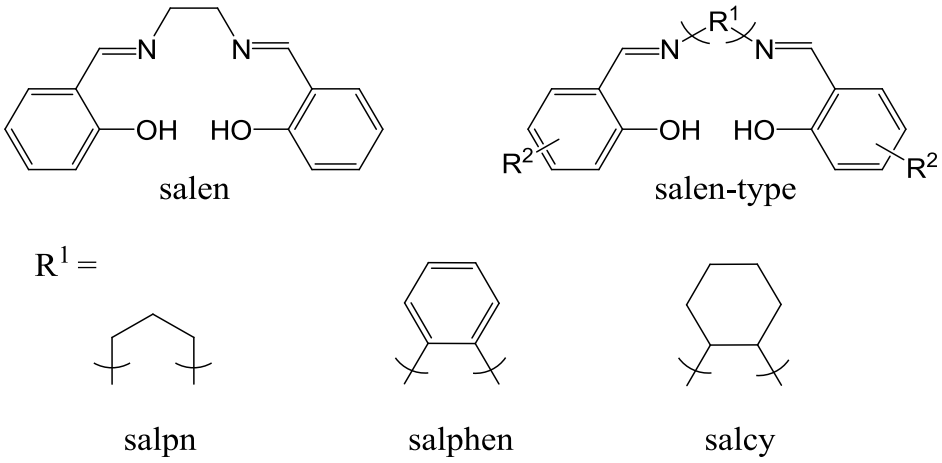

Figure 3.3. Salen and most common salen-type ligands. R^2 represents possible substitution on the aromatic ring.

The syntheses of tetradentate Schiff base ligands are versatile due to their modular nature (see Figure 3.4). An alkanediamine backbone starting material can easily be transformed into a tetradentate ligand by condensation with two equivalents of an aldehyde.

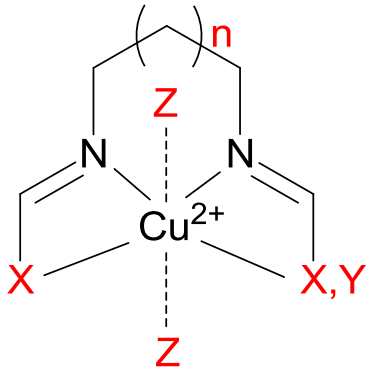

Figure 3.4. General structure of copper(II) complexes with tetradentate Schiff base ligands. X, Y = donor group (e.g. pyridyl or phenolate), Z = counterion in axial position and n = number of -(CH_2)- units.

Examples of how different tetradentate Schiff base donors influence the Cu(II)/Cu(I) redox potential of their corresponding complexes have been reported in the literature [24, 28-31]. It has been shown that the length of the alkane chain of the diamine unit plays an important role in the redox behavior of the metal ion [28], as this type of ligand variation selects for different coordination geometries [29], (e.g. tetrahedral versus square planar). Crystal structures of copper(II) complexes with ligands of varying chain length within the diamine unit and X = 2-hydroxybenzyl (Figure 3.4) were reported in the past and show distortion of the coordination geometry from n = 2 being square planar towards n > 2 showing increased distortion towards tetrahedral with increasing chain length. When n = 5 (see Figure 3.5) or 6, dimeric square planar, complexes are obtained and no geometrical strain around the copper ion is observed [29].

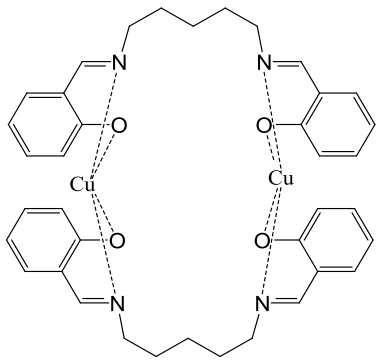

Figure 3.5. Schematic depiction of coordination of Cu(II) ions by a salen-type ligand with pentyldiamine.

When X = pyridyl (Figure 3.4) and the chain length of the diamine is varied from propyl to hexyl, the redox potential for the copper ion is shifted towards more positive potentials (with an overall shift of 210 mV) [28]. This seems reasonable because the increase in chain length, like shown in ref. [29], does favor tetrahedral distortion of the complex, thus allowing for easier reduction of the copper(II) ion.

In a different study, variation of the weakly coordinated counterion in the axial position of the quadridentate Schiff base copper complex was shown to influence the electrochemistry of the copper redox couple [30].

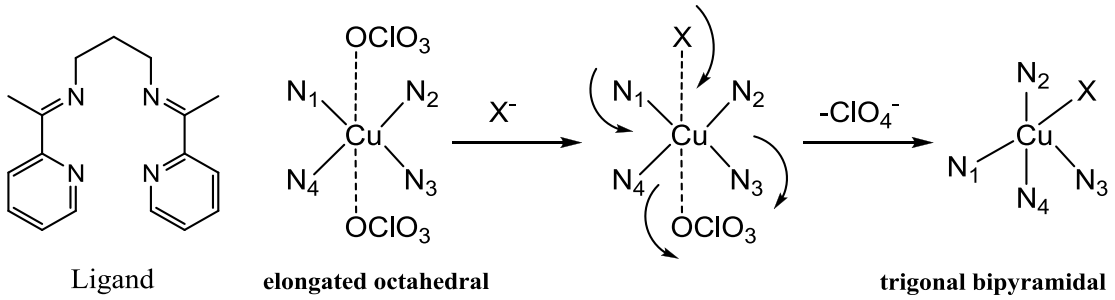

Figure 3.6. Ligand (left, representing N_1–N_4) and copper(II) complexes with different counter ions. X= SCN^-, N_3^- or NO_2^-. Figure is redrawn from reference [30].

The copper(II) complex with two perchlorate counter ions (see elongated octahedral structure in Figure 3.6) is easily modified to other complexes *via* counter ion metathesis with stronger coordinating ions like SCN^-, N_3^- and NO_2^-. This causes rearrangement in geometry from Jahn-Teller distorted octahedral to trigonal bipyramidal. Electrochemical studies show shifts in the redox potential for the copper ion within a range of 240 mV depending on the counter ion. The nitrite ion causes the most rearrangement towards trigonal bipyramidal and therefore the largest shift of the redox potential towards more negative potentials.

Although diamines should allow stepwise condensation of two different aldehydes and therefore more variation, not much has been reported on the electrochemistry of copper complexes with asymmetric ligands. Ghosh and coworkers have shown that the mono-condensed product of 1,3-propanediamine and 1-benzoylacetone generated via the high dilution method can be used as a precursor for condensation with 2-pyridinecarboxaldehyde or 2-acetylpyridine to form asymmetric ligands (see Figure 3.7a, b) [31]. Although the ligands were not isolated, copper complexes with the ligands were isolated and studied.

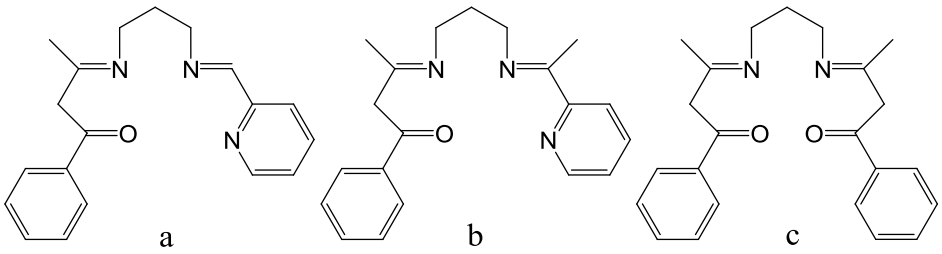

Figure 3.7. Asymmetric and symmetric ligands derived from 1,3-propanediamine and 1-benzoylacetone reported in reference [31].

The asymmetric copper complexes with ligand a and b show drastic shifts in redox potentials (about 400 mV) of the copper ion towards more negative potentials

compared to the symmetric condensation product of 1,3-propanediamine with two equivalents of 1-benzoylacetone (see Figure 3.7c) [31]. The authors believe that the change in redox potential is also influenced by geometrical strain towards tetrahedral for the complex with the symmetric ligand c. Another asymmetric system was introduced to the literature by the same group, again using the high dilution method [24]. The asymmetric copper complex of the 1:1:1 condensation of 1,3-propanediamine, 2,4-pentanedione and 2-pyridinecarboxaldehyde showed irreversible reductions and the copper complexes readily reorganized into their symmetric complexes in the presence of catalytic amounts of acid and copper(II) ions (see Figure 3.8) [24].

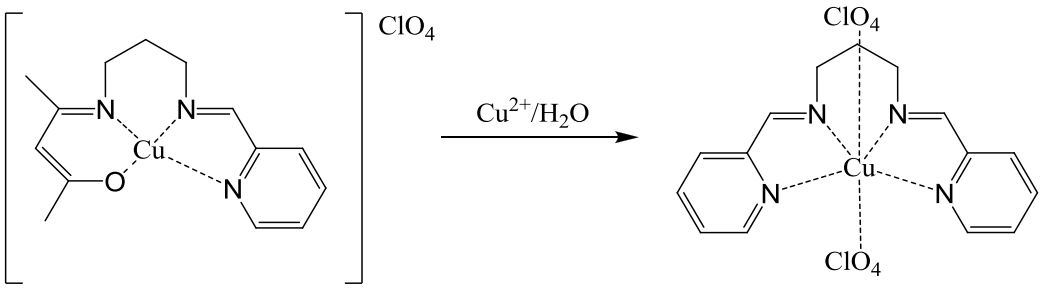

Figure 3.8. Decomposition of the asymmetric copper complex into the symmetric one upon addition of free copper(II) ions or acid. Figure is redrawn from reference [24].

In the following section some concepts of asymmetric Schiff base ligand design will be discussed. The isolation of copper(II) complexes of these asymmetric ligands would allow for fine tuning of the redox potential and access to intermediate redox potentials. Generally, there are three ways of breaking the symmetry in salen-type ligands as depicted in Figure 3.9.

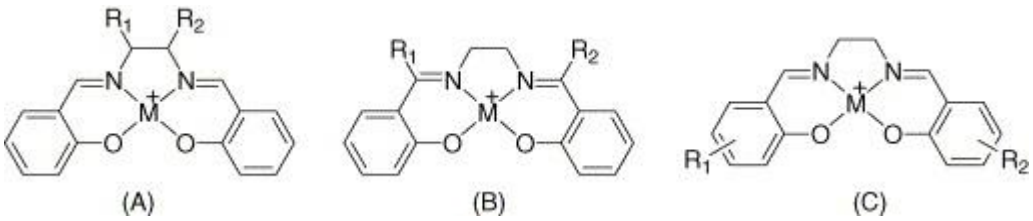

Figure 3.9. Possible derivatization of salen-type ligands to obtain asymmetric tetradentate Schiff bases. Figure is adapted from reference [32].

Most common is the synthesis of salen-type ligands with asymmetric diamines like 1,2-diaminocyclohexane (Figure 3.9A). Complexes with this ligand are well known in the literature. Jacobsen's catalyst is the complex with M = manganese and has been used in asymmetric expoxidation catalysis [33]. Ito and Katsuki reported another A-type complex (Figure 3.10, complex 4) [34]. Complexes with B-type ligands are generated with the use of special strategies. Some examples were mentioned earlier (see Figure 3.7) where high dilution techniques yield asymmetric complexes. Another example is shown below (Figure 3.10, complex 5), which was also introduced by Jacobsen [35] .

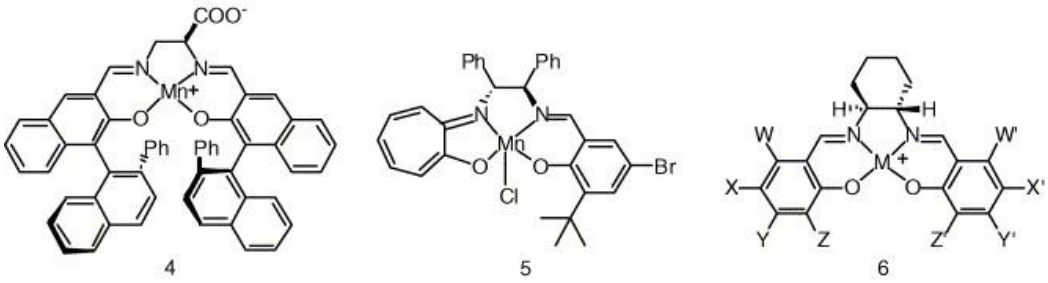

Figure 3.10. Asymmetric complexes used in catalysis. Figure is adapted from reference [32].

The general issues with the synthesis of asymmetric complexes are acid promoted equilibration of the asymmetric ligand to the symmetric versions (see Scheme 3.1) and contamination with symmetric diimine and free amine in the step-wise condensation with two aldehydes (see scheme 3.2).

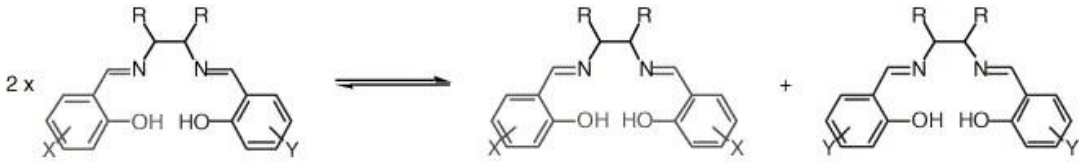

Scheme 3.1. Equilibrium between asymmetric and symmetric diimes. Figure is adapted from reference [32].

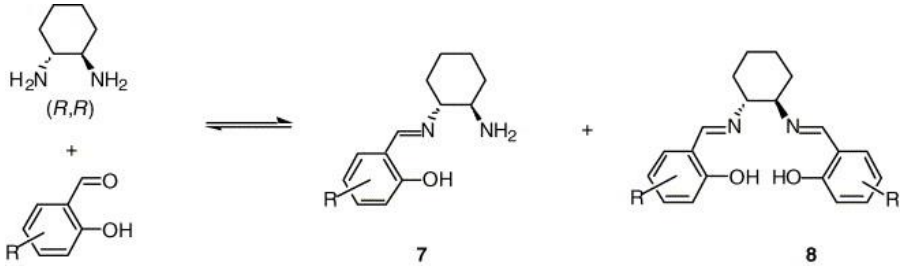

Scheme 3.2. Equilibrium between mono-, diimine and free amine. Figure is adapted from reference [32].

The group of Gilheany studied the synthesis of asymmetric complexes of type C (Figure 3.9C) and developed a strategy for the generation of complex 6 (see Figure 3.10) [32]. The key idea was to isolate the monoimine with the use of a tartaric acid to form an ammonium tartrate salt and then add one equivalent of a different aldehyde to form the asymmetric Schiff base.

In this chapter a strategy for the synthesis of 1,3-propylenediamine derived asymmetric Schiff bases will be discussed (see 3.2). The synthesis of two new ligands is presented (one of them being asymmetric) and difficulties in purification will be discussed. The formation of two new copper(II) complexes with these ligands is shown in part 3.3. Also, the spectroscopic and electrochemical properties of the asymmetric copper complex are compared and contrasted to the two symmetric analogues (see 3.4–3.5).

3.2 Introduction

In this chapter the electrochemical properties of copper(II) complexes of three related tetradentate Schiff base ligands, H_2L^1, HL^2, and L^3 are contrasted. Recently the synthesis of a symmetric Schiff base ligand H_2L^1 (Figure 3.11), derived from 2-methyl-2-pyridin-2-yl-propane-1,3-diamine (ppda) and 2-hydroxybenzaldehyde was reported by the Houser group [36]. Herein, the synthesis of the more electron deficient bis(pyridyl) bis(imine), L^3, and the asymmetric hybrid version containing both a pyridyl group and a phenol group, namely HL^2 are reported (see Figure 3.11). The latter ligand allows access to intermediate electronic properties between the two strictly symmetric ligands.

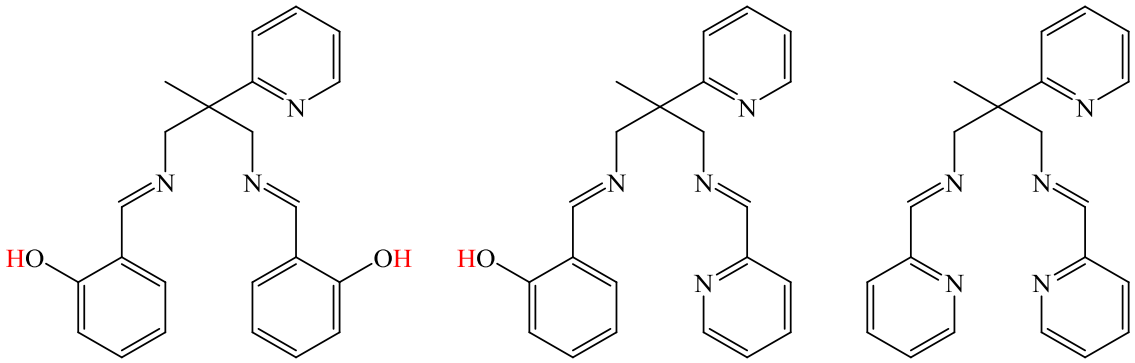

H_2L^1 HL^2 L^3

Figure 3.11. Structures of the previously synthesized ligand H_2L^1 and the two novel ligands HL^2 and L^3. Ionizable protons are highlighted in red.

While H_2L^1 and L^3 can be obtained by addition of two equivalents of the respective aldehyde to ppda, there are challenges in the synthesis of asymmetric ligands like HL^2, such as the step-wise condensation of different aldehydes with the diamine starting material. Some examples of asymmetric bis(imine) and bis(amine) ligands, as well as their metal complexes can be found in the literature [37-41]. An additional

difficulty that must be taken into account in the step-wise condensation of 1,3-propanediamine units with two different aldehydes is the tendency in formation of hexahydropyrimidines (through cyclization) with the first equivalent of aldehyde [42]. The advantage of the cyclization, though, is the directed yield in mono condensed products over a mix of doubly condensed and unreacted species. The most challenging aspect is the hydrolysis of asymmetric bis(imine)s followed by condensation to their symmetric analogues. However, this problem can be overcome by metal chelation, which prevents decomposition and rearrangement.

In the next part the strategy for synthesizing HL^2 will be further explained. Locke and coworkers have shown that electron-rich aldehydes like 2-hydroxybenzaldehyde shift the equilibrium towards bis(imine) formation when 1,3-propanediamine is used [42]. Therefore, if one would just add one equivalent of each, ppda, 2-pyridinecarboxaldehyde and 2-hydroxybenzaldehyde, the expected products would be mostly the salen-type Schiff base (condensation with the benzaldehyde). Even with the use of only one equivalent 2-hydroxybenzaldehyde, bis(imine) formation is favored [42]. However, when one equivalent of 2-pyridinecarboxaldehyde, an electron-poor aldehyde, is added to 1,3-propanediamine, the formation of a hexahydropyrimidine ring is observed rather than imine production [42]. A summary of the condensation products using 1,3-propamediamine with selected aromatic aldehydes is given in the Figure 3.12 below.

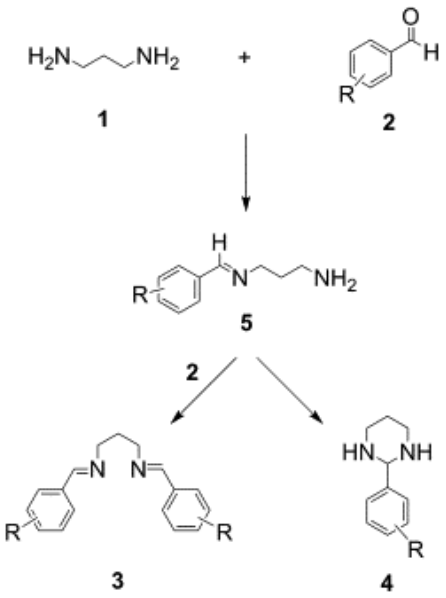

Aldehyde	Reaction with **1**	
	%**4**	%**3**
2a *p*-Nitrobenzaldehyde	70[c]	30
2b *p*-Cyanobenzaldehyde	81[c]	19
2c *p*-Bromobenzaldehyde	68[c]	32
2d *p*-Chlorobenzaldehyde	0	100
2e Benzaldehyde	52	48
2f *p*-Methylbenzaldehyde	11	48
2g *p*-Methoxybenzaldehyde	0	100
2h *p*-Hydroxybenzaldehyde	57	43
2i *o*-Hydroxybenzaldehyde	0	100
2j 2-Pyridine carboxaldehyde	82[c]	18

Figure 3.12. Reaction of 1,3-propanediamine with various aromatic aldehydes. Figure is adapted from reference [42].

According to the previous work published, it should be possible to first generate the hexahydropyrimidine species upon addition of one equivalent 2-pyridinecarboxaldehyde to ppda, then HL^2 should be obtained upon reaction with one equivalent of 2-hydroxybenzaldehyde. The synthesis plan is shown in Figure 3.13.

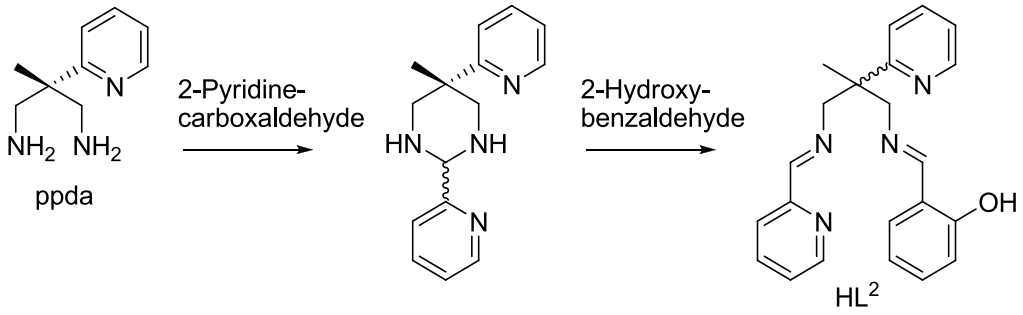

Figure 3.13. Synthesis plan for HL^2.

In the following, the synthesis of the ligands, including a discussion of their stability, will be given in 3.3 (see sections 3.3.1 and 3.3.2). The results of the copper

complexes are discussed in part 3.4 (including the syntheses of the copper complexes in 3.4.1, sections 3.4.2–3.4.4 will deal with the properties of the copper(II) complexes, which are divided into the solid state structures, spectroscopic properties and electrochemical behavior.)

3.3 Ligands

3.3.1 Syntheses of Ligands

The previously reported ligand H_2L^1 (Figure 3.11) was prepared through Schiff base condensation of ppda with two equivalents of 2-hydroxybenzaldehyde, and isolated in high yields in our laboratory [36]. Using the same approach, two novel ligands HL^2 and L^3 (see Figure 3.11) were synthesized in this work. HL^2 is a potentially monoanionic ligand with an N_4O donor set, whereas L^3 is neutral with an N_5 donor set. HL^2 and L^3 were synthesized via condensation of ppda with one equivalent each of 2-pyridinecarboxaldehyde and 2-hydroxybenzaldehyde, or two equivalents of 2-pyridinecarboxaldehyde, respectively. However, it was not possible to obtain HL^2 and L^3 in high purity.

Attempts to purify L^3 through chromatography (silica, CH_2Cl_2:CH_3OH, 95/5%) resulted in its decomposition. The two collected fractions were identified as one of the starting materials, 2-pyridinecarboxaldehyde, and a mixture of compounds (the majority being most likely the *cis* and *trans* isomers of the hexahydropyrimidine L^4: see Scheme 3.1 and the ^{1}H NMR spectrum in Figure 3.14).

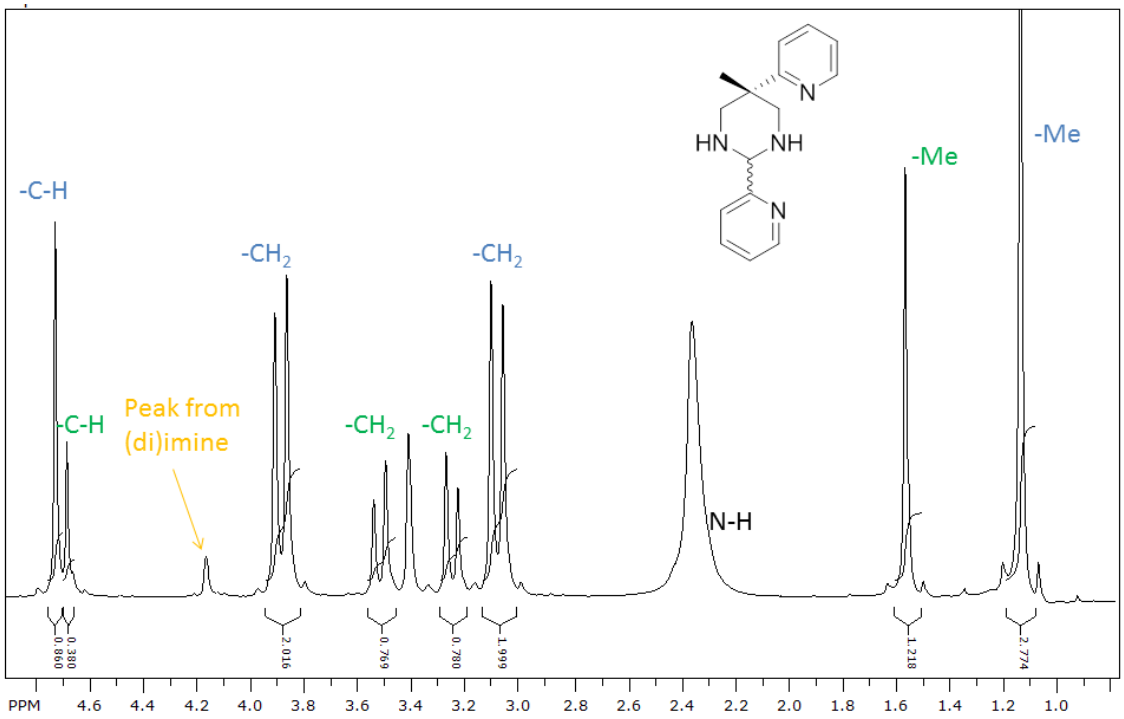

Figure 3.14. ^{1}H NMR of L^{4} (300 MHz, $CDCl_3$, 293K), isolated after chromatography of L^{3}. (Expanded view of the 1–5 ppm region of the spectrum with peak assignments of the two isomers of L^{4}.)

The ^{1}H NMR spectrum of L^{4} shown in Figure 3.14 shows two sets of protons (one set labeled in green, the other one in blue). The integration of each set of signals matches a 3:2:2:1 ratio for Me:CH_2:CH_2:CH of the hexahydropyrimidine ring. Aromatic peaks are omitted for clarity. The ratio of one set of peaks to the other set is about 30% to 70%. This indicates that one isomer is preferred over the other one. It is possible that the hexahydropyrimidine is in equilibrium with the mono-imine form, allowing for conversion between the *cis* and *trans* isomers. This hypothesis will be discussed in section 3.3.2 and suggestions for the structure of the conformers will be made.

In addition, it is observed that both ligands HL^{2} and L^{3} decompose in solution over time, to 2-pyridinecarboxaldehyde and possibly the hexahydropyrimidine species, which was indicated by the growth in the ^{1}H NMR spectrum of the aldehydic proton of

2-pyridinecarboxaldehyde signal, and the appearance of additional signals in the methyl, methylene and aromatic regions. ^{1}H NMR spectra of solutions of H_2L^1, HL^2 and L^3, taken immediately and taken after four days are shown in the following Figures 3.15, 3.16 and 3.17, respectively. The spectrum of H_2L^1 only shows a growth in the water peak signal while HL^2 and L^3 show decomposition.

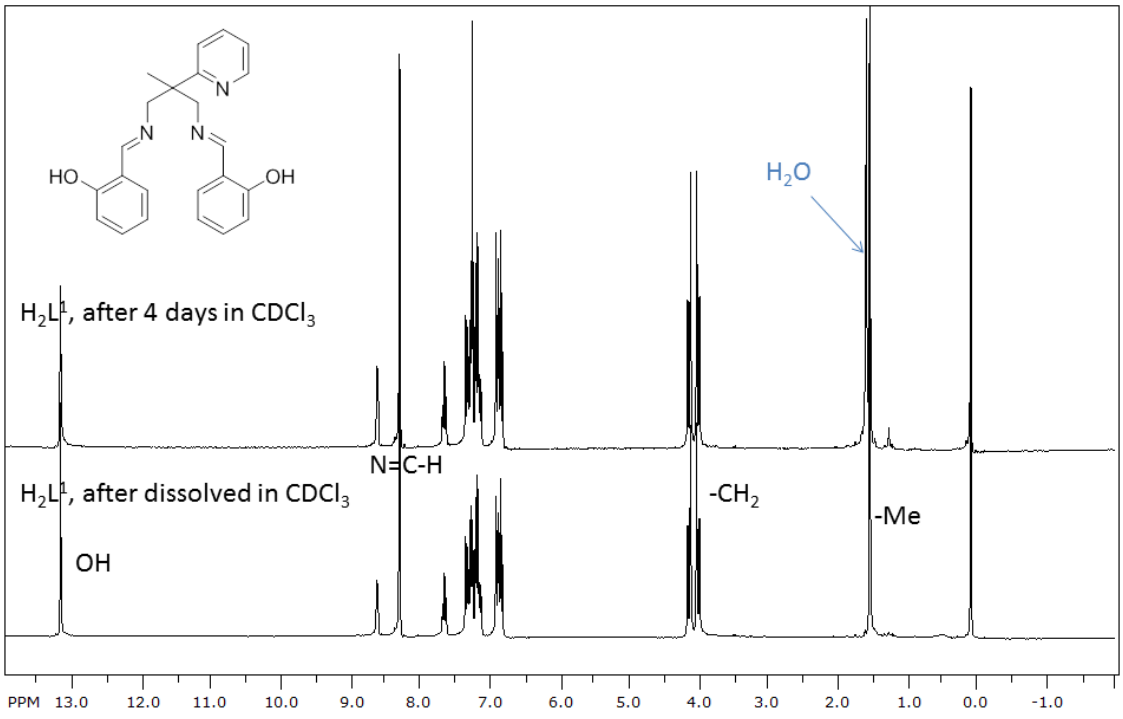

Figure 3.15. ^{1}H NMR of H_2L^1 (300 MHz, $CDCl_3$, 293K), bottom: freshly prepared solution of H_2L^1; top: NMR retaken after four days.

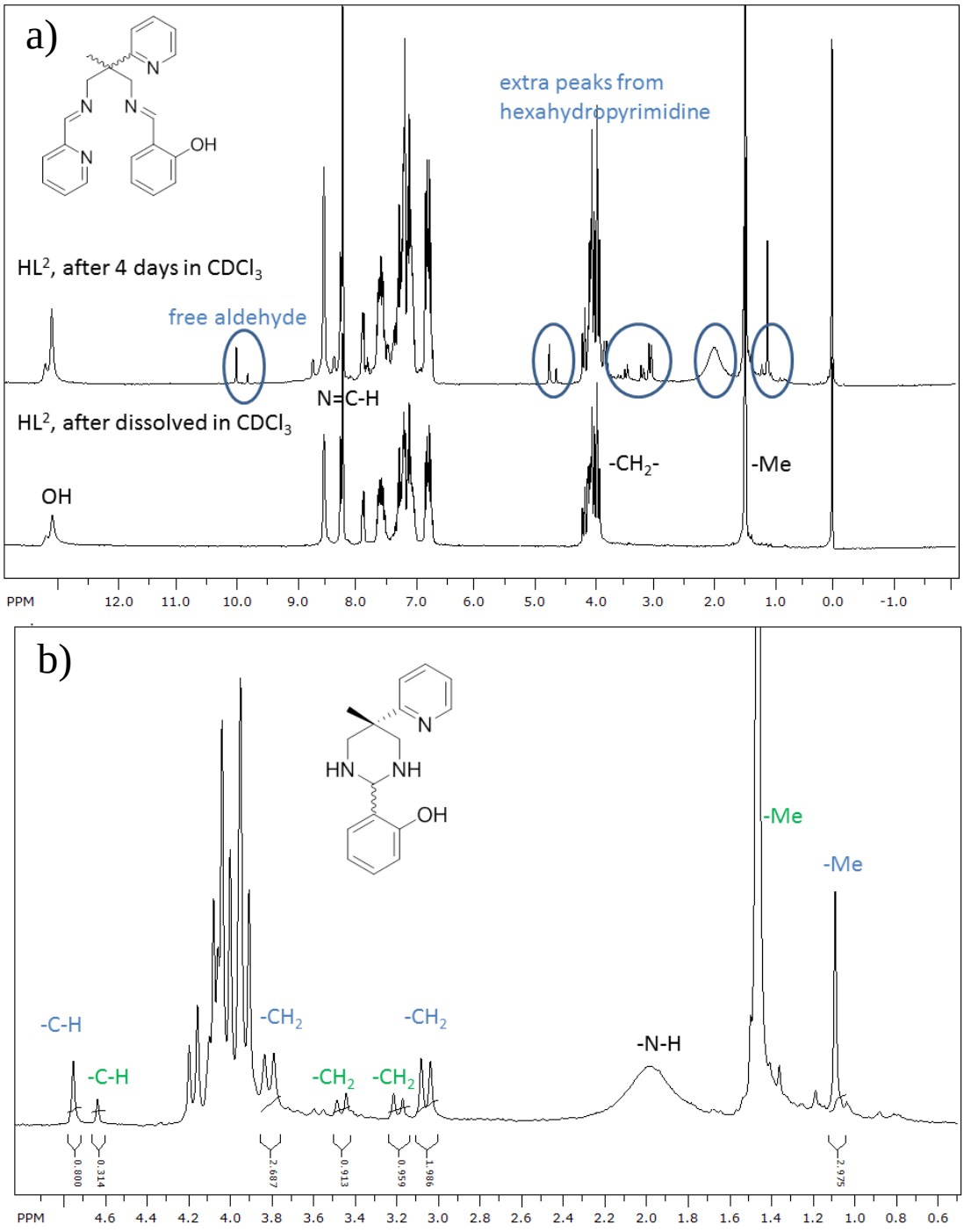

Figure 3.16. a) ^{1}H NMR of HL^{2} (300 MHz, $CDCl_3$, 293K), bottom: freshly prepared solution of HL^{2}; top: NMR retaken after four days. Hydrolysis product peaks are circled in blue. b) Expanded view of the 1–5 ppm region of the spectrum with peak assignments.

The incoming aldehyde peak at around 10.2 ppm in Figure 3.16a after 4 days suggests that 2-pyridinecarboxaldehyde is released, rather than 2-hydroxybenzaldehyde (smaller peak at around 9.8 ppm).

In contrast to the ^{1}H NMR of HL^{2}, taken immediately (Figure 3.16a), which looks very clean and therefore indicates high purity of the ligand, L^{3} cannot be obtained in very high purity. Figure 3.17a shows a small amount of free aldehyde and extra peaks in the methyl, and methylene region which indicate impurities. These peaks increase in intensity upon hydrolysis. These results are consistent with the work done by Locke, where 34% of hexahydropyrimidine was found upon reaction of 1,2-propanedimamine with two equivalents of 2-pyridinecarboxaldehyde [42]. The ^{1}H NMR spectrum obtained from decomposition of L^{3} looks similar to the ^{1}H NMR spectrum obtained when ppda is only reacted with one equivalent of 2-pyridinecarboxaldehyde (see Figure 3.18).

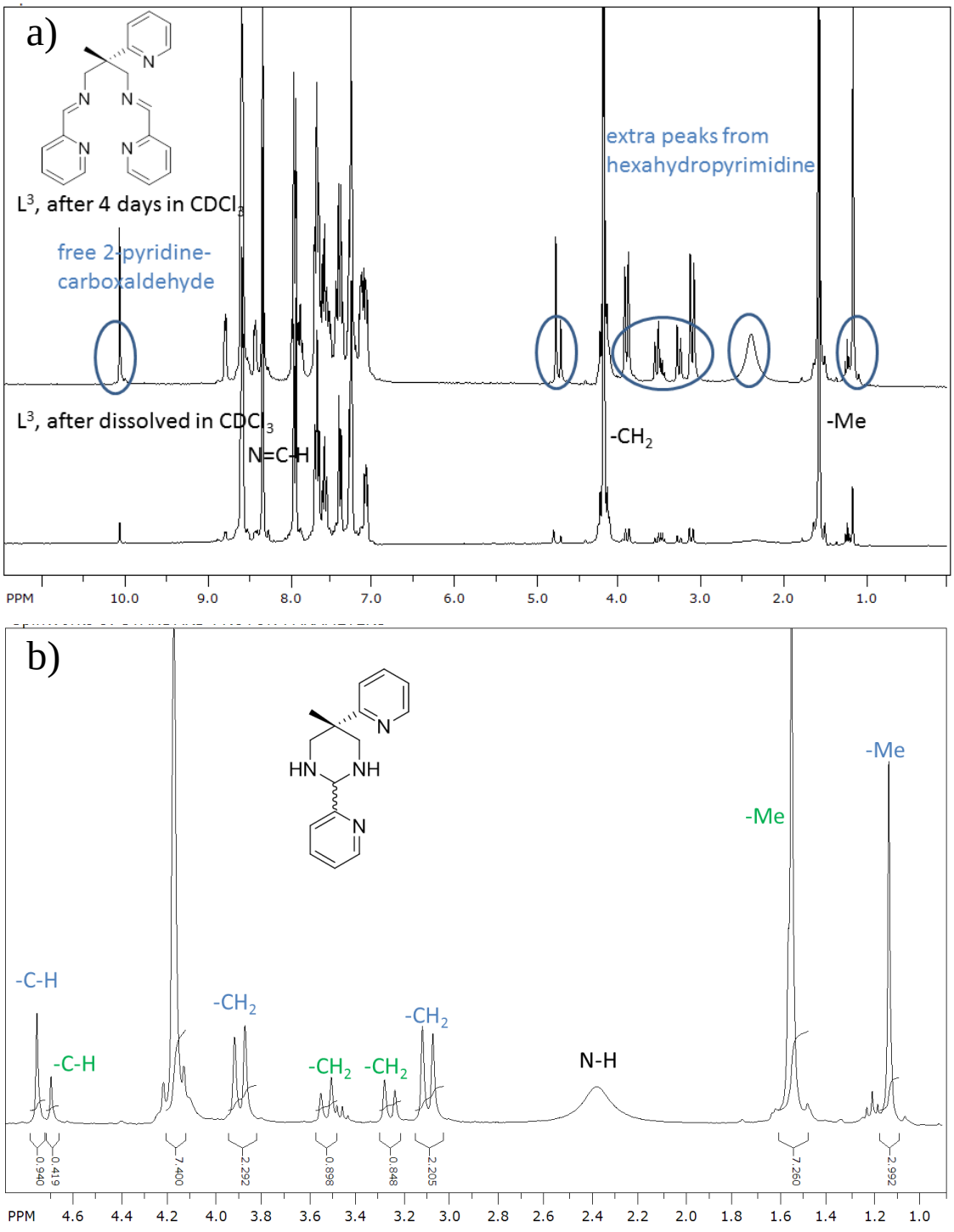

Figure 3.17. a) ^{1}H NMR of L^{3} (300 MHz, $CDCl_3$, 293K), bottom: freshly prepared solution of L^{3}; top: NMR retaken after four days. b) Expanded view of the 1–5 ppm region of the spectrum with peak assignments.

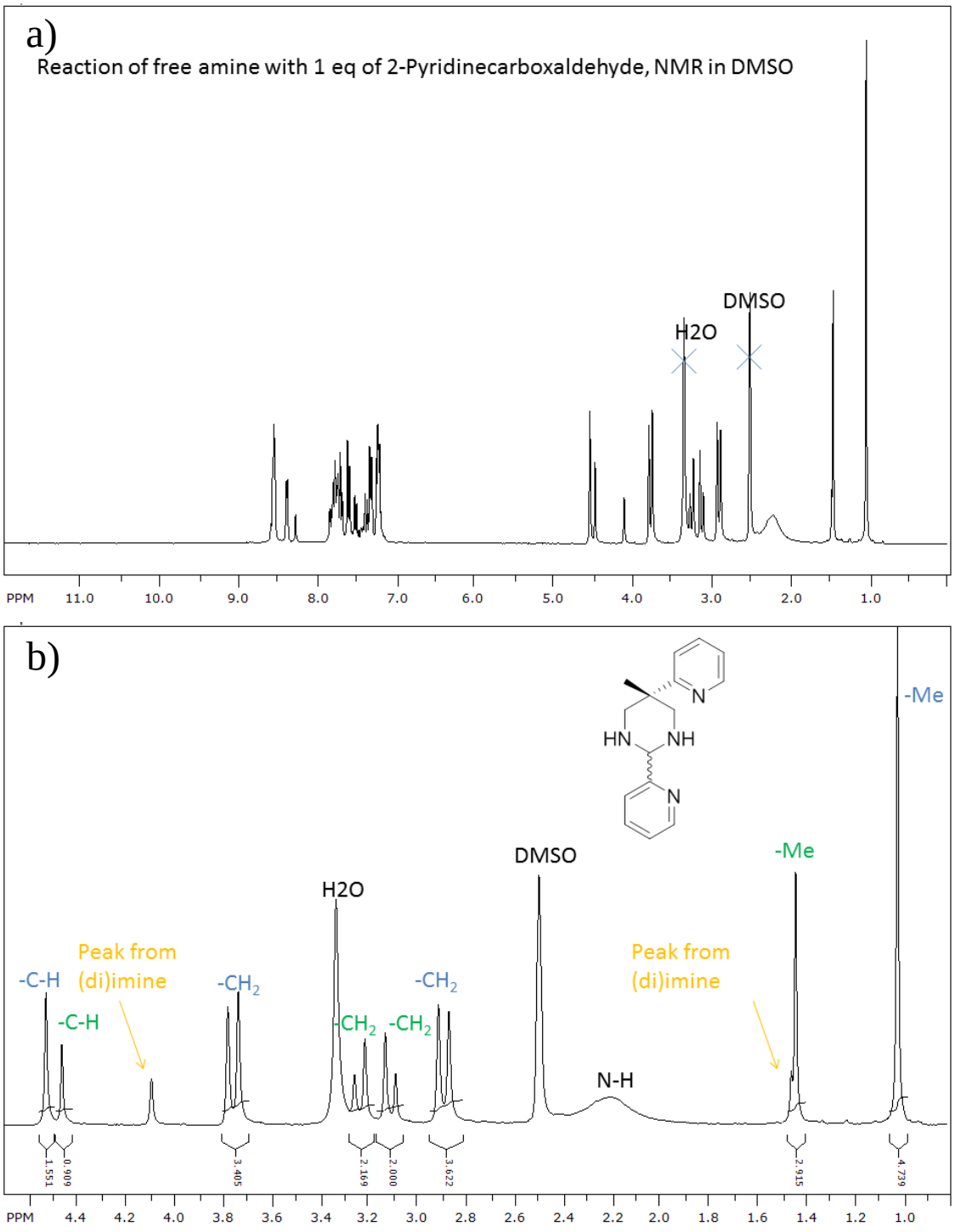

Figure 3.18. a) ^{1}H NMR of crude L^{4} (300 MHz, DMSO-d^{6}, 293K) after reaction of ppda with 1 eq of 2-pyridinecarboxaldehyde. b) Expanded view of the 1–5 ppm region of the spectrum with peak assignments of the two isomers of L^{4}.

3.3.2 Confomers of the Hexahydropyrimidine Molecule

The observations on the instability of ligands HL^2 and L^3 are in good agreement with recently published work on the formation of bis(imine)s and hexahydropyrimidines *via* the condensation of 1,3-propanediamine with various aldehydes (Figure 3.12) [42]. When two equivalents of aldehyde were used, the product was always the bis(imine), except in the case of 2-pyridinecarboxaldehyde about 34% of hexahydropyrimidine was found.

Also, the potential for the formation of intramolecular hydrogen bonds between the phenol hydrogen atoms and the imine nitrogen atoms in H_2L^1 may stabilize the bis(imine), while L^3 cannot develop similar hydrogen bonding, see below in Figure 3.19.

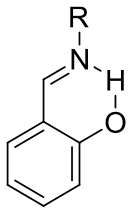

Figure 3.19. Possible hydrogen bonding interaction in H_2L^1.

Unlike in a cyclohexane chair conformation, the hexahydropyrimidine ring does not show typical 1,3 diaxial interactions of the substituents. Instead pyridine substituents favor hydrogen bonding from the pyridine N-atom to the N-H of the hexahydropyrimidine. This interaction has been shown previously in similar structures with the ppda backbone [43, 44]. In crystal structures published by Grohmann et al., the pyridine N-atom hydrogen bonds to the axially oriented N-H group of the ring (see Figures 3.20 and 3.21).

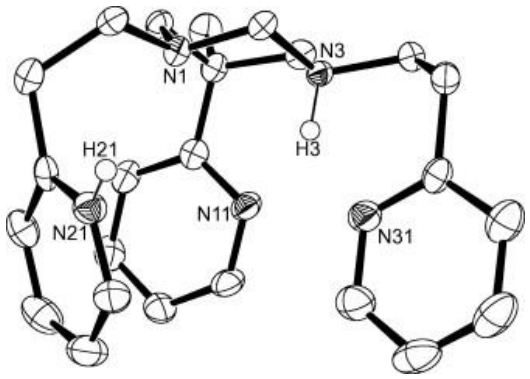

Figure 3.20. Hydrogen bonding between N11 and H3-N3. Figure is adapted from reference [43].

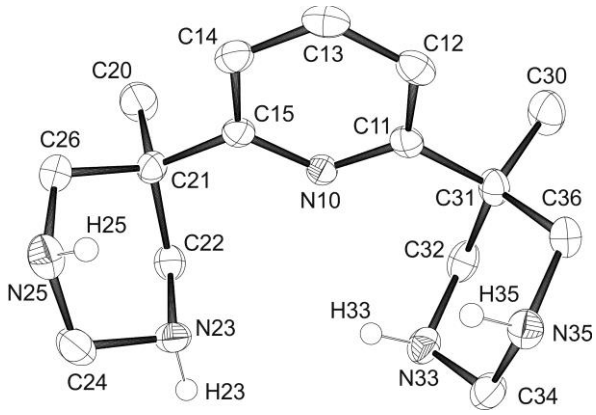

Figure 3.21. Hydrogen bonding between N10 to H33-N33. Figure is adapted from reference [44].

The two structures reported previously support the suggested structure shown in Figure 3.22. The pyridine substituent should be in the axial position and hydrogen bonded to the axially aligned N-H of the ring.

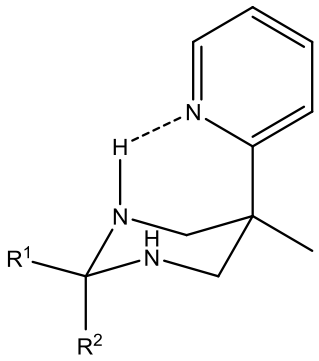

Figure 3.22. Possible hydrogen bonding of the ppda-Pyridine-N atom to the axial standing N-H of the hexahydropyrimidine.

Now the question arises of where the other pyridine ring would most likely be found. Should it be in position of R^1 or R^2? A recent publication shows the crystal structure of a pyridine substituted hexahydropyrimidine (Figure 3.23). According to the schematic depiction in 3.22 the pyridine substituent is found at the R^2 or axial position and the equatorial N-H is forming a hydrogen bond to the N-atom of pyridine [45].

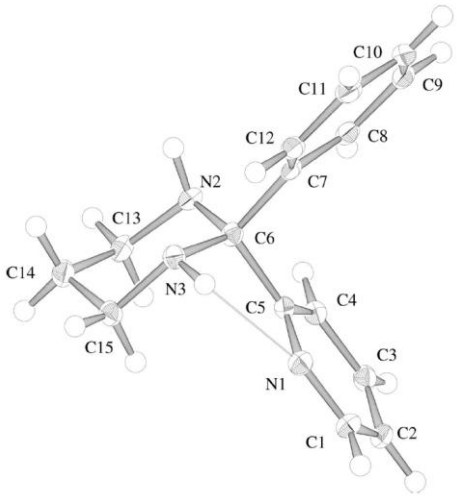

Figure 3.23. Crystal structure of a pyridyl-hexahydropyrimidine. Figure is adapted from reference [45].

Combining all information, the structure depicted below (Figure 3.24) should lead to the most stable structure with the two pyridine rings in axial position and therefore the *trans*-conformation of the molecule.

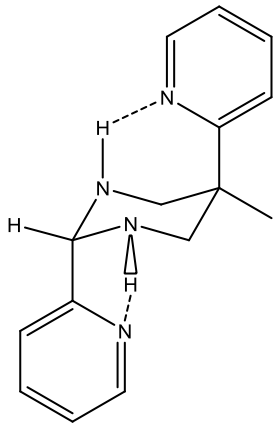

Figure 3.24. Most stable structure for L^4, *trans* conformer.

Theoretical studies carried out on hexahydropyrimide further support the hypothesized structure. According to Salzner, the hexahydropyrimidine having N-H in the axial/equatorial (ae) and axial/axial (aa) position is energetically favored, while the equatorial/equatorial (ee) position is less likely to form (see structures below in Figure 3.25).

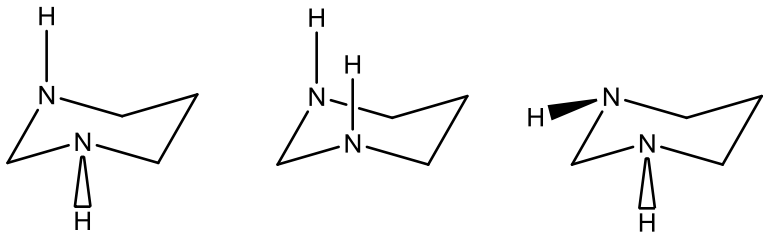

Figure 3.25. Conformers of hexahydropyrimidine.

The *trans* conformation of L^4 is in equilibrium with the open, monoimine form, and ring closure to the *cis* conformer is possible by nucleophilic attack from the other side. In fact, a peak for the imine is seen in the ^1H NMR spectrum together with 2 sets of protons, one for the *trans* and the other one for the *cis* form (see Figure 3.14). Tautomerism between all forms of L^4 is shown in figure 3.26.

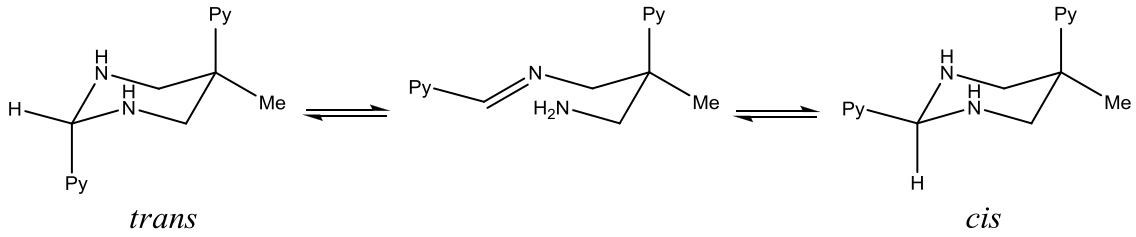

Figure 3.26. Tautomerism between the *cis* and *trans* isomers of the hexahydropyrimidine through the open monoimine in L^4.

3.4 Synthesis of the Copper Complexes

Despite difficulties in isolating HL^2 and L^3, it was possible to obtain pure metal complexes of the two ligands upon coordination to copper(II) salts. A methanolic solution of either crude HL^2 or L^3 was typically treated with copper(II) perchlorate to yield $[Cu(HL^2)]_2(ClO_4)_4$ or $[Cu(L^3)](ClO_4)_2$ as olive-green and light blue precipitates, respectively (Scheme 3.3, a and e).

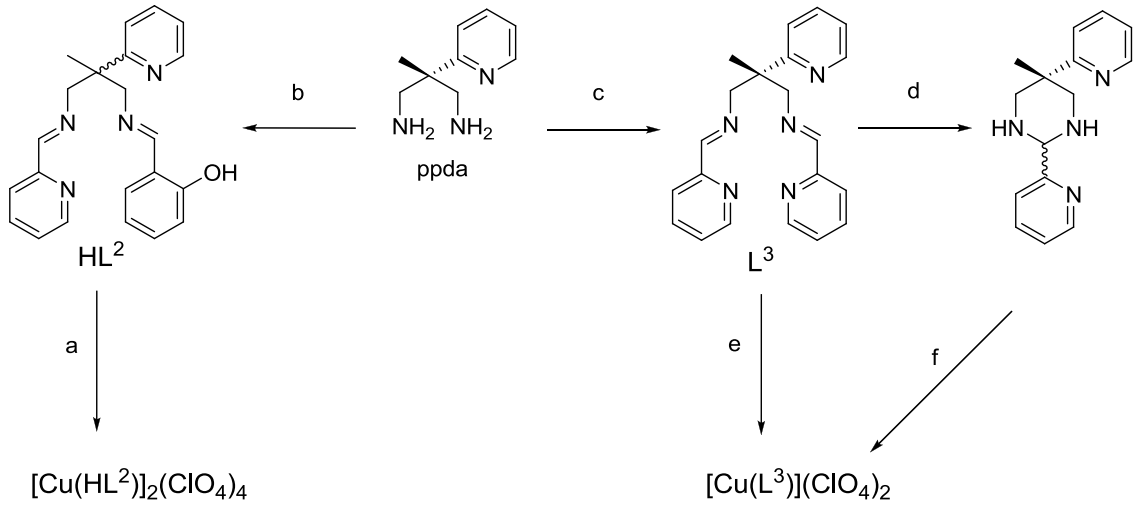

Scheme 3.3. Synthesis of HL^2, L^3, $[Cu(HL^2)]_2(ClO_4)_4$ and $[Cu(L^3)](ClO_4)_2$. (a) $Cu(ClO_4)_2 \cdot 6H_2O$; (b) 1 eq 2-pyridinecarboxladehyde, 1 eq 2-hydroxybenzaldehyde; (c) 2 eq 2-pyridinecarboxladehyde; (d) column chromatography on silica, or decomposition in solution; (e) $Cu(ClO_4)_2 \cdot 6H_2O$; (f) 1 eq 2-pyridinecarboxladehyde, $Cu(ClO_4)_2 \cdot 6H_2O$.

$[Cu(L^3)](ClO_4)_2$ was also obtained when L^3 was generated in situ from L^4 in solution, along with one equivalent of 2-pyridinecarboxaldehyde followed by subsequent addition of cupric perchlorate as shown in Scheme 1-f. Crystals suitable for X-ray structural analysis were obtained after recrystallization of the powders. The solid state structures will be discussed in 3.4.2. $[Cu(HL^2)]_2(ClO_4)_4$ was found in the solid state to be a dimeric species of two $[Cu(HL^2)]^{2+}$ subunits where the proton on the phenol group has migrated to the pyridyl N atom. The ligand in $[Cu(HL^2)]_2(ClO_4)_4$ is therefore still neutral despite the deprotonated phenolate due to the protonated pyridinium group. In contrast to $[Cu(HL^2)]_2(ClO_4)_4$, the complex with L^3 was isolated as a monomer $[Cu(L^3)](ClO_4)_2$. Solutions of $[Cu(HL^2)]_2(ClO_4)_4$ in methanol and acetonitrile seem to dissociate into monomers as ascertained by the solution magnetic moment and mass spectrometry. Low intensity peaks in the ESI-MS show a small amount of dimer present, as well as monomer with solvent coordinated. Additionally,

EPR and CV data indicate that there may be small amounts of dimer in solution (see Sections 3.4.3 and 3.4.4, respectively). Unfortunately, due to solubility constraints in non-coordinating solvent it was not possible to study the nature of the dimer in solution.

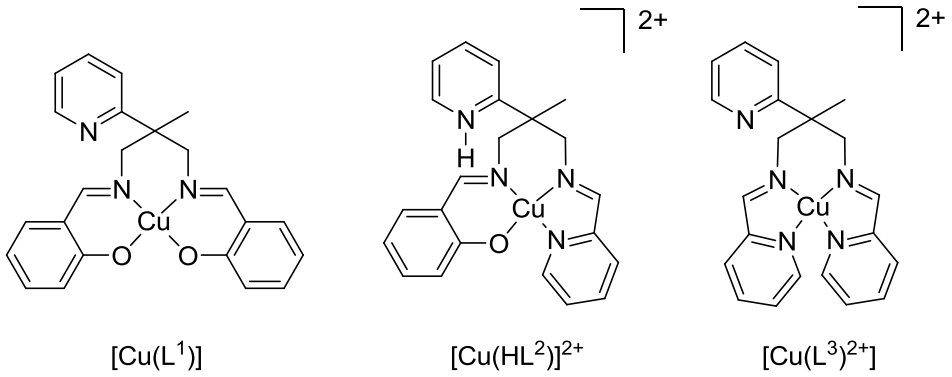

Figure 3.27. Structures of the copper imine complexes discussed in this work. The synthesis and structure of $[Cu(L^1)(CH_3OH)]$ was reported previously [36]. $[Cu(HL^2)]_2(ClO_4)_4$ is a dimer in the solid state but is monomeric, e.g. $[Cu(HL^2)]^{2+}$, in solution. $[Cu(L^3)](ClO_4)_2$ is a monomer in solution.

Attempts to synthesize $[CuL^2]^+$ by the deprotonation of HL^2 were unsuccessful. The potentially monoanionic ligand HL^2 was treated with base either before or after the addition of copper(II) ions in order to investigate the formation of complexes with $(L^2)^-$. Addition of base to the ligand in methanol with subsequent complexation of copper(II) ions resulted in an accumulation of a mixture of a green and blue precipitate. According to mass spectrometry, complexes $[Cu(HL^2)]_2(ClO_4)_4$ and $[Cu(L^3)](ClO_4)_2$ were present in this mixture. Upon recrystallization of the crude powder, crystals of $[Cu(L^3)](ClO_4)_2$ were obtained. When complex $[Cu(HL^2)]_2(ClO_4)_4$ was treated with two equivalents of base (or water) in acetonitrile, no ligand rearrangement was observed according to mass spectrometry. Diffusion of diethyl ether into a solution of $[Cu(HL^2)]_2(ClO_4)_4$ in CH_3CN and NEt_3 did not form any crystalline material. The use of base before complex formation prohibits isolation of pure complex and leads to ligand rearrangement.

Treatment of $[Cu(HL^2)]_2(ClO_4)_4$ with base to generate a copper(II) complex with $(L^2)^-$ was unsuccessful, despite HL^2 being stable towards decomposition and/or rearrangement of the arms when coordinated to the metal ion.

3.5 X-ray Crystal Structures

The previously published structure of $[Cu(L^1)(CH_3OH)]$ (Figure 3.28) revealed that the copper ion was in a square pyramidal geometry with an N_2O_2 donor atom set from the $(L^1)^{2-}$ ligand in the equatorial plane and an axial O atom from a coordinated methanol molecule [36]. The pyridyl group does not coordinate in $[Cu(L^1)(CH_3OH)]$, most likely due to geometric constraints that the bis(imine) ligand imposes on the complex. Compared to similar ligands with amine functional groups [43, 46], the more planar geometry imposed by the ligand due to the imine C-N double bonds in $[Cu(L^1)(CH_3OH)]$ prevent the pyridyl N atom from folding into position where it can coordinate to the copper. This same constraint is seen in complexes $[Cu(HL^2)]_2(ClO_4)_4$ and $[Cu(L^3)](ClO_4)_2$ (*vide infra*).

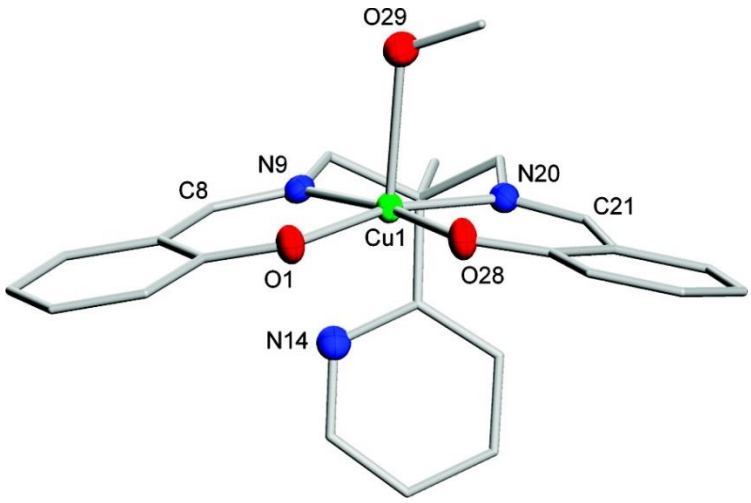

Figure 3.28. Representation of the X-ray structure of $[Cu(L^1)(CH_3OH)]$ with H atoms removed for clarity. Figure is adapted from reference [36].

According to the X-ray crystal structure of $[Cu(HL^2)]_2(ClO_4)_4$ (Figure 3.29), each copper(II) ion is coordinated in a square pyramidal geometry with a τ_5 parameter [47] of 0.024 (Figure 3.29). The N_3O donor atom set from the ligand occupies the basal plane of the pyramid with the μ_2-phenolato O atom from another complex coordinating in the apical position. The resulting structure contains two copper ions with bis(μ_2-O) bridging phenolate groups in a diamond core fashion. The apical O atom bond donor distance to the copper ion (Cu–O1#1 = 2.487 Å) is longer than the basal donors (ranging from 1.922 to 2.020Å) due to the Jahn-Teller effect. The pyridyl ring from the ligand backbone is non-coordinating and, surprisingly, protonated at the N atom position. The overall +4 charge is balanced by four perchlorate counterions (Figure 3.29), two of which are weakly interacting with the copper(II) in the apical position *trans* to the phenolate O atom of each monomeric unit (Cu···O = 2.763 Å), while the other two are non-coordinating. Hydrogen bonding between the pyridinium hydrogen and the non-coordinating methanol oxygen atom (N14–H14···O1S), as well as between the perchlorate ion oxygen and the methanol hydrogen atom (O1S–H1S···O1A#2), stabilizes the structure in the solid state (Figure 3.30, Table 3.2).

A complex similar to $[Cu(HL^2)]_2(ClO_4)_4$ was reported by Lee and coworkers with the ligand *N*-(salicylidene)-*N*'-(2-pyridylaldene)propanediamine [25]. This ligand differs from HL^2 only in the absence of the methyl and pyridyl groups on the propylene backbone. $[Cu(HL^2)]_2(ClO_4)_4$ adopts the same Cu_2(μ-phenolato)$_2$ diamond core, and has the same N_2O donor atom set as the complex with *N*-(salicylidene)-*N*'-(2-pyridylaldene)propanediamine [25]. Since HL^2 and *N*-(salicylidene)-*N*'-(2-pyridylaldene)propanediamine are effectively the same except for the pyridine group,

both ligands coordinate in the same fashion, and the ligand-copper bond lengths and angles are very similar [25].

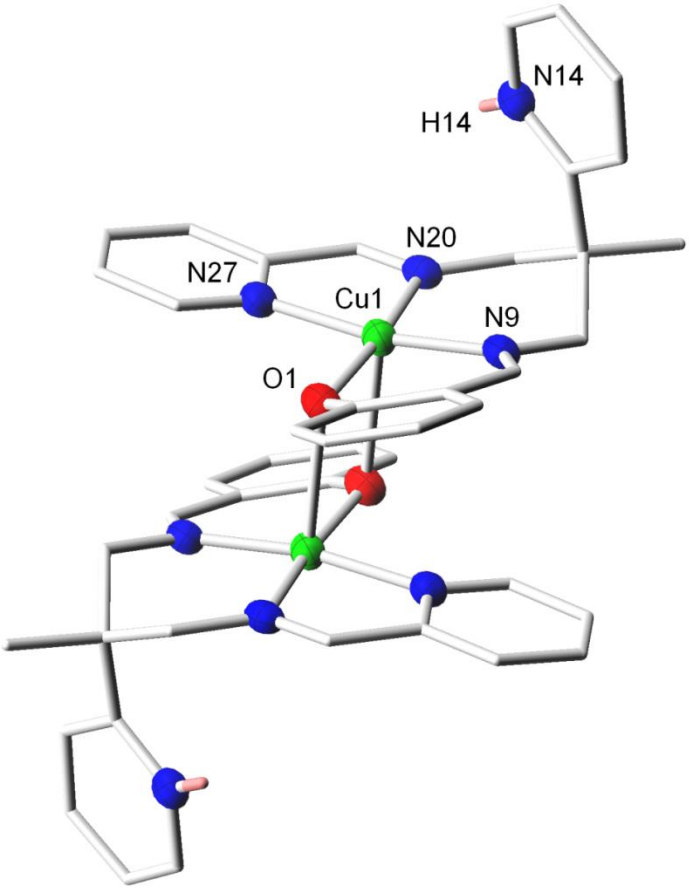

Figure 3.29. Representation of the X-ray structure of $[Cu(HL^2)]_2^{2+}$ with all H atoms except for the protonated pyridyl NH protons removed for clarity. Perchlorate anions and methanol solvent of crystallization molecules are also removed for clarity. Symmetry information used to generate equivalent positions: ($-x + ½, -y + ½, -z$).

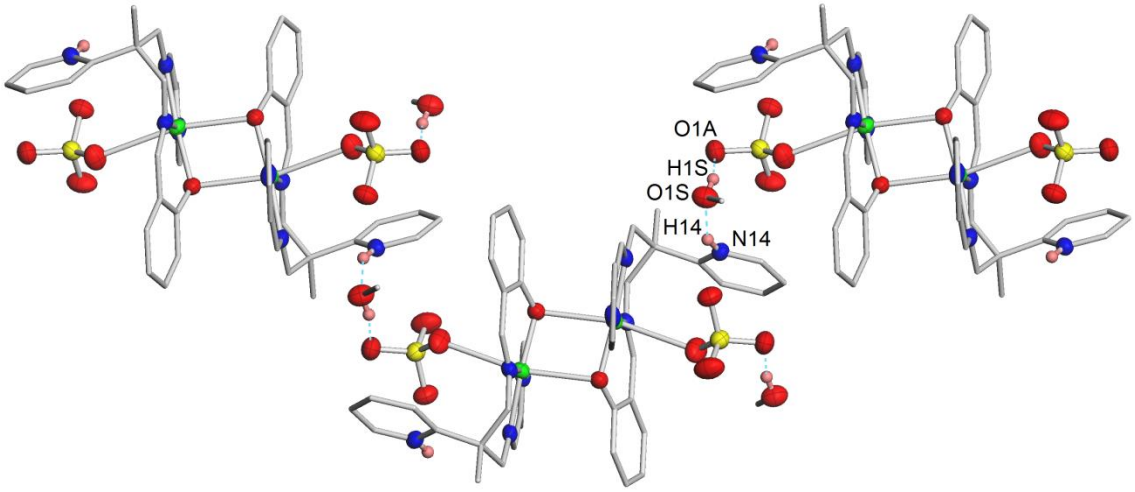

Figure 3.30. Representation of the X-ray structure of $[Cu(HL^2)]_2(ClO_4)_4$ including solvent molecules and anions with intermolecular H-bonding represented by light blue dashed lines.

The X-ray structure of $[Cu(L^3)](ClO_4)_2$ consists of a mononuclear copper(II) complex of L^3 and two perchlorate anions (Figure 3.31). The coordination geometry in $[Cu(L^3)](ClO_4)_2$ is axially elongated six-coordinate tetragonal. The L^3 ligand coordinates in a slightly distorted square planar (τ_4 = 0.154) [48] manner while the perchlorate oxygens are weakly coordinating in the axial positions (Cu1–O1A = 2.660 Å and Cu1–O1B = 2.573 Å). As observed in other Cu(II) complexes with our bis(imine) family of ligands, here the ligand backbone pyridine nitrogen atom is non-coordinating. The geometrical constraints imposed by the ligand prevent the pyridyl ring from getting close enough to coordinate to the copper ion. As in $[Cu(HL^2)]_2(ClO_4)_4$, there is significant bond elongation between the copper(II) ion and the axial donor atoms versus the donors in the basal plane.

A complex similar to $[Cu(L^3)](ClO_4)_2$ was reported by Ray and coworkers with the ligand *N*,*N*'-bis(2-pyridylaldene)propane-1,3-diamine [24]. Similar to HL^2 and its analog, L^3 and *N*,*N*'-bis(2-pyridylaldene)propane-1,3-diamine coordinate via the same

N_4 donor atom set. Both complexes show the same N_4 coordination mode, with similar ligand-copper bond lengths and angles, due to the ligands sharing same ligand backbone and the fact that the pyridyl group of L^3 does not coordinate the copper atom.

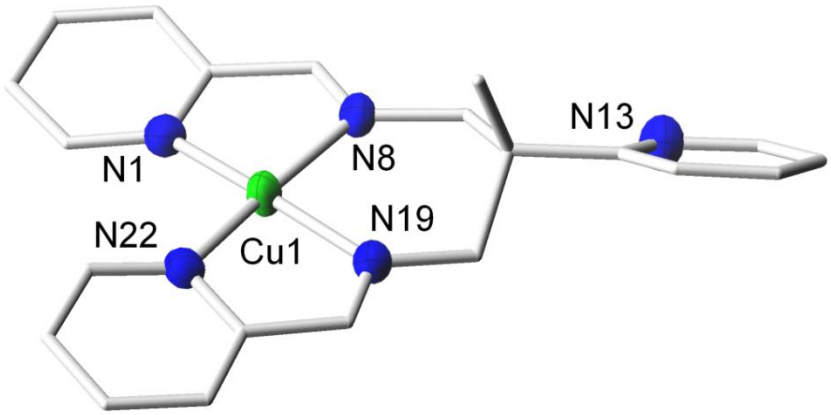

Figure 3.31. Representation of the X-ray structure of $[Cu(L^3)]^{2+}$ with all H atoms removed for clarity. Perchlorate anions are also removed for clarity.

H_2L^1, HL^2 and L^3 have a common coordination mode to copper(II) ions. While the pyridine nitrogen atom of each ligand backbone is non-coordinating, the remaining N and O donors chelate in the basal plane around the metal ion (see Figure 3.27). The pyridyl ring does not coordinate in all three complexes presented because of geometric constraints imposed by the rigid imine groups in H_2L^1, HL^2 and L^3. This stands in contrast to copper complexes of the more flexible series of bis(amine) ligands synthesized in our laboratory [46]. The geometry of $[Cu(L^1)(CH_3OH)]$ is similar to $[Cu(HL^2)]_2(ClO_4)_4$ but features a CH_3OH oxygen donor atom (not shown in Figure 3.27) in the axial position rather than a bridging phenolate. Therefore, $[Cu(L^1)(CH_3OH)]$ is found as a monomeric species. $[Cu(HL^2)]_2(ClO_4)_4$ and $[Cu(L^1)(CH_3OH)]$ show bond elongation in the axial positions (2.34 Å for

$[Cu(L^1)(CH_3OH)]$ and 2.49 Å for $[Cu(HL^2)]_2(ClO_4)_4$) compared to the basal donors, averaging in metal-ligand atom bond distances from 1.92 Å to 2.02 Å. Although $[Cu(L^3)](ClO_4)_2$ was synthesized in CH_3OH and crystallized from CH_3CN, no solvent molecule occupies the axial position. Instead, perchlorate anions are found in weak association to the metal ion in the axial positions (2.57 Å and 2.66 Å).

Selected bond lengths and angles for $[Cu(HL^2)]_2(ClO_4)_4$ and $[Cu(L^3)](ClO_4)_2$ are summarized in Table 3.1. Hydrogen bonding information of $[Cu(HL^2)]_2(ClO_4)_4$ is represented in Table 3.2. Crystal data for $[Cu(HL^2)]_2(ClO_4)_4$ and $[Cu(L^3)](ClO_4)_2$ are summarized in Table 3.4.

Table 3.1. Selected bond lengths (Å) and angles (deg) for $[Cu(HL^2)]_2(ClO_4)_4$ and $[Cu(L^3)](ClO_4)_2$.

$[Cu(HL^2)]_2(ClO_4)_4$			
Cu1-O1	1.922(2)	Cu1-N9	1.956(3)
Cu1-N20	2.020(2)	Cu1-N27	2.010(3)
Cu1-O1#1	2.487(2)	Cu1-O2A	2.763(3)
O1-Cu1-N9	94.22(9)	O1-Cu1-N27	91.35(9)
N9-Cu1-N20	93.97(9)	N27-Cu1-N20	80.94(9)
N9-Cu1-N27	169.94(9)	O1-Cu1-N20	171.38(9)
O1-Cu1-O1#1	82.52(8)	N27-Cu1-O1#1	89.87(8)
N9-Cu1-O1#1	99.14(8)	N20-Cu1-O1#1	93.55(8)
$[Cu(L^3)](ClO_4)_2$			
Cu1-N19	1.966(2)	Cu1-N8	1.996(2)
Cu1-N1	2.018(2)	Cu1-N22	2.050(2)
Cu1-O1B	2.573(2)	Cu1-O1A	2.660(2)
N19-Cu1-N8	91.65(9)	N19-Cu1-N1	168.37(9)
N8-Cu1-N1	82.63(9)	N19-Cu1-N22	81.35(9)
N8-Cu1-N22	169.95(9)	N1-Cu1-N22	105.50(9)
N19-Cu1-O1B	106.80(9)	N8-Cu1-O1B	85.17(8)
N1-Cu1-O1B	82.89(9)		

Symmetry information used to generate equivalent positions: ($–x + ½, –y + ½, –z$).

Table 3.2. Hydrogen bonds (Å) and angles (deg) for $[Cu(HL^2)]_2(ClO_4)_4$.

D-H···A	d(D-H)	d(H···A)	d(D···A)	<(DHA)
N14-H14···O1S	0.83(3)	2.01(3)	2.764(3)	151(3)
O1S-H1S···O1A#2	0.74(4)	2.24(4)	2.864(3)	144(4)

Symmetry information used to generate equivalent positions: (*–x* + ½, *–y* + ½, *–z*).

3.6 Spectroscopic Characterization

Electrospray mass spectrometry suggests that CH_3OH and CH_3CN solutions of $[Cu(HL^2)]_2(ClO_4)_4$ dissociate mostly into monomeric species. A peak at *m/z* = 420.1 corresponding to $[Cu(L^2)]^+$, and a peak at *m/z* = 452.1 corresponding to $[Cu(L^2)(CH_3OH)]^+$ are indicative of monomeric species. A peak with very low intensity at *m/z* = 941.1 corresponding to $[(Cu(L^2))_2ClO_4]^+$, indicating a dimeric species, was also detected. This dissociative behavior in solution is further supported by a solution magnetic moment of 1.76 μB/Cu. This magnetic moment, which is close to the spin-only value of 1.73 μB/Cu, suggests the absence of any magnetic coupling and therefore supports the existence of a monomeric species in solution.

$[Cu(HL^2)]_2(ClO_4)_4$ was dissolved in methanol at room temperature to allow equilibration and subsequently frozen. EPR spectra show two sets of peaks, which originate from two typical axial EPR signals (Figure 3.32, red). Those two sets of signals most likely correspond to monomeric and dimeric forms ($[Cu(HL^2)](ClO_4)_2$ and $[Cu(HL^2)]_2(ClO_4)_4$, respectively). Due to differences in the coordination environment around the copper ions between the monomer and the dimer, it is expected to see differences in *g* values and therefore two sets of axial EPR signals. To further support this hypothesis, solutions of $[Cu(HL^2)]_2(ClO_4)_4$ were allowed to equilibrate in a dry

ice/acetone bath for two hours before freezing the sample in liquid nitrogen. The corresponding EPR spectrum (Figure 3.32, black) only shows one set of signals which would be expected for only one species, which should correspond to the dimeric $[Cu(HL^2)]_2(ClO_4)_4$.

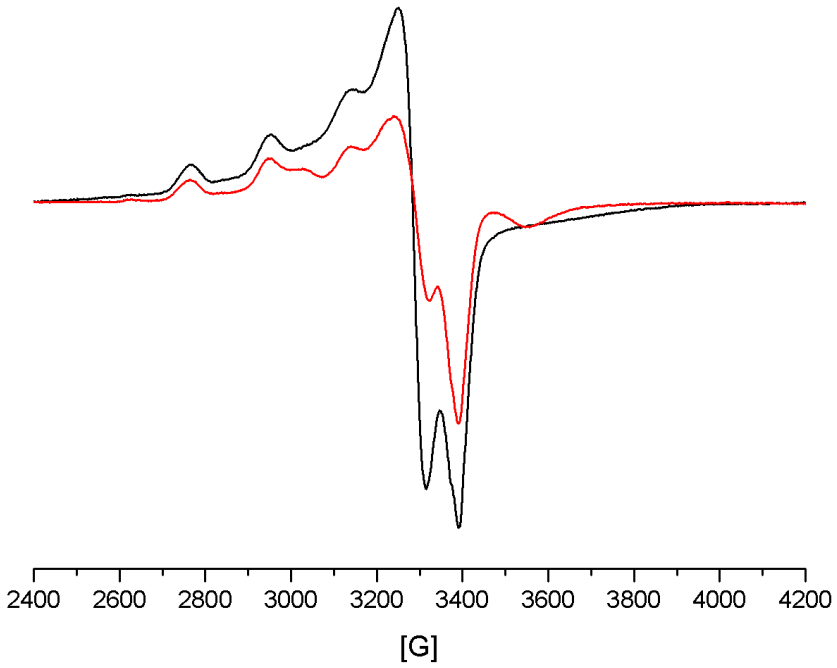

Figure 3.32. EPR spectra of frozen solutions of $[Cu(HL^2)]_2(ClO_4)_4$ (9.466 GHz, mod. amp. 25.0 G, CH_3OH, 77K). Black: $[Cu(HL^2)]_2(ClO_4)_4$ in CH_3OH was kept in an EPR tube for two hours in a dry ice/acetone bath before subsequent freezing in liquid nitrogen and acquisition of the spectrum, red: $[Cu(HL^2)]_2(ClO_4)_4$ was dissolved in CH_3OH at room temperature before subsequent freezing in liquid nitrogen and acquisition of the spectrum.

Frozen solutions of $[Cu(HL^2)]_2(ClO_4)_4$ in CH_3CN only show one axial EPR signal. $[Cu(HL^2)]_2(ClO_4)_4$ has a much greater solubility in CH_3CN than in CH_3OH and due to the solubility difference it is reasonable to assume that $[Cu(HL^2)]_2(ClO_4)_4$ dissociates immediately in CH_3CN. The slight shift in *g* for the monomers is likely due to solvent coordination (CH_3OH vs. CH_3CN).

CH_3CN solutions of $[Cu(L^3)](ClO_4)_2$ were found to contain monomeric species, as ascertained by electrospray mass spectrometry (*m/z* = 505, corresponding to $[Cu(L^3)ClO_4]^+$) and solution magnetic moment measurements (1.75 μB/Cu). $[Cu(L^3)](ClO_4)_2$ likewise possesses an axial EPR spectrum.

3.7 Electrochemical Studies

The redox behavior of $[Cu(HL^2)]_2(ClO_4)_4$ and $[Cu(L^3)](ClO_4)_2$ were studied by cyclic voltammetry and compared to the previously reported electrochemical parameters for $[Cu(L^1)(CH_3OH)]$ [36] (Figure 3.33). The cyclic voltammograms (CVs) show reversible one-electron redox couples with $E_{1/2}$ = –1099 mV versus Fc/Fc^+ and ΔE = 77 mV for $[Cu(HL^2)]_2(ClO_4)_4$, and $E_{1/2}$ = –438 mV versus Fc/Fc^+ and ΔE = 64 mV for $[Cu(L^3)](ClO_4)_2$. The CV of $[Cu(HL^2)]_2(ClO_4)_4$ is complicated by a small reduction feature immediately before the E_{pc} peak that disappears on successive scans (this unusual redox behavior is undergoing further study). The CV in Figure 3.33 is therefore the second scan, and the full first-scan CV of $[Cu(HL^2)]_2(ClO_4)_4$ is shown in Figure 3.34.

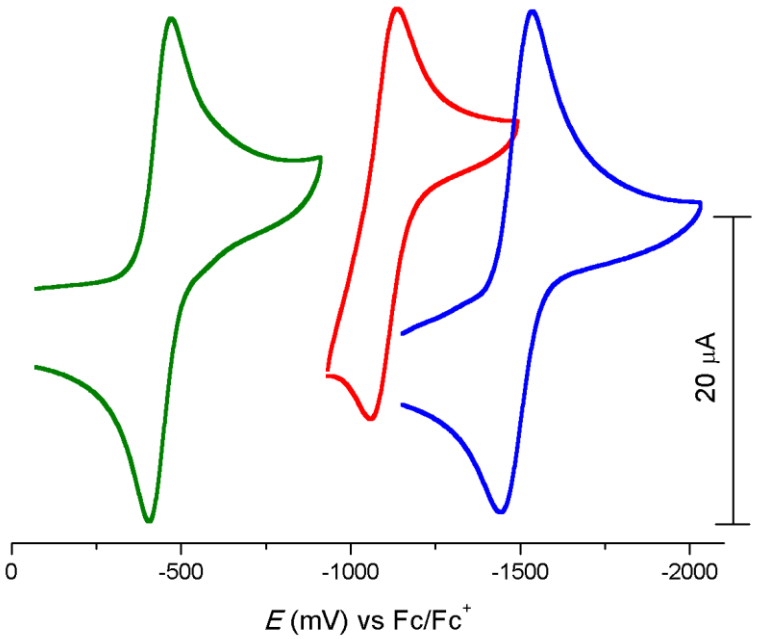

Figure 3.33. Cyclic voltammograms of 1.0 mM CH_3CN solutions of $[Cu(L^1)(CH_3OH)]$ (blue), $[Cu(HL^2)]_2(ClO_4)_4$ (red) and $[Cu(L^3)](ClO_4)_2$ (green), (scan rate = 100 mV s^{-1}; 0.1 M $TBAPF_6$ supporting electrolyte).

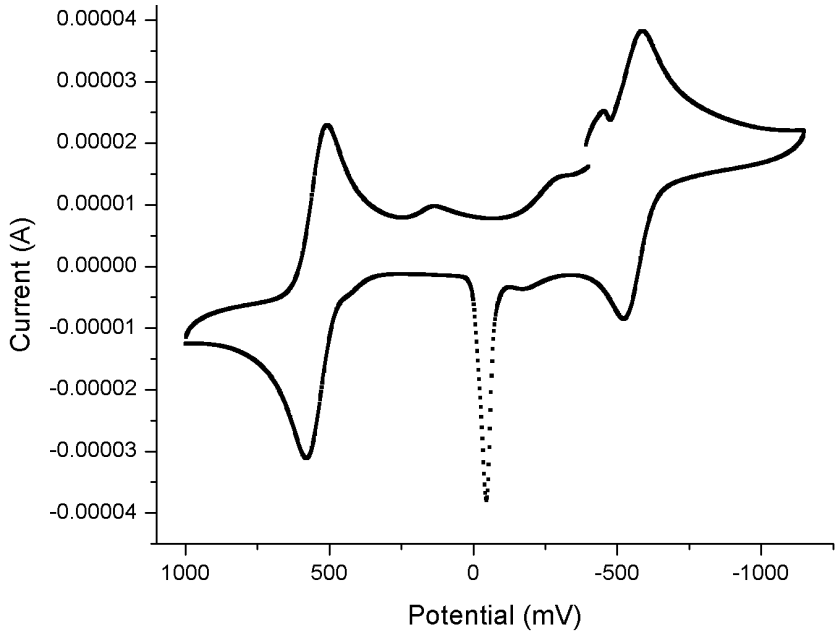

Figure 3.34. Cyclic voltammogram of a 1.5 mM CH_3CN solution of $[Cu(HL^2)]_2(ClO_4)_4$ (vs Ag/AgCl; scan rate = 100 mV s^{-1}; 0.15 M $TBAPF_6$ supporting electrolyte). Ferrocene was added as an internal standard (ferrocene/ferrocenium couple is centered around 500 mV).

Additional redox features in the CV are most likely due to some dimeric species. The redox couples, which were measured in CH_3CN, were assigned to the Cu(II)/Cu(I) pair. In contrast, the previously synthesized complex $[Cu(L^1)(CH_3OH)]$ exhibits its redox couple, which was measured in CH_2Cl_2, at $E_{1/2}$ = –1585 mV and ΔE = 136 mV. The CV for $[Cu(L^1)(CH_3OH)]$ in CH_3CN was measured and the $E_{1/2}$ was slightly lower than it was in CH_2Cl_2, with $E_{1/2}$ = –1489 mV and ΔE = 93 mV. The potential needed to reduce the copper(II) ion is most negative for the bis(phenol)bis(imine), $[Cu(L^1)(CH_3OH)]$, followed by the hybrid bis(imine) $[Cu(HL^2)]_2(ClO_4)_4$, and finally the most positive for the bis(pyridyl)bis(imine) $[Cu(L^3)](ClO_4)_2$, all differing by about half of a volt. This trend can be explained by the electronic nature of the ligands. H_2L^1, being the most electron donating as the dianionic $(L^1)^{2-}$, stabilizes the copper ion in the higher oxidation state and disfavors reduction of the copper(II) ion. On the other extreme, the neutral L^3 ligand is the least electron donating ligand, which results in favorable acceptance of an electron by the metal ion to form a cuprous species and a less negative $E_{1/2}$.

Table 3.3. Electrochemical data for complexes presented in this work and literature complexes containing similar ligand sets.[a]

complex	solvent	$E_{1/2}$ (V)	ΔE (mV)	i_{pc}/i_{pa}	ref
$[Cu(L^1)(CH_3OH)]$	CH_2Cl_2	–1.585	136	0.99	[36]
$[Cu(L^1)(CH_3OH)]$	CH_3CN	–1.489	93	1.19	this work
McMillin $[Cu(N_2O_2)]$ complex	DMF	–1.300	325	—	[49]
$[Cu(HL^2)]_2(ClO_4)_4$	CH_3CN	–1.099	77	—	this work
McMillin $[Cu(N_3O)]$ complex	DMF	–0.932	280	—	[49]
$[Cu(L^3)](ClO_4)_2$	CH_3CN	–0.438	64	1.06	this work
Nakahara $[Cu(N_4)]$ complex	DMF	–0.550	—	—	[28]
McMillin $[Cu(N_4)]$ complex	CH_3CN	–0.526	150	—	[49]

[a] All potentials referenced to the Fc/Fc^+ redox couple. CVs for solutions of complexes presented in this work (1.0 mM) were recorded using a glassy carbon electrode with scan rates of 100 mV s^{-1}, and with 0.1 M $TBAPF_6$ supporting electrolyte.

The same trend with similar absolute redox potentials for the Cu(II)/(I) couple was observed on related Cu(II) complexes by McMillin and coworkers [49]. In their study, copper(II) complexes of the Schiff bases *N*,*N*'-bis(salicylidene)propane-1,3-propanediamine (N_2O_2 donor), *N*-(salicylidene)-*N*'-(2-pyridylaldene)-1,3-propanediamine (N_3O donor) and *N*,*N*'-bis(2-pyridylaldene)-1,3-propanediamine (N_4 donor) were prepared and the copper-centered redox couple determined through cyclic voltammetry. For comparison with our data (see Table 3.3) these potentials were corrected to the ferrocene/ferrocenium reference (Fc = 0.312 V vs. SSCE) [50].

The difference in potential between our N_2O_2-donor complex, $[Cu(L^1)(CH_3OH)]$, and the copper(II) complex with McMillin's ligand [49] is 285 mV. For the N_3O set, despite the fact that our complex has a ClO_4^- as the counterion while McMillin's complex has a NO_3^- counterion, the potentials are less than 100 mV different. Similarly, the redox potentials for the N_4 complexes are very similar. The N_4 copper(II) complex of *N*,*N*'-bis(2-pyridylaldene)-1,3-propanediamine was synthesized and characterized by Nakahara as well [28]. The redox potential for their complex was measured against SCE, and in order to compare to our complex it was corrected to be versus ferrocene/ferrocenium (Fc = 0.470 V vs. SCE in DMF, $[NBu_4][ClO_4]$) [51]. Nakahara and coworkers' reported electrochemistry matches nicely with McMillin's, even though it was measured in a different solvent. The relatively minor differences ranging from 100 to 285 mV between our complexes and ones in the literature may be due to the differences in substitution of the propanediamine backbone. In general, it is difficult to compare redox potentials directly due to errors in conversion to different references/electrodes and systems, but the overall trends are in good agreement.

3.8 Conclusion

In summary, two new copper(II) complexes, $[Cu(HL^2)]_2(ClO_4)_4$ and $[Cu(L^3)](ClO_4)_2$, were synthesized using novel tetradentate Schiff base ligands HL^2 and L^3, respectively. A strategy for the synthesis of the asymmetric ligand (HL^2) was successfully followed to produce high yields of HL^2 rather than the common symmetric analogues. The stepwise condensation reaction, using one equivalent of 2-pyridinecarboxaldehyde first, yielded in high purity of L^4, which can then be further

reacted with another equivalent of an aldehyde; here 2-hydroxybenzaldehyde was used to obtain HL^2. The stability of the less stable Schiff bases derived from 2-pyridinecarboxaldehyde (HL^2 and L^3) was studied and the conformation of the decomposition product, namely a hexahydropyrimidine, explored. $[Cu(HL^2)]_2(ClO_4)_4$ and $[Cu(L^3)](ClO_4)_2$ were compared with our previously synthesized copper(II) complex, $[Cu(L^1)(CH_3OH)]$, which contains related tetradentate Schiff base ligand H_2L^1. Structurally, all three copper complexes are very similar, with the ligand coordinating to the square pyramidal copper center in the equatorial square plane. The ligand in $[Cu(L^1)(CH_3OH)]$ (H_2L^1), which is deprotonated at the phenol group, coordinates through the two imine N atoms and two phenolate O atoms. $[Cu(HL^2)]_2(ClO_4)_4$ is coordinated by one pyridyl and two imine N atoms, and one phenolate O atom, also in the equatorial plane of the square pyramid. While the axial ligand in $[Cu(L^1)(CH_3OH)]$ is a coordinated methanol molecule, a bridging phenolate O atom sits in the axial position of $[Cu(HL^2)]_2(ClO_4)_4$, forming a dimer. $[Cu(L^3)](ClO_4)_2$ is coordinated by two pyridyl and two imine N atoms in the equatorial plane, having weakly coordinated perchlorate anions in the axial positions. The ligands in all three complexes do not coordinate through the pyridine nitrogen of the ligand backbone. The inability of the pyridyl group from the ligand backbone to coordinate is likely due to steric and geometric constraints of the rigid imine skeletons of the ligands. The electrochemical properties of all three copper complexes were probed by cyclic voltammetry, showing a correlation of the electronic properties of the ligands to the redox potentials of the cupric/cuprous ion couple. The more electron rich, dianionic $(L^1)^{2-}$ ligand in $[Cu(L^1)(CH_3OH)]$ with its N_2O_2 donor atom set highly favors the +2

oxidation state and has the most negative redox potential. The neutral L^3 ligand with its N_4 donor atom set has a redox potential that is more than a volt more positive, while the mixed ligand HL^2 with its N_3O donor atom set is midway between the other two. The electrochemical trends observed for the three copper complexes presented here conform with the electrochemical properties of copper(II) complexes with similar ligands [28, 49].

3.9 Experimental

3.9.1 General Procedures

Unless otherwise stated, all reagents were used as received from commercial sources. 2-methyl-2-(pyridine-2-yl)propane-1,3-diamine (ppda) was synthesized according to the published procedure [52]. H_2L^1 and $[Cu(L^1)(CH_3OH)]$ were synthesized according to the published procedures [36]. Solvents used were doubly purified using alumina columns in a MBraun solvent purification system (MB-SPS). Infrared spectra were measured from 4000 to 400 cm^{-1} as KBr pellets on a BIO-RAD FTS 155 FTIR spectrometer. ^1H NMR spectra were measured using a Varian 300 MHz instrument using solvent ($CHCl_3$) as an internal standard. Mass spectra were measured on a Q-TOF quadrupole time-of-flight mass spectrometer (Micromass, Manchester, U.K.) equipped with a Z-spray electrospray ionization (ESI) source. Elemental analyses were performed by Atlantic Microlab, Norcross, GA. UV-visible spectra were measured using a Shimadzu UV2401PC spectrophotometer in the range 250 to 900 nm on solutions ranging in concentration from 1.0×10^{-3} M to 1.0×10^{-4} M. Cyclic voltammetry experiments were performed using a BAS 50W potentiometer and a

standard three-electrode cell with a glassy-carbon working electrode, a Pt-wire auxiliary electrode, and an Ag/AgCl pseudo-reference electrode under an inert atmosphere at room temperature. X-band EPR spectra of the complexes were recorded at 77K using a Bruker EMX spectrometer. Solution magnetic susceptibilities were measured at 294K by the Evans method [53].

Caution! *Perchlorate salts of metal complexes with the organic ligands are potentially explosive. Although no difficulty was encountered during the syntheses described herein, they should be prepared in small amounts and handled with caution.*

3.9.2 Synthesis of HL^2

2-Pyridinecarboxaldehyde (0.127g, 1.15 mmol) was added dropwise to a solution of ppda (0.190 g, 1.15 mmol) in CH_3OH (5 mL). The resulting yellow solution was heated to reflux the solvent overnight, causing a color change to light orange. The solvent was removed in vacuo to give L^4 as an orange-brown oil (0.290 g). ^1H NMR (300 MHz, DMSO-d^6, 293K) δ 1.02–1.44 (m, 3H), 2.89–4.51 (m, 4H), 4.47–4.54 (m, 1H), 7.18–7.90 (m, 6H), 8.27-8.62 (m, 2H). Crude L^4 was redissolved in CH_3OH (5 mL) without further purification, and 2-hydroxybenzaldehyde (0.136 g, 1.11 mmol) was added. While refluxing overnight the solution turned light green. The solvent was removed in vacuo, yielding HL^2 as a highly viscous orange oil (0.400 g). The oil was kept under nitrogen and solidified after several months. According to NMR spectroscopy the composition of the ligand did not change upon solidification. ^1H NMR (300 MHz, $CDCl_3$, 293K) δ 1.54 (m, 3H), 3.95–4.30 (m, 4H), 6.78–6.93 (m, 2H), 7.05–

7.43 (m, 5H), 7.55–7.74 (m, 2H), 7.92–7.99 (m, 1H), 8.26–8.37 (m, 2H), 8.56–8.66 (m, 2H), 13.14–13.34 (m, 1H).). ESI-MS (CH_3OH): *m/z* = 359.2 $[HL^2 + H]^+$, 255.2 $[L^4 + H]^+$ (minor). Solutions of HL^2 decompose within hours, probably due to hydrolysis in the presence of moisture. Due to the highly viscous, sticky nature of the ligand, no elemental analysis was performed. Purification was achieved through complex formation with copper(II) ions.

3.9.3 Synthesis of L^3

2-Pyridinecarboxaldehyde (0.363g, 3.39 mmol) was added dropwise to a solution of ppda (0.280 g, 1.69 mmol) in CH_3OH (5 mL). The resulting yellow solution was heated to reflux the solvent overnight, causing a color change to light orange. The solvent was removed in vacuo to give the ligand as a highly viscous dark orange oil (0.575 g). ^1H NMR (300 MHz, $CDCl_3$, 293K) δ 1.55 (s, 3H), 4.12–4.24 (m, 4H), 7.05–7.11 (m, 1H), 7.24–7.30 (m, 2H), 7.37–7.42 (m, 1H), 7.55–7.62 (m, 1H), 7.64–7.72 (m, 2H), 7.92–7.98 (m, 2H), 8.32–8.37 (m, 2H), 8.57–8.63 (m, 3H). ESI-MS (CH_3OH): *m/z* = 344.2 $[L^3 + H]^+$. 255.2 $[L^4 + H]^+$. Solutions of L^3 decompose within hours, probably due to hydrolysis in the presence of moisture. Due to the highly viscous, sticky nature of the ligand, no elemental analysis was performed. Purification was achieved through complex formation with copper(II) ions.

3.9.4 Synthesis of $[Cu(HL^2)]_2(ClO_4)_4$

$Cu(ClO_4)_2 \cdot 6H_2O$ (0.220 g, 0.586 mmol) dissolved in methanol (1 mL) was added to a solution of ligand HL^2 (0.210 g, 0.586 mmol) in CH_3OH (10 mL). The

resulting dark green solution was stirred overnight at room temperature to yield an olive-green precipitate which was isolated by filtration, washed with methanol and diethylether (0.200 g, 53%). Anal. Calcd for $[Cu(HL^2)]_2(ClO_4)_4 \cdot 2H_2O$, powder, $C_{44}H_{48}Cl_4Cu_2N_8O_{20}$: C, 41.36; H, 3.79; N, 8.77. Found: C, 41.47; H, 3.51; N, 8.83. X-ray quality crystals were obtained from Et_2O diffusion into a solution of $[Cu(HL^2)]_2(ClO_4)_4$ in methanol/acetonitrile. Anal. Calcd for $[Cu(HL^2)]_2(ClO_4)_4$, crystals, $C_{44}H_{44}Cl_4Cu_2N_8O_{18}$: C, 42.56; H, 3.57; N, 9.02. Found: C, 42.08; H, 3.86; N, 9.41. UV/vis (CH_3CN) [λ_{max}, nm (ε, $M^{-1}cm^{-1}$)]: 243 (18,300), 272 (15,600), 369 (5,470), 573 (128). EPR (9.468 GHz, mod. amp. 25.0 G, CH_3CN, 77K): $g_{\|}$ = 2.19, $g_{\perp}$ = 2.06, and $A_{\|}$ = 205 G. EPR (9.466 GHz, mod. amp. 25.0 G, CH_3OH, 77K): $g_{\|}(1)$ = 2.22, $g_{\perp}(1)$ = 2.04, and $A_{\|}(1)$ = 190 G; $g_{\|}(2)$ = 2.31, $g_{\perp}(2)$ = 2.04, and $A_{\|}(2)$ = 200 G. FTIR (KBr): 2364, 2343, 1616, 1537, 1468, 1448, 1402, 1328, 1301, 1106, 1089, 1030, 964, 780, 768, 624, 533, 508, 417 cm^{-1}. ESI-MS (CH_3CN or CH_3OH): *m/z* = 420.1 $[Cu(L^2)]^+$, 941.1 $[(Cu(L^2))_2ClO_4]^+$. Solid state magnetic moment (MSB-Auto, 4.5 kG, 22.0 °C): 4.4 μ_B. Solution magnetic moment (Evans method, 20.9 °C, 16.3 x 10^{-3} M, acetonitrile-d_3): 1.76 μ_B.

3.9.5 Synthesis of $[Cu(L^3)](ClO_4)_2$

2-Pyridinecarboxaldehyde (0.027 g, 0.254 mmol) was added dropwise to a solution of hexahydropyrimidine (0.065 g, 0.254 mmol) in CH_3OH (5 mL) and the reaction mixture heated to reflux the solvent for 3 hours. After cooling to room temperature $Cu(ClO_4) \cdot 6H_2O$ (0.094 g, 0.254 mmol) in methanol (1 mL) was added. The resulting turquoise solution was stirred overnight at room temperature to yield a light

blue precipitate which was isolated by filtration, and washed with methanol, diethylether and pentane (0.120 g, 78 %). X-ray quality crystals were obtained from Et_2O diffusion into a solution of $[Cu(L^3)](ClO_4)_2$ in acetonitrile. Anal. Calcd for $C_{21}H_{21}Cl_2CuN_5O_8$: C, 41.63; H, 3.49; N, 11.56. Found: C, 41.89; H, 3.54; N, 11.64. UV/vis (CH_3CN) [λ_{max}, nm (ε, $M^{-1}cm^{-1}$)]: 281 (15,900), 661 (117). EPR (9.441 GHz, mod. amp. 25.0 G, CH_3CN, 77K): $g_{\|}$ = 2.19, $g_{\perp}$ = 2.07 and $A_{\|}$ = 185 G. FTIR (KBr): 2364, 2343, 1653, 1602, 1564, 1475, 1429, 1311, 1267, 1230, 1121, 1090, 1023, 981, 954, 787, 760, 671, 622, 502, 420 cm^{-1}. ESI-MS (CH_3CN): *m/z* = 505 $[Cu(L^3)ClO_4]^+$. Solid state magnetic moment (MSB-Auto, 4.5 kG, 22.0 °C): 3.5 μ_B. Solution magnetic moment (Evans method, 20.9 °C, 16.8 x 10^{-3} M, acetonitrile-d_3): 1.75 μ_B.

3.9.6 X-ray Crystal Structure Determination

Intensity data for $[Cu(HL^2)]_2(ClO_4)_4$ and $[Cu(L^3)](ClO_4)_2$ were collected using a diffractometer with a Bruker APEX ccd area detector [54, 55]. Data were collected using graphite-monochromated Mo Kα radiation (λ = 0.71073 Å). The samples were cooled to 100(2) K. Cell parameters were determined from a non-linear least squares fit of the data. The data were corrected for absorption by the semi-empirical method [56]. The structures were solved by direct methods and refined by full-matrix least-squares methods on F^2 [57, 58]. Hydrogen atom positions of hydrogens bonded to carbons were initially determined by geometry and refined by a riding model. Hydrogens bonded to nitrogens or oxygens were located on a difference map, and their positions were refined independently. Non-hydrogen atoms were refined with anisotropic displacement

parameters. Hydrogen atom displacement parameters were set to 1.2 (1.5 for methyl) times the displacement parameters of the bonded atoms.

Table 3.4. Crystallographic data for $[Cu(HL^2)]_2(ClO_4)_4$ and $[Cu(L^3)](ClO_4)_2$.

	$[Cu(HL^2)]_2(ClO_4)_4 \cdot 2CH_3OH$	$[Cu(L^3)](ClO_4)_2$
formula	$C_{46}H_{52}Cl_4Cu_2N_8O_{20}$	$C_{21}H_{21}Cl_2CuN_5O_8$
fw	1305.84	605.87
Crystal system	Monoclinic	Triclinic
Space group	*C*2/*c*	*P*–1
a (Å)	20.587(12)	9.183(4)
b (Å)	12.266(7)	10.365(4)
c (Å)	21.779(12)	12.064(5)
α (deg)	90	88.416(8)
β (deg)	110.162(16)	84.424(10)
γ (deg)	90	85.125(12)
V (Å^3)	5163(5)	1138.5(8)
Z	4	2
ρ_{calcd} mg/m^3	1.680	1.767
μ (mm^{-1})	1.119	0.71073
θ (deg)	1.97 to 28.52	1.70 to 28.42°
*R*1,[a] *wR*2[b] [$I > 2\sigma(I)$]	0.0456, 0.1118	0.0553, 0.1359
GOF on F^2	1.001	1.001

(a) $R1 = \Sigma||F_{obs}| - |F_{calc}|| / \Sigma|F_{obs}|$. (b) $wR^2 = \{\Sigma[w(F_{obs}^2 - F_{calc}^2)^2] / \Sigma[w(F_{obs}^2)^2]\}^{½}$.

3.10 References

1. Rubino, J. T.; Franz, K. J., *Coordination chemistry of copper proteins: How nature handles a toxic cargo for essential function.* Journal of Inorganic Biochemistry **2012,** *107*, 129-143.

2. Cotton, F. A., *Advanced Inorganic Chemistry A Comprehensive Text*. 1980, USA: John Wiley & Sons, Inc.

3. Alarco, J. A.; Talbot, P. C., *A phenomenological model for the structure–composition relationship of the high Tc cuprates based on simple chemical principles.* Physica C: Superconductivity **2012,** *476*, 32-47.

4. Solomon, E. I.; Hadt, R. G., *Recent advances in understanding blue copper proteins.* Coordination Chemistry Reviews **2011,** *255*, 774-789.

5. Gray, H. B.; Malmström, B. G.; Williams, R. J. P., *Copper coordination in blue proteins.* J. Biol. Inorg. Chem. **2000,** *5*, 551-559.

6. Nagasawa, Y.; Fujita, K.; Katayama, T.; Ishibashi, Y.; Miyasaka, H.; Takabe, T.; Nagao, S.; Hirota, S., *Coherent dynamics and ultrafast excited state relaxation of blue copper protein; plastocyanin.* Physical Chemistry Chemical Physics **2010,** *12*, 6067-6075.

7. Marshall, N. M.; Garner, D. K.; Wilson, T. D.; Gao, Y.-G.; Robinson, H.; Nilges, M. J.; Lu, Y., *Rationally tuning the reduction potential of a single cupredoxin beyond the natural range.* Nature **2009,** *462*, 113-116.

8. Rorabacher, D. B., *Electron Transfer by Copper Centers.* Chemical Reviews **2004,** *104*, 651-698.

9. Hirotsu, M.; Kuwamura, N.; Kinoshita, I.; Kojima, M.; Yoshikawa, Y.; Ueno, K., *Steric, geometrical and solvent effects on redox potentials in salen-type copper(ii) complexes.* Dalton Transactions **2009,** *0*, 7678-7683.

10. Doménech, A.; García-España, E.; Luis, S. V.; Marcelino, V.; Miravet, J. F., *Electrochemistry of copper complexes with polyaza[n]paracyclophanes. Influence of ATP as an exogen ligand on the relative stability of the Cu(II) and Cu(I) oxidation states.* Inorganica Chimica Acta **2000,** *299*, 238-246.

11. Nishikawa, M.; Nomoto, K.; Kume, S.; Nishihara, H., *Reversible Copper(II)/(I) Electrochemical Potential Switching Driven by Visible Light-Induced Coordinated Ring Rotation.* Journal of the American Chemical Society **2012,** *134*, 10543-10553.

12. Comba, P.; Kerscher, M., *Computation of structures and properties of transition metal compounds.* Coordination Chemistry Reviews **2009,** *253*, 564-574.

13. Jacobsen, E. N.; Zhang, W.; Guler, M. L., *Electronic tuning of asymmetric catalysts.* Journal of the American Chemical Society **1991,** *113*, 6703-6704.

14. Das, O.; Paine, T. K., *Aerobic oxidation of primary alcohols catalyzed by copper complexes of 1,10-phenanthroline-derived ligands.* Dalton Transactions **2012,** *41*, 11476-11481.

15. Bursten, B. E., *Ligand additivity: applications to the electrochemistry and photoelectron spectroscopy of d6 octahedral complexes.* Journal of the American Chemical Society **1982,** *104*, 1299-1304.

16. Fabbrizzi, L.; Lari, A.; Poggi, A.; Seghi, B., *.sigma. and .pi. Effects on the copper(II)/copper(I) redox couple potential in tetraazamacrocyclic complexes.* Inorganic Chemistry **1982,** *21*, 2083-2085.

17. Kuchynka, D. J.; Amatore, C.; Kochi, J. K., *Manganese(0) radicals and the reduction of cationic carbonyl complexes: selectivity in the ligand dissociation from 19-electron species.* Inorganic Chemistry **1986,** *25*, 4087-4097.

18. Murphy, D. M.; Caretti, I.; Carter, E.; Fallis, I. A.; Göbel, M. C.; Landon, J.; Doorslaer, S. V.; Willock, D. J., *Visualizing Diastereomeric Interactions of Chiral Amine–Chiral Copper Salen Adducts by EPR Spectroscopy and DFT.* Inorganic Chemistry **2011,** *50*, 6944-6955.

19. Orio, M.; Jarjayes, O.; Kanso, H.; Philouze, C.; Neese, F.; Thomas, F., *X-Ray Structures of Copper(II) and Nickel(II) Radical Salen Complexes: The Preference of Galactose Oxidase for Copper(II).* Angewandte Chemie International Edition **2010,** *49*, 4989-4992.

20. Clever, G. H.; Reitmeier, S. J.; Carell, T.; Schiemann, O., *Antiferromagnetic Coupling of Stacked CuII–Salen Complexes in DNA.* Angewandte Chemie International Edition **2010,** *49*, 4927-4929.

21. Storr, T.; Verma, P.; Pratt, R. C.; Wasinger, E. C.; Shimazaki, Y.; Stack, T. D. P., *Defining the Electronic and Geometric Structure of One-Electron Oxidized Copper−Bis-phenoxide Complexes.* Journal of the American Chemical Society **2008,** *130*, 15448-15459.

22. Glaser, T.; Heidemeier, M.; Strautmann, J. B. H.; Bögge, H.; Stammler, A.; Krickemeyer, E.; Huenerbein, R.; Grimme, S.; Bothe, E.; Bill, E., *Trinuclear Copper Complexes with Triplesalen Ligands: Geometric and Electronic Effects on Ferromagnetic Coupling via the Spin-Polarization Mechanism.* Chemistry – A European Journal **2007,** *13*, 9191-9206.

23. Taylor, M. K.; Reglinski, J.; Berlouis, L. E. A.; Kennedy, A. R., *The effect of donor groups and geometry on the redox potential of copper Schiff base complexes.* Inorganica Chimica Acta **2006,** *359*, 2455-2464.

24. Ray, M. S.; Bhattacharya, R.; Chaudhuri, S.; Righi, L.; Bocelli, G.; Mukhopadhyay, G.; Ghosh, A., *Synthesis, characterisation and X-ray crystal structure of copper(II) complexes with unsymmetrical tetradentate Schiff base ligands: first evidence of Cu(II) catalysed rearrangement of unsymmetrical to symmetrical complex.* Polyhedron **2003,** *22*, 617-624.

25. Kao, C.-H.; Wei, H.-H.; Liu, Y.-H.; Lee, G.-H.; Wang, Y.; Lee, C.-J., *Structural correlation of catecholase-like activities of oxy-bridged dinuclear copper(II) complexes.* Journal of Inorganic Biochemistry **2001,** *84*, 171-178.

26. Cozzi, P. G., *Metal-Salen Schiff base complexes in catalysis: practical aspects.* Chemical Society Reviews **2004,** *33*, 410-421.

27. Miyasaka, H.; Saitoh, A.; Abe, S., *Magnetic assemblies based on Mn(III) salen analogues.* Coordination Chemistry Reviews **2007,** *251*, 2622-2664.

28. Sakurai, T.; Kimura, M.; Nakahara, A., *A Facile Reduction of Copper(II) Leading to Formation of Stable Copper(I) Complexes. Redox Properties of Four- and Five-coordinate Copper Complexes.* Bulletin of the Chemical Society of Japan **1981,** *54*, 2976-2978.

29. Nathan, L. C.; Koehne, J. E.; Gilmore, J. M.; Hannibal, K. A.; Dewhirst, W. E.; Mai, T. D., *The X-ray structures of a series of copper(II) complexes with tetradentate Schiff base ligands derived from salicylaldehyde and polymethylenediamines of varying chain length.* Polyhedron **2003,** *22*, 887-894.

30. Chattopadhyay, S.; Drew, M. G. B.; Ghosh, A., *Synthesis, characterization, and anion selectivity of copper(II) complexes with a tetradentate Schiff base ligand.* Inorganica Chimica Acta **2006,** *359*, 4519-4525.

31. Sarkar, B.; Bocelli, G.; Cantoni, A.; Ghosh, A., *Copper(II) complexes of symmetrical and unsymmetrical tetradentate Schiff base ligands incorporating 1-benzoylacetone: Synthesis, crystal structures and electrochemical behavior.* Polyhedron **2008,** *27*, 693-700.

32. Renehan, M. F.; Schanz, H.-J.; McGarrigle, E. M.; Dalton, C. T.; Daly, A. M.; Gilheany, D. G., *Unsymmetrical chiral salen Schiff base ligands: Synthesis and use in metal-based asymmetric epoxidation reactions.* Journal of Molecular Catalysis A: Chemical **2005,** *231*, 205-220.

33. Jacobsen, E. N.; Zhang, W.; Muci, A. R.; Ecker, J. R.; Deng, L., *Highly enantioselective epoxidation catalysts derived from 1,2-diaminocyclohexane.* Journal of the American Chemical Society **1991,** *113*, 7063-7064.

34. Ito, Y. N.; Katsuki, T., *What is the origin of highly asymmetric induction by a chiral (salen)manganese(III) complex? Design of a conformationally fixed complex and its application to asymmetric epoxidation of 2, 2-dimethylchromenes.* Tetrahedron Letters **1998,** *39*, 4325-4328.

35. E. N. Jacobsen, M. H. W., *Comprehensive Asymmetric Catalysis, vol. II*. 1999, New York: Springer.

36. Shakya, R.; Jozwiuk, A.; Powell, D. R.; Houser, R. P., *Synthesis and Characterization of Polynuclear Copper(II) Complexes with Pyridylbis(phenol) Ligands.* Inorganic Chemistry **2009,** *48*, 4083-4088.

37. Atkins, R.; Brewer, G.; Kokot, E.; Mockler, G. M.; Sinn, E., *Copper(II) and nickel(II) complexes of unsymmetrical tetradentate Schiff base ligands.* Inorganic Chemistry **1985,** *24*, 127-134.

38. Kwiatkowski, E.; Kwiatkowski, M., *A novel unsymmetrical quadridentate ligand 1-(2'-aminophenyl)-6-methyl-2,5-diazanona-l,6-diene-8-one and its complexes with copper(II), nickel(II) and palladium(II).* Inorganica Chimica Acta **1986,** *117*, 145-149.

39. Luo, H.; Fanwick, P. E.; Green, M. A., *Synthesis and Structure of a Novel Cu(II) Complex with a Monoprotic Tetradentate Schiff Base Ligand.* Inorganic Chemistry **1998,** *37*, 1127-1130.

40. Luo, H.; Lo, J.-M.; Fanwick, P. E.; Stowell, J. G.; Green, M. A., *Monoprotic Tetradentate N3O-Donor Ligands and Their Cu(II) and Ni(II) Complexes.* Inorganic Chemistry **1999,** *38*, 2071-2078.

41. Biswas, A.; Drew, M. G. B.; Ghosh, A., *Nickel(II) and copper(II) complexes of unsymmetrical tetradentate reduced Schiff base ligands.* Polyhedron **2010,** *29*, 1029-1034.

42. Locke, J. M.; Griffith, R.; Bailey, T. D.; Crumbie, R. L., *Competition between cyclisation and bisimine formation in the reaction of 1,3-diaminopropanes with aromatic aldehydes.* Tetrahedron **2009,** *65*, 10685-10692.

43. Schmidt, M.; Wiedemann, D.; Grohmann, A., *First-row transition metal complexes of a novel pentadentate amine/imine ligand containing a hexahydropyrimidine core.* Inorganica Chimica Acta **2011,** *374*, 514-520.

44. Jozwiuk, A.; Ünal, E. A.; Leopold, S.; Boyd, J. P.; Haryono, M.; Kurowski, N.; Escobar, F. V.; Hildebrandt, P.; Lach, J.; Heinemann, F. W.; Wiedemann, D.; Irran, E.; Grohmann, A., *Copper Complexes of "Superpodal" Amine Ligands and Reactivity Studies towards Dioxygen.* European Journal of Inorganic Chemistry **2012,** *2012*, 3000-3013.

45. Jayaratna, N. B.; Norman, R. E., *2-Phenyl-2-(pyridin-2-yl)hexahydropyrimidine.* Acta Crystallographica Section E **2010,** *66*, o3149.

46. Shakya, R.; Wang, Z.; Powell, D. R.; Houser, R. P., *Tetradentate vs Pentadentate Coordination in Copper(II) Complexes of Pyridylbis(aminophenol) Ligands Depends on Nucleophilicity of Phenol Donors.* Inorganic Chemistry **2011,** *50*, 11581-11591.

47. Addison, A. W.; Rao, T. N.; Reedijk, J.; van Rijn, J.; Verschoor, G. C., *Synthesis, structure, and spectroscopic properties of copper(II) compounds containing nitrogen-sulphur donor ligands; the crystal and molecular structure of aqua[1,7-bis(N-methylbenzimidazol-2[prime or minute]-yl)-2,6-dithiaheptane]copper(II) perchlorate.* Journal of the Chemical Society, Dalton Transactions **1984,** *0*, 1349-1356.

48. Yang, L.; Powell, D. R.; Houser, R. P., *Structural variation in copper(i) complexes with pyridylmethylamide ligands: structural analysis with a new four-coordinate geometry index, [small tau]4.* Dalton Transactions **2007,** *0*, 955-964.

49. Elder, R. C.; Blubaugh, E. A.; Heineman, W. R.; Burke, P. J.; McMillin, D. R., *Thin-layer spectroelectrochemical studies of copper and nickel unsymmetrical Schiff base complexes.* Inorganic Chemistry **1983,** *22*, 2777-2779.

50. Nishihara, H., *Redox chemistry and functionalities of conjugated ferrocene systems*, in *Advances in Inorganic Chemistry*. 2002, Academic Press. p. 41-86.

51. Chang, D.; Malinski, T.; Ulman, A.; Kadish, K. M., *Electrochemistry of nickel(II) porphyrins and chlorins.* Inorganic Chemistry **1984,** *23*, 817-824.

52. Friedrich, S.; Schubart, M.; Gade, L. H.; Scowen, I. J.; Edwards, A. J.; McPartlin, M., *Titanium and Zirconium Complexes Containing a Novel Dianionic Trifunctional Amido Ligand.* Chemische Berichte **1997,** *130*, 1751-1759.

53. Evans, D. F., *400. The determination of the paramagnetic susceptibility of substances in solution by nuclear magnetic resonance.* Journal of the Chemical Society (Resumed) **1959,** *0*, 2003-2005.

54. Bruker-AXS, *SMART Software Reference Manual*, 1998: Madison, WI, USA.

55. Bruker-AXS, *SAINT Software Reference Manual*, 1998: Madison, WI, USA.

56. Sheldrick, G. M., *SADABS Program for Empirical Absorption Correction of Area Detector Data*, 2002: University of Göttingen, Germany.

57. Sheldrick, G. M., *SHELXTL Version 6.10 Reference Manual*, B.A. Inc., Editor 2000: Madison, Wisconsin, USA.

58. *International Tables of Crystallography, vol. C*, ed. Kluwer. 1995, Boston.

CHAPTER 4

Strained Copper(II) Complexes of [2.2]Paracyclophane-derived Schiff Base Ligands

4.1 Background

4.1.1 Blue Copper Proteins and Their Properties

Blue copper (BC) proteins, also called cupredoxins, are a class of electron transfer proteins which are found in a variety of biological systems, ranging from bacteria to humans [1]. These proteins are involved in photosynthesis (plastocyanin is responsible for electron transfer from cytochrome *f* to photosystem I) [2]; lignin synthesis (performed by laccase) [3]; respiration (rusticyanin acts as an electron shuttle between cytochromes) [4, 5]; and in reduction of nitrite in nitrite reductase (azurin) [6, 7]. In common for all BC proteins is a mononuclear copper site, where the copper ion cycles between the cupric and cuprous oxidation states. Ligation of the copper ion is accomplished through two histidines and one cysteine in the equatorial plane (see trigonal planar coordination geometry for laccase).

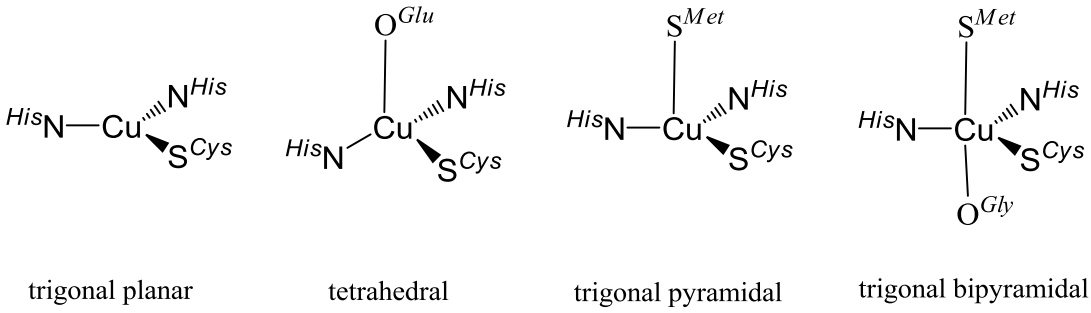

Figure 4.1. Geometries around the copper ion for different kinds of blue copper proteins: trigonal planar (laccase), tetrahedral (stellacyanin), trigonal pyramidal (rusticyanin, plastocyanin, pseudoazurin), trigonal bipyramidal (azurin).

A fourth ligand can be present (either methionine, as in plastocyanine, or glutamine as in stellacyanin, to yield strained four-coordinated geometries [8]). Azurins are trigonal bipyramidal in structure with methionine and glycine in the axial positions. A schematic depiction of the possible geometries of BC proteins is shown in Figure 4.1

and Table 4.1 shows a summary of BC protein geometries from crystal strcuctures and their redox potentials.

Table 4.1. Coordination and redoxpotential of Cu(II) in blue proteins. Table is adapted from reference [9].

Protein	Coordination	PDB code	E° (mV vs. NHE)
A. xylosoxidans azurin I (pH 8.0)[a,b]	5 [N_2S(OS)] trigonal bipyramidal (2.51 Å, 3.18 Å)	1RKR [57]	305 (pH 7.5)
A. xylosoxidans azurin II (pH 6.5)	5 [N_2S(OS)] trigonal bipyramidal (2.75 Å, 3.26 Å)	1ARN [58]	305 (pH 7.5)
P. aeruginosa azurin (pH 9.0)[a]	5 [N_2S(OS)] trigonal bipyramidal (2.93 Å, 3.13 Å)	5AZU [59]	293 (pH 8.0)
P. aeruginosa azurin (pH 5.5)[a]	5 [N_2S(OS)] trigonal bipyramidal (2.97 Å, 3.15 Å)	4AZU [59]	310
P. fluorescens azurin	5 [N_2S(OS)] trigonal bipyramidal (2.99 Å, 3.23 Å)	1JOI [60]	–
A. denitrificans azurin (pH 5.0)[a]	5 [N_2S(OS)] trigonal bipyramidal (3.13 Å, 3.11 Å)	2AZA [61]	285
P. putida azurin (pH~7)[a]	5 [N_2S(OS)] trigonal bipyramidal (3.14 Å, 3.01 Å)	1NWP [62]	295[c]
C. sativus stellacyanin	4 [N_2SO] distorted tetrahedral	1JER [63]	260
A. denitrificans (M121Q)azurin[a]	4 [N_2SO] distorted tetrahedral	1URI [64]	263
A. denitrificans (M121H)azurin (pH 3.5)[a,b,d]	4 [N_2SO] distorted tetrahedral	1A4C [65]	350
P. aeruginosa (M121E)azurin (pH 6.0)[a,b]	4 [N_2SO] distorted tetrahedral	1ETJ [66]	220 (pH 7.0)
cucumber basic protein	4 [(N_2S)(S)] trigonal pyramidal (2.60 Å)	2CBP [67]	317
A. xylosoxidans nitrite reductase	4 [(N_2S(S)] trigonal pyramidal (2.62 Å)	1BQ5 [68]	280 (pH 7.0)
A. xylosoxidans nitrite reductase[b]	4 [(N_2S(S)] trigonal pyramidal (2.63 Å)	1NDT [69]	260 (pH 7.0)
S. sp. PCC 6803 (A42D, D47P, A63L) plastocyanin[a,b]	4 [(N_2S(S)] trigonal pyramidal (2.64 Å)	1PCS [70]	325
M. extorquens pseudoazurin	4 [N_2S(S)] trigonal pyramidal (2.66 Å)	1PMY [71]	260 (pH 7.0)[e]
U. pertusa plastocyanin	4 [N_2S(S)] trigonal pyramidal (2.69 Å)	1IUZ [72]	363 (pH 7.0)
P. laminosum plastocyanin (pH 6.0)[a,b]	4 [N_2S(S)] trigonal pyramidal (~2.7 Å)	1BAW [73]	–
A. cycloclastes pseudoazurin	4 [N_2S(S)] trigonal pyramidal (2.70 Å)	1ZIA [74]	260 (pH 7.0)
A. faecalis pseudoazurin (pH 7)	4 [N_2S(S)] trigonal pyramidal (2.71 Å)	8PAZ [75]	269
P. aeruginosa (M121A)azurin (pH 5.1)[a,b]	4 [N_2S(O) trigonal pyramidal (2.74 Å)	2TSA [76]	373
S. pratensis plastocyanin[b]	4 [N_2S(S)] trigonal pyramidal (2.74 Å)	1BYO [77]	–
A. faecalis pseudoazurin (pH 6.8)	4 [N_2S(S)] trigonal pyramidal (2.76 Å)	1PAZ [78]	269
P. nigra plastocyanin (pH 6.0)	4 [N_2S(S)] trigonal pyramidal (2.82 Å)	1PLC [79]	370 (pH 7.5)
C. pepo medullosa ascorbate oxidase (pH 5.5)[a]	4 [N_2S(S)] trigonal pyramidal (2.86 Å)	1AOZ [80]	344
T. ferrooxidans rusticyanin (pH 4.6)	4 [N_2S(S) trigonal pyramidal (2.88 Å)	1RCY [81]	680
S. oleracea (G8D)plastocyanin (pH~4.4)	4 [N_2S(S)] trigonal pyramidal (2.88 Å)	1AG6 [82]	379
C. reinhardtii plastocyanin	4 [N_2S(S)] trigonal pyramidal (2.89 Å)	2PLT [83]	–
P. denitrificans amicyanin (pH 5–6)	4 [N_2S(S)] trigonal pyramidal (2.91 Å)	1AAC [84]	294
E. prolifera plastocyanin	4 [N_2S(S)] trigonal pyramidal (2.92 Å)	7PCY [85]	369 (pH 7.0)
D. crassirhizoma plastocyanin (pH 4.5)	4 [N_2S(S)] trigonal pyramidal (2.94 Å)	1KDJ [86]	387 (pH 7.0)
Human ceruloplasmin (Cu41, Cu61)[b]	4 [N_2S(S)] trigonal pyramidal (~3.0 Å)	1KCW [87]	490, 580
C. cinereus laccase (type-2 Cu depleted)[b]	3 [N_2S] trigonal planar	1A65 [88]	550
Human ceruloplasmin (Cu21)[b]	3 [N_2S] trigonal planar	1KCW [87]	>1000 [Cu(I)] site[f]

The first crystal structure of a BC protein, namely plastocyanin (PC), was presented by Freeman [2, 10]. A representation of the protein structure and the geometric structure of the active site of PC is shown in Figure 4.2. The copper ion is coordinated via a N_2S_2 donor manifold from two histidines, one cysteine and

methionine and results in distorted tetrahedral coordination geometry around the metal ion.

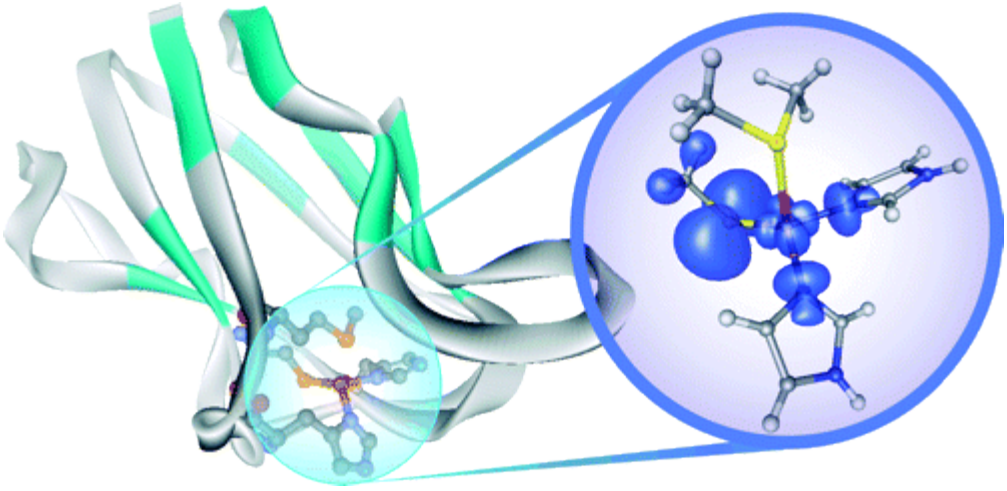

Figure 4.2. Crystal structure of plastocyanin and an expanded view of the geometric and electronic structure of the active site. Figure is adapted from reference [11].

In the following section the terms “rack state” and “entatic” will be introduced, which will help in understanding why blue copper proteins are extremely evolved electron mediators with fast electron transfer kinetics. Malmström introduced the concept of “rack-induced bonding” for the first time in 1964 [12]. The idea is that small ligands, when coordinating a metal ion, are fairly flexible and therefore will always arrange around the ion in a way that results in preferred geometry. In a protein, on the other hand, there are cooperative effects from a large number of weak interactions, which all together stabilize the tertiary structure of the protein resulting in little flexibilty and geometrical changes within the binding site for the metal ion. Vallee and Williams [13, 14] intoduced the term “entatic state” to the literature in 1952 and onwards. In the context of BC, entatic simply means that the copper ion is forced into an unusual geometric state. The strain forced upon the metal ion allows for unusual

properties like high reduction potentials, fast electron transfer and distinct EPR properties. These anomalous properties will be discussed in the following sections.

First normal copper complexes will be considered. As already discussed in Chapter 3, in synthetic copper complexes there is an energetically favorable geometry for Cu(II) being square planar and Cu(I) being mostly tetrahedral (see Figure 4.3). Strained geometries would decrease the stabilty for a particular oxidation state and as visualized below, an intermediate geometry between square planar and tetrahedral should allow for easier access of both oxidation states.

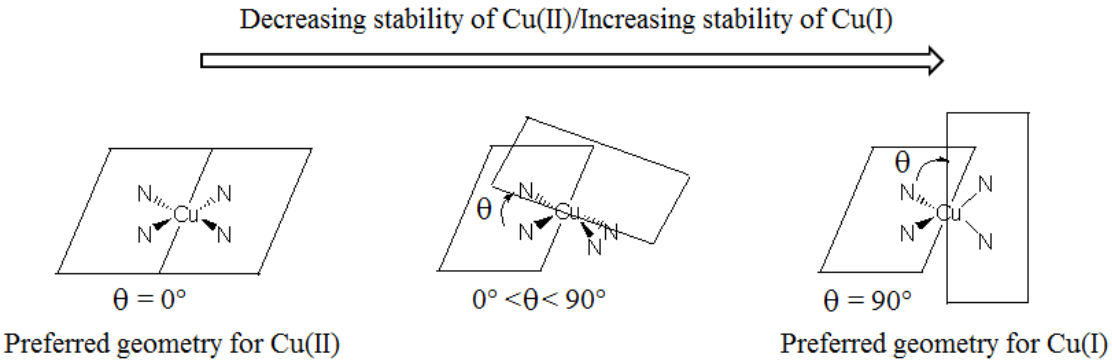

Figure 4.3. Schematic depiction of the favorable geometry for Cu(I) and Cu(II).

In BC proteins, here PC shown in Figure 4.4, the geometrical changes upon reduction or oxidation of the metal ion are minimal. This allows for minimal reorganization energies (see Marcus theory [15, 16]) upon redox change, and therefore causes higher (or more positive) reduction potentials within the protein compared to normal copper complexes.

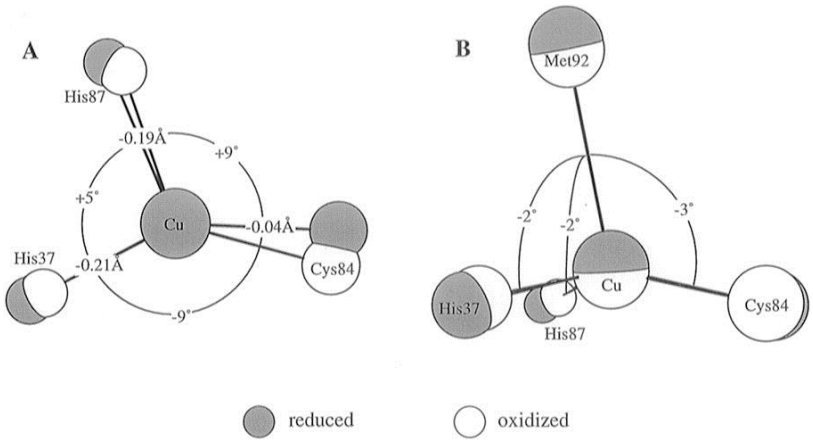

Figure 4.4. Geometrical changes of the active site in PC upon change in oxidation states. Figure is adapted from reference [17].

Rate constants for self-exchange are determined to be in the range of 10^4–10^6 M^{-1} s^{-1} for blue copper proteins, while for aquo Cu^+ and Cu^{2+} it was estimated to be only in the order of 10^{-5} M^{-1} s^{-1} [18]. This is again a measure of low reorganization energies in BC proteins, whereas with flexible ligands higher geometrical changes and greater energy barriers have to be overcome for change in redox state.

When first discovered, researchers were curious about the intense blue color of BC proteins in the oxidized state, which they are named after. The color is caused by a band at around 600 nm (or ~16 000 cm^{-1}) with an intensity of around 5000 M^{-1} cm^{-1} (see Figure 4.5 B). This band is assigned as a ligand to metal charge transfer from the cysteine-sulfur to the Cu(II) ion [19]. This is a very unique feature of BC proteins (and not seen in normal copper complexes; see Figure 4.5 B with comparison). In tetragonal Cu(II) complexes there are low intensity (up to 100 M^{-1} cm^{-1}) d-d transitions expected in this region.

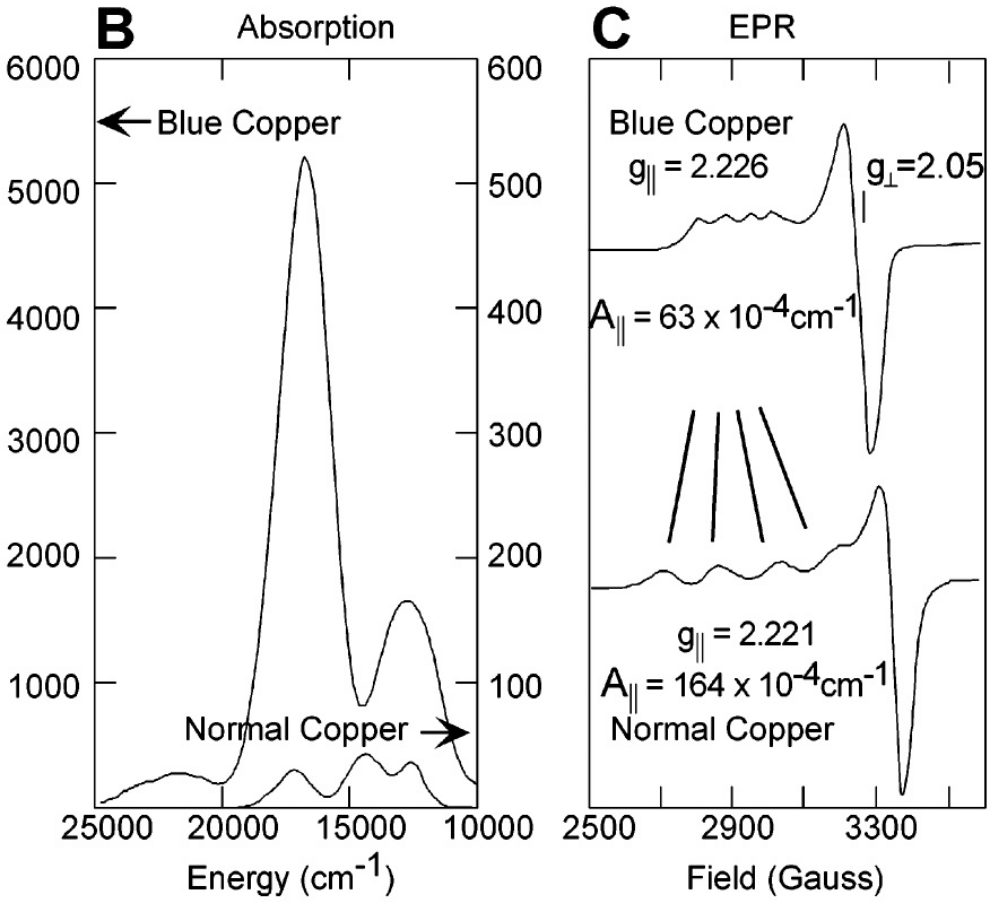

Figure 4.5. B) UV-Vis spectrum of normal and blue copper, C) EPR spectrum of plastocyanin (top) and D_{4h} $[CuCl_4]^{2-}$ (bottom). Figure is adapted from reference [11, 20].

EPR spectra are shown for normal and BC proteins in Figure 4.5 C. While normal copper sites exhibit large hyperfine coupling constants ($A_{\|}$ ~|164| × 10^{-4} cm^{-1}), BC proteins show distinct small values (|63| × 10^{-4} cm^{-1}) [20]. In 1960, the unusually small hyperfine coupling constants were believed to be caused by delocalization of the unpaired electron [21]. There are three components, namely Fermi contact (A_F, negative value), the spin dipolar term (A_S, negative value), and the orbital dipolar term (A_L, positive value), which all together contribute to the overall metal hyperfine coupling A. The Fermi contact is associated with unpaired electron spin density at the nucleus, e.g.

in a normal Cu(II) center it involves the $3d_{x^2-y^2}$ electron spin polarizing the 1s, 2s and 3s metal core electrons. The spin dipolar term expresses the interaction of the free electron averaged over the shape of the 3d-orbital with the nuclear spin of the metal ion. The orbital dipolar term involves the orbital angular momentum, which is derived from spin-orbit mixing; or simply said it is dependent on the coordination geometry and therefore the ligand field around the metal [22]. In BC proteins, the SOMO (singly occupied molecular orbital, or the orbital that is occupied by the unpaired electron) is delocalized over the thiolate sulfur atom, which reduces A_F and A_S, and therefore results in a small hyperfine constant. Normal copper complexes can have small a hyperfine coupling due to distortion because it results in a larger A_L [23].

4.1.2 Strained Coordination Compounds in Catalysis

Strain was shown to influence the properties of metal complexes in proteins, as discussed in section 4.1.1. In this section the focus will lie on synthetic coordination compounds and the effect of strain onto catalytic properties of the metal complex will be discussed. Comba has nicely reviewed the properties of blue copper proteins and brought them into relationship with synthetic catalysis. In general, rigid ligands can be used to cause strained geometries in a metal complex which will influence thermodynamic, kinetic and electronic properties [24]. To the best of my knowledge there are only a few examples [25-27] of strained metal complexes reported, where the distortion enhances catalysis and the most interesting ones will be introduced below.

The nacnac^{Bn}CuO*i*Pr complex was shown to be highly efficient in lactide polymerization due to strained coordination geometry [28]. The synthesis of the catalyst, compound 2, and steps in lactide polymerization are shown in Scheme 4.1.

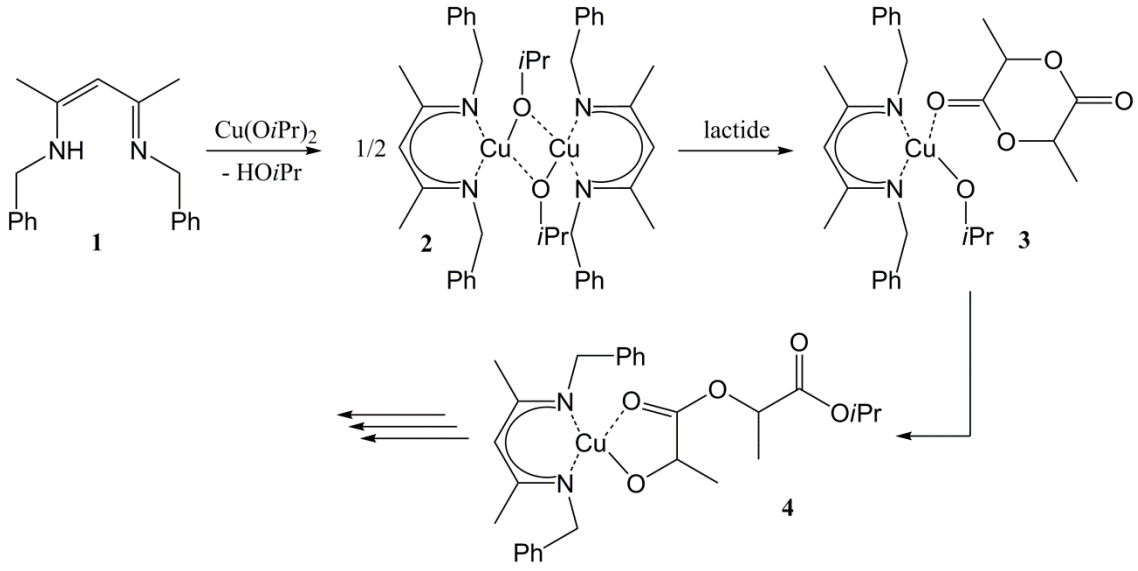

Scheme 4.1. Synthesis of (nacnac^{Bn}CuO*i*Pr)$_2$ and lactide polymerization. Figure is redrawn from reference [28].

Complex 2, (nacnac^{Bn}CuO*i*Pr)$_2$, was isolated and structurally characterized using X-ray diffraction, which revealed that the coordination geometry around the copper ion is distorted square planar. Once lactide is added to the dimer, polymerization starts without an induction period and a monomer is believed to be the active species (see species 3 in Scheme 4.1). Due to steric hindrance (geometrical distortion of the complex), the authors believe that intermediate 3 is destabilized and polymerization is initiated.

Another example recently introduced to the literature, shows activation of an enantioselective Friedel-Crafts alkylation with the use of a highly strained planar-chiral platinacycle [29].

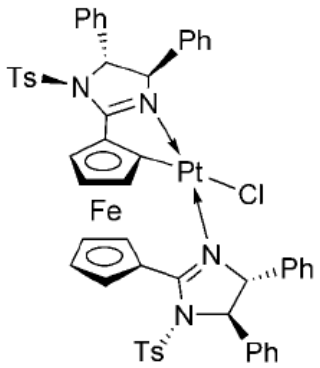

Figure 4.6. Highly strained platinum complex. Figure is adapted from reference [29].

A crystal structure of the platinum complex, schematically shown in Figure 4.6, verifies the distorted square planar geometry around the platinum ion. The authors hypothesize that olefin coordination is accelerated due to the highly strained Pt(II) ion which enhances reactivity. It was shown that this catalyst performs intramolecular enantioselective Friedel-Crafts alkylation of indoles.

4.2 Introduction

Salen-type ligands have been used widely as ligands in metal catalysis, mostly because they are fairly simple to synthesize and easily variable in structure and electronics by the use of different building blocks (amine or aldehyde). A broad background on the synthesis of Schiff base type ligands and complexes is presented in Chapter 3. Here, the focus will be on a special class of amines that can be used as an asymmetric Schiff base precursor. Previous work done in the group of Dr. Glatzhofer showed that the mono- or diamino substituted [2.2]paracyclophane (see Figure 4.7) can be used as the amine building block for Schiff base ligands and that the resulting copper(II) complexes have good activity in catalysis.

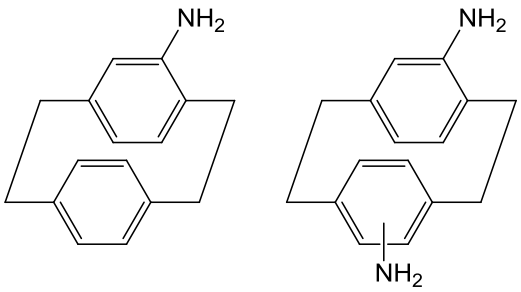

Figure 4.7. Structures of mono- and diamino[2.2]paracyclophane.

Masterson reported that copper(II) complexes of Schiff base ligands derived from amino-[2.2]paracyclophane can be used in asymmetric cyclopropanation reactions [30-32]. In his earlier work it was shown that ligands A and B, see Figure 4.8, can perform enantioselective cyclopropanation on stilbene and styrene derived substrates [30, 31]. Ligand B was observed to be more enantioselective and even more efficient than the ligand introduced by Nozaki [33]. In a recent publication Masterson et al. have presented work with ligand C and it was shown that 95% ee can be achieved in enantioselective cyclopropanations.

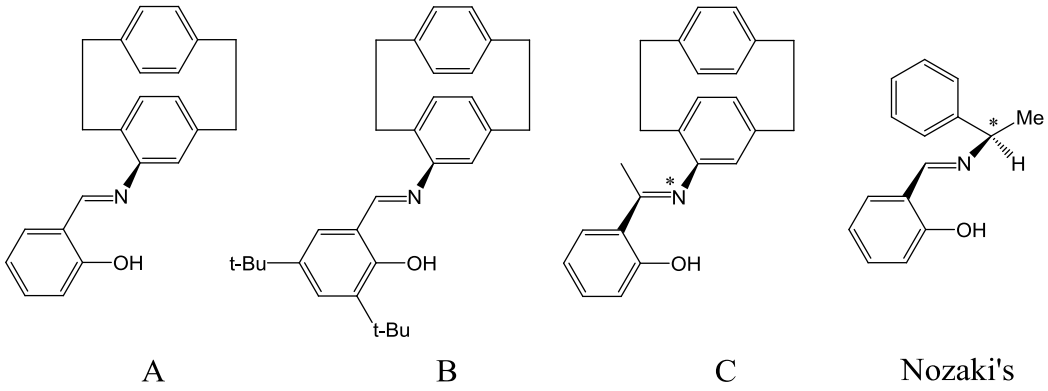

Figure 4.8. Ligands by Masterson used for cyclopropanation reactions with comparison to Nozaki's ligand.

Morvant has shown that *pseudo-ortho*-4,16-diamino[2.2]paracyclophane (see structure in Figure 4.10) in the presence of copper(II) ions can also be used for cyclopropanation reactions [34]. He reported the synthesis of the copper(II) complex and performed initial experiments on catalytic cyclopropanation. Little activity was observed using *trans*-4,4'-dimethylstilbene as the substrate. The copper(II) complex lacked in spectroscopic analysis and structural characterization. One of the goals of this work was to fully characterize the known complex and draw conclusions on the complexes reactivity in the cyclopropanation reaction. It was also desirable to synthesize *pseudo-gem*-4,15-diamino[2.2]paracyclophane and to study the Cu(II) complex structurally and spectroscopically in order to compare it to the ortho-substituted version. An oxidation reaction, namely the allylic oxidation of cyclohexene (see Figure 4.9, and last section below) was chosen to compare the difference in reactivity and product distribution using the two copper complexes. Additionally, the question should be answered of whether it was possible to generate and isolate complexes with other divalent metal ions and characterize those.

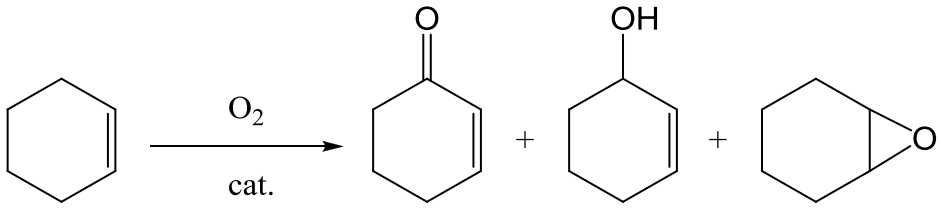

Figure 4.9. Allylic oxidation of cyclohexene to the most common oxidation products (2-cyclohexen-1-one, 2-cyclohexen-1-ol, cyclohexane oxide).

In the following section, more information on the allylic oxidation will be given. There are many different variations of allylic oxidation known to organic chemists. Andrus *et al.* have recently published a review paper to give an overview of the most

common varieties [35]. In the Kharasch-Sosnovsky reaction, either Cu(I) or Cu(II) ions in the presence of peracids are used to generate allylic esters [36]. Another example is the formation of allylic alcohols using SeO_2 and tert-butyl hydroperoxide by Sharpless and coworkers [37] or the use of mercury [38] or palladium actetate [39] to obtain allylic acetates.

The allylic oxidation of alkenes with the use of only molecular oxygen as the oxidant is an attractive reaction as there is no other oxidant like hydrogen peroxide or a peracid needed. This is considered “green chemistry”. Recently, copper(II) Schiff base complexes have been used to catalyze the allylic oxidation of cyclohexene to give mainly products shown in Figure 4.9 [40-42]. As this type of reaction is proposed to go through a radical mechanism, the formation of other side products is possible. Chemoselectivity for product formation is of great importance and enones and allylic alcohols are the most desired products. The copper ion cyles between the cupric and cuprous oxidation state during the catalytic cycle [41].

In this study, it should be further explored whether geometrical strain in the Cu(II) Schiff base complex would allow for better selectivity and higher reactivity than the salen-type, square planar, Cu(II) complexes and initial studies should be performed. The idea is that geometrical strain causes a shift in redox potential which may help cycling between Cu(II) and Cu(I) or that strain would help in opening a coordination site (by dissociating one of the ligand donor atoms) for faster substrate coordination.

4.3 Syntheses and Characterization of Ligands

Ligands $H_2L^{5\text{-ortho}}$ and $H_2L^{5\text{-gem}}$ (see structures below, Figure 4.10) were obtained in high purity (see NMR spectra in Appendix, Figure A.1 and A.2) upon Schiff base condensation of two equivalents of 2-hydroxybenzaldehyde with the corresponding diamine *pseudo-ortho*-4,16-diamino[2.2]paracyclophane or *pseudo-gem*-4,15-diamino[2.2]paracyclophane, respectively. $H_2L^{5-ortho}$ was previously introduced to the literature by Morvant [34].

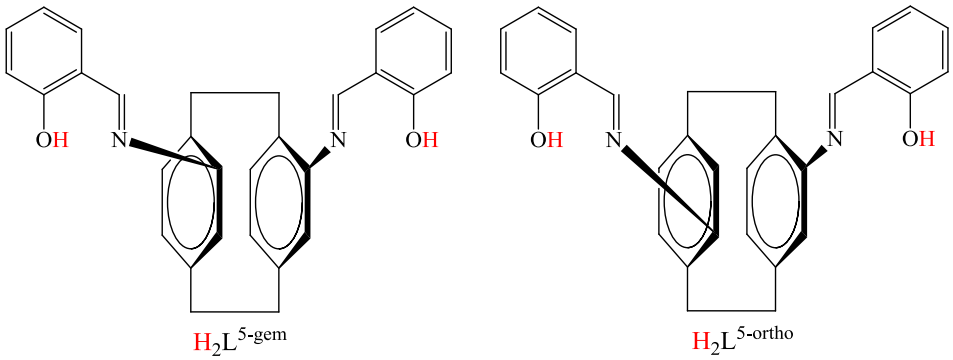

$H_2L^{5\text{-gem}}$ $H_2L^{5\text{-ortho}}$

Figure 4.10. Structures of novel $H_2L^{5\text{-gem}}$ and the previously synthesized ligand $H_2L^{5\text{-ortho}}$ [34].

In a typical reaction, exact stoichiometric amounts of reactants were suspended in ethanol and refluxed for two hours. All starting materials dissolve within a few minutes of heating and the product begins to precipitate in the heat after about ten minutes. Bright yellow to orange-yellow powders are obtained after filtration. No further purification is required, except the removal of residual solvent under reduced pressure. $H_2L^{5\text{-gem}}$ and $H_2L^{5\text{-ortho}}$ were characterized via ^{1}H NMR, IR and UV-Vis spectroscopy. The proton NMR of both ligands is very clean and integration, as well as type of signals, match (see Appendix, Figure A.1 and A.2). Both ligands show a strong peak at 1614 cm^{-1} in the IR, which is assigned to the C=N stretch and a peak at 1283

cm^{-1} and 1281 cm^{-1} corresponding to the phenolate C–O stretch for $H_2L^{5\text{-gem}}$ and for $H_2L^{5\text{-ortho}}$, respectively. These assignments are consistent with previously described stretches of similar Schiff bases [43]. Upon coordination of a metal ion by the ligand these two stretching frequencies are expected to shift, which will be used later as a quick and cheap method to confirm complexation reactions.

The electronic absorption spectra of the two Schiff bases are shown as an overlay with their corresponding copper(II) complexes in Figure 4.17. For the ligands, the two dominating bands in the UV (at around 230 nm and 270 nm) are assigned to π to π* transitions from the aromatic ring and correspond to the E_2 and B band, respectively [44]. Each band represents the sum of the absorption of the [2.2]paracyclophane ring and the benzene ring from the 2-hydroxy aryl group. The band in the visible region at about 350 nm corresponds to the π to π* transitions from the C=N functional group (azomethine). This band shifts to higher wavelength upon coordination to a metal ion [45].

Both ligands have a N_2O_2 donor set and have two easily deprotonable phenols. The acidic protons are highlited in red (Figure 4.10) and upon metal coordination the ligand is potentially dianionic.

4.4 Synthesis of Transition Metal Complexes with $H_2L^{5\text{-ortho}}$ and $H_2L^{5\text{-gem}}$

Copper (II) complexes of the ligands $H_2L^{5\text{-ortho}}$ and $H_2L^{5\text{-gem}}$ were synthesized upon addition of exact stoichiometric amounts of anhydrous cupric chloride salts to a suspension of ligand and NEt_3 as a base in methanol. To aid complex formation, the reaction mixtures were refluxed over night, which yielded clear brown solutions. To

purify the complexes, recrystallization was conducted. Therefore, methanol was removed under reduced pressure and the residue redissolved in toluene. Crystals suitable for X-ray structural analysis of both complexes were obtained upon pentane diffusion into the toluene solution. Schematic depictions of the copper complexes are shown in Figure 4.11. Both complexes, [$CuL^{5\text{-ortho}}$] and [$CuL^{5\text{-gem}}$], are neutral and the copper ion is coordinated through all atoms from the N_2O_2-donor manifold. The solid structure of the complexes will be described in Section 4.4.2.

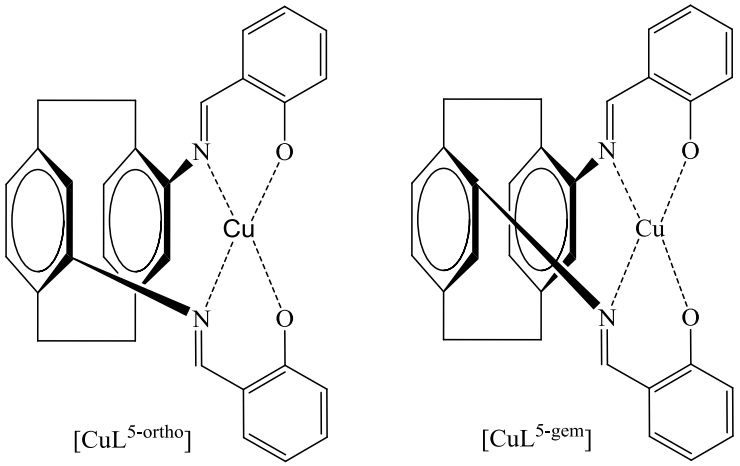

Figure 4.11. Structures of copper complexes with $H_2L^{5\text{-ortho}}$ and $H_2L^{5\text{-gem}}$.

The monomeric structure for the two copper complexes is further supported by ESI-MS studies, although a small peak for a dimer, $[CuL^{5\text{-ortho}}]_2 + H^+$ and $[CuL^{5\text{-gem}}]_2 + H^+$ is found. Elemental analysis of both complexes confirms high purity and all data was collected on crystalline samples. EPR and CV data are presented in Section 4.4.3 and 4.4.4, respectively.

Attempts to isolate other metal complexes with these two ligands were not very succesful. Reactions of hydrous perchlorate salts of Co(II), Ni(II), Zn(II), Fe(III) with and without the presence of NEt_3 as a base in MeOH and CH_2Cl_2 did not allow for

complexation; even the use of anhydrous chloride salts of Fe(II), Zn(II), Ni(II), Co(II) and $Mn(OTf)_2$ under anhydrous conditions in MeOH and CH_2Cl_2 mixtures in presence of NaOMe as a base did not allow for isolation of the respective metal complexes. The only crystals obtained upon diffusion or slow evaporation of reaction solutions were yellow in color. IR measurements of the latter confirmed the nature of those crystals to be pure ligand. Also, reaction solutions were reduced in volume and resulting precipitates were analyzed by IR. In all cases the evident stretches, C=N and C-O (phenolate), did not shift and therefore suggest that no coordination occurred. The ligands most likely impose too much strain and an unfavourable geometry upon coordination which explains the difficulties in metal complex formation. It is not surprising though, that copper complexes were formed readily because of copper's ability to adopt strained geometries. This concept was explained earlier in the background and relates back to geometries found in blue copper proteins.

However, one cobalt(II) complex was obtained upon reaction of $H_2L^{5\text{-gem}}$ and cobalt(II) perchlorate in the presence of NEt_3 as a base in a mixture of CH_2Cl_2 and MeOH. The resulting brown-red solution produces pink-purple needle-like crystals upon slow evaporation. The structure was identified to be dimeric in the solid state and a schematic depition is shown in Figure 4.12.

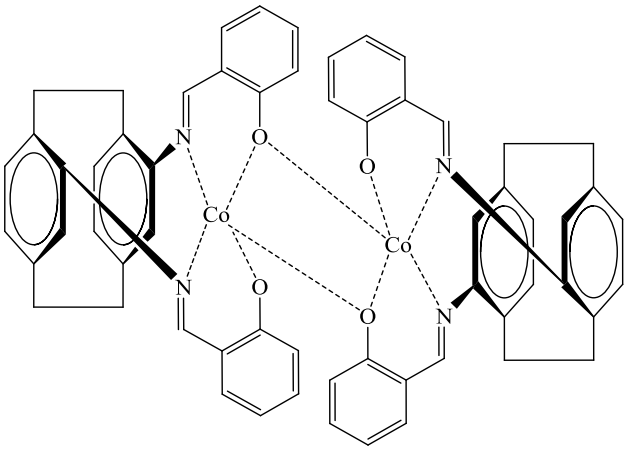

Figure 4.12. Structure of the Co(II) complex with $H_2L^{5\text{-gem}}$.

As evidenced by MS-ESI, the cobalt(II) complex could be dimeric and monomeric in solution. A highly intense peak is found for the dimer, and a signal that is about 1/10 of the dimer peak corresponds to the monomer. According to NMR, the complex is paramagnetic but no EPR signal was detected at 77 K or at room temperature. It has been shown in the literature that high spin Co(II) complexes have fast spin relaxation times and therefore EPR spectra need to be acquired at very low temperature, below 10 K [46]. The performance of such an experiment is rather inconvenient as liquid helium needs to be used for cooling of the sample. Spectroscopic and CV data will be discussed in Section 4.4.3. and 4.4.4, respectively.

4.5 X-ray Crystal Structures

According to the X-ray crystal structure of [$CuL^{5\text{-gem}}$] (Figure 4.13), the complex is chiral upon coordination to copper ions and both enantiomers are found within the unit cell. One of the enantiomers shows hydrogen bonding (O1S–H1S···O1B = 1.83(6) Å) to a trapped methanol molecule (see Figure 4.13 and Table 4.2, 4.3 and 4.6 for

parameters). Figure 4.14 is generated to align the enantiomeric pair as mirror images and help visualize the chirality of the complex. Each copper(II) ion is fourfold coordinated through the N_2O_2 donor atom set and the coordination geometry is in between square planar and tetrahedral. The τ_4 [47] parameters are 0.39 and 0.44 for the two enantiomers which classifies the complex as distorted square planar. The metal to donor atom bonds and angles for the two complexes are similar. However, the hydrogen bonding of one enantiomer to the methanol solvent most likely causes slight differences between the two enantiomers. O1B shows a shorter Cu–O bond distance than the equivalent Cu–O (with O34A) bond in the other complex (1.915 Å versus 1.905 Å, respectively). This is not surprising because O1B will have less electron density that can be donated to the copper ion. This most likely causes other bond lengths to be different and results in slightly different donor–Cu–donor angles.

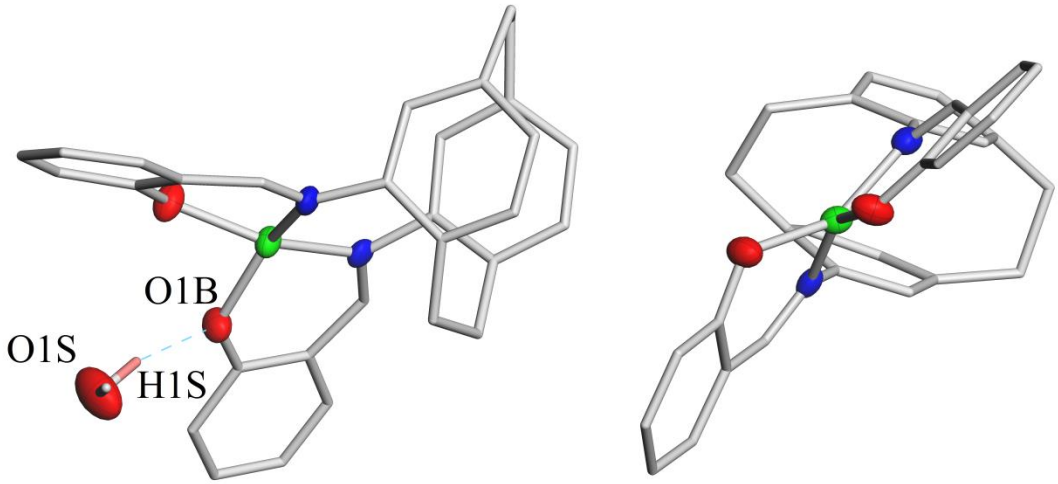

Figure 4.13. Crystal structure of the enantiomeric pair of [$CuL^{5\text{-gem}}$]. Methanol is hydrogen bonded to one of the structures.

Table 4.2. Hydrogen bonds and angles for [CuL$^{5\text{-gem}}$] in Å and °.

D–H···A	d(D–H)	d(H···A)	d(D···A)	<(DHA)
O1S–H1S···O1B	0.95(6)	1.83(6)	2.764(5)	165(5)

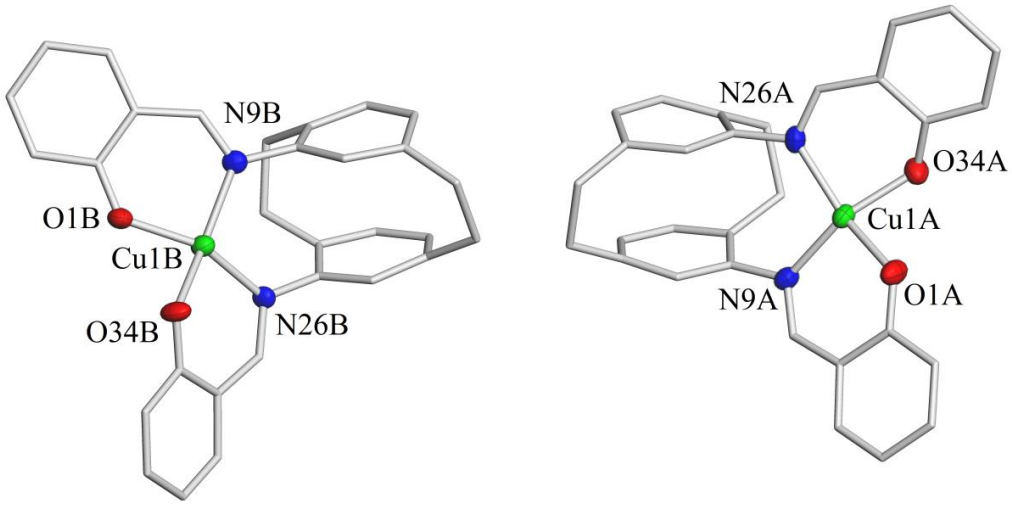

Figure 4.14. Enantiomeric pair of [CuL$^{5\text{-gem}}$] aligned as mirror images. Methanol solvent molecule was removed for clarity.

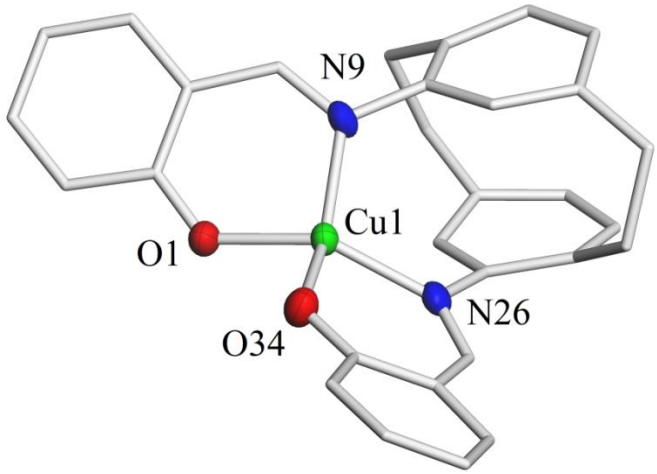

Figure 4.15. Crystal structure of [CuL$^{5\text{-ortho}}$].

The crystal structure of [$CuL^{5\text{-ortho}}$] reveals a similar distorted coordination environment around the copper ion (see structure in Figure 4.15 and Table 4.6 for parameters). Only one enantiomer is found in the unit cell. The τ_4 [47] parameter is 0.50 which indicates even more distortion than found in [$CuL^{5\text{-gem}}$]. This value is exactly in between tetrahedral and square planar geometry. Copper to donor atom distances, as well as bond angles of [$CuL^{5\text{-ortho}}$], are more comparable to the [$CuL^{5\text{-gem}}$] complex that has no solvent interaction. Selected bond lengths and angles for both complexes are listed in Table 4.3.

Table 4.3. Selected bond lengths (Å) and angles (deg) for [$CuL^{5\text{-gem}}$] and [$CuL^{5\text{-ortho}}$].

Complex [$CuL^{5\text{-gem}}$]			
Cu1A-O1A	1.896(3)	Cu1B-O34B	1.897(3)
Cu1A-O34A	1.905(3)	Cu1B-O1B	1.915(3)
Cu1A-N9A	1.976(4)	Cu1B-N9B	1.976(4)
Cu1A-N26A	2.016(4)	Cu1B-N26B	1.986(4)
O1A-Cu1A-O34A	83.27(14)	O34B-Cu1B-O1B	85.87(13)
O1A-Cu1A-N9A	93.49(14)	O34B-Cu1B-N9B	151.35(14)
O34A-Cu1A-N9A	152.76(14)	O1B-Cu1B-N9B	92.58(14)
O1A-Cu1A-N26A	152.39(14)	O34B-Cu1B-N26B	92.44(14)
O34A-Cu1A-N26A	90.44(14)	O1B-Cu1B-N26B	146.42(15)
N9A-Cu1A-N26A	103.80(15)	N9B-Cu1B-N26B	104.05(15)
Complex [$CuL^{5\text{-ortho}}$]			
Cu1-O34	1.8942(18)	Cu1-N26	1.991(2)
Cu1-O1	1.9097(17)	Cu1-N9	1.996(2)
O34-Cu1-O1	90.17(7)	O34-Cu1-N9	145.41(8)
O34-Cu1-N26	93.07(8)	O1-Cu1-N9	93.15(8)
O1-Cu1-N26	143.69(8)	N26-Cu1-N9	104.04(8)

[$CoL^{5\text{-gem}}$] crystallizes as a dimer (see Figure 4.16). The N_2O_2 set from the ligand is coordinating one cobalt ion and one of the phenolate arms is also bridging in μ-fashion between two metal centers resulting in a diamond core structure ([$(CoL)_2$(μ-O(Phenolate))$_2$]). The cobalt ions are penta-coordinated in trigonal pyramidal fashion with τ_5 [48] parameters of 0.74 and 0.79 for Co2 and Co1, respectively. There are small

differences between the bond length and distances of the two metal sites. If respective bond length were identical, there would be an inversion center in the molecule allowing conversion of the one site into the other. For Co1 N9A, O34A and O1B define the basal plane around the cobalt ion while O1A and N26A are in apical positions. Co2 shows O1A, O34A and N9B in equatorial positions and N26B and O1B in axial positions. Selected bond lengths and angles are listed in Table 4.4.

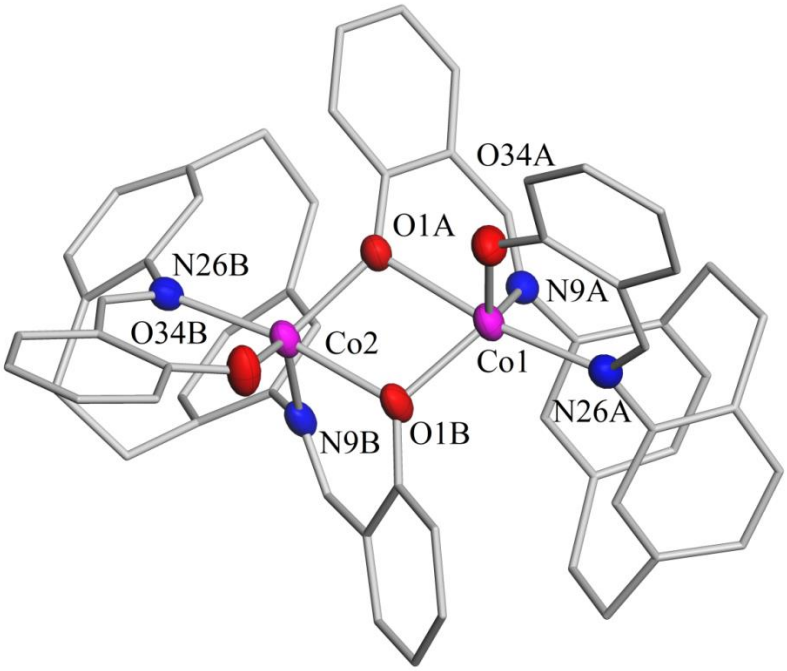

Figure 4.16. Crystal structure of $[CoL^{5\text{-gem}}]_2$.

Table 4.4. Selected bond lengths (Å) and angles (deg) for [$CoL^{5\text{-gem}}$].

Co1-O34A	1.954(3)	Co2-O34B	1.954(3)
Co1-O1B	1.966(2)	Co2-O1A	2.000(2)
Co1-N26A	2.086(3)	Co2-N9B	2.089(3)
Co1-N9A	2.089(3)	Co2-N26B	2.096(3)
Co1-O1A	2.188(3)	Co2-O1B	2.152(3)
O34A-Co1-O1B	110.65(12)	O34B-Co2-O1A	116.69(11)
O34A-Co1-N26A	92.25(12)	O34B-Co2-N9B	126.23(12)
O1B-Co1-N26A	113.79(11)	O1A-Co2-N9B	108.14(11)
O34A-Co1-N9A	124.17(12)	O34B-Co2-N26B	90.39(12)
O1B-Co1-N9A	115.75(11)	O1A-Co2-N26B	114.43(11)
N26A-Co1-N9A	95.93(12)	N9B-Co2-N26B	97.05(12)
O34A-Co1-O1A	83.58(11)	O34B-Co2-O1B	83.33(11)
O1B-Co1-O1A	74.42(10)	O1A-Co2-O1B	74.56(10)
N26A-Co1-O1A	171.74(10)	N9B-Co2-O1B	81.40(11)
N9A-Co1-O1A	80.67(11)	N26B-Co2-O1B	170.78(10)

4.6 Spectroscopic Characterization of the Metal Complexes

High resolution electrospray mass spectrometry suggests that MeCN solutions of the two copper complexes are mostly monomeric with some amounts of dimeric species. The peak at *m/z* = 508.1210 corresponds to the $[Cu(L^{5\text{-ortho}})] + H^+$ and 508.1219 to the $[Cu(L^{5\text{-gem}})] + H^+$ species. A peak with lower intensity at *m/z* = 1015.2342 represents $[Cu(L^{5\text{-ortho}})]_2 + H^+$ and *m/z* = 1015.2343 represents $[Cu(L^{5\text{-gem}})]_2 + H^+$. The formation of the dimeric species in solution is somewhat surprising since the solid state

does not show dimeric structures. This could have been a result of the ionization method within the mass spectrometer. Solution magnetic moment measurements by the Evans method [49] in chloroform yielded in a magnetic moment of 1.53 μ_B/Cu for [Cu($L^{5\text{-ortho}}$)] and 1.63 μ_B/Cu for [Cu($L^{5\text{-gem}}$)]. These values are slightly lower but close to the spin-only value of 1.73 μ_B/Cu. Since the complexes were measured in chloroform, it is possible that a small amount of solvent evaporated during sample preparation and thus resulted in an increase in concentration. This automatically gives too low values because the concentration of a paramagnetic species is inversely proportional to its effective magnetic moment μ_B [50].

CH_2Cl_2 solutions of the cobalt(II) complex were studied by high resolution electrospray ionization mass spectrometry and indicate monomeric and dimeric species in solution. The peak at *m/z* = 504.1244 corresponds to [Co($L^{5\text{-gem}}$)] + H^+, and another peak at *m/z* = 1007.2400 with tenfold intensity of the former one represents [Co($L^{5\text{-gem}}$)]$_2$ + H^+. From MS it is not conclusive of whether the cobalt(II) complex is a dimer or a monomer in solution because processes within the mass spectrometer can cause association or dissociation. The electrochemical behavior of the cobalt complex in solution is discussed in Section 4.4.4.

Utilizing IR-spectroscopy, for all three metal complexes typical shifts for the C=N stretch as well as C–O stretch from phenolate are seen compared to the free ligand [43, 51]. As expected for salen-type ligands, characteristic stretching frequencies for $H_2L^{5\text{-ortho}}$ and $H_2L^{5\text{-gem}}$ are 1614 cm^{-1} (C=N) and 1281-1283 cm^{-1} (C–O). Upon coordination to the metal ion the C=N stretch shifts towards lower wavenumbers (1609 cm^{-1} for [Cu($L^{5\text{-ortho}}$)], 1607 cm^{-1} for [Cu($L^{5\text{-gem}}$)] and 1605 cm^{-1} for [Co($L^{5\text{-gem}}$)]). The

disappearance of the medium intensity peak at 1281-1283 cm^{-1} is observed for all three complexes. This stretch shifts towards higher wavenumbers [51] but it is not possible to exactly assign which peak corresponds to the metal complex based C–O stretch because multiple peaks are found in this area.

The electronic absorption spectra of the two Schiff bases as well as the resulting copper(II) complexes are shown as an overlay in Figure 4.17. For the ligands the two dominating bands in the UV (200 to 300 nm) are assigned to π to π* transitions from the aromatic rings. The band in the visible region represents the π to π* transitions from the C=N functional group, as discussed in 4.3.

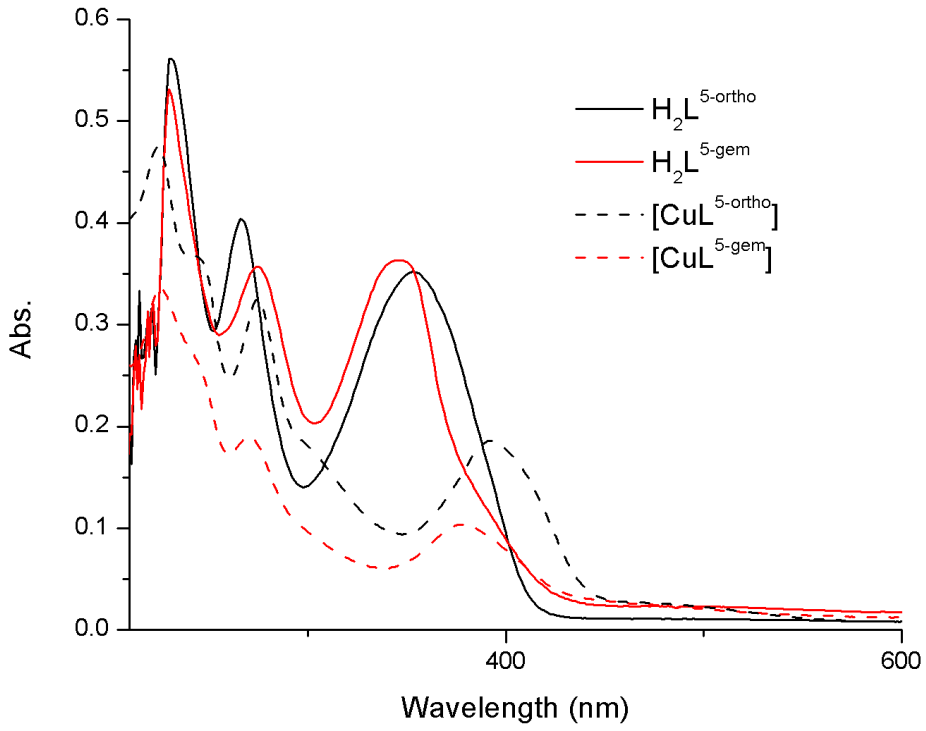

Figure 4.17. UV-Vis of $H_2L^{5\text{-ortho}}$ and $H_2L^{5\text{-gem}}$ (solid black line and solid red line, respectively), conc. = 1.3 x 10^{-5} M in CH_2Cl_2; $[CuL^{5\text{-ortho}}]$ and $[CuL^{5\text{-gem}}]$ (dashed black line and dashed red line, respectively), conc. = 1.0 x 10^{-5} M and 0.6 x 10^{-5} M, respectively in MeCN.

The two copper complexes show a shift of all bands found for the ligands as well as additional peaks. The shoulder peak in the UV at around 240 nm is probably due to the metal to ligand charge transfer (MLCT) and a very weak and broad feature just below 500 nm could be assigned as the d–d transition within the metal ion. However, tetrahedrally distorted complexes show d–d transitions in the near-IR [52] and it is possible that [$CuL^{5\text{-ortho}}$] and [$CuL^{5\text{-gem}}$] show absorption in that region as well (no band was detected up to 1100 nm).

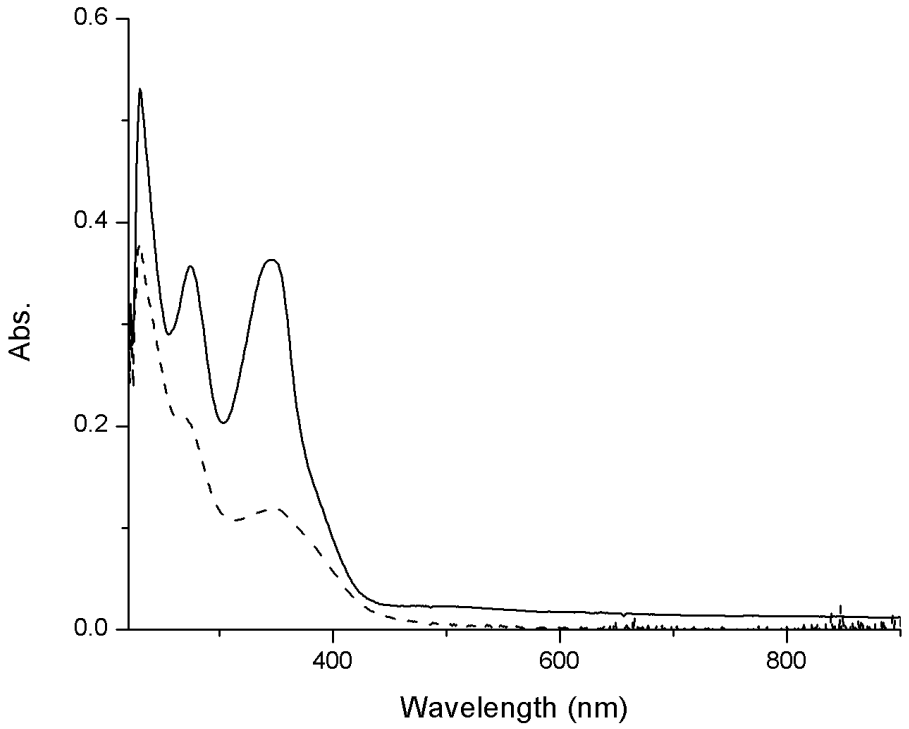

Figure 4.18. UV-Vis spectrum of $L^{5\text{-gem}}$ (solid line) and [$CoL^{5\text{-gem}}$] (dashed line) in CH_2Cl_2. Concentrations are 1.3 x 10^{-5} M and 0.7 x 10^{-5} M for the ligand and the cobalt complex, respectively.

In Figure 4.18 the electronic absorption spectrum of [$CoL^{5\text{-gem}}$] is shown as an overlay with the corresponding ligand. When comparing the UV-Vis bands, there is not much of a shift between the free ligand and the cobalt(II) complex, except broadening

of the band at around 350 nm. These bands are most likely arising from the ligand transitions as assigned for the copper complexes. The broad band at 350 nm for [$CoL^{5\text{-gem}}$] could be due to an overlap of the ligand band and a CT transition from the complex. There are no other bands in the UV-Vis spectrum, which can be assigned to d–d transitions of the cobalt(II) ion. Again, as in the Cu(II) complexes, a d–d transition is possible to be present in the near-IR [52]. Maybe the cobalt complex dissociates in solution which would cause a strained geometry for the monomer.

EPR spectra of the two copper complexes were taken from toluene solutions at room temperature as well as frozen solutions at 77 K. The EPR spectra taken at room temperature (see Figure 4.19) show a typical isotropic signal for both complexes with g_{iso} = 2.13, A_{iso} = 60 x 10^{-4} cm^{-1} (60 G) for [$CuL^{5\text{-ortho}}$] and g_{iso} = 2.12, and A_{iso} = 74 x 10^{-4} cm^{-1} (75 G) for [$CuL^{5\text{-gem}}$]. The splitting of the signal into four peaks is due to the hyperfine interaction of the unpaired electron with the copper nucleus. The isotropic signal is due free tumbling motion at room temperature, where enough energy is available to shorten and elongate metal-ligand bonds and thus the spectrum represents random distribution of a variety of different bond lengths [53, 54]. Since the motion of the atoms is faster than the EPR time scale all species are observed as the average. In the following the EPR spectrum of frozen glasses of the complexes will be discussed. Typically, at low temperature there is only limited energy available. Therefore the switching of bond lengths is limited and the EPR spectrum should show anisotropy due to preferred elongation of particular bonds [53].

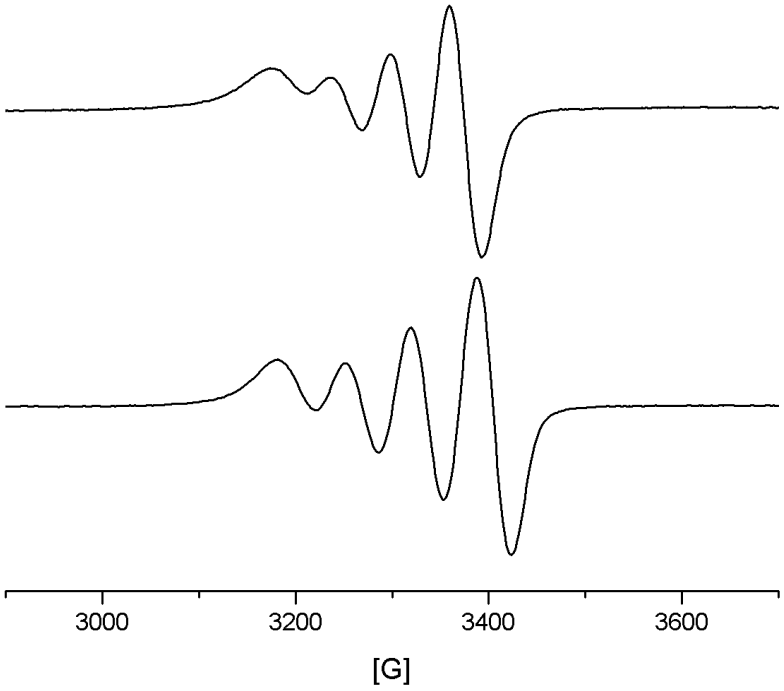

Figure 4.19. EPR spectra of [$CuL^{5\text{-ortho}}$] (top spectrum) and [$CuL^{5\text{-gem}}$] (bottom spectrum) solutions at room temperature in toluene.

Figure 4.20 depicts the EPR spectra taken at 77 K. Again both spectra for the two different copper complexes look similar. This time a typical axial signal with $g_{\|}$ = 2.25, $g_{\perp}$ = 2.05, and $A_{\|}$ = 163 x 10^{-4} cm^{-1} (155 G) for [$CuL^{5\text{-ortho}}$] and $g_{\|}$ = 2.26, $g_{\perp}$ = 2.04, and $A_{\|}$ = 169 x 10^{-4} cm^{-1} (160 G) for [$CuL^{5\text{-gem}}$] is observed, which suggests tetragonal elongation due to Jahn-Teller distortion and a d_{x2-y2} ground state.

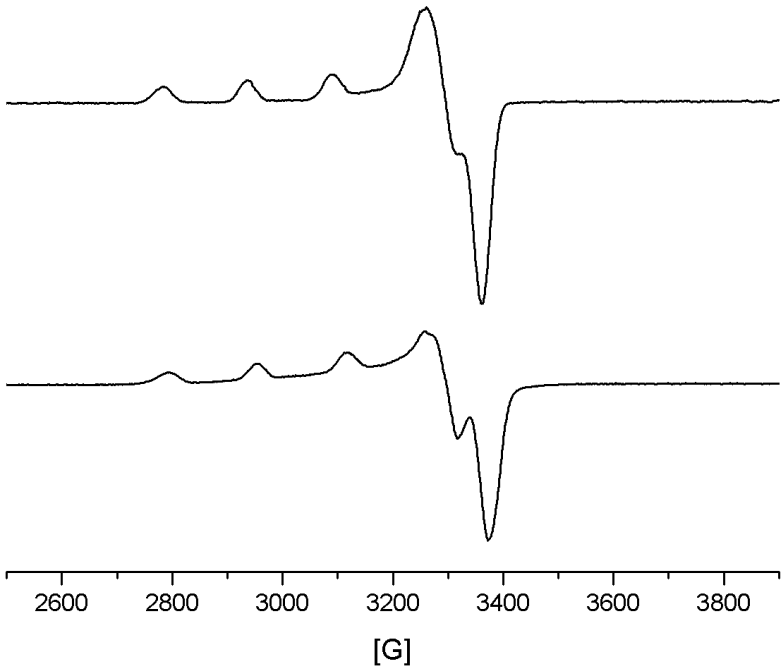

Figure 4.20. EPR spectra of [$CuL^{5\text{-ortho}}$] (top spectrum) and [$CuL^{5\text{-gem}}$] (bottom spectrum) on frozen glasses from toluene solutions at 77 K.

According to EPR studies at room temperature as well as at 77 K, both copper complexes show significant distortion when compared to similar square planar complexes. Typically a g_{iso} of around 2.10, $g_{\|}$ of 2.21–2.23 and an A_{iso} of around 85 G, $A_{\|}$ of 180 to 200 G is found for square planar salen-type complexes [55]. [Cu(salen)] in particular has low g_{iso} values (2.10), $g_{\|}$ values (2.19) and high A_{iso} values (90 x 10^{-4} cm^{-1}), $A_{\|}$ values (200 x 10^{-4} cm^{-1}) at room and at low temperature, respectively [56]. It has been shown that lattice force can cause "artificial" strain onto the complex which is reduced or insignificant in the solution state [57]. A recent example that strain (here particularly axial compression) can be an artifact of crystal packing has been published by the Houser group [58]. Our EPR measurements indicate that the strain in our complexes is not caused by such packing forces.

From the crystal structures of the two copper(II) complexes it can be seen that [$CuL^{5\text{-ortho}}$] is a little bit more strained towards tetrahedral geometry than [$CuL^{5\text{-gem}}$]. This trend is still reflected in the EPR data. [$CuL^{5\text{-ortho}}$] exhibits smaller $A_{\|}$ and A_{iso}, meaning that [$CuL^{5\text{-ortho}}$] has more distortion towards the tetrahedral geometry.

Electrochemical data of both complexes shows that [$CuL^{5\text{-ortho}}$] features a more reversible Cu(II)/Cu(I) redox couple than [$CuL^{5\text{-gem}}$], allowing for more reversible electron transfer. (Electrochemical behavior of all metal complexes will be discussed in detail in 4.4.4). It has been shown that there is a correlation between the electrochemical reversibility of the Cu(II)/Cu(I) redox couple and *A* (lower *A* values lead to more reversible redox couples) [54].

4.7 Electrochemical Studies

The redox behavior of copper(II) and cobalt(II) complexes was studied by cyclic voltammetry in acetonitrile and an overlay of the CVs of [$CuL^{5\text{-gem}}$] and [$CuL^{5\text{-ortho}}$], with ferrocene as the internal standard, is given in Figure 4.21. There is only one redox feature for both copper(II) complexes observed, which is assigned to the Cu(II)/Cu(I) redox couple. The potential for this couple in [$CuL^{5\text{-gem}}$] and [$CuL^{5\text{-ortho}}$] is nearly the same with a value of about –1150 mV vs. Fc (see Table 4.5 for electrochemical data). At a scan rate of 100 mV/s the redox couple for [$CuL^{5\text{-ortho}}$] appears reversible with ΔE = 66 mV and a peak current ratio of I_{pa}/I_{pc} = 0.93. On the other hand, the Cu(II)/Cu(I) redox couple of [$CuL^{5\text{-gem}}$] is quasi-reversible with ΔE = 77 mV and I_{pa}/I_{pc} = 0.79. Plots of CVs for both copper(II) complexes at different scan rates are shown in Figures 4.22 and 4.23.

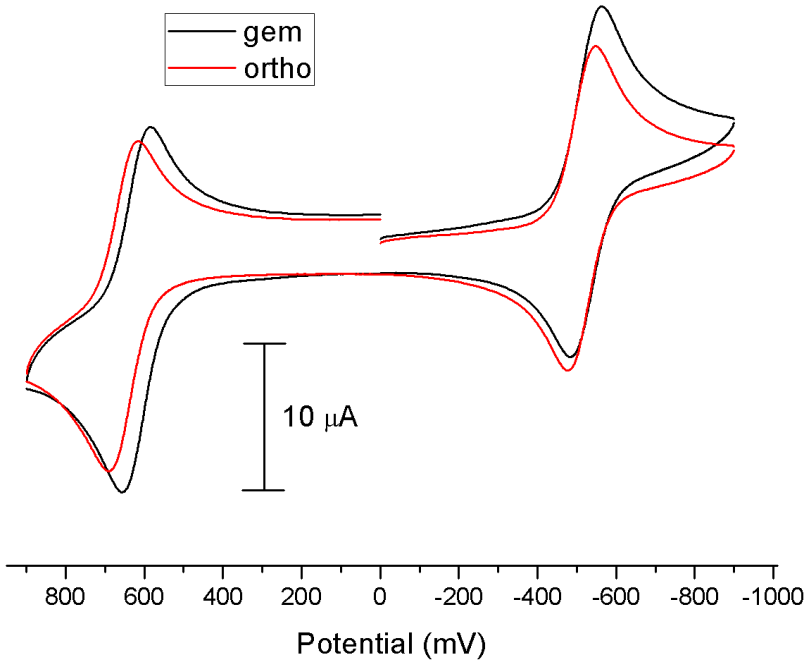

Figure 4.21. CV of 1.0 mM solution of [CuL$^{5\text{-gem}}$] and [CuL$^{5\text{-ortho}}$] in MeCN at 100 mV/s; 0.1 M TBAH as supporting electrolyte, GC as working electrode, Pt counter electrode and Ag as pseudo reference electrode. Ferrocene is added as an internal standard producing the redox couple at around +600 mV.

Table 4.5. Electrochemical data for [CuL$^{5\text{-ortho}}$] and [CuL$^{5\text{-gem}}$].

Complex	$E_{1/2}$ vs. Fc (mV)	ΔE (mV)	I_{pa}/I_{pc}
[**CuL$^{5\text{-ortho}}$**]	–1169	66	0.93
[**CuL$^{5\text{-gem}}$**]	–1147	77	0.79

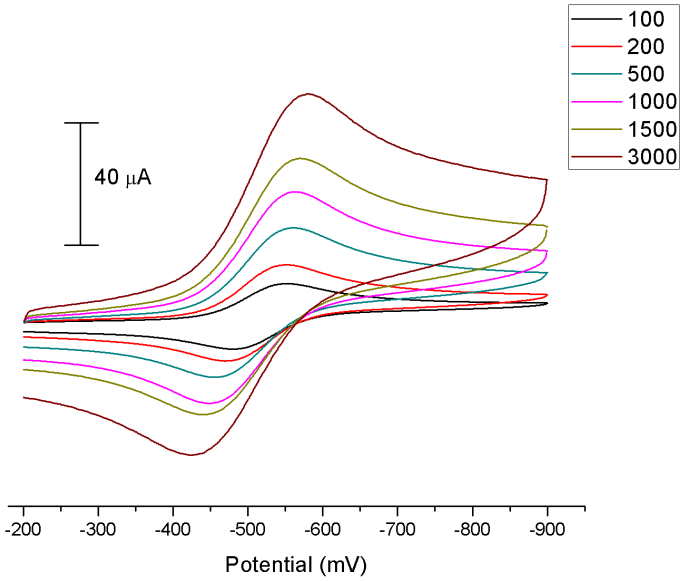

Figure 4.22. Plot of different scan rates of 1.0 mM solution of [$CuL^{5\text{-gem}}$] in MeCN; 0.1 M TBAH as supporting electrolyte, GC as working electrode, Pt counter electrode and Ag as pseudo reference electrode.

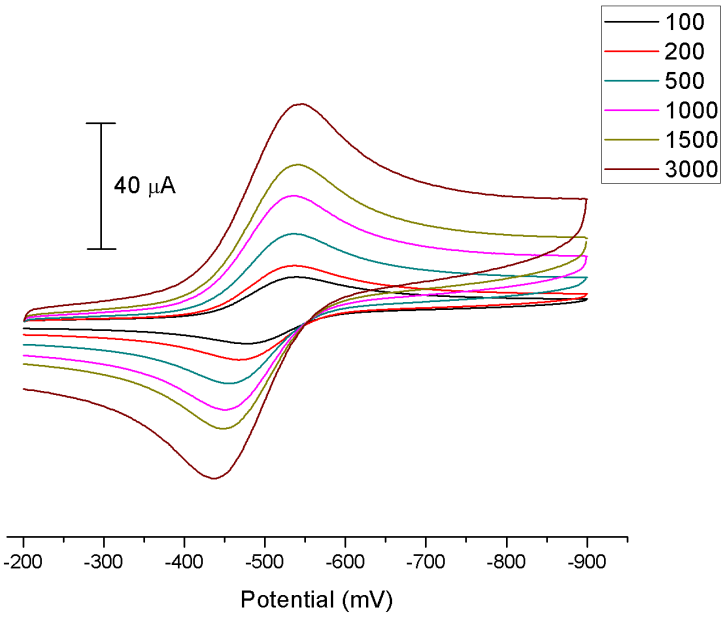

Figure 4.23. Plot of different scan rates of 1.0 mM solution of [$CuL^{5\text{-ortho}}$] in MeCN; 0.1 M TBAH as supporting electrolyte, GC as working electrode, Pt counter electrode and Ag as pseudo reference electrode.

When the redox potential of Cu(II)/Cu(I) for [$CuL^{5\text{-gem}}$] and [$CuL^{5\text{-ortho}}$] is compared to similar Schiff base complexes with N_2O_2 donors, the complexes reported herein allow for about 300–600 mV easier reduction of the copper(II) ion [55, 59]. This dramatic shift of the redox potentials is most likely due to the strained geometry in the new complexes compared to the almost square planar complexes described in the literature.

The CV for [$CoL^{5\text{-gem}}$] is shown in Figure 4.24. The full scan from –1500 to +1500 mV reveals that there are no reductive features of the complex but instead oxidation processes are observed. There is one quasi-reversible feature at around +800 mV, which is further studied and shown in Figure 4.25.

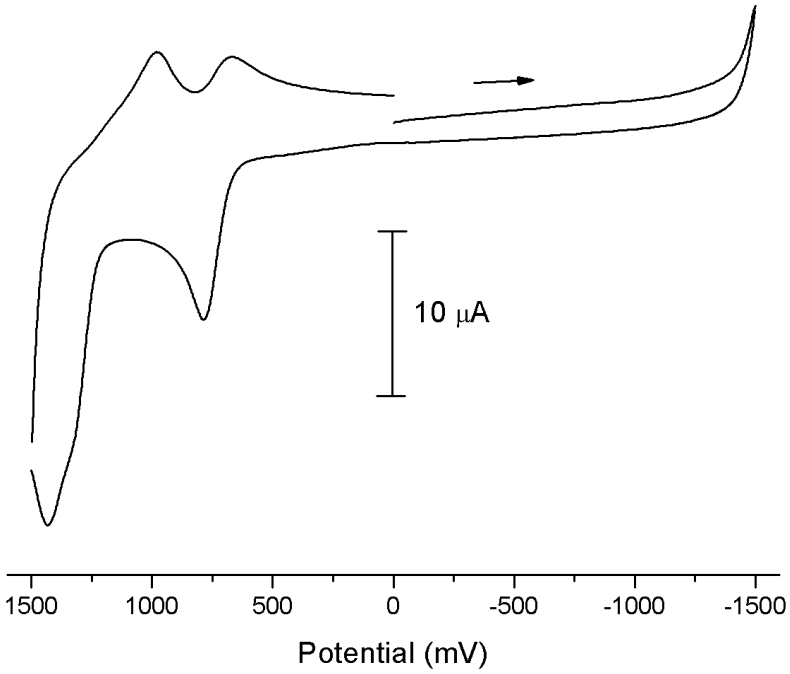

Figure 4.24. CV of 1.0 mM solution of [$CoL^{5\text{-gem}}$] in CH_2Cl_2 at 100 mV/s; 0.1 M TBAH as supporting electrolyte, GC as working electrode, Pt counter electrode and Ag as pseudo reference electrode.

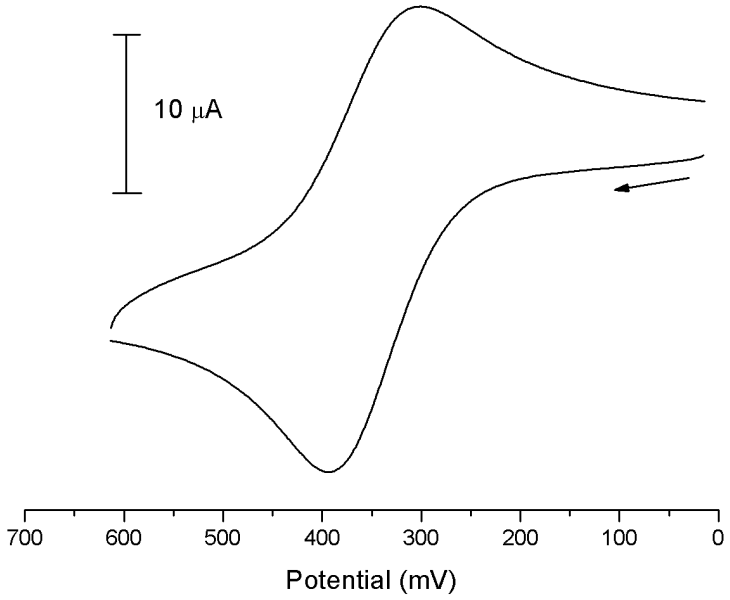

Figure 4.25. Scan of the redox couple shown at +800 mV against the redox potential of Me_2Fc (under same conditions as in Figure 4.24).

The quasi-reversible oxidation is assigned to oxidation of Co(II) to Co(III) with $E_{1/2}$ vs. Me_2Fc = 351 mV, ΔE = 82 mV, I_{pc}/I_{pa} = 0.65. The electrochemical properties of the planar [Co(salen)] have been studied in DMF and DMSO (with NBu_4ClO_4 as the supporting electrolyte) and the half potential for the Co(II)/Co(III) couple was assigned to be 0.09 V [60] and 0.03 V [61] vs. Ag/AgCl, respectively. Depending on the solvent and electrolyte, the potential of Me_2Fc vs. Ag/AgCl is about 0.5 V [62]. With this conversion, [$CoL^{5\text{-gem}}$] is more than half a Volt harder to oxidize than the salen-based complex. Nishinaga et al. reported the CV of [Co(salen)] in DMF (NBu_4PF_6 as the supporting electrolyte) and the potential for the Co(II)/Co(III) couple was determined to be –466 mV vs. Fc, which also confirms that [$CoL^{5\text{-gem}}$] is about 0.5 V harder to oxidize as [$CoL^{5\text{-gem}}$] overlaps with the redox couple of ferrocene. The same group has conducted CV studies on substituted [Co(salen)] complexes (with –Cl, $–NO_2$, –*t*Bu, –Me and –OMe substituents on the aromatic ring) and the total range of $E_{1/2}$ is only

about 100 mV wide (from –337 to –482 mV vs. Fc). This again, implies that the geometry in [$CoL^{5\text{-gem}}$] most likely influences the shift in redox potential greatly.

4.8 Initial Studies on Allylic Oxidation

Initial studies on the reactivity of allylic oxidation of cyclohexene (see introductory section) were conducted in two solvents using molecular oxygen as the oxidant (see experimental section for reaction details) and cyclohexene was freshly distilled before the reactions. First a study in MeCN was performed, where the two copper complexes ([$CuL^{5\text{-ortho}}$] and [$CuL^{5\text{-gem}}$]) were evaluated on their performance for selectivity and catalytic enhancement of the reaction (see Figure 4.26).

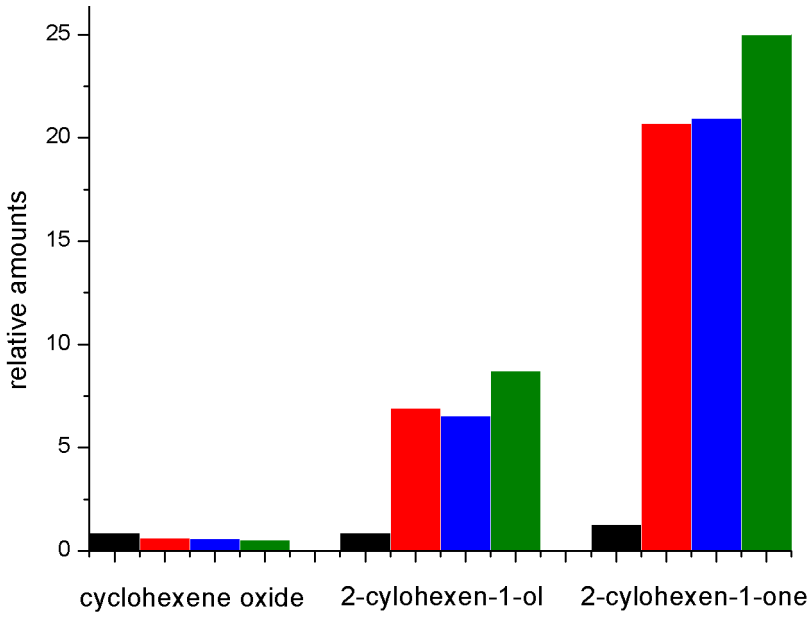

Figure 4.26. Product formation upon allylic oxidation of cylohexene in MeCN (all data is presented as a ratio to same amounts of the internal standard naphthalene). Black: no catalyst (auto oxidation); red: [$CuL^{5\text{-ortho}}$]; blue: [$CuL^{5\text{-gem}}$]; green:$CuCl_2$.

In the presence of molecular oxygen, cyclohexene can autooxidize to cyclohexene oxide, 2-cyclohexen-1-ol and 2-cyclohexen-1-one. Only small amounts of

these oxidation products are detected though as seen in Figure 4.26, black bars. In the presence of copper(II) ions (see red, blue and green bars in Figure 4.26) the reactivity can be enhanced. It appears that favorably 2-cyclohexen-1-ol (about seven times more) and 2-cyclohexen-1-one (about 20-fold more) are formed when copper complexes are present, while the amount of cyclohexene oxide created is about the same as if no catalyst is present. It is also worth mentioning that [$CuL^{5\text{-ortho}}$] and [$CuL^{5\text{-gem}}$] are more selective towards almost exclusively forming the main oxidation products, while "free", non-ligated copper(II) ions (see chromatogram in Figure 4.27) create a variety of additional oxidation products such as 1,2-cyclohexanediol, cyclohex-2-ene-1,4-dione, 2-hydroxy-cyclohexanone.

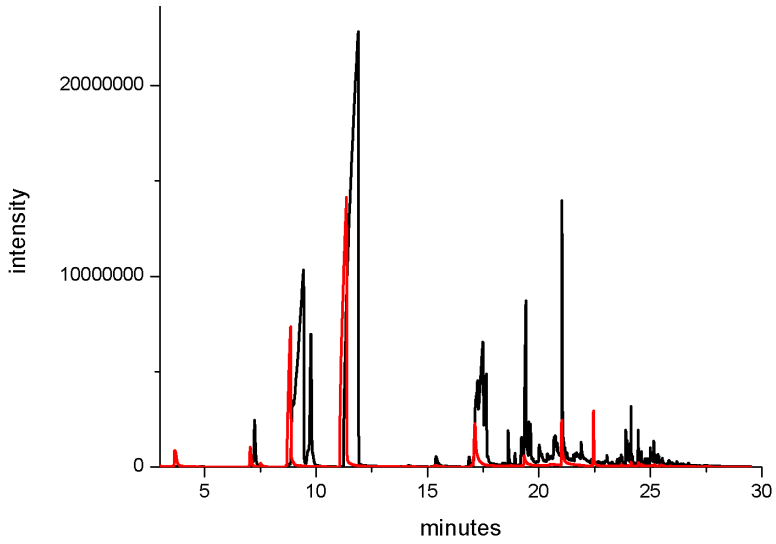

Figure 4.27. Overlay of chromatograms after oxidation of cyclohexene. Red: in the presence of [$CuL^{5\text{-gem}}$]; black: in the presence of $CuCl_2$. Major oxidation products are: at 7.0 min. cyclohexene oxide; at 8.8 min. 2-cyclohexen-1-ol; at 11.2 min. 2-cyclohexen-1-one (internal standard naphthalene at 21.3 min.).

To investigate whether the strain in [$CuL^{5\text{-ortho}}$] or [$CuL^{5\text{-gem}}$] further enhances the reactivity and/or selectivity of this reaction, Cu(II)salen (which has square planar geometry) was prepared according to a literature procedure [63]. Unfortunately, Cu(II)

salen is insoluble in MeCN (most likely because of its stacked dimer structure [64]), and therefore reactions had to be repeated in CH_2Cl_2 solutions.

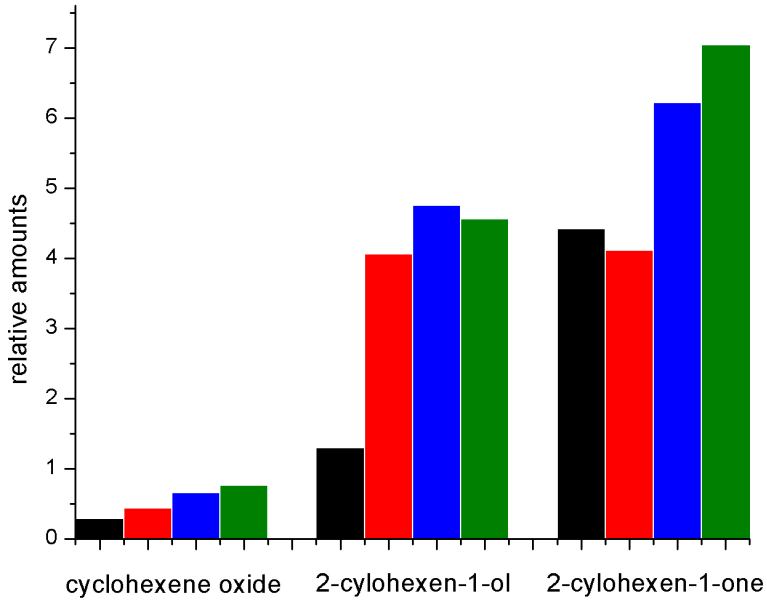

Figure 4.28. Product formation upon allylic oxidation of cylohexene in CH_2Cl_2 (all data is presented as a ratio to same amounts of the internal standard naphthalene). Black: no catalyst (auto oxidation); red: [$CuL^{5\text{-ortho}}$]; blue: [$CuL^{5\text{-gem}}$]; green:Cu(II)salen.

The reaction in methylene chloride overall suggests that copper ions do not enhance product formation by much (there is some increase in formation of 2-cylohexen-1-ol by less than four-fold with any of the copper(II) complexes used). The square planar Cu(II)salen complex yields about the same product distribution as well as amounts of oxidation products as the strained complexes synthesized in this work (see Figure 4.28). However, it may not be fair to evaluate the effect of strain in this particular reaction because all copper(II) complexes perform poorly in dichloromethane, and unfortunately, Cu(II)salen is insoluble in acetontrile, where the allylic oxidation occurs more favorably.

4.9 Conclusion

It appears that $H_2L^{5\text{-ortho}}$ and $H_2L^{5\text{-gem}}$, when coordinating to copper(II) ions, induce strain to the coordination geometry in the complex in the solid state. EPR and CV measurements further indicate that strain is also present in solution. In nature, copper is readily found in strained geometries (see blue copper proteins) whereas other metals typically don't undergo geometrical strain (here between square planar and tetrahedral). Thus it is not surprising that it was not possible to easily isolate any other metal complexes besides the ones with copper ions in the solid state. Even the cobalt(II) complex, which was characterized in the solid state, most likely underwent dimerization to prevent the strained tetradentate coordination and rather formed a trigonal bipyramide. In solution, the strain in the complexes may be slightly released. Therefore, other metals should form complexes with the two ligands in solution. In fact, this is indicated by the color change of metal salt addition to ligand ($H_2L^{5\text{-ortho}}$) solutions in the presence of base (see Figure 4.29 left). Figure 4.29 right shows the colors of the divalent metal salts in methanol. It seems reasonable to say that Mn, Co and Fe most certainly are coordinated in solution as indicated by the significant color change. Judging only by the change in color it can not be concluded, if Zn and Ni are coordinated because the ligand is yellow and Zn^{2+} does not contribute to changes in the visible spectrum due to the d^{10} configuration. In the case of Ni the problem of weak solubility occurred (see Figure 4.29 left and right, suspension with Ni).

Figure 4.29. Left: colored solutions of divalent metal ions with $H_2L^{5\text{-ortho}}$ (Zn, Mn, Co, Ni, Fe: from left to right). Right: solutions of the corresponding metal ions in methanol.

Since catalysis reactions are perfomed in solution, it is not necessary to actually isolate the solid structures of metal complexes. These initial results are promising that other metal complexes can be generated in the solution state and should be tested for catalytic activity. Initial studies on the allylic oxidation of cyclohexene using [$CuL^{5\text{-ortho}}$] and [$CuL^{5\text{-gem}}$] reveal that these complexes are selective towards formation of 2-cyclohexen-1-ol and even more towards 2-cyclohexen-1-one. It was not possible to evaluate, if the strain iduced on the copper(II) ion would enhance selectivity and reactivity.

4.10 Future Work

Further experiments on the allylic oxidation, perhaps in a different solvent, should be conducted to evaluate if the strain induced in the new complexes, [$CuL^{5\text{-ortho}}$] and [$CuL^{5\text{-gem}}$], enhances reactivity and selectivity towards the oxidation products. Maybe a different model complex (with better solubility in MeCN), other than Cu(II)salen, can be used for comparison. Additionally, the new copper(II) complexes

should be tested as catalysts for other types of reactions. Both complexes are chiral and therefore could be used in asymmetric catalysis.

Initial studies on complex formation of $H_2L^{5\text{-ortho}}$ with other divalent metal ions revealed that complexes, even though unable to isolate in the solid state, are formed. Most likely these complexes have some geometrical strain, just like the copper(II) complexes and for that reason it would be very interesting to test their potency as catalysts as well.

4.11 Experimental

4.11.1 General Procedures

Unless otherwise stated, all reagents were used as received from commercial sources. Pseudo-ortho-N,N'-bissalicylidene-4,16-diamino[2.2]paracyclophane was resynthesized according to the procedure described by Morvant [34]. The novel ligand pseudo-gem-N,N'-bissalicylidene-4,15-diamino[2.2]paracyclophane was prepared in the same way. Solvents used were doubly purified using alumina columns in a MBraun solvent purification system (MB-SPS). Infrared spectra were measured from 4000 to 400 cm^{-1} as KBr pellets on a BIO-RAD FTS 155 FTIR spectrometer. ^1H NMR spectra were measured using a Varian 300 MHz instrument using solvent ($CHCl_3$) as an internal standard. Mass spectra were measured on a Q-TOF quadrupole time-of-flight mass spectrometer (Micromass, Manchester, U.K.) equipped with a Z-spray electrospray ionization (ESI) source. Elemental analyses were performed by Atlantic Microlab, Norcross, GA. UV-visible spectra were measured using a Shimadzu UV2401PC spectrophotometer in the range 250 to 900 nm on solutions ranging in concentration from 1.0×10^{-3} M to 1.0×10^{-5} M. Cyclic voltammetry experiments were

performed using a BAS 50W potentiometer and a standard three-electrode cell with a glassy-carbon working electrode, a Pt-wire auxiliary electrode, and an Ag/AgCl pseudo-reference electrode under an inert atmosphere at room temperature. X-band EPR spectra of the complexes were recorded at 295 K and 77 K using a Bruker EMX spectrometer. Solution magnetic susceptibilities were measured at 294 K by the Evans method. GC-MS measurements were performed on an Agilent/HP 6980 gas chromatograph with 5973 mass spectrometric detector (Santa Clara, CA) and Alltech EC-5 column (GRACE, Deerfield, IL). The inlet and transfer line were held at 200° C and 280° C, respectively. With helium as the carrier gas and a split ratio of 10:1, the GC was run in constant flow mode with a total flow of 25.2 mL/min. The oven temperature program was as follows: 35° C for 5 minutes, 2° C /minute to 60° C, 20° C/minute to 200° C, and hold for 5 minutes at 200° C. The oxidation products were matched to the National Institute of Standards and Technology's (NIST) 2008 library of mass spectral data.

Caution! *Perchlorate salts of metal complexes with organic ligands are potentially explosive. Although no difficulty was encountered during the syntheses described herein, they should be prepared in small amounts and handled with caution.*

4.11.2 Synthesis of ($H_2L^{5\text{-ortho}}$)

Salicylic aldehyde (0.212g, 1.736 mmol) was added dropwise to a solution of pseudo-ortho-4,16-diamino[2.2]paracyclophane (0.199 g, 0.836 mmol) in EtOH (20 mL). The resulting yellow slurry was heated to reflux the solvent for two hours. After several minutes all material dissolved and 10 min. later the product started to precipitate

out of the solution. Once cooled to room temperature, the precipitate was collected through filtration. $H_2L^{5\text{-ortho}}$ was further dried under high vacuum yielding a fluffy bright yellow solid (0.320 g, 86 %). M.p. 228–230° C. ^{1}H NMR (300 MHz, $CDCl_3$, 293K) δ 2.78–2.93 (m, 2H, –C<u>H</u>$_2$–), 3.10–3.25 (m, 4H, –C<u>H</u>$_2$–), 3.58–3.68 (m, 2H, –C<u>H</u>$_2$–), 6.46 (s, 2H, Ar–<u>H</u>), 6.62 (dd, 4H, Ar–<u>H</u>), 6.83 (t, 2H, Ar–<u>H</u>), 7.03 (m, 4H, Ar–<u>H</u>), 7.36 (t, 2H, Ar–<u>H</u>), 8.25 (s, 2H, N=C–<u>H</u>), 13.77 (s, 2H, –O<u>H</u>). UV/Vis (CH_2Cl_2) [λ_{max}, nm (ε, $M^{-1}cm^{-1}$)]: 231(43,200), 267 (31,100), 353 (27,100). FTIR (KBr): 2930, 1614 (C=N), 1578, 1555, 1485, 1456, 1408, 1281 (phenolate O–C), 1204, 1150, 905, 893, 876, 837, 822, 797, 750, 723, 652, 492 cm^{-1}.

4.11.3 Synthesis of ($H_2L^{5\text{-gem}}$)

Salicylic aldehyde (0.115g, 0.943 mmol) was added dropwise to a solution of pseudo-gem-4,15-diamino[2.2]paracyclophane (0.102 g, 0.429 mmol) in EtOH (10 mL). The resulting yellow slurry was heated to reflux the solvent for two hours. After several minutes all material dissolved and 10 min. later the product started to precipitate out of the solution. Once cooled to room temperature, the precipitate was collected through filtration. $H_2L^{5\text{-gem}}$ was further dried under high vacuum yielding a fluffy yellow-orange solid (0.150 g, 78 %). M.p. 233–235° C. ^{1}H NMR (300 MHz, $CDCl_3$, 293K) δ 3.02–3.20 (m, 6H, –C<u>H</u>$_2$–), 3.69–3.78 (m, 2H, –C<u>H</u>$_2$–),6.36 (s, 2H, Ar–<u>H</u>), 6.54–6.73 (m, 8H, Ar–<u>H</u>), 7.08 (d, 2H, Ar–<u>H</u>), 7.14 (t, 2H, Ar–<u>H</u>), 8.27 (s, 2H, N=C–<u>H</u>), 13.25 (s, 2H, –O<u>H</u>). UV/Vis (CH_2Cl_2) [λ_{max}, nm (ε, $M^{-1}cm^{-1}$)]: 230 (40,900), 275 (27,500), 346 (28,000). FTIR (KBr): 2918, 2849, 1614 (C=N), 1576, 1549, 1479, 1454, 1408, 1364, 1283 (phenolate O–C), 1206, 1144, 964, 907, 876, 791, 745, 482 cm^{-1}.

4.11.4 Synthesis of [CuL$^{5\text{-ortho}}$]

Anhydrous $CuCl_2$ (0.030 g, 0.223 mmol) dissolved in methanol (1 mL) was added to a suspension of ligand $H_2L^{5\text{-ortho}}$ (0.099 g, 0.222 mmol) in CH_3OH (50 mL) and NEt_3 (0.045 mg, 0.446 mmol). The resulting light green solution containing white solid was heated to reflux the solvent overnight to yield a brown-reddish clear solution. Upon cooling to room temperature, the solvent was removed under reduced pressure and subsequently redissolved in toluene. X-ray quality crystals (orange-brown) were obtained upon pentane diffusion into the filtered toluene solution (0.068 g, 61 %). Anal. Calcd for [$CuL^{5\text{-ortho}}$], $C_{30}H_{24}CuN_2O_2$: C, 70.92; H, 4.76; N, 5.51. Found: C, 70.05; H, 4.58; N, 5.43. UV/Vis (CH_3CN) [λ_{max}, nm (ε, $M^{-1}cm^{-1}$)]: 224 (47,500), 275 (32,400), 393 (18,600). EPR (9.469 GHz, mod. amp. 25.0 G, toluene, 77 K): $g_{\|}$ = 2.25, $g_{\perp}$ = 2.05, and $A_{\|}$ = 155 G; (9.748 GHz, mod. amp. 25.0 G, toluene, 298 K): g_{iso} = 2.13, A_{iso} = 60 G. FTIR (KBr): 1609 (C=N), 1584, 1530, 1464, 1441, 1410, 1377, 1327, 1196, 1148, 916, 887, 758, 577 cm^{-1}. ESI-MS (CH_3CN): *m/z* = 508.1210 [Cu($L^{5\text{-ortho}}$)] + H^+, 1015.2342 [Cu($L^{5\text{-ortho}}$)]$_2$ + H^+. Solution magnetic moment (Evans method, 293.95 K, 34.9 x 10^{-3} M, $CDCl_3$): 1.53 μ_B/Cu.

4.11.5 Synthesis of [CuL$^{5\text{-gem}}$]

Anhydrous $CuCl_2$ (0.020 g, 0.149 mmol) dissolved in methanol (1 mL) was added to a suspension of ligand $H_2L^{5\text{-gem}}$ (0.063 g, 0.141 mmol) in CH_3OH (50 mL) and NEt_3 (0.020 mg, 0.287 mmol). The resulting light green solution containing white solid was heated to reflux the solvent overnight to yield a brown-yellow clear solution. Upon cooling to room temperature, the solvent was removed under reduced pressure and

subsequently redissolved in toluene. Crystals (yellow-brown) were obtained upon pentane diffusion into the filtered toluene solution (0.038 g, 53 %). Initially X-ray quality crystals were obtained from slow evaporation of a methanolic solution of the crude complex. Anal. Calcd for [$CuL^{5\text{-gem}}$], $C_{30}H_{24}CuN_2O_2$: C, 70.92; H, 4.76; N, 5.51. Found: C, 71.10; H, 4.71; N, 5.52. UV/Vis (CH_3CN) [λ_{max}, nm (ε, $M^{-1}cm^{-1}$)]: 225 (57,900), 270 (32,800), 377 (17,900). EPR (9.467 GHz, mod. amp. 25.0 G, toluene, 77 K): $g_{\|}$ = 2.26, $g_{\perp}$ = 2.04, and $A_{\|}$ = 160 G; (9.748 GHz, mod. amp. 25.0 G, toluene, 298 K): g_{iso} = 2.12, and A_{iso} = 75 G. FTIR (KBr): 2928, 1607 (C=N), 1580, 1528, 1464, 1435, 1381, 1325, 1194, 1148, 1088, 1024, 920, 895, 758, 563, 519, 449 cm^{-1}. ESI-MS (CH_3CN): *m/z* = 508.1219 [$Cu(L^{5\text{-gem}})$] + H^+, 1015.2343 [$Cu(L^{5\text{-gem}})]_2$ + H^+. Solution magnetic moment (Evans method, 293.95 K, 15.8 x 10^{-3} M, $CDCl_3$): 1.63 μ_B/Cu.

4.11.6 Synthesis of [$CoL^{5\text{-gem}}$]$_2$

$Co(ClO_4)_2 \cdot 6H_2O$ (0.015 g, 0.041 mmol) dissolved in methanol (1 mL) was added to a solution of ligand $H_2L^{5\text{-gem}}$ (0.015 g, 0.034 mmol) in 1:1 CH_3OH:CH_2Cl_2 (2 mL) and NEt_3 (0.080 mg, 0.079 mmol). The resulting brown-orange solution was stirred for one hour at room temperature and subsequently the solvent was removed under reduced pressure. The crude residue was redissolved in CH_2Cl_2 and filtered through celite. About the same amount of MeOH as CH_2Cl_2, was added to the solution. Crystals (pink-purple) were obtained upon slow evaporation of the solution (0.013 g, 75 %). UV/Vis (CH_2Cl_2) [λ_{max}, nm (ε, $M^{-1}cm^{-1}$)]: 230 (56,100), 269 (30,800), 373 (14,200). EPR in CH_2Cl_2 is silent at room temperature as well as 77 K and NMR appears to be paramagnetic. FTIR (KBr): 2928, 1605 (C=N), 1580, 1560, 1528, 1510, 1491, 1466,

1439, 1412, 1321, 1300, 1192, 1152, 914, 760, 669, 662 cm^{-1}. ESI-MS (CH_2Cl_2): *m/z* = 504.1244 $[Co(L^{5\text{-gem}})] + H^+$, *m/z* = 1007.2400 $[Co(L^{5\text{-gem}})]_2 + H^+$.

4.11.7 Allylic Oxidation in MeCN

In a typical experiment 0.006 mmol of copper(II) complex (in the case of the blank no copper ions were used) was dissolved in MeCN (2 mL). After all complex was dissolved under stirring, 100 μL (0.987 mmol, ~160 equivalents) of freshly distilled cyclohexene were added and the solution mixture was purged with dioxygen for 120 s. Subsequently the reaction vial was sealed with tape and stirred at room temperature for two days. Solutions were kept sealed for three more days without stirring and then analyzed via GC-MS. Thereafter, 500 μL of each reaction mixture was taken out and to that 50 μL of internal standard (naphthalene), with the same concentration for each sample, was added. 1 μL of this solution was injected into the GC and analyzed. The amounts of products in each sample are ratios of product to the internal standard and allow for qualitative analysis.

4.11.8 Allylic Oxidation in CH_2Cl_2

In a typical experiment 0.006 mmol of copper(II) complex/salt (in the case of the blank no copper ions were used) was dissolved in CH_2Cl_2 (2 mL). After all complex was dissolved under stirring, 50 μL (0.494 mmol, ~80 equivalents) of freshly distilled cyclohexene was added and the solution mixture was purged with dioxygen for 120 s. Subsequently the reaction vial was sealed with tape and stirred at room temperature for two days. 450 μL of each reaction mixture was taken out of the vial and to that 50 μL

(0.0005 mmol) of internal standard (naphthalene) was added. 2 μL of this solution was injected into the GC and analyzed. The amounts of products in each sample are ratios of product to the internal standard and allow for qualitative analysis.

4.11.9 X-ray Crystal Structure Determination

Single crystals of $[CuL^{5\text{-gem}}]_2 \cdot CH_3OH$ were obtained from slow evaporation of a methanolic solution of the crude complex. X-ray quality crystals of $[CuL^{5\text{-ortho}}]$ were obtained by diffusion of pentane into a toluene solution of $[CuL^{5\text{-ortho}}]$. Single crystals of $[CoL^{5\text{-gem}}]_2 \cdot CH_2Cl_2$ were obtained by slow evaporation of a mixture of methanol and dichloromethane solution of $[CoL^{5\text{-gem}}]$. Intensity data for all the compounds were collected using a diffractometer with a Bruker APEX ccd area detector [65, 66] and graphite-monochromated Mo-*K*α radiation (λ = 0.71073 Å). The samples were cooled to 100(2) K. Cell parameters were determined from a non-linear least-squares fit of the data. The data were corrected for absorption by the semi-empirical method [67]. The structure was solved by direct methods and refined by full-matrix least-squares methods on F^2 [68, 69]. Hydrogen atom positions of hydrogen atoms bonded to carbon atoms were initially determined by geometry and were refined by a riding model. Hydrogen atoms bonded to nitrogen or oxygen atoms were located on a difference map, and their positions were refined independently. The hydrogen bonded to the methanol oxygen in $[CuL^{5\text{-gem}}]_2 \cdot (CH_3OH)$ was located on a difference map, and its position was refined independently. Non-hydrogen atoms were refined with anisotropic displacement parameters. Hydrogen atom displacement parameters were set to 1.2 (1.5 for methyl) times the displacement parameters of the bonded atoms. Crystal data for

$[CuL^{5\text{-gem}}]_2\cdot(CH_3OH)$, $[CuL^{5\text{-ortho}}]$ and $[CoL^{5\text{-gem}}]_2\cdot CH_2Cl_2$ are summarized in Table 4.6 and 4.7. Selected bond lengths and angles for $[CuL^{5\text{-gem}}]_2\cdot(CH_3OH)$, $[CuL^{5\text{-ortho}}]$ and $[CoL^{5\text{-gem}}]_2\cdot CH_2Cl_2$ are summarized in Table 4.3 and 4.4. Hydrogen bonds for $[CuL^{5\text{-gem}}]_2\cdot(CH_3OH)$ are listed in Table 4.2.

Table 4.6. Crystallographic data for [$CuL^{5\text{-gem}}$] and [$CuL^{5\text{-ortho}}$].

	[$CuL^{5\text{-gem}}$]	[$CuL^{5\text{-ortho}}$]
formula	$2(C_{30}H_{24}CuN_2O_2)\cdot(CH_3OH)$	$C_{30}H_{24}CuN_2O_2$
fw	1048.15	508.05
Crystal system	Monoclinic	Monoclinic
Space group	$P2_1/n$	$C2/c$
a (Å)	20.822(3)	21.4538(11)
b (Å)	10.3572(14)	17.2128(8)
c (Å)	22.863(3)	12.4304(6)
α (deg)	90	90
β (deg)	103.371(2)	104.502(2)
γ (deg)	90	90
V (Å^3)	4796.9(11)	4444.0(4)
Z, Z'	4, 2	8, 1
ρ_{calcd} mg/m^3	1.451	1.519
μ (mm^{-1})	0.945	1.016
θ (deg)	1.83 to 26.11°	1.54 to 28.32
$R1$,[a] $wR2$[b] [$I > 2\sigma(I)$]	0.0618, 0.1530	0.0442, 0.1086
GOF on F^2	1.000	1.024

(a) $R1 = \Sigma||F_{obs}| - |F_{cacl}|| / \Sigma|F_{obs}|$. (b) $wR2 = \{\Sigma[w(F_{obs}^2 - F_{calc}^2)^2] / \Sigma[w(F_{obs}^2)^2]\}^{½}$.

Table 4.7. Crystallographic data for $[CoL^{5\text{-gem}}]_2$.

	$[CoL^{5\text{-gem}}]_2$
formula	$(C_{60}H_{48}Co_2N_4O_4)\cdot(CH_2Cl_2)$
fw	1091.81
Crystal system	Monoclinic
Space group	$P2_1/n$
a (Å)	10.9375(8)
b (Å)	33.881(2)
c (Å)	13.1335(9)
α (deg)	90
β (deg)	92.335(2)
γ (deg)	90
V (Å^3)	4862.9(6)
Z, Z'	4, 1
ρ_{calcd} mg/m^3	1.491
μ (mm^{-1})	0.849
θ (deg)	1.66 to 28.31
$R1$,[a] $wR2$[b] [$I > 2\sigma(I)$]	0.0666, 0.1670
GOF on F^2	1.092

(a) $R1 = \Sigma||F_{obs}| - |F_{cacl}|| / \Sigma|F_{obs}|$. (b) $wR2 = \{\Sigma[w(F_{obs}^2 - F_{calc}^2)^2] / \Sigma[w(F_{obs}^2)^2]\}^{½}$.

4.12 References

1. Bertini, G., Stiefel, Valentine, *Biological Inorganic Chemistry Structure & Reactivity*, ed. J. Stiefel. 2007, USA: University Science Books.

2. Mitchell Guss, J.; Freeman, H. C., *Structure of oxidized poplar plastocyanin at 1·6 Å resolution.* Journal of Molecular Biology **1983,** *169*, 521-563.

3. Piontek, K.; Antorini, M.; Choinowski, T., *Crystal Structure of a Laccase from the FungusTrametes versicolor at 1.90-Å Resolution Containing a Full Complement of Coppers.* Journal of Biological Chemistry **2002,** *277*, 37663-37669.

4. Yamada, T.; Hiraoka, Y.; Gupta, T. K. D.; Chakrabarty, A. M., *Rusticyanin, a Bacterial Electron Transfer Protein, Causes G1 Arrest and Apoptosis in Human Cancer Cells.* Cell Cycle **2004,** *3*, 1180-1185.

5. Walter, R. L.; Ealick, S. E.; Friedman, A. M.; Blake Ii, R. C.; Proctor, P.; Shoham, M., *Multiple Wavelength Anomalous Diffraction (MAD) Crystal Structure of Rusticyanin: a Highly Oxidizing Cupredoxin with Extreme Acid Stability.* Journal of Molecular Biology **1996,** *263*, 730-751.

6. Petratos, K.; Papadovasilaki, M.; Dauter, Z., *The crystal structure of apo-pseudoazurin from Alcaligenes faecalis S-6.* FEBS Letters **1995,** *368*, 432-434.

7. Paraskevopoulos, K.; Sundararajan, M.; Surendran, R.; Hough, M. A.; Eady, R. R.; Hillier, I. H.; Hasnain, S. S., *Active site structures and the redox properties of blue copper proteins: atomic resolution structure of azurin II and electronic structure calculations of azurin, plastocyanin and stellacyanin.* Dalton Transactions **2006,** *0*, 3067-3076.

8. Koch, M.; Velarde, M.; Harrison, M. D.; Echt, S.; Fischer, M.; Messerschmidt, A.; Dennison, C., *Crystal Structures of Oxidized and Reduced Stellacyanin from Horseradish Roots†.* Journal of the American Chemical Society **2004,** *127*, 158-166.

9. Gray, H. B.; Malmström, B. G.; Williams, R. J. P., *Copper coordination in blue proteins.* J. Biol. Inorg. Chem. **2000,** *5*, 551-559.

10. Guss, J. M.; Bartunik, H. D.; Freeman, H. C., *Accuracy and precision in protein structure analysis: restrained least-squares refinement of the structure of poplar plastocyanin at 1.33 A resolution.* Acta Crystallographica Section B **1992,** *48*, 790-811.

11. Solomon, E. I.; Szilagyi, R. K.; DeBeer George, S.; Basumallick, L., *Electronic Structures of Metal Sites in Proteins and Models: Contributions to Function in Blue Copper Proteins.* Chemical Reviews **2004,** *104*, 419-458.

12. Malmström, B., *Rack-induced bonding in blue-copper proteins*, in *EJB Reviews 1994*. 1995, Springer Berlin Heidelberg. p. 157-164.

13. Vallee, B. L.; Williams, R. J., *Metalloenzymes: the entatic nature of their active sites.* Proceedings of the National Academy of Sciences **1968,** *59*, 498-505.

14. Williams, R. J. P., *Energised (entatic) states of groups and of secondary structures in proteins and metalloproteins.* European Journal of Biochemistry **1995,** *234*, 363-381.

15. Marcus, R. A.; Sutin, N., *Electron transfers in chemistry and biology.* Biochimica et Biophysica Acta (BBA) - Reviews on Bioenergetics **1985,** *811*, 265-322.

16. Rorabacher, D. B., *Electron Transfer by Copper Centers.* Chemical Reviews **2004,** *104*, 651-698.

17. Holm, R. H.; Kennepohl, P.; Solomon, E. I., *Structural and Functional Aspects of Metal Sites in Biology.* Chemical Reviews **1996,** *96*, 2239-2314.

18. Sykes, A. G., *Active-Site Properties Of The Blue Copper Proteins*, in *Advances in Inorganic Chemistry*, A.G. Sykes, Editor. 1991, Academic Press. p. 377-408.

19. Solomon, E.; Penfield, K.; Wilcox, D., *Active sites in copper proteins an electronic structure overview*, in *Copper, Molybdenum, and Vanadium in Biological Systems*. 1983, Springer Berlin Heidelberg. p. 1-57.

20. Solomon, E. I.; Hadt, R. G., *Recent advances in understanding blue copper proteins.* Coordination Chemistry Reviews **2011,** *255*, 774-789.

21. Malmström, B. G.; Vänngård, T., *Electron spin resonance of copper proteins and some model complexes.* Journal of Molecular Biology **1960,** *2*, 118-124.

22. Yoon, J.; Solomon, E. I., *High Resolution EPR Applications to Metalloenzymes and Metals in Mediciine*, ed. L.B. Graeme Hanson. 2009: Springer.

23. Potapov, A.; Lancaster, K. M.; Richards, J. H.; Gray, H. B.; Goldfarb, D., *Spin Delocalization Over Type Zero Copper.* Inorganic Chemistry **2012,** *51*, 4066-4075.

24. Comba, P., *Coordination compounds in the entatic state.* Coordination Chemistry Reviews **2000,** *200–202*, 217-245.

25. Lipkowitz, K. B.; Schefzick, S.; Avnir, D., *Enhancement of Enantiomeric Excess by Ligand Distortion.* Journal of the American Chemical Society **2001,** *123*, 6710-6711.

26. You, M.; Seo, M. S.; Kim, K. M.; Nam, W.; Kim, J., *Structure and Properties of a Nonheme Pentacoordinate Iron(II) Complex with a Macrocyclic Triazapyridinophane Ligand.* Bulletin of the Korean Chemical Society **2006,** *27*, 1140-1144.

27. Chung, T. C.; Lu, H. L.; Li, C. L., *Functionalization of polyethylene using borane reagents and metallocene catalysts.* Polymer International **1995,** *37*, 197-205.

28. Whitehorne, T. J. J.; Schaper, F., *Nacnac BnCuOiPr: a strained geometry resulting in very high lactide polymerization activity.* Chemical Communications **2012,** *48*, 10334-10336.

29. Huang, H.; Peters, R., *A Highly Strained Planar-Chiral Platinacycle for Catalytic Activation of Internal Olefins in the Friedel–Crafts Alkylation of Indoles.* Angewandte Chemie International Edition **2009,** *48*, 604-606.

30. Masterson, D. S.; Hobbs, T. L.; Glatzhofer, D. T., *Catalytic enantioselective cyclopropanation of olefins using N-salicylidene-4-amino[2.2]paracyclophane as an asymmetric ligand.* Journal of Molecular Catalysis A: Chemical **1999,** *145*, 75-81.

31. Masterson, D. S.; Glatzhofer, D. T., *Catalytic enantioselective cyclopropanation of styrene derivatives using N-(2',4'-di-tert-butyl)salicylidene-4-amino[2.2]paracyclophane as an asymmetric ligand.* Journal of Molecular Catalysis A: Chemical **2000,** *161*, 65-68.

32. Masterson, D. S.; Shirley, C.; Glatzhofer, D. T., *N-(4-[2.2]paracyclophanyl)-2'-hydroxyacetophenone imine: An effective paracyclophane Schiff-base ligand for use in catalytic asymmetric cyclopropanation reactions.* Journal of Molecular Catalysis A: Chemical **2012,** *361–362*, 111-115.

33. Nozaki, H.; Moriuti, S.; Takaya, H.; Noyori, R., *Asymmetric induction in carbenoid reaction by means of a dissymmetric copper chelate.* Tetrahedron Letters **1966,** *7*, 5239-5244.

34. Morvant, M. C., *Synthesis, Properties, and applications of polynitro- and polyamino[2.2]paracyclophanes.* Dissertation **1996,** Norman, Oklahoma.

35. Andrus, M. B.; Lashley, J. C., *Copper catalyzed allylic oxidation with peresters.* Tetrahedron **2002,** *58*, 845-866.

36. Rawlinson, D. J.; Sosnovsky, G., *One-Step Substitutive Acyloxylation at Carbon. Part I. Reactions Involving Peroxides.* Synthesis **1972,** *1972*, 1-28.

37. Umbreit, M. A.; Sharpless, K. B., *Allylic oxidation of olefins by catalytic and stoichiometric selenium dioxide with tert-butyl hydroperoxide.* Journal of the American Chemical Society **1977,** *99*, 5526-5528.

38. Rappoport, Z.; Winstein, S.; Young, W. G., *Allylic oxidation of olefins by mercuric acetate.* Journal of the American Chemical Society **1972,** *94*, 2320-2329.

39. McMurry, J. E.; Kočotovský, P., *A method for the palladium-catalyzed allylic oxidation of olefins.* Tetrahedron Letters **1984,** *25*, 4187-4190.

40. Chang, Y.; Lv, Y.; Lu, F.; Zha, F.; Lei, Z., *Efficient allylic oxidation of cyclohexene with oxygen catalyzed by chloromethylated polystyrene supported tridentate Schiff-base complexes.* Journal of Molecular Catalysis A: Chemical **2010,** *320*, 56-61.

41. Chang, Y.; Wang, Y.; Zha, F.; Wang, R., *Preparation and catalytic properties of chitosan bound Schiff base copper complexes.* Polymers for Advanced Technologies **2004,** *15*, 284-286.

42. Yun, X.; Hu, X.; Jin, Z.; Hu, J.; Yan, C.; Yao, J.; Li, H., *Copper-salen catalysts modified by ionic compounds for the oxidation of cyclohexene by oxygen.* Journal of Molecular Catalysis A: Chemical **2010,** *327*, 25-31.

43. Bhunora, S.; Mugo, J.; Bhaw-Luximon, A.; Mapolie, S.; Van Wyk, J.; Darkwa, J.; Nordlander, E., *The use of Cu and Zn salicylaldimine complexes as catalyst precursors in ring opening polymerization of lactides: ligand effects on polymer characteristics.* Applied Organometallic Chemistry **2011,** *25*, 133-145.

44. Yadav, L. D. S., *Organic Spectroscopy*. 2005, U.S.A.: Kluwer Academic Publisher.

45. Zhang, Y.-L.; Ruan, W.-J.; Zhao, X.-J.; Wang, H.-G.; Zhu, Z.-A., *Synthesis and characterization of axial coordination cobalt(III) complexes containing chiral Salen ligands.* Polyhedron **2003,** *22*, 1535-1545.

46. Narayanan, J.; Solano-Peralta, A.; Ugalde-Saldivar, V. M.; Escudero, R.; Höpfl, H.; Sosa-Torres, M. E., *New dinuclear cobalt(II) octaaza macrocyclic complexes with high oxidation redox potentials: Their crystal structure and unusual magnetic properties.* Inorganica Chimica Acta **2008,** *361*, 2747-2758.

47. Yang, L.; Powell, D. R.; Houser, R. P., *Structural variation in copper(i) complexes with pyridylmethylamide ligands: structural analysis with a new four-coordinate geometry index, [small tau]4.* Dalton Transactions **2007,** *0*, 955-964.

48. Addison, A. W.; Rao, T. N.; Reedijk, J.; van Rijn, J.; Verschoor, G. C., *Synthesis, structure, and spectroscopic properties of copper(II) compounds containing nitrogen-sulphur donor ligands; the crystal and molecular structure of aqua[1,7-bis(N-methylbenzimidazol-2[prime or minute]-yl)-2,6-dithiaheptane]copper(II) perchlorate.* Journal of the Chemical Society, Dalton Transactions **1984,** *0*, 1349-1356.

49. Evans, D. F., *400. The determination of the paramagnetic susceptibility of substances in solution by nuclear magnetic resonance.* Journal of the Chemical Society (Resumed) **1959,** *0*, 2003-2005.

50. Grant, D. H., *Paramagnetic Susceptibility by NMR: The "Solvent Correction" Reexamined.* Journal of Chemical Education **1995,** *72*, 39.

51. Szlyk, E.; Surdykowski, A.; Barwiolek, M.; Larsen, E., *Spectroscopy and stereochemistry of the optically active copper(II), cobalt(II) and nickel(II) complexes with Schiff bases N,N'-(1R,2R)-(−)-1,2-cyclohexylenebis(3-methylbenzylideneiminato) and N,N'-(1R,2R)-(−)-1,2-cyclohexylenebis(5-methylbenzylideneiminato).* Polyhedron **2002,** *21*, 2711-2717.

52. Matsunaga, Y.; Fujisawa, K.; Ibi, N.; Miyashita, Y.; Okamoto, K.-i., *Structural and Spectroscopic Characterization of First-Row Transition Metal(II) Substituted Blue Copper Model Complexes with Hydrotris(pyrazolyl)borate.* Inorganic Chemistry **2004,** *44*, 325-335.

53. Astley, T.; Headlam, H.; Hitchman, M. A.; Keene, F. R.; Pilbrow, J.; Stratemeier, H.; Tiekink, E. R. T.; Zhong, Y. C., *Crystal structures and electron paramagnetic resonance spectra of [Cu{P(C5H4N)3}2]Br2[middle dot]8H2O and Cu2+-doped [Zn{P(C5H4N)3}2]Br2[middle dot]8H2O, examples of a dynamic Jahn-Teller effect in two dimensions.* Journal of the Chemical Society, Dalton Transactions **1995,** *0*, 3809-3818.

54. Yokoi, H.; Addison, A. W., *Spectroscopic and redox properties of pseudotetrahedral copper(II) complexes. Their relation to copper proteins.* Inorganic Chemistry **1977,** *16*, 1341-1349.

55. Butsch, K.; Günther, T.; Klein, A.; Stirnat, K.; Berkessel, A.; Neudörfl, J., *Redox chemistry of copper complexes with various salen type ligands.* Inorganica Chimica Acta **2013,** *394*, 237-246.

56. Bhadbhade, M. M.; Srinivas, D., *Effects on molecular association, chelate conformation, and reactivity toward substitution in copper Cu(5-X-salen) complexes, salen2- = N,N'-ethylenebis(salicylidenaminato), X = H, CH3O, and Cl: synthesis, x-ray structures, and EPR investigations.* Inorganic Chemistry **1993,** *32*, 5458-5466.

57. Knapp, S.; Keenan, T. P.; Zhang, X.; Fikar, R.; Potenza, J. A.; Schugar, H. J., *Preparation, structure, and properties of pseudotetrahedral, D2d complexes of copper(II), nickel(II), cobalt(II), copper(I), and zinc(II) with the geometrically constraining bidentate ligand 2,2'-bis(2-imidazolyl)biphenyl. Examination of electron self-exchange for the Cu(I)/Cu(II) pair.* Journal of the American Chemical Society **1990,** *112*, 3452-3464.

58. Pal Chaudhuri, U.; Shakya, R.; McClain, J. M.; Klein, E. L.; Powell, D. R.; Grohmann, A.; Houser, R. P., *Copper(II), iron(II), and manganese(II) complexes of 2-methyl-2-(2-pyridinyl)-1,3-propanediamine.* Polyhedron **2013,** *54*, 84-90.

59. Jozwiuk, A.; Wang, Z.; Powell, D. R.; Houser, R. P., *Copper(II) complexes of symmetric and asymmetric bis(imine) ligands: Tuning the Cu(I)/Cu(II) redox couple.* Inorganica Chimica Acta **2013,** *394*, 415-422.

60. Shimakoshi, H.; Ninomiya, W.; Hisaeda, Y., *Reductive coupling of benzyl bromide catalyzed by a novel dicobalt complex having two salen units.* Journal of the Chemical Society, Dalton Transactions **2001,** *0*, 1971-1974.

61. Ortiz, B.; Park, S.-M., *Electrochemical and Spectroelectrochemical Studies of Cobalt Salen and Salophen as Oxygen Reduction Catalysts.* Bulletin of the Korean Chemical Society **2000,** *21*, 405-411.

62. Langmaier, J.; Trojánek, A.; Samec, Z., *Use of the 1,1'-dimethylferrocene oxidation process for the calibration of the reference electrode potential in organic solvents immiscible with water.* Journal of Electroanalytical Chemistry **2008,** *616*, 57-63.

63. Ribeiro da Silva, M. D. M. C.; Gonçalves, J. M.; Silva, A. L. R.; Oliveira, P. C. F. C.; Schröder, B.; Ribeiro da Silva, M. A. V., *Molecular thermochemical study of Ni(II), Cu(II) and Zn(II) complexes with N,N'-bis(salicylaldehydo)ethylenediamine.* Journal of Molecular Catalysis A: Chemical **2004,** *224*, 207-212.

64. Nathan, L. C.; Koehne, J. E.; Gilmore, J. M.; Hannibal, K. A.; Dewhirst, W. E.; Mai, T. D., *The X-ray structures of a series of copper(II) complexes with tetradentate Schiff base ligands derived from salicylaldehyde and polymethylenediamines of varying chain length.* Polyhedron **2003,** *22*, 887-894.

65. Bruker-AXS, *SMART Software Reference Manual*, 1998: Madison, WI, USA.

66. Bruker-AXS, *SAINT Software Reference Manual*, 1998: Madison, WI, USA.

67. Sheldrick, G. M., *SADABS Program for Empirical Absorption Correction of Area Detector Data*, 2002: University of Göttingen, Germany.

68. Sheldrick, G. M., *SHELXTL Version 6.10 Reference Manual*, B.A. Inc., Editor 2000: Madison, Wisconsin, USA.

69. *International Tables of Crystallography, vol. C*, ed. Kluwer. 1995, Boston.

Appendix A

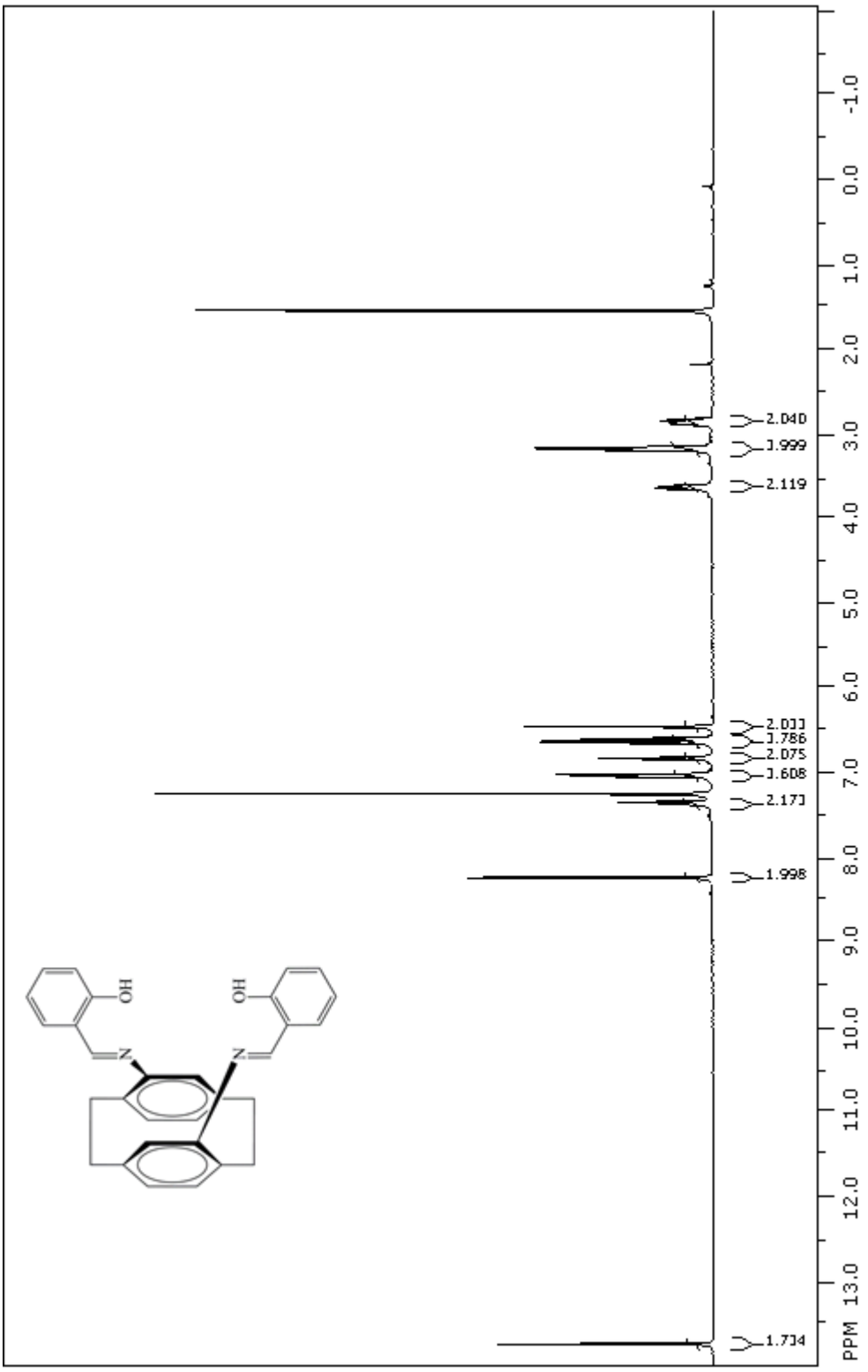

Figure A.1. ^{1}H NMR spectrum of $H_2L^{5\text{-ortho}}$.

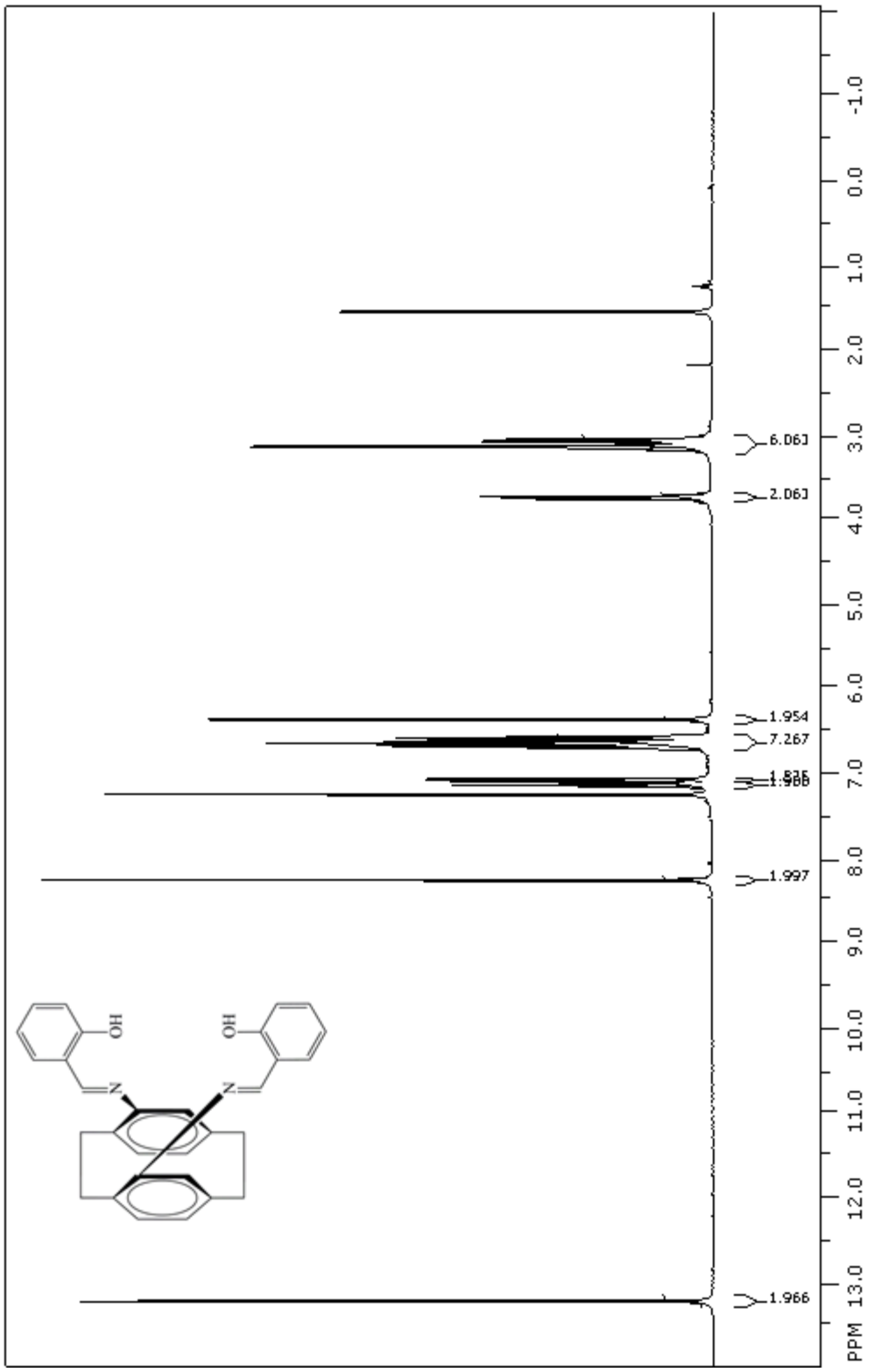

Figure A.2. ^{1}H NMR spectrum of $H_2L^{5\text{-gem}}$.